RUHR-UNIVERSITÄT BOCHUM

RUB

# A Combined Experimental and Theoretical Study on Hydroxypyrene Super-Photoacids

## Dissertation

zur Erlangung des Doktorgrades der Naturwissenschaften
**Doctor rerum naturalium (Dr. rer. nat.)**

der Fakultät für Chemie und Biochemie
der Ruhr-Universität Bochum

vorgelegt von
**Niklas Sülzner**
aus
**Dortmund**

Bochum, Januar 2023

This work has been carried out between October 2018 and August 2019 under the supervision of Prof. Dr. Patrick Nürnberger at the Department of Physical Chemistry II—Ultrafast Photochemistry Group at the Ruhr-Universität Bochum and between October 2020 and January 2023 under the supervision of Prof. Dr. Christof Hättig at the Department of Theoretical Chemistry—The Quantum Chemistry Group at the Ruhr-Universität Bochum.

Date of submission: January 10, 2023

Supervisor: Prof. Dr. Christof Hättig

Examination committee: Prof. Dr. Christof Hättig
Prof. Dr. Lars Schäfer
Prof. Dr. Patrick Nürnberger

Disputation: March 06, 2023

# Acknowledgments

This dissertation is the culmination of a highly interesting, yet also non-linear personal journey at the Ruhr-Universität Bochum (RUB) and I would like to use this opportunity to thank all the people who accompanied and supported me during these years.

First of all, I would like to thank my current supervisor, **Prof. Dr. Christof Hättig**, for giving me the opportunity to (re-)join your research group, although I had lost contact to you and your group toward the end of my Master's studies. This thesis would not exist without your share. In particular, I now value a lot your initial efforts for planning a meaningful continuation of my previous (experimental research) in order to avoid losing further time in my PhD project. Your ongoing support and your very organized and structured way of working gave me clearly defined guidance and help, whenever it was needed. You were always available for open questions and encouraged the participation at scientific conferences and workshops. In the time within your research group, I broadened my knowledge on quantum chemistry, particularly theoretical spectroscopy. Moreover, I also enjoyed our numerous group activities and your valuing of work–life balancing.

I would like to express my gratitude to my previous supervisor, **Prof. Dr. Patrick Nürnberger**, who accompanied my academic career since joining his group in my Master's studies in 2017 and later gave me the opportunity of becoming a PhD student in his group in 2018. In spite of your decision of moving to the University of Regensburg and the resulting parting of our paths, we stayed both in personal and professional good contact and it did luckily not *thwart* my proceeding time as a PhD student. And look, now our paths rejoined with you agreeing on being one of the referees for my PhD thesis! I always highly appreciated your open-minded character and our many scientific—and non-scientific—discussions. From the very first day on, I felt very welcome in your group and enjoyed the great working experience. In particular, I would like to thank you for a splendid and prolific visit in Regensburg in December, 2022 for working on getting our two manuscripts finally published. As a member of your work group, I learned a lot about the fascinating topic of time-resolved spectroscopy. Overall, I must admit that the time with you was not at all *snegative*.

I would also like to thank my second supervisor, **Prof. Dr. Lars Schäfer**, for his help and support, and for acting as a referee. I appreciated your relaxed character and your ideas in discussions regarding my project. Moreover, I also enjoyed your very interesting lecture on Biomolecular Simulations.

I would to thank **Prof. Dr. Poul Petersen** for giving me the opportunity of working as a research assistant in his group from August 2019 to September 2020 at RUB. During that time, I learned a lot

about various types of non-linear infrared spectroscopies. I also appreciate the experience of working in an environment that is shaped by an exotic fusion of US-American culture and working spirit and German regulations. I wish you and your group all the best for the future!

Additionally, my gratitude goes to **Prof. Dr. Gregor Jung** and **Alexander Grandjean** (Universität des Saarlandes) for the stimulating and productive collaboration on photoacids, especially our discussions on the interpretation of the results. His group also provided us with the molecular sample and original spectroscopic data in acetone that is used in this study as experimental reference. I would be happy if we could keep up this fruitful collaboration also regarding future theoretical studies.

In the following, I would like to thank all the members of the **Quantum Chemistry** and the **Ultrafast Photochemistry Groups** for the nice working atmosphere, the great team spirit, and a wonderful time. I very much enjoyed working with all of you. In detail, I would like to personally thank:

- **Dr. Ali Ghiami-Shomami** for being the best office mate and establishing a great working atmosphere. I very much value our frequent discussions on various scientific (especially photoacids), but also non-scientific (e.g., politics, life in Germany, etc.) topics. I think that we have a very synergistic scientific exchange at our office.

- **Dr. Bastian Geißler** for your wide knowledge and excellent skills regarding the streak-camera time-resolved fluorescence setup, programming (e.g., in MATLAB), and your help in the lab. Thank you for teaching me basically everything I needed to know for working in the laser lab. I also enjoyed the time sharing an office with you in the Ultrafast Photochemistry Group.

- **Dr. Robert Treß** for listening to and talking about many work-related topics. You always make sure that the group lunch is not forgotten (as long as you are not working from home). You also contribute to a funny atmosphere during our group lunch and social activities.

- **Julia Haberhauer** for taking over parts of the calculations on the photoacids and for the making the excellent decision of becoming a new PhD student soon, backing up the solvent-related subgroup of our research group.

- **Dr. Gunnar Schmitz** for being a tremendously helping hand with all cluster and computer-related issues that needed to be resolved.

- **Dr. Arjeta Rushiti** for contributing to an open and very nice atmosphere in the group. Furthermore, you helped me when I was in the process of making the decision of returning to the Hättig group.

- **Dr. Shota Tsuru** for establishing a particularly intercultural atmosphere in the group due to countless discussions during lunch. Your wide knowledge and thirst for new information seems almost endless.

- **Dr. Özlem Yönder** for nicely welcoming me back at the office when I joined the group. I admire your sustainable way of life and your energetic charisma.
- **Bastian Schnieder** for his interest and efforts of getting involved with the cluster administration in order to take this over once I will have left.
- **Dr. Kevin Artmann, Niklas Geßner, and Svenja Wortmann** for being wonderful colleagues during my time in the Ultrafast Photochemistry group.

I would also like to acknowledge the **Deutsche Forschungsgemeinschaft** for funding under the Cluster of Excellence RESOLV (EXC 2033) and within the Research Training Group *Confinement-Controlled Chemistry* (GRK 2376).

Finally, my most personal and intimate thanks go to my **family**, especially my parents, **Anja and Rudolf**, and my girlfriend, **Helen**, for their unconditional love and support over all the years. You always believed in me and I could not have done it without you!

# Contents

**1. Introduction** **1**

1.1. Motivation of this Project . . . . . 1

1.2. State of Research at the Beginning of the Project . . . . . 3

1.3. Research Questions . . . . . 19

1.4. Outline of this Dissertation . . . . . 22

**2. Methodology** **23**

2.1. Experimental Techniques . . . . . 23

2.2. Computational Methods . . . . . 32

**3. ESPT in Acetone–Water Mixtures** **51**

**4. ESPT in Neat Acetone** **67**

**5. Prediction of Ground-State p$K_a$ in Acetone** **83**

**6. Theoretical Spectroscopy in DMSO** **97**

**7. Toward Explicit Solvent Effects and Specific Photoacid–Base Interactions** **113**

7.1. Introduction . . . . . 113

7.2. Computational Details . . . . . 113

7.3. Theoretical Spectroscopy in Acetone with Implicit Solvation . . . . . 115

7.4. Beyond Implicit Solvation . . . . . 124

7.5. Conclusions . . . . . 134

**8. Conclusions and Outlook** **137**

8.1. Conclusions from the Experimental Part . . . . . 137

8.2. Conclusions from the Theoretical Part . . . . . 140

**Bibliography** **I**

**A. Experimental Details** **A1**

A.1. Time-Resolved Fluorescence Spectroscopy . . . . . A1

A.2. Transient UV/Vis Absorption Spectroscopy . . . . . A3

**B. Supporting Information of the Articles** **B1**

B.1. ESPT in Acetone–Water Mixtures . . . . . B1

B.2. Prediction of Ground-State p$K_a$ in Acetone . . . . . B13

B.3. Theoretical Spectroscopy in DMSO . . . . . B19

**C. Additional Materials for Chapter 7** **C1**

C.1. Numerical Complements to Plotted Data . . . . . C1

C.2. NTO Analysis . . . . . C3

C.3. Additional Results . . . . . C3

# 1. Introduction

## 1.1. Motivation of this Project

Proton transfer (PT) is omnipresent in chemistry and its related fields, including countless examples from biochemistry, chemical synthesis, and catalysis, as well as industrial applications[1–3]. It is at the heart of acid–base catalysis[4,5] and continues to be relevant in today's research, e.g., in the development of fuel cells[6]. In biochemical systems, to name a few examples, the structure and functioning of proteins is determined by the protonation states of the amino acid side chains[7,8]. Proton gradients along biomolecular membranes act as driving forces for the ATP synthesis—the energy currency of cells—in mitochondria as well as in chloroplasts[9]. These gradients can only be built up in the first place by the use of proton pumps and ion-selective channels are relevant for harvesting the stored energy thereafter. Many enzymes either directly catalyze—at least in one step of their catalytic cycle—an acid–base reaction[10] or their activity involves proton transfer along a conduction wire, i.e., a preformed hydrogen-bond network of amino acids and water molecules (e.g., in photosystem II[11]). Proton transfer can also take place in an electronically excited state, e.g., as in green fluorescent protein[12–15] or in the chromophore of Firefly's D-Luciferin[16–22]. Such an excited-state proton transfer (ESPT) of anthocyanin pigments in plants is biologically relevant for the protection from photo damage since the ESPT provides a fast deactivation channel, efficiently converting the absorbed light energy into heat[23,24]. A related but slightly different phenomenon is proton-coupled electron transfer (PCET) which plays an important role for many enzymes[25–27].

Owing to this fundamental importance, there has been a huge interest in the study of proton-transfer reactions since the beginnings of chemistry[28,29], both with respect to the underlying thermodynamics as well as the chemical kinetics. From a thermodynamic perspective, the acid dissociation constant $K_\mathrm{a}$ or the $\mathrm{p}K_\mathrm{a}$, i.e., its negative decadic logarithm, is the most important quantity as it quantifies the Brønsted acid strength[30]. Although water is often considered the most interesting solvent due to its unique role in the chemistry of life (*vide supra*), many other solvents are also equally important, e.g., for technical applications. While the experimental determination of $\mathrm{p}K_\mathrm{a}$ has nowadays become a standard in aqueous solution owing to a broad variety of well-established techniques (e.g., potentiometric, NMR-spectroscopic, or spectrophotometric titrations)[31], the situation is much more complicated in non-aqueous solution since the drastically lower acidity constants in combination with other complications such as low solubilities or homoconjugation challenge the accuracy of experimental detection methods[32,33]. Due to these difficulties, computational $\mathrm{p}K_\mathrm{a}$ predictions have become much more important in these environments, providing an alternative path to $\mathrm{p}K_\mathrm{a}$ values[34,35].

Regarding the kinetics, a molecular probe is typically required to experimentally obtain information on the PT mechanisms including relevant intermediates as well as rate constants for the individual steps.

For this task, so-called photoacids have established as particularly powerful tools during the last decades (*vide infra*). These photoacids are molecules that exhibit an increase in acidity (i.e., a decrease in p$K_a$) upon electronic excitation[36,37]. In other words, such a photoacid is a stronger acid in its electronically excited state (usually the lowest lying singlet state $S_1$) compared to the (singlet) ground state ($S_0$). Thus, the excited-state p$K_a$ (from now on referred to as p$K_a^*$) is smaller than the ground-state p$K_a$. As a consequence, photo-excitation can trigger an excited-state proton transfer (ESPT)[38] from the photoacid to a nearby proton acceptor, e.g., the solvent or any other Brønsted base[39]. A special variant of ESPT is ESIPT (I for intramolecular) where the ESPT takes place intramolecularly[40]. In particular, the use of pulsed lasers has made it possible to temporally initiate the ESPT event, which conveniently allows to investigate the associated dynamics in real time using time-resolved spectroscopy[41,42]. Other applications of photoacids include their use as proton sources for (photo)catalysis[43,44], as pH-dependent imaging agents in biological cells[45–49], and for single-molecule microscopy[50,51]. While most (weak) photoacids (p$K_a^* > 0$) are—due to limited acid strength—restricted to ESPT in neat water[52,53] and aqueous solutions containing an additional base[54] or co-solvent[55–58], those with a negative p$K_a^*$ can also perform an ESPT in other protic (e.g., alcohols)[59,60] or even aprotic solvents such as dimethyl sulfoxide (DMSO)[48,61].

The current project presents a combined experimental and theoretical approach to study the ESPT of particularly strong photoacids, previously introduced by Gregor Jung and co-workers[48], in acetoneous environment, i.e., in neat acetone as well as in acetone–water mixtures. As an aprotic and only moderately basic solvent, acetone is a quite unusual medium for PT reactions. Here, time-resolved spectroscopy is used to experimentally study the ESPT kinetics, while a quantum-chemical approach is chosen for a complementary theoretical description of the ESPT thermodynamics focusing on the p$K_a^*$ value.

## 1.2. State of Research at the Beginning of the Project

### 1.2.1. Photoacid Background

#### The Phenomenon of Photoacidity

Photoacids have been the subject of scientific studies since their initial description in the first half of the 20th century by Weber (1932)[62], Terenin and Kariakin (1947)[63], Petersen (1949)[64], and Förster (1949, 1950)[65–67], who had reported pH-dependent changes in the fluorescence spectra of several dye molecules; including 1,4-naphthylaminosulfonate, acridine, 3-aminopyrene-5,8,10-trisulfonate, as well as 3-hydroxypyrene-5,8,10-trisulfonate and 3,5-dihydroxypyrene-8,10-disulfonate, respectively. Not much later it has been also Förster who introduced the idea of considering a thermodynamic cycle that takes into account the acid–base equilibria for both the electronic ground state and the excited state to rationalize the phenomenon of photoacidity[65–68]. In his memory, this cycle is today referred to as Förster cycle (Fig. 1.1). This thermodynamic cycle relates $\Delta \mathrm{p}K_\mathrm{a}$, the difference between the excited-state ($\mathrm{p}K_\mathrm{a}^*$) and ground-state ($\mathrm{p}K_\mathrm{a}$) acidity, to the difference in the Gibbs free electronic excitation energies ($\Delta G_\mathrm{exci}$) of the protonated (ROH) and deprotonated ($\mathrm{RO}^-$) species, as expressed in Eq. (1.1)

$$\Delta \mathrm{p}K_\mathrm{a} = \mathrm{p}K_\mathrm{a}^* - \mathrm{p}K_\mathrm{a} = \frac{\Delta G_\mathrm{exci}(\mathrm{RO}^-) - \Delta G_\mathrm{exci}(\mathrm{ROH})}{RT \ln(10)} \tag{1.1}$$

with the ideal gas constant $R$ and the absolute temperature $T$.

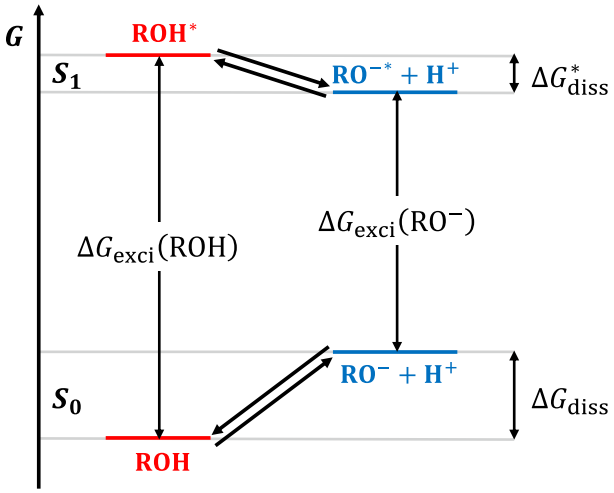
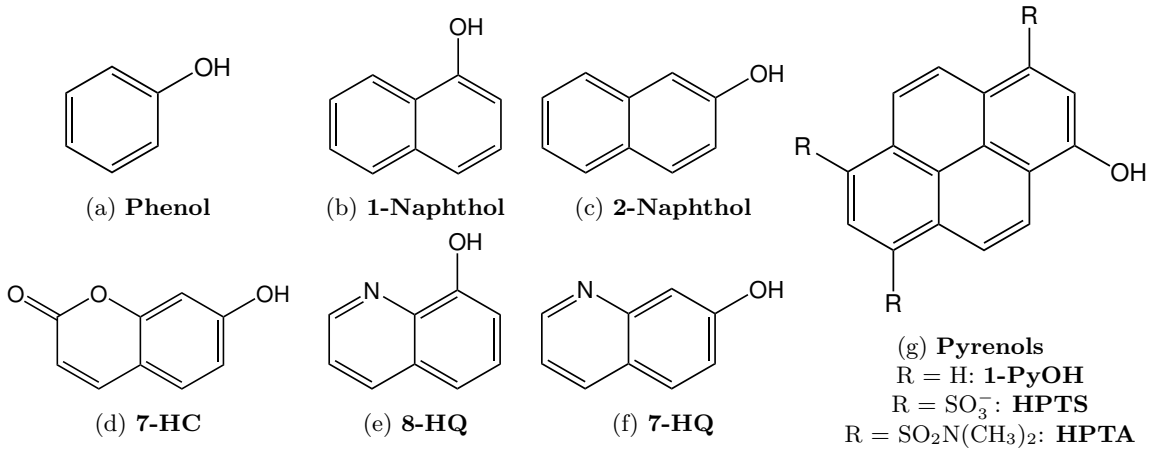



Figure 1.1.: **The Förster cycle.** Reproduced with permission from Ref. 69. Copyright © 2022 American Chemical Society.

If the ground-state $\mathrm{p}K_\mathrm{a}$ is known, Eq. (1.1) can be used to calculate $\mathrm{p}K_\mathrm{a}^*$ from the electronic transition energies; if the $\mathrm{p}K_\mathrm{a}$ is unknown, still the $\Delta \mathrm{p}K_\mathrm{a}$ can be determined. Ideally, 0–0 transition energies should be inserted into Eq. (1.1). Owing to its simplicity, the Förster cycle has become the most common route to $\mathrm{p}K_\mathrm{a}^*$ for both experiments and theory, although also other approaches exist (see Sec. 1.2.6).




(a) **Phenol** (b) **1-Naphthol** (c) **2-Naphthol**

(d) **7-HC** (e) **8-HQ** (f) **7-HQ**

(g) **Pyrenols**
R = H: **1-PyOH**
R = $SO_3^-$: **HPTS**
R = $SO_2N(CH_3)_2$: **HPTA**

Figure 1.2.: **Overview on the different classes of photoacids.** The corresponding naphthylamines and aminopyrenes are obtained by substituting the OH group by an $NH_2/NH_3^+$ in (b, c) or (g), respectively. [Abbreviations: Hydroxycoumarin (HC) and hydroxyquinoline (HQ).]

Photoacids are typically hydroxyarene or aminoarene compounds and thus the acidic functional group is either a hydroxy (OH) or an amino ($NH_2$)—more specifically an ammonium ($NH_3^+$)—group. The most common classes of photoacids include naphthols[70–76] (Fig. 1.2b–c), hydroxyquinolines[77–81] (Fig. 1.2e–f), hydroxycoumarins[82–88] (Fig. 1.2d), and hydroxypyrenes[48,66,89,90] (Fig. 1.2g), although also some naphthylamines[62,64,91] and aminopyrenes[66,92–94] are known. Phenols (Fig. 1.2a) also exhibit photoacid character ($\Delta pK_a \sim -6$)[95–97], but their UV absorption ($\sim$ 270 nm) and weak fluorescence make them impractical for applications. The counterparts of photoacids, i.e., PHOTOBASES, also exist, but are much less studied[98–102]. These photobases are compounds that become more basic in the excited state. To rationalize and quantify photobasicity, one simply has to switch the perspective: a photobase is a species whose conjugate acid becomes less acidic in the electronically excited state compared to the ground state. The term photobase is often used incorrectly for the corresponding base of an excited photoacid, which is in fact exactly the opposite of a photobase since these species are particularly weak excited-state bases. While the aromatic OH group is typical for many photoacids, a common feature of photobases are N-heterocyclic, aromatic frameworks. It is no surprise that photoacids and photobases are aromatic compounds as the potential acidic or basic functional group needs to be located in a chromophore (i) whose excitation energies are not too high and (ii) which has a sufficiently long lifetime. Both conditions are readily fulfilled by aromatics.

### The Molecular Origin of Photoacidity

The most fundamental origin of photoacidity can be found in the electronic charge redistribution upon excitation. As commonly explained, photoacidity is caused by an intramolecular charge transfer (ICT) in the excited state of the acid (ROH) from the O atom in the OH group to the aromatic ring, more precisely the distal ring in the case of condensed aromatics[76,103]. However, despite its plausibility, this explanation is incomplete since it does not take into account the corresponding base $RO^-$, as pointed out

by Agmon[37]. As for the ground-state, (photo-)acidity is the mutual outcome of both a destabilization of ROH and a stabilization of $RO^-$. If no charge transfer was found for $RO^-$, the proposed ICT of ROH would actually lead to an increased ROH–$RO^-$ energy gap that would make the excited-state deprotonation less favored. Thus, an even larger ICT must occur for the base, which is indeed confirmed by experiments, e.g. in solvatochromism[104–107] or Stark spectroscopy[108]. Therefore, photoacidity is the net effect of an excess $RO^-$ stabilization.

Another possibility to rationalize this phenomenon is in terms of Hückel's (anti)aromaticity[109], as originally proposed by Agmon[37,110] and recently reviewed by Wen *et al.*[111]. Aromatic molecules experience an energetic stabilization due to a beneficial electronic configuration, whereas molecules that would be classified as antiaromatic are energetically destabilized leading to structural perturbations, e.g., non-planarity or bond length alternation, in order to avoid the antiaromatic structure[112]. For both excited triplet and singlet states, it has been shown that the situation changes and Hückel aromatics become less aromatic, i.e., more antiaromatic, and vice versa antiaromatics become more aromatic[113–115]. Prototypic hydroxyarene photoacids such as phenols or naphthols are aromatic in their protonated form. However, after deprotonation the negative charge is stabilized by delocalizing it in the conjugated $\pi$ system at the expense of including an additional electron pair in the conjugation and lowering its aromatic character. Due to the reversal of aromaticity and antiaromaticity in the $S_1$ state (*vide supra*), the protonated species is less aromatic in the excited state ($S_1$) and hence becomes destabilized compared the ground state ($S_0$). Even more important, the deprotonated species increases in aromaticity corresponding to a stabilization in accordance with the strong ICT. These differences in the aromatic character of the acid and the base and between $S_1$ and $S_0$ typically lead to larger Stokes shifts for the acid compared to the base and correspondingly stronger structural changes for the acid[110,116].

## 1.2.2. Showcase HPTS—The Most Studied Photoacid

The research on photoacids has been largely stimulated by Huppert and co-workers, reaching back to the 1980s when Huppert—at that time under the supervision of Kolodney—had joined the photoacid community[117,118]. After almost 40 years of research, Huppert can be considered a pioneer in photoacid chemistry. Moreover, he has also catalyzed the huge interest in 8-Hydroxypyrene-1,3,6-trisulfonate (HPTS or pyranine), which is one of the first studied photoacids[119]. To date, HPTS has become the probably most studied photoacid of all time. The ESPT of HPTS has been investigated in a vast number of environments, with many different experimental techniques, and also with theoretical approaches; as highlighted in the following.

### ESPT in Different Environments

Among the various environments, aqueous solutions pertain an outstanding role. The ESPT to the solvent in bulk water has been analyzed in great detail[42,52,53,94,108,120–140], but also the ESPT to an additional base such as acetate[41,54,136,141–147] or (per)chloroacetate[148–150] and in solvent mixtures consisting of

water and a co-solvent like methanol[117,151–154] or DMSO[55,155]. Other parameters include the effect of additional salts[118,152,156–159], temperature[160,161], and pressure[162] on the ESPT process. Challenging the limits of ESPT, even the ESPT of HPTS in ice and doped ices[160,163–169], in the confined water nanopools of various reverse micelles (with anionic, neutral or cationic surfactants)[170–174], or in Nafion fuel cell membranes[170,175] have been addressed. This scope also includes many biological environments such as the cavity of cyclodextrin[176–178], other supramolecular assemblies[179], adsorbing bio-materials (hydrophobic insulin amyloid fibrils and hydrophilic cellulose surfaces; chitin, starch, chitosan)[180–185], hydrogels[186–188], the presence of proteins[189], or even living cells[190–192]. Apart from these aqueous environments including the above-mentioned water mixtures, studies on ESPT of HPTS in non-aqueous solution are very scarce though, and mainly involve acetate in methanol[193] and ionic liquids[194,195]. Moreover, due to the high triple and quadruple negative charges, the study of HPTS is restricted to actual solutions, in contrast to other photoacids (e.g., naphthols that are also studied in gas-phase solvent clusters[196–199]).

#### Different Spectroscopic Techniques

Many different spectroscopic techniques have been applied to HPTS, each with their own advantages and accessible information. Changes in the electronic structure upon deprotonation allow visible spectroscopies such as UV/Vis absorption and fluorescence emission to be used for distinguishing the protonated from the deprotonated form. Moreover, since the molecular vibrations are highly specific to intermolecular interactions, mid infrared (mIR) absorption or Raman scattering spectroscopy can be used to further characterize possible PT intermediates such as ion pairs. In general, time-resolved spectroscopy is needed to obtain information on the dynamics, i.e., the actual kinetics of the ESPT.

Therefore, steady-state UV/Vis absorption and fluorescence emission spectroscopy have been applied since the early days for a qualitative characterization of the ground-state and excited-state equilibria of HPTS in water[66], but also more recently to its solvatochromism[104,107]. The earliest transient absorption spectroscopy of HPTS in aqueous solution was reported by Förster and Völker (1975)[119] and Lundy-Douglas and Schelly (1976)[200], both using flash photolysis (tens of ns time resolution), followed by laser photolysis experiments by Gutman, Huppert, and Pines (1981, 1983)[201,202]. In parallel, early time-resolved fluorescence spectroscopy on the ps to ns timescale using initially streak cameras and later time-correlated single photon counting (TCSPC)—both limited by a rather poor ps time resolution based on today's standards—was used to study the slower excited-state dynamics[117,118,203], which allowed Agmon, Pines, and Huppert in 1986 to establish their well-known two-step model for the ESPT of HPTS to water (*vide infra*)[120–126].

Only later in 1996, Tran-Thi and co-workers applied fs fluorescence up-conversion for the first time to study the ultrafast dynamics of HPTS in water[128] and combined it later (in 2000) with transient UV/Vis absorption[129]. In the same year, ultrafast transient absorption measurements on HPTS were also performed by Huppert *et al.*, but for the bimolecular ESPT of HPTS to acetate[54]. Owing to a much better time resolution compared to the previous TCSPC experiments, the results by Tran-Thi

*et al.* revealed the additional involvement of two fast processes in the ESPT kinetics that precede the proton-transfer step, which had been previously unknown and then started to challenge Huppert's two-step model for the ESPT (see Sec. 1.2.4)[116,128–131]. Particularly in the course of this debate but also in other studies on HPTS, transient mIR absorption[41,134–136,143–145,148–150,159,204] and fs stimulated Raman scattering[43,139,140,146,153,205–208] have been established as routines, and even the use of more exotic techniques such as Stark spectroscopy[108] has been reported. Most recently, time-resolved THz spectroscopy has been applied to directly study the photo-induced solvent response of water in the vicinity of HPTS[42], while UV-pump–X-ray-probe spectroscopy has been used to monitor the electronic structure changes of the proton donating group of the related photoacid 8-aminopyrene-1,3,6-trisulfonicacid (APTS) upon photo-excitation and the subsequent proton transfer dynamics[209].

#### Theoretical Studies on HPTS

In addition to this rich scope of experiments, HPTS has also become the subject of many theoretical studies in the recent years. However, the relatively large size of the HPTS molecule in combination with the fundamental requirement for an accurate description of the electronic excitations hindered the theoretical investigations of photoacids in general and HPTS in particular for a long time. Moreover, for HPTS, the triple and quadruple negative charges of the protonated and deprotonated species leads to the additional requirement that a description of the solvent needs to be included in the calculations.

This is why the early theoretical, and more precisely, quantum-chemical studies (in the early 2000s) have focused on smaller and simpler photoacids as model systems, such as phenol and cyanophenols (using state-specific CASSCF calculations combined with PCM)[116] or cyanonaphthols (using semi-empirical AM1 calculations)[110]. The first computational study on HPTS itself has been reported not much later by Hynes and co-workers (in 2002)[131], but was still restricted to semi-empirical (CS-INDO) calculations at that time because of high computational costs for a full wavefunction-based treatment using multi-reference methods. Only about 15 years later, HPTS became the subject of a purely *ab initio* study in (implicit) solution by Cimino *et al.* (in 2016)[210], using TDDFT as a cheaper method for electronic excitation energies. During that time, TDDFT—often in combination with some variant of the continuum solvation model PCM—has also been applied to many other photoacids[211–226] and particularly also to the prediction of $pK_a^*$ values[227–235] (*vide infra*).

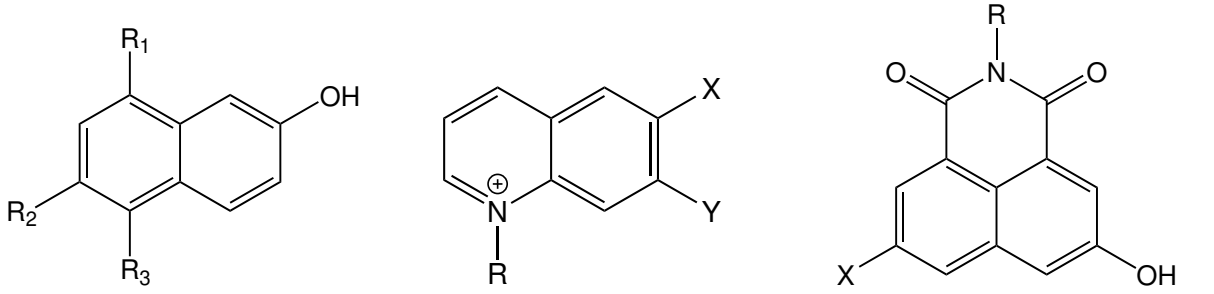
Over the past five years and besides quantum chemistry, HPTS has also been investigated theoretically using molecular dynamics simulations, mostly with quantum-mechanics/molecular-mechanics (QM/MM) approaches for the sake of computational efficiency. One of the first examples is the combined experimental–theoretical study on the ESPT of HPTS to acetate by Heo *et al.*, which revealed a coherent wave packet motion of the reactant (acid) and the product (conjugate base) and identified the vibrational modes that actively participate in this coherent proton transfer[147]. The excited-state vibrational dynamics of HPTS have been extensively addressed by Rega and co-workers, e.g., in neat water[236,237] and in acetate-containing aqueous solution[238,239]. Similarly, the ESPT dynamics of HPTS in 1-methylimidazole[240]

and in water[241] have been recently investigated in an experimental–theoretical study by Fayer and co-workers and Martínez and co-workers. Even the ESPT dynamics of a particularly strong—a so-called super-photoacid (*vide infra*)—in water has been subject to a theoretical study by Raucci *et al.*[242].

### 1.2.3. Super-Photoacids

Despite this wealth in photoacid research, HPTS (*vide supra*) and most other early photoacids, especially naphthols[56–58,243–245], are mainly restricted to perform an ESPT in aqueous solutions (*vide supra*) due to limited acid strength, i.e., too large $pK_a^*$ values. To overcome this, i.e., to enhance the photoacidity by lowering the $pK_a^*$ value, Tolbert and Haubrich (in 1990) had the idea to substitute 2-naphthol with electron-withdrawing cyano (CN) groups at different ring positions[246]. The CN group was chosen as a compromise between strength and stability since the commonly used sulfonate ($SO_3^-$) group is only a weak electron acceptor, whereas the nitro ($NO_2$) group is one of the strongest electron acceptors, but nitro compounds are typically photo-labile and do not fluoresce[247]. Owing to the drastically enhanced photoacidity for some of these cyanonaphthols, particularly with the CN at the 5 or 7 position (shifting the $pK_a^*$ to $-1.2$ and $-1.3$, respectively), Tolbert and Haubrich also introduced the term Super-Photoacids, from then on referring to photoacids with a negative $pK_a^*$ value.

Driven by the enhancement in photoacidity, the ESPT of such super-photoacids is strongly accelerated, leading to an ultrafast deprotonation in water and rendering the ESPT possible in non-aqueous solution (*vide infra*). For example, as one of the first super-photoacids, the above-mentioned compound 5-cyano-2-naphthol (5CN2, Fig. 1.3a) has been thoroughly studied with respect to its ESPT in many different solvents including water[248], alcohols[249], DMSO[61], solvent mixtures[250–252], and gas-phase solvent clusters[196] as well as to its solvatochromism in a variety of organic solvents[106,249].




(a) **Naphthols**
$R_1 = R_2 = H$, $R_3 = CN$: **5CN2**
$R_2 = H$, $R_1 = R_3 = CN$: **DCN2**
$R_1 = R_3 = H$, $R_2 = SO_2CF_3$: **6F3**

(b) **Hydroxyquinolines**
$X = OH$, $Y = H$, $R = CH_3$: **NM6HQ**$^+$
$X = H$, $Y = OH$, $R = CH_3$: **NM7HQ**$^+$
$X = OH$, $Y = H$, $R = O^-$: **6HQNO**

(c) **1,8-Naphthalimides**
$X = SO_3^-$, R = EG: **EG-SHONI**
X = OH, R = EG: **EG-dHONI**
X = OH, R = COOH: **COOH-dHONI**

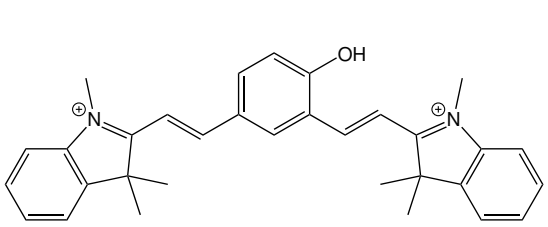
Figure 1.3.: **A selection of super-photoacids I.** Naphthol, hydroxyquinoline, and 1,8-naphthalimide derivatives. [Abbreviation: Ethylene glycol residue (EG = $CH_2CH_2OCH_2CH_2OH$).]

#### The Route Toward Strongest Super-Photoacids

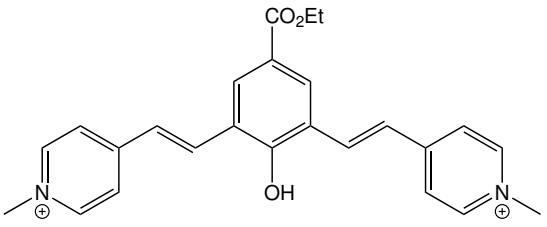
The initial discovery of super-photoacids triggered a competition for designing increasingly strong (super-) photoacids in order to both (i) further accelerate the ESPT and push the kinetics toward the solvent-

controlled kinetic regime and (ii) move to less proton-accepting solvents (see Fig. 1.3–1.4). Hence, the next generation of super-photoacids first included simply further functionalized 2-naphthols, making use of the increased effect of multiple substituents, utilizing either two cyano groups[253,254] or a newly perfluoroalkylsulfonyl group[255] (Fig. 1.3a). Among these, 5,8-dicyano-2-naphthol (DCN2, Fig. 1.3a; $pK_a^* = -4.5$[253]) has become most thoroughly studied, e.g., regarding the ESPT in water[253] and various alcohols[256–258], under high pressures[259–265], or even in ionic liquids[266].

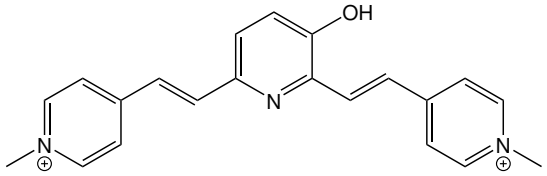
Hydroxyquinolines (Fig. 1.3b) pose another interesting compound class. These compounds possess dual photoacid–photobase character though, which leads to more complicated kinetics involving tautomerization reactions[77,78]. Therefore, Kim and Topp revived the original idea by Bardez *et al.*[79] of blocking the photobasic nitrogen site of hydroxyquinolines *via* methylation in order to switch off the photobase character and make use of the largely enhanced photoacid character of the corresponding hydroxyquinolinium cation[80]. Upon these, NM6HQ$^+$ ($pK_a^* =\sim -7$)[267] has been studied experimentally in water and in various alcohols by Popov *et al.*[267,268], and the related (non-*N*-methylated) 6HQ as well as NM6HQ$^+$ in the same solvents and additionally in water-acetonitrile mixtures by Pérez Lustres *et al.*[269–271]. Moreover, the ESPT of NM7HQ$^+$ ($pK_a^* = -2.3$[272]) in hydrogen-bonded complexes with methanol, ethanol, and DMSO in the solvent acetonitrile has been studied by Park *et al.*[272–275]. Later, Solntsev *et al.* have tested *N*-oxidation as an alternative to *N*-methylation, giving access to a new class of hydroxyquinoline-*N*-oxide photoacids[276]. However, while, in comparison to the parent compound, the photoacidity was successfully enhanced and also the tautomerization disabled, a lack of photo-stability was introduced due to an unwanted, yet efficient non-reversible side-reaction, which made them unpractical.



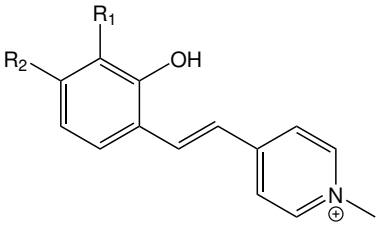

(a) **QCy7**




(b) **QCy9**




(c) **HPPC**




(d) **Cyanine Picolinium (CyP)**
$R_1 = R_2 = H$: **PCyP**
$R_1 = H$, $R_2 = COOCH_3$: **BCyP**
$R_1 = Cl$, $R_2 = COOCH_3$: **CBCyP**

Figure 1.4.: **A selection of super-photoacids II.** Quinone cyanine dyes.

Rather, the subsequent design of super-photoacids by Huppert and co-workers has followed the direction of cyanine fluorochrome dyes (see Fig. 1.4), originally known from near-infrared (NIR) imaging due to their pronounced NIR emission[277,278]. This importantly includes the quinone cyanines QCy7 (Fig. 1.4a, $pK_a^* = -6.5$)[279] and QCy9 (Fig. 1.4b, $pK_a^* = -8.5$)[280]. Both are able to readily perform an ESPT in liquid[279,280] or even solid[281,282] $H_2O$ (or $D_2O$) as well as in typical alcohols such as methanol and ethanol[59], and also in ethanol–trifluoroethanol solvent mixtures in the case of QCy9[283]. Due to its immense (photo-)acidity, the ESPT rate of QCy9, which continues to be the strongest photoacid to date, reaches a value of $k_{PT} \sim 10^{13}$ $s^{-1}$ (i.e., a lifetime of 100 fs) that is identical in water, methanol, and ethanol, indicating ESPT kinetics beyond the solvent-controlled regime[59]. Even more recently, Huppert and co-workers have continued to fine-tune the properties of these dyes and reported newly synthesized 3-hydroxypyridine-dipicolinium cyanine (HPPC, Fig. 1.4c; $pK_a^* \sim -6$)[284], phenol cyanine picolinium (PCyP, Fig. 1.4d; $pK_a^* \sim -1$)[285], chloro benzoate cyanine picolinium (CBCyP, Fig. 1.4d; $pK_a^* \sim -6$)[60,286], and phenol benzoate cyanine picolinium (BCyP, Fig. 1.4d; $pK_a^* \sim -7$)[287] salt super-photoacids. Apart from the common solvents for ESPT (i.e., water, methanol, ethanol), CBCyP is one of the very few photoacids that has also been studied in acetonitrile–water mixtures[288].

#### Kumpulainen's Napthalimides

As highlighted above, the design of new super-photoacids mainly pursued the route of functionalizing already known weaker photoacids or promising candidates (e.g., fluorescent dyes) with electron-withdrawing groups in order to shift the $pK_a^*$ into the negative regime. This strategy also applies to the super-photoacidic HPTS derivatives developed by Jung and co-workers[48], to which a later section (Sec. 1.2.5) has been dedicated. However, as the final example here, the super-photoacids based on 1,8-naphthalimide introduced by Kumpulainen *et al.* are presented.

Substituted 1,8-naphthalimides (NI) had been known as fluorescent probes and sensors for a long time[289–291] and even the excited-state ion-pair formation of 3- and 4-hydroxy-*N*-methyl-1,8-naphthalimides in organic solvents had been studied *via* fluorescence[292–294]. However, due to the missing data for aqueous solutions in combination with the promising properties of these compounds, Kumpulainen *et al.* have developed three new NI-based super-photoacids (see Fig. 1.3c) with $pK_a^*$ values ranging from $-1.2$ to $-1.9$[295]. These compounds differ only in the number of OH groups and in the substituent at the N atom of the NI framework. EG-SHONI ($pK_a^* = -1.9$) contains an ethylene glycol (EG) moiety at the N, one OH (HO) group in the first aromatic ring, and a sulfonate (S) group in the second ring. In contrast, this sulfonate group is replaced by another OH group in EG-dHONI ($pK_a^* = -1.2$), having two (dual) OH groups in total. Lastly, COOH-dHONI ($pK_a^* = -1.4$) is similar to EG-dHONI, but the ethylene glycol is replaced by a carboxy (COOH) group. All three compounds exhibit deprotonation upon excitation in alcohols and in DMSO[295]. EG-dHONI has been subject to more detailed kinetic studies in water, which revealed that ESPT follows a two-step model involving a short-range proton transfer under formation of a contact ion pair and its diffusive separation[295]. Moreover, the complex formation and the ESPT of

other dHONI photoacids and different organic bases in acetonitrile and benzonitrile solution has been studied, strongly indicating a three-step model for the ESPT in these environments involving hydrogen-bonded complexes and a solvent-separated ion pair as additional intermediates[296]. Later, EG-SHONI has been studied more detailed using a combination of fluorescence up-conversion, transient UV/Vis absorption, and transient mIR absorption to decipher the ultrafast ESPT in DMSO, revealing not only a reversibility of the initial PT step that yields the contact ion pair, but also a breakdown of the (two-step) Eigen-Weller model—despite excellent agreement with the experimental data—due to solvent control *via* solvent relaxation[297,298].

## 1.2.4. Kinetics of the ESPT Process

### Separating Different Timescales

ESPT reactions are the outcome of numerous consecutive elementary processes that in total cover a wide range of timescales, from the sub-fs to the ns regime, comprising[37]:

- electronic redistribution upon excitation (sub-fs)
- hydrogen-bond rearrangement near the (photo)acidic functional group (fs)
- proton dissociation and proton solvation (ps)
- geminate recombination and excited-state decay (ns).

Simkovitch *et al.* proposed a classification of the photoacids into four regimes[299]:

(**I**) $pK_a^* \gtrsim 0$ (weak photoacids): relatively slow ESPT ($k_{PT} \sim 10^{10}$ s$^{-1}$), efficient only in water; limited by covalent interactions within the proton-transferring complex; e.g., HPTS

(**II**) $-4 \leq pK_a^* \leq 0$ (typical super-photoacids): faster ESPT in water, also more efficient in many protic solvents; e.g., HPTS derivatives (HPTA, **A**–**E** (Fig. 1.6))

(**III**) $-6 \leq pK_a^* \leq -4$ (strong super-photoacids): rapid ESPT under solvent control in water, efficient in aprotic solvents; limited by solvent reorientation; e.g., NM6HQ$^+$

(**IV**) $pK_a^* < -7$ (strongest super-photoacids): ultrafast ESPT beyond solvent control in water, methanol, and ethanol ($k_{PT} \approx 10^{13}$ s$^{-1}$); limited by donor–aceptor distance within complex; e.g., QCy7

When moving from regime I to IV, the photoacid strength and ESPT rate increase, i.e. the capability to transfer protons to the solvent grows. In a nutshell, this classification reflects the competition between the ESPT rate constant, which is determined by the $pK_a^*$ of a given photoacid and the solvent, and the radiative decay rate. Only if the photoacid is sufficiently strong, the ESPT is fast enough to happen within the typical fluorescence lifetime of a few ns. This distinction also highlights that the exact mechanism of the ESPT depends on the photoacid strength (*vide infra*).

### Multi-Step Models for ESPT

The Förster cycle (cf. Fig 1.1) marks the simplest starting point for any description of the ESPT process, involving only the protonated species ($ROH^*$) and the fully separated pair (FIP) consisting of the deprotonated species ($RO^{-*}$) and the dissociated proton (attached to some proton acceptor) in the excited state. However, since this one-step model was proposed based on a purely thermodynamic view that does not necessarily correspond to any mechanism, it often constitutes a drastic oversimplification. Instead, owing to the pioneering work of Eigen [4,300,301] and Weller [70–72], a multi-step model for acid dissociation (in water) has been established that involves multiple proton-transfer intermediates in a stepwise dissociation. With respect to photoacids, the Eigen-Weller model has become particularly popular due to the work by Huppert and co-workers who have extensively applied it to the ESPT kinetics of HPTS [120–127,151] and other weak (anionic) photoacids (e.g., naphthol sulfonates) [243,248–252] in aqueous solution. Consisting of only two steps in the early description, this model has been extended over the years to a total of four steps, i.e., involving five species, in its most general formulation (see Fig. 1.5).

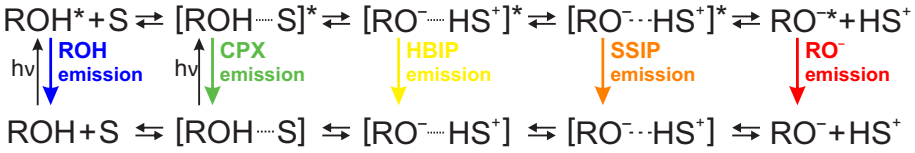



Figure 1.5.: **Four-Step Eigen-Weller Model.** Five reactive species are considered: the free photoacid (ROH), the reaction complex (CPX), the hydrogen-bonded ion pair (HBIP), the solvent-separated ion pair (SSIP), and the free anion ($RO^-$).

According to the early two-step model for HPTS in water, the $ROH^*$ species first transfers its proton to a nearby water molecule under formation of a (hydrogen-bonded) contact ion pair (CIP or HBIP) within 90 ps [120,121]. Only in a second step, this CIP is separated in a diffusive process, yielding the free $RO^{-*}$. It is important to note here that diffusion plays a central role in the special case of HPTS. Due to its quadruple negative charge, geminate recombination of $RO^{-*}$ and the dissociated proton is largely enhanced by the Coulomb attraction, giving rise to non-exponential (de-)population kinetics for $ROH^*$ and $RO^{-*}$, manifesting in a characteristic long-time tail with a $t^{-3/2}$ power-law asymptote [126,127]. Thus, a mathematical treatment of the ESPT kinetics requires a (numerical) solution to the Debye-Smoluchowski equation (DSE) [122–125]. However, for most strong neutral or even cationic photoacids, solving the DSE is not necessary as diffusion has only a minor effect [59,268,280].

Later, the rise of ultrafast time-resolved measurements revealed additional contributions to the ESPT of HPTS in water on the timescale of $\sim$ 300 fs and $\sim$ 3 ps, preceding the actual proton-transfer step, which challenged the existing two-step model [128–131]. While the first (fastest) contribution was originally assigned by Tran-Thi *et al.* to solvation dynamics of an initial locally excited (LE) state and has been widely accepted [129], the interpretation of the second (intermediate) contribution became heavily debated. Interpretations are multifold and range from a conversion of an initial LE state into another electronic state (Tran-Thi) [131], a reorganization of the surrounding water molecules to form a water wire (Bakker) [145],

a slow charge redistribution prior to the PT step (Spry/Fayer)[108,138], the formation of a solvent-separated ion pair (Huppert)[132,133], the hydration of the proton during deprotonation (Fang)[140], and vibrational energy transfer into the first hydration shell (Hoberg)[42]. In particular, the assignment to a solvent-separated ion pair (SSIP) as an additional intermediate between the CIP and the FIP by Huppert and co-workers lead to an expansion of their two-step into a three-step Eigen-Weller model[132,133] (compare Fig. 1.5). Moreover, in light of the new knowledge on HPTS during 30 years of research and specifically a discrepancy regarding recent results by Lawler and Fayer[174] for HPTS in water, Simkovitch *et al.* have recently presented a retrospective on their analysis[52,53]. By repeating the experiments using newer equipment with better time resolution, they reaffirmed their previous reports regarding the $t^{-3/2}$ power-law behavior, but they adopt the interpretation by Spry and Fayer (*vide supra*) for the 3 ps contribution as a slow charge rearrangement.

#### ESPT in Non-Aqueous Solution

Several characteristics of the ESPT change when moving from aqueous to non-aqueous solutions. For example, in contrast to the most protic solvent water, excited ion pairs such as the HBIP and SSIP are no longer short-lived in alcohols[270,298,302] and even longer-lived in aprotic solvents[270,295–298], owing to lower proton conductivities (as argued by Kumpulainen *et al.*[296]). Moreover, diffusion-assisted geminate recombination usually has a negligible effect in aprotic solvents and thus the DSE does not need to be considered, as demonstrated by Agmon and co-workers who discussed a (general) kinetic transition in reversible excited state reactions as a function of the excited-state lifetimes of the involved species[61,303–306]. However, the reduced proton-acceptor ability in the case of protic or polar-aprotic solvents (e.g., DMSO) raises in parallel the need for complex formation prior to the ESPT. Therefore, if the photoacid and the proton acceptor are not in direct proximity prior to excitation, the (diffusive) formation of an encounter complex will typically constitute the first step, which requires another expansion of the kinetic model into a four-step Eigen-Weller model[270,296] (Fig. 1.5). In the extreme, further restraining proton dissociation by changing to even less polar solvents (e.g., acetonitrile) finally completely prevents the ESPT unless a strong base is present for this complexation[272,296]. Similarly, also in aqueous solution this demand for pre-coordination with a base is reflected in the formation of water wires during (or prior to) the ESPT in water–co-solvent mixtures[56–58].

### 1.2.5. Jung's HPTS Derivatives

The fundamental importance of HPTS for the field of photoacids, but also its effective restriction to aqueous solutions as a major drawback has been demonstrated in the previous sections. Moreover, even before the concept of functionalization with electron-withdrawing groups for the design of new (super-) photoacids was systematically applied, some HPTS derivatives were already known. The most common examples include 8-hydroxy-*N*,*N*,*N*',*N*',*N*",*N*"-hexamethylpyrene-1,3,6-trisulfonamide (HPTA)[89,138,175], in which all three sulfonate groups of HPTS are converted into sulfonamides of dimethylamine, and 8-

aminopyrene-1,3,6-trisulfonicacid (APTS)[28,94,138], in which the OH group of HPTS is replaced by an ammonium ($NH_3^+$) group (see Fig. 1.2g). Due to this positive charge in the (photo)acidic group, APTS is frequently referred to in the literature as a cationic photoacid and HPTS as a neutral photoacid, despite their net negative charges in solution[94]. In contrast, HPTA is a truly non-charged photoacid and exhibits a higher excited-state acidity ($pK_a^* = -0.8$)[94] compared to the parent compound HPTS ($pK_a^* = 1.4$)[122].

This enhancement in the photoacidity of HPTA over HPTS along with the aim of improving the properties of HPTS for biological applications motivated Jung and co-workers to design a new class of non-charged HPTS derivatives (see Fig. 1.6). They introduced electron-withdrawing perfluoroalkyl ester (**A**–**B**)—similar to the substituents used to enhance the photoacidity of 2-naphthol (*vide supra*)—and amide (**C**–**E**) moieties to the sulfonate groups of HPTS[48]. Note that **F** is identical to HPTA. Overall, the substitution does not significantly alter the $pK_a$ drop upon excitation ($\sim$ 6 units), but allows to downshift the $pK_a^*$ by up to 5 units by changing the ground-state $pK_a$, yielding a set of photoacids with $pK_a^*$ between $-0.8$ and $-3.9$. Owing to the larger effect of the fluorinated esters, compounds **A** and **B** are stronger photoacids compared to **C**–**F**, while **B** is the strongest ($pK_a^* = -3.9$) of this class. The N atom of the amide group(s) in compound **C** is directly attached to a methoxy ($OCH_3$) group, which makes **C** slightly more acidic compared to photoacids **D**–**F**. However, compounds **D** and **E**, which turned out to have similar strengths as the existing **F** (HPTA), were actually (successfully) designed to improve the water solubility compared to **F**, whereas **C** shows a high permeability through biological membranes.

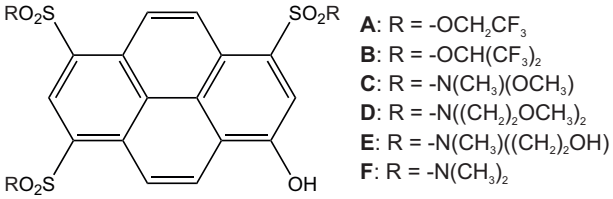



Figure 1.6.: **Molecular Structures of Jung's Photoacids A–F with the Different Substituents R.** Reproduced with permission from Ref. 69. Copyright © 2022 American Chemical Society.

Previous work has demonstrated the high photo-stability and large fluorescence quantum yields of these pyrene-based super-photoacids[48], which have enabled their use as versatile probes for single-molecule microscopy[49–51] and time-resolved spectroscopy[302,307,308]. The solvatochromism in a broad range of 29 solvents[309] and the ESPT kinetics (on the ps–ns timescale) in DMSO[48] have been studied for the full set of these new photoacids (**A**–**E**). In addition, for the strongest photoacid **B** of this class, namely tris(1,1,1,3,3,3-hexafluoropropan-2-yl)-8-hydroxypyrene-1,3,6-trisulfonate, as well as for **E**, the ESPT has been studied more thoroughly in water, methanol, and ethanol using ultrafast time-resolved fluorescence spectroscopy (sub-ps timescale), demonstrating that geminate recombination is not crucial in these cases and that multi-exponential fits describe the kinetics sufficiently well[302]. For photoacid **B**, ESPT rate constants ($k_{PT}$) of $3 \times 10^{11}$ $s^{-1}$ (water), $8 \times 10^9$ $s^{-1}$ (methanol), and $5 \times 10^9$ $s^{-1}$ (ethanol) have been reported[302]. For comparison, in the aprotic solvent DMSO[48], the ESPT rate constant further drops to a value of $1.25 \times 10^9$ $s^{-1}$. Moreover, the recombination kinetics of photoacids **A**–**C** have been addressed

using photon anti-bunching experiments, revealing the involvement of hydrogen-bonded ion pairs as intermediates, at least in the ground state[307,308]. Aiming at even stronger photoacids that are capable of performing an ESPT in even more exotic environments, Maus *et al.* recently synthesized an HPTA-based photoacid in analogy to the HPTS derivative **A**, which is strong enough to protonate concentrated sulfuric acid ($H_2SO_4$), hence being attributed the name MAGIC PHOTOACID[310].

Whereas most standard photoacids cannot transfer their proton to DMSO, the super-photoacid **B** shows indications to do so even in the aprotic, weakly basic solvent acetone[48]. In particular, acetone appears to be a solvent that has not been the subject of any ESPT study to date. However, impurities of water have been known to interfere with the ESPT in such aprotic environments, e.g., as known for 6-hydroxyquinolinium in acetonitrile–water mixtures[270]. Therefore, a systematic study on the ESPT of photoacid **B** in acetone–water mixtures is first needed before moving to the ESPT in neat acetone afterward. Furthermore, in order to complement our kinetic measurements, additional information on the thermodynamics, i.e., the $pK_a^*$ value in acetone and insights into the electronic state of these photoacids will be highly useful.

## 1.2.6. Prediction of Excited-State Acidity Constants

### Accessing $pK_a^*$ via the Förster Cycle

The Förster cycle[65–67] has been established as the most frequent route to $pK_a^*$ in both experimental and theoretical investigations[311]. From an experimental perspective, UV/Vis absorption and fluorescence emission spectroscopy are typically used to determine the band maximum positions for the first electronic transition of the two species and then the average absorption–emission energy is used in Eq. (1.1), as an approximation to the true 0–0 transition energy[36,68]. This implicitly assumes that the shape of the potential energy surfaces in both electronic states are similar (i.e., the harmonic force constants are alike), allowing the vibrational contributions to the vibronic 0–0 transition and the differences between absorption and fluorescence emission to effectively cancel out in the average[312]. However, the main problem arises from the use of the fluorescence energies in the first place since full equilibration is not generally given in the excited state, depending on the lifetime, which can cause $pK_a^*$ to be effectively treated as a non-equilibrium quantity. Moreover, the Förster cycle requires knowledge on $pK_a$, which is usually straightforward in aqueous solution, but becomes more difficult in non-aqueous solution (*vide supra*). Alternatively, $pK_a^*$ can also be determined experimentally by use of fluorescence titration[313,314], which identifies $pK_a^*$ as the inflection point in the plot of the fluorescence intensity ratio $I(\mathrm{ROH})/(I(\mathrm{ROH}) + I(\mathrm{RO^-}))$ against pH, or by direct kinetic measurements of the excited-state proton dissociation and recombination rate constants[37]; both with their own limitations. Fluorescence titration is virtually limited to aqueous solutions due to the requirement of having a defined pH, which becomes non-trivial in non-aqueous solutions where no unified pH has yet been established[315–318]. The direct kinetic method is in principle most accurate, but such measurements are technically more demanding

and also the (missing) reversibility of the ESPT process can become an issue again[319]. Therefore, the Förster cycle continues to be the standard route for experimental p$K_a^*$ determination.

In contrast, theoretical approaches (*vide infra*) do not necessarily rely on the Förster cycle, but can use any target thermodynamic cycle of interest instead, including direct approaches that avoid dealing with the ground state equilibrium[227,231,232]. However, each thermodynamic cycle comes at a certain prize and has its own advantages and disadvantages[320–323]. Such direct approaches basically shift the requirement for the ground-state p$K_a$ to requiring knowledge on the total Gibbs free energy in solution of the proton ($G_{\text{soln.}}(\text{H}^+)$) and its Gibbs free energy of solvation ($\Delta G_{\text{solv.}}(\text{H}^+)$). While the former can be calculated based on the Sackur-Tetrode equation from statistical thermodynamics[324], determining the latter is cumbersome theoretically and is usually taken from experiments[322]. Moreover, $\Delta G_{\text{solv.}}(\text{H}^+)$ is nowadays known in water with a high certainty, i.e., a value of $(-264.6 \pm 0.2)$ kcal mol$^{-1}$ with an agreement between most recent experimental and theoretical values[320,325–327], but typically unknown in other solvents including acetone. To keep a certain proximity with the experimental results for comparison reasons, also theoretical work frequently uses the Förster cycle[227–232]. This highlights two aspects: First, particular attention needs to be paid to the precise determination method of p$K_a^*$ when comparing experimental and theoretical p$K_a^*$, and second, p$K_a^*$ will often not be a pure equilibrium quantity (*vide supra*).

#### Overview on Existing Theoretical Studies on p$K_a^*$

To date, the set of computational studies in the literature on photoacids in general and theoretical approaches to p$K_a^*$ in particular is still very sparse. Early calculations by Gao *et al.* used a quantum-mechanics–molecular-mechanics (QM/MM) formalism—treating the solute at the Complete Active Space Self Consistent Field (CASSCF) and multi-reference second-order perturbation theory (CASPT2) levels and the solvent classically—to determine the $\Delta$p$K_a$ of phenol in water[328]. Later, Granucci *et al.* also applied CASSCF and CASPT2, but in combination with the Polarizable Continuum Model (PCM)[329] for implicit solvation to study the excited-state acidity of phenol and cyanophenols in the gas phase and in water[116]. The use of such high-level multi-reference methods is generally restricted to smaller molecules due to the size of the active space. This is the reason why larger systems such as pyrenols[131], but even naphthols[110] could only be studied within semi-empirical frameworks for a long time. In addition, also some molecular simulation studies on p$K_a^*$, e.g., on pyrimidine in aqueous solution by Gao *et al.* (using semi-empirical AM1 for the electronic structure)[330] or the biologically relevant phytochromobilin chromophore by Borg *et al.* (using TDDFT in combination with IEF-PCM for the electronic excitations; tested against CIS, CIS(D), SAC-CI, and CASSCF)[331,332] have been reported.

Although electronic excitation energies could be calculated using multi-reference methods (e.g, MRCI, CASSCF, CASPT2) already decades earlier, it was not before the rise of time-dependent density functional theory (TDDFT) that electronically excited states became accessible much cheaper and in a more easy-to-use fashion in quantum chemistry (e.g., see Ref. 333 for an overview on DFT methods for excited states).

TDDFT was particularly important for the application of calculating electronic excitation energies to larger systems and/or to the optimization of excited-state geometries (since these are much more expensive than a single-point energy calculation) as well as for the combination with solvent models (since this is technically more demanding for multi-reference methods)[334–336]. Jacquemin *et al.* have described a computational protocol for the theoretical prediction of $pK_a^*$ for coumarins that is purely based on TDDFT in combination with PCM[227]. This approach has been further extended by Houari *et al.* to the classes of naphthols and cyanonaphthols by critically comparing the results for the Förster cycle and the direct (Born-Haber) cycle as well as for the linear response (LR) and state-specific (SS) variants of PCM[231]. Later, Houari *et al.* have applied their improved protocol for $pK_a^*$ prediction based on TDDFT and (SS-)PCM again to the coumarins, while also addressing the effect of explicit solvent (water) in the first solvation shell of these photoacids[214]. Recently, Aquino and co-workers have used TDDFT in combination with PCM or the Conductor-Like Screening Model (COSMO) to study the photoacidity of two different hydroxyflavylium cations[233,235].

In general, TDDFT has become extremely popular for the study of photoacids—as examples of typical (organic) fluorescent dye molecules[337,338]—also apart from $pK_a^*$, e.g., regarding the reaction mechanism of the ESPT (kinetics)[210–216,218,219,221], spectral characterization and insights into the origin of photoacidity through the electronic structure[217,220,222,339–341], or as the method of choice for treating the electronic excitations in numerous QM/MM molecular dynamics (MD) studies (see Sec. 1.2.2)[236–242]. While the use of TDDFT for electronic excitation energies is for sure not an issue on its own (TDDFT has established as a rich field that continuously develops and validates new methods)[342–344], standard DFT methods can still not be said to be fully generally reliable[345,346]. Prominent examples of such failures for TDDFT include charge-transfer or Rydberg excitations, and these have been addressed in the literature, e.g., by using range-separated functionals such as CAM-B3-LYP[347]. However, TDDFT sometimes gives wrong shapes for the potential energy surfaces of the excited states[348] and suffers from relatively low accuracies for vertical excitations (0.3 eV)[349]. In an extreme case, TDDFT can even predict a wrong order of the electronic states under certain circumstances. For example, naphthols and arenes in general usually possess two low-lying electronic states with $\pi \rightarrow \pi^*$ and $n \rightarrow \pi^*$ character, referred to as $^1L_a$ and $^1L_b$ (if fully symmetric), differing in the orientation and magnitude of the transition dipole moment and thus depending differently on the solvent[350,351]. Recently, Acharya *et al.* have demonstrated that TDDFT fails to predict the correct order of the $^1L_a$ and $^1L_b$ states of the photoacids 1- and 2-naphthol by comparison with Equation-Of-Motion Coupled Cluster Singles and Doubles (EOM-CCSD) and experimental results (all calculations using C-PCM)[352]. Similar observations had been previously made by Grimme and Parac[353], who assigned this imbalanced description of the two states with TDDFT to an underestimation of the interaction of the ionic components in the corresponding $^1L_a$-state wave functions with current standard functionals, and by Prlj *et al.*[354], who extended the scope of this issue to a set of fused heteroaromatics and demonstrated that the $^1L_b$ state is highly sensitive to correlation effects, while the $^1L_a$ state suffers from the same drawbacks as charge transfer excitations.

**Highlights of the Theoretical Approach in this Work**

Based on these limitations, the current work refrains from using TDDFT for the description of the electronic excitations for the pyrene-based photoacids studied here (cf. Fig. 1.6). Instead, the wavefunction theory (WFT) methods algebraic diagrammatic construction scheme through second order (ADC(2)) and approximate coupled cluster singles and doubles method (CC2), which are known to be more accurate (0.1–0.2 eV) and more robust[349], are selected and combined with the implicit solvent model COSMO. Although this approach is not the first one that uses WFT for $pK_a^*$, e.g., CASSCF and CASPT2 have already been used (*vide supra*), ADC(2) and CC2 are much applicable in a black-box fashion and with respect to the computational costs compared to multi-reference methods. Up to now, the only study that used ADC(2) in the calculations of the excitation energies for (photoacid) $pK_a^*$ is the recent work by Wang *et al.* on the photoacidity of cationic hydroxypyranoanthocyanins[234]. However, in the actual computation of $pK_a^*$ values, they restrict themselves to B3-LYP TDDFT instead of ADC(2) despite—or due to—a close similarity between the results for these two methods. Related studies by the same groups (i.e., Aquino, Quina, and co-workers) on similar pyranoanthocyanins[223,224] or other hydroxyflavylium cations[225,226] also use ADC(2) in combination with COSMO for describing the electronically excited states, but do not deal with $pK_a^*$ values. Therefore, to the best of my knowledge, there is still basically no approach to $pK_a^*$ beyond TDDFT that actually uses accurate, but easy-to-apply WFT methods like ADC(2) or CC2 yet.

In the theoretical part of this work, the $pK_a^*$ values of Jung's pyrene-based super-photoacids will be computed by following a Förster-cycle based approach. Therefore, the electronic excitation energies of the protonated and deprotonated species as well as the ground-state $pK_a$ values are needed. While absorption and emission energies from WFT using ADC(2) and CC2 in combination with COSMO will be used for the former (*vide supra*), various established protocols exist for the latter[34,35,355–357].

Whereas the PCM model is a popular choice for the quantum-chemical calculation of $pK_a$ in other studies[358], the Conductor-like Screening Model for Real Solvents (COSMO-RS) is chosen here due to its close relation to the COSMO model. In short, COSMO-RS[359–362] is an extension of COSMO[362–364] to reintroduce specific solute–solvent interactions and it has been already successfully applied to $pK_a$ calculations in water[365,366], DMSO[365], and acetonitrile[367]. The $pK_a$ in acetone was not implemented at the beginning of this project and hence constitutes one key step in the theoretical project part. Details on all used methods will be given in Chapter 2.

## 1.3. Research Questions

As a combination of experiment and theory, this project dissects into an experimental project part on ESPT kinetics (consisting of two sub-projects) and a theoretical project part on ESPT thermodynamics (consisting of three sub-projects).

In the experimental part, the focus is set to the ESPT of photoacid **B** in acetone–water mixtures (Chap. 3) and in neat acetone (Chap 4), studied using different techniques for steady-state and time-resolved spectroscopy. Steady-state UV/Vis absorption is used to check for ground-state complex formation between the photoacid and water and fluorescence emission to probe for the involvement of ESPT intermediates such as hydrogen-bonded ion pairs. Afterward, time-resolved spectroscopy allows to further investigate the ESPT mechanism in acetone with water admixtures with respect to the kinetics, i.e., the rate constants of the elementary reaction steps. Thereby, this part aims at making a contribution to the understanding of ESPT of such strong photoacids ($pK_a^* \sim -4$ in water) in non-aqueous, weakly basic solution.

The theoretical part then moves the focus to $pK_a^*$ values obtained based on the Förster cycle *via* $pK_a$ using COSMO-RS (Chap. 5) and excitation energies ($\Delta pK_a$) using ADC(2) or CC2 (Chap. 6–7) in combination with different solvent models. By studying the full set of Jung's photoacids (**A**–**F**) in DMSO (Chap. 6) or acetone (Chap. 7), relative trends between the photoacids as well as differences between the solvents can be compared. Moreover, also the need to go beyond implicit solvation and account for explicit solvent effects is investigated by opposing results for the continuum solvent model COSMO and a hybrid implicit–explicit treatment in the solvents acetone, DMSO, and water. This contributes to the design of a protocol for $pK_a^*$ prediction that accounts for both bulk and local solvent effects.

### 1.3.1. Sub-Project I—ESPT in Acetone-Water Mixtures

Commercially available acetone—even of highly pure, spectroscopic grade—always contains residual water to some extent. This poses a problem in the ESPT experiments since water can act as a competing proton acceptor. Therefore, the effect of water as an impurity in acetone needed to be studied first, before considering the ESPT in actual neat acetone. This comprises the following research questions:

1. What is the effect of water on the spectral properties of photoacid **B** in acetone?
2. How are the ESPT kinetics in acetone affected by the presence of water?
3. What is the mechanism for ESPT in acetone–water mixtures and which species are involved?
4. How does the ESPT rate (constant) depend on the water concentration?
5. Is there a way to control or counteract the effect of water in acetone?

These questions will be addressed in Chapter 3 based on a systematic study on a series of samples with photoacid **B** and increasing water content using a combination of steady-state UV/Vis absorption and fluorescence emission as well as time-resolved fluorescence spectroscopy on the ps timescale.

### 1.3.2. Sub-Project II—ESPT in Neat Acetone

After having quantified the effect of water and discovered a way how to deal with possible residual amounts of water (*via* acidification), the ESPT of photoacid **B** in neat acetone can be studied next. Since the previous results point toward solvation dynamics on the ps timescale and an ESPT that is basically described by one time constant, the experiments are continued by ultrafast spectroscopy. Here, the focus is set to the following questions:

1. Which processes contribute to the underlying sub-ps dynamics?
2. Is there a function of pH, i.e., do these dynamics differ in neutral compared to acidic solution?
3. What are the relevant steps (and the associated timescales) for ESPT in acetone?
4. What are the contributions to the transient spectra?

In Chapter 4, time-correlated single-photon counting and fs transient absorption measurements are combined to unravel these ultrafast dynamics.

### 1.3.3. Sub-Project III—p$K_a$ Prediction in Acetone

The theoretical part of this project is dedicated to the thermodynamics of the ESPT, as described by p$K_a^*$, i.e., the thermodynamic measure of acidity in the first electronically excited state. The Förster cycle provides access to p$K_a^*$ *via* the ground-state p$K_a$ and the electronic excitation energies. As the first step, a quantum-chemical route to p$K_a$ in acetone based on COSMO-RS is described and the required linear free-energy relationship (LFER) parameters are determined. In this context, the following aspects are considered:

1. Which experimental reference data on p$K_a$ in acetone is available?
2. How does COSMO-RS perform for p$K_a$ in acetone, i.e., how good is the correlation?
3. Is there a relevant difference in performance between the levels BP-TZVP and BP-TZVPD-FINE?
4. Can the data set be described by a common set of LFER parameters or does it split?
5. (How much) Do the parameters differ from their theoretical values?
6. How do the LFER parameters for acetone compare to those for other solvents, in particular the related solvent acetonitrile?

These aspects are addressed in Chapter 5 using quantum-chemical DFT calculations in combination with the COSMO model (with TURBOMOLE) and COSMO-RS calculations for the Gibbs free energy in solution (with COSMO*therm*).

### 1.3.4. Sub-Project IV—Theoretical Spectroscopy in DMSO

As a second input for $pK_a^*$, the electronic excitation energies are needed. However, before predicting $pK_a^*$ in acetone, the performance of the selected computational tools, i.e., the continuum solvation model COSMO in combination with the correlated wavefunction-based methods ADC(2) and CC2 is investigated first. This validation is performed for the full set of Jung's photoacids (**A**–**F**) in the related solvent DMSO, chosen due to (i) the availability of experimental spectroscopic data and (ii) a good compromise in accuracy for COSMO as a polar aprotic solvent. The key research questions are:

1. How well does COSMO in combination with ADC(2) or CC2 perform for the theoretical spectroscopy of these photoacids in DMSO?
2. Is implicit solvation as described by COSMO enough to achieve a sufficient accuracy?
3. Which trends are observed in the calculated absorption and emission energies, as well as in the $pK_a$, $\Delta pK_a$, and $pK_a^*$ values? How can these be rationalized?
4. Are these photoacids able to perform an efficient ESPT in DMSO?
5. What is the origin of photoacidity for these photoacids?

The computational study presented in Chapter 6 deals with these objectives.

### 1.3.5. Sub-Project V—Exceeding Implicit Solvation

Having laid down the theoretical basis, this approach is finally extended to the solvent acetone. By predicting the $pK_a^*$ values of these photoacids in acetone, both the general possibility of ESPT to solvent for a given photoacid as well as the relative strengths can be judged. Moreover, solvent effects are studied by comparing the spectra and $\Delta pK_a$ values of photoacid **B** in different solvents (acetone, DMSO, and water). In this context, the role of explicit solvation, i.e., the need to go beyond implicit solvation effects by including explicit solvent molecules is also of interest. As an outlook, this sub-project also tries to complement the experimental work in acetone-water mixtures (Sub-Project I) by explicitly comparing acetone and water as interaction partners in acetone. The aim is to answer the following questions:

1. Do the selected methods that were tested in DMSO still work in acetone?
2. How well does COSMO perform in acetone? What is the accuracy with respect to the experimental data?
3. How much does explicit solvation affect the results? How do acetone, DMSO, and water differ in this regard?
4. How do water and acetone compare as complexation partners in acetone?

These questions are addressed in the quantum-chemical study presented in Chapter 7.

## 1.4. Outline of this Dissertation

The remaining part of this thesis is structured as follows:

- **Chapter 2** introduces the main experimental and computational methods that are used in this work. This includes time-resolved fluorescence spectroscopy based on time-correlated single photon counting or streak cameras and transient absorption spectroscopy for the experiments, as well as the implicit solvent model COSMO, its extension COSMO-RS, and the electronic structure methods MP2, ADC(2), and CC2 for the quantum-chemical calculations.
- **Chapters 3–7** contain the results of the individual research areas defined in Section 1.3. Hereby, Chapters 3–6 consist of published articles that are reprinted in their original format, whereas Chapter 7 contains the latest unpublished results.
- **Chapter 8** gives a summary of the results of this project and rates their relevance according to the actual state of research. An outlook on possible future extensions of this work is also included.
- The **Appendix** includes experimental details (**Chapter A**), a compilation of the corresponding Supporting Information to the articles (**Chapter B**), and a supplement to Chapter 7 (**Chapter C**).

# 2. Methodology

In this chapter, the relevant background of the experimental techniques (Sec. 2.1) and computation methods (Sec. 2.2) that have been used will be discussed. The purpose is to explain which methods have been used and to provide rationales for their selection. In addition, the characteristics of these methods will be presented in order to highlight their capabilities as well as their limitations.

## 2.1. Experimental Techniques

Steady-state (Sec. 2.1.1) as well as time-resolved fluorescence emission (Sec. 2.1.2) and UV/Vis absorption techniques (Sec. 2.1.3) have been chosen as the main experimental techniques in this work. These allow to characterize and to distinguish the different photoacid species, i.e., the protonated (ROH) and deprotonated ($RO^-$) photoacid, as changes in the electronic distribution upon deprotonation affect the electronic spectra.

### 2.1.1. Steady-State Spectroscopy

The key quantity in absorption spectroscopy is the absorbance $A$, which is defined as

$$A = A(\lambda) = \log\left(\frac{I_0(\lambda)}{I(\lambda)}\right) = -\log\left(\frac{I(\lambda)}{I_0(\lambda)}\right) \tag{2.1}$$

based on the fraction of the initial intensity of light $I_0(\lambda)$ at a given wavelength $\lambda$ and the remaining intensity $I(\lambda)$ after passing through the sample. Usually, the absorbance follows the Beer-Lambert law

$$A = \epsilon c d \tag{2.2}$$

and thus depends linearly on either the attenuation coefficient $\epsilon$, the sample concentration $c$, and the path length $d$. It is important to note that the molecular information enters in eq. (2.2) through the molecule-specific and wavelength-dependent attenuation coefficient $\epsilon = \epsilon(\lambda)$. On the other hand, the key quantity in steady-state fluorescence emission spectroscopy is the fluorescence intensity $I_{\mathrm{SS}}(\lambda)$, which can be understood as a time average of the fluorescence intensity decay $I(\lambda, t)$ (cf. Sec. 2.1.2)

$$I_{\mathrm{SS}}(\lambda) = \langle I(\lambda)\rangle \propto \int_{t=0}^{\infty} I(\lambda, t)\mathrm{d}t. \tag{2.3}$$

In general, steady-state absorption spectroscopy allows to monitor the ground-state proton-transfer equilibrium

$$\mathrm{ROH} \rightleftharpoons \mathrm{RO^-} + \mathrm{H^+}, \tag{2.4}$$

whereas, steady-state fluorescence can capture the corresponding excited-state reaction

$$\mathrm{ROH}^* \rightleftharpoons \mathrm{RO}^{-*} + \mathrm{H}^+. \tag{2.5}$$

Although the excited-state proton transfer (eq. (2.5)) in principle also resembles a chemical equilibrium, the finite fluorescence lifetime has an effect on the formation of the equilibrium in the excited state. In the extreme, i.e., if the equilibration was slow and the fluorescence decay very fast, the excited-state equilibrium would have no time to be reached.

With respect to the study of photoacids, fluorescence spectroscopy is particularly powerful as it provides a direct access to probing the excited state, which is the relevant electronic state for ESPT. In particular, this also applies to steady-state spectroscopy as the dynamics are still implicitly encoded in the time-averaged picture. Steady-state absorption is rather used to characterize the ground-state equilibrium, i.e., provide information on the sample prior to excitation. Moreover, the fluorescence emission of photoacids has been found to be particularly sensitive toward the deprotonation, which allows to identify proton-transfer intermediates. However, an important drawback is that these ESPT intermediates usually show a massive spectral overlap, which makes it hard to distinguish them in the (fluorescence) spectra. Generally, an ordering of the spectra (e.g., the emission peak maxima) of the different species is observed [132,271,296]:

$$\lambda(\mathrm{ROH}^*) < \lambda(\mathrm{CPX}^*) < \lambda(\mathrm{HBIP}^*) < \lambda(\mathrm{SSIP}^*) < \lambda(\mathrm{FIP}^*), \tag{2.6}$$

i.e., the higher the degree of dissociation (the distance of $\mathrm{RO}^{-*}$ and the $\mathrm{H}^+$), the stronger the red shift.

### 2.1.2. Time-Resolved Fluorescence Spectroscopy

As mentioned above, the steady-state fluorescence emission intensity provides only time-averaged information, but none on the actual fluorescence dynamics. To obtain information on the time evolution, i.e., the fluorescence intensity decay ($I(t)$), time-resolved fluorescence spectroscopy (TRF) is needed instead. Different techniques with different characteristics, especially regarding the time resolution, and for different purposes have been developed (*vide infra*). In the context of photoacids, temporally resolving the fluorescence emission from $\mathrm{ROH}^*$ (as the initial species) and $\mathrm{RO}^{-*}$ (as the final species) with additional contributions from potential intermediates allows to study the ESPT dynamics, i.e., the mechanism and the kinetics.

The unperturbed fluorescence intensity decay (at a given wavelength $\lambda$) of a single molecular species follows a mono-exponential decay

$$I(\lambda, t) = A(\lambda)\exp(-kt) = A(\lambda)\exp(-t/\tau) \tag{2.7}$$

with a (wavelength-dependent) amplitude $A(\lambda)$ and the decay constant $k = \tau^{-1}$ or the associated fluorescence lifetime $\tau$. If an excited-state equilibrium is involved, i.e., if the emitting species is in

a chemical equilibrium with another one, the fluorescence intensity decay becomes bi-exponential[133]. Moreover, more than one species can be involved, which will also lead to deviations from a purely mono-exponential decay at a (single) given wavelength. Therefore, multi-exponential fitting of the fluorescence decay within the framework of Global Target Analysis (GTA)[368,369] has become a standard procedure to deduce information on the rate constants from the lifetimes.

#### Different Techniques for Time-Resolved Fluorescence Spectroscopy

Temporally resolving the fluorescence intensity can be achieved either electronically or optically. For both types, the development of ultrafast pulsed lasers has been crucial since the defined, temporal control over the initial excitation event is a prerequisite in time-resolved fluorescence. Electronic techniques use advanced electronics to either count the photons, as done in Time-Correlated Single Photon Counting (TCSPC)[370], or translate the time information into a spatial information, as done by streak cameras[371] (*vide infra*). These electronic techniques allow investigations on a time scale down to a few ps as the lower limit and practically without an upper limit (statistics and the laser repetition rate may play a role), but they are limited to somewhat poorer time resolutions.

In contrast, optical techniques use an optical delay that is introduced by changing the relative path length between the excitation pulse and the emitted fluorescence in combination with a non-linear optical phenomenon to basically cut out a temporal portion of the fluorescence intensity by gating it *via* another laser pulse. The most important examples of such optically time-resolved techniques are fluorescence up-conversion[372], where the sum-frequency generation (SFG) signal of the fluorescence and an ultrafast UV/Vis laser pulse is generated in a non-linear crystal, and Kerr gating[373], where a near-IR gate pulse is used to control a Kerr medium (i.e., a medium in which the refractive index depends on the intensity) to gate a temporal part of the fluorescence intensity. The main difference between these two is that fluorescence up-conversion is basically limited to a single-wavelength detection (due to the phase-matching requirement for the SFG), whereas the full spectrum can be monitored at once *via* Kerr gating. Broadband fluorescence up-conversion is also possible, but requires the different wavelengths to hit from different directions, and thus angles, onto the crystal to be all phase-matched[374]. Compared to their electronic counterparts, these optical techniques typically have a much better time resolution that is mostly determined by the duration of the laser pulse, but they are limited to a time frame of a few ns at maximum (practical limitation in the optical delay generation). As a summary, a comparison of TCSPC, streak cameras, and fluorescence up-conversion is given in Tab. 2.1.

In this work, TCSPC and a streak camera were used for time-resolved fluorescence measurements since they both allow to investigate the ps–ns timescale, which has been found in previous work to be most relevant for the ESPT of photoacid **B**[48,302]. TCSPC gives the best signal/noise (S/N) ratios, but at the same time suffers from long detection times due to the low (exponentially decaying) probability of counting photons at late times and the additional restriction to single-wavelength detection. In this regard, the streak camera is a powerful device as it allows for very fast direct measurements on the full

(linear) timescale, but with worse S/N ratios and a hence a smaller dynamic intensity range. Because of this selection, further details on the working principles of these two techniques are given in the following. For further reference, experimental details on the TRF spectroscopy as used here are given in Sec. A.1, including a sketch of the setup (Fig. A.1 in Sec. A.1.1) and a description of the post-processing procedure of the data (Sec. A.1.2).

Table 2.1.: **A comparison of different techniques for ultrafast time-resolved fluorescence spectroscopy.**

| | **TCSPC** | **Up-Conversion** | **Streaking** |
|---|---|---|---|
| *Working Principle* | Repetitive counting of the sole photon of fluorescence emission signals under attenuated excitation | Generating a signal proportional to the emission by passing through a gated up-conversion crystal (sum frequency generation) | Dispersion of photo electrons, produced by the impact of emitted light on a photo cathode, across an imaging screen |
| *Temporal separation* | Measuring time between excitation pulse and detected photon | Variation of the optical delay time | Translation into a spatial component |
| *Intensity information* | Photon counts vs. time yield a histogram resembling the evolution | Intensities of the up-converted signals for differing delay times | Pixels of the image on CCD |
| *Time resolution* | Dependent on detector and electronics (sub-ns) | Determined by width of cross-correlation between excitation and gate laser pulse (sub-ps- to fs-range) | Several ps |
| *Wavelength detection* | One wavelength | One wavelength | Full spectrum at once |
| *Time demand* | Small | Large | Negligible |
| *Advantages* | High sensitivity; low degree of systematic errors; long time decays | Best time resolution | Fast; simultaneous measurements of frequency- and time-resolved decays; long time decays observable |
| *Drawbacks* | Slow: small counting rate caused by electronics; time demanding; no fast kinetics | Rather complex instrumentation; restricted to delay times smaller than a few ns | Poor time resolution compared to upconversion; similar to TCSPC |
| *Recent developments* | Continuously replaced by pulsed-laser diodes and LEDs | Broadband up-conversion by Ernsting *et al.*[374] | Photon-counting streak camera; reaching sub-ps time resolution |

### TCSPC

Historically, the first and most important method for sub-ns time-resolved fluorescence spectroscopy was TCSPC[375] and it still continues to be the most widely used to date. The development of cheap semiconductor lasers and fast photo-multipliers initiated an increasing replacement of expensive TCSPC systems for many applications though. According to its name, only one single photon of an optical pulse of interest is detected which is realized by sophisticated electronics (see Fig. 2.1).

Starting with an excitation pulse, the arrival time of this pulse is accurately measured using a constant function discriminator (CFD) and converted into an electric signal. After this, a time-to-amplitude

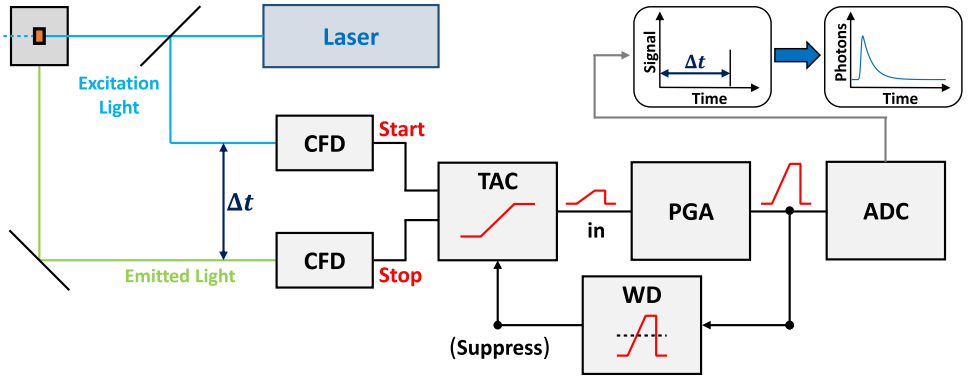



Figure 2.1.: **Principles of TCSPC.** The time delay $\Delta t$ between an excitation pulse and signal is measured by using constant function discriminators (CFDs). Both a start and stop signal are sent to the time-to-amplitude converter (TAC) when the CFDs detect the first photons, respectively. The voltage (proportional to $\Delta t$) produced by the TAC is amplified by a programmable gain amplifier (PGA). If the signal exceeds a certain threshold it is digitized by an analog-to-digital converter (ADC), otherwise, the signal is suppressed by a window discriminator (WD). Repeating the measurements numerous times yields a histogram of photon counts. Figure adapted from Ref. 376.

converter (TAC) generates a linearly increasing voltage ramp triggered by this signal. A second CFD detects, in the meantime, the arrival of an emitted light pulse and sends a termination signal to the TAC. Consequently, the TAC has produced a voltage which is proportional to the time delay. After amplification by use of a programmable gain amplifier (PGA), the signal is converted into a number by an analog-to-digital converter (ADC). Furthermore, if the TAC voltage does not fall within a given range it is suppressed by a window discriminator (WD) in order to exclude false readings. This is why a TCSPC setup is both highly sensitive for fluorescence emission and robust towards noise.

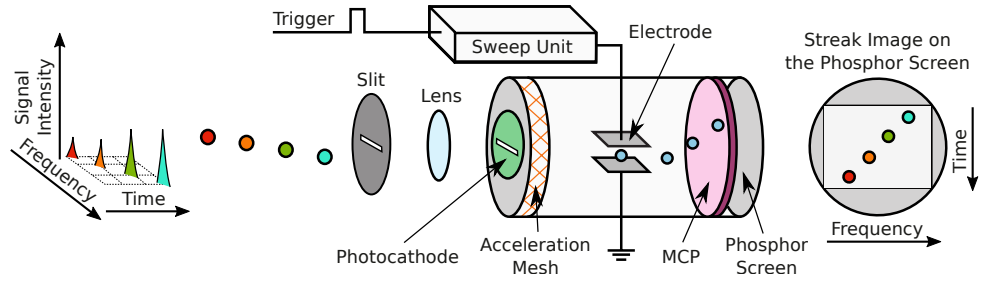
Under TCSPC conditions, less than one photon per pulse is detected; typically 100 excitation pulses are needed to detect one photon. This limited counting rate is chosen based on statistical reasons (if two photons were emitted, always only the earlier one would be detected, falsifying the histogram) and to avoid photon losses due to the dead time of the TCSPC device. Using a pulsed laser with a defined repetition rate as the source of excitation light, the above-described process takes place numerous times such that a plot of photon counts against the measured time delays yields a histogram. If the counting rule ($< 1$ photon/pulse) is fulfilled, this histogram corresponds to the waveform of the emitted light and thus contains the temporal evolution at the selected wavelength.

In conclusion, TCSPC is excellent when fluorophores revealing large intensity ratios are measured, but exhibits high time demands for performing spectral scans and a restriction to processes on the nanosecond timescale.

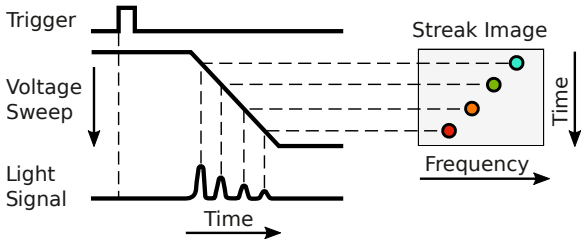
### Streak Cameras

A common limitation of TCSPC or fluorescence up-conversion is the high time demand due to the restriction of measuring one wavelength at a time. One technique that is very fast and can provide multi-wavelength data acquisition are streak cameras[371]. Despite its name, a streak camera does not record an

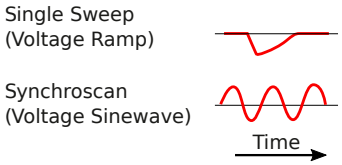
image, but converts the time information of an optical signal into a spatial displacement, hence also the term streak scope is used. A streak camera generally gives intensity vs. time vs. position information, which allows for various applications, not only spectroscopy (where position represents wavelength). For spectroscopic usage, a spectroscope is set in front of the streak camera to spatially separate sequential optical signals in the horizontal direction. After passing through the streak camera, the time delay of each pulse will be translated into an additional vertical position; eventually resulting in a two-dimensional arrangement. The principle of streaking is be described in more details in the following by referring to Fig. 2.2a.




(a) The principle of streaking




(b) Sweep voltage timing




(c) Sweep modes

Figure 2.2.: **Concepts of Streaking.** Illustrating the streaking of an optical signal consisting of four sequential short pulses (a). The timing of the sweep voltage controlled by a trigger signal (b) and two important sweeping modes (c). Figure reprinted with permission and in modified version from Ref. 377 (originally adapted from Ref. 378).

The light of interest, e.g. fluorescence emission of a sample, first enters the streak camera through a slit. In case that a spectroscope was applied prior, this light is already horizontally ordered by wavelength. The light is afterward focused onto the photocathode where photon impact leads to a release of electrons into the streak tube, the main part of the streak camera, caused by the inner photoelectric effect. Inside the streak tube, the electrons are accelerated towards the tube's end and vertically dispersed by use of two plane-parallel sweep electrodes. A linearly increasing sweep voltage, triggered by an external signal, is applied, building up an electric field which orders the electrons from top to bottom, as shown in Fig. 2.2b. By that, the temporal delay is translated into the vertical position (with the electrons still arriving at slightly different times). Depending on the operation mode, the streak camera can either sweep once (single-sweep mode) or repeatedly using a high-frequency sine-wave voltage (synchroscan mode), see Fig 2.2c.

Single pulses are usually very weak and the process of streaking further reduces the signal intensity with respect to the non-streaked signal such that amplification is needed. For this purpose, the primary electrons pass a micro-channel plate (MCT) which consists of multiple µm-sized channels, allowing for the simultaneous amplification of individual channels on the basis of secondary electrons (similar to a photomultiplier). Finally, the intensified free electron beams strike on the phosphor screen where the actual image is produced. Importantly, the streak image provides full information on the initial optical signal. The vertical position reflects the time ordering of the pulses, whereas the horizontal position is retained, and intensities are represented by the brightness on the screen. All this information can be read out and stored electronically using a high-sensitivity camera, e.g. a Charge-Coupled Device (CCD) sensor. Setups using streak cameras are to some extent superior to TCSPC systems because of better time resolutions ($\sim$ ps), a faster operation, and the possibility to directly observe the complete emission spectrum.

Interesting in the context of photoacidity, the first TRF spectroscopy of photoacids on the ps timescale has—to the best of my knowledge—been performed in fact with a streak camera (and, e.g., not with TCSPC) by Smith, Kaufman, Huppert, and Gutmann in 1979 on 2-naphthol-3,6-disulfonate and HPTS in water (with a time resolution of a few tens of ps)[203]. Later, in 1981, streak cameras have again been used by Huppert and Kolodney to study HPTS and 2-naphthol-6-sulfonate in alcohol–water mixtures[117], and by Shizuka *et al.* for 1-aminopyrene in acetonitrile–water mixtures ($\sim$ 30 ps time resolution)[92]; actually with the same model (Hamamatsu C979). This is a tremendous improvement compared to the time-resolved spectrophotometers with ns time resolution (e.g., pulse duration of $\sim$ 10 ns) that were commonly used for TRF on the ns timescale at that time, e.g., compare with previous studies by Tsutsumi *et al.*[75,91]. Despite this initially strong presence around 1980, streak cameras appear to have been much less common for ps TRF spectroscopy, in contrast to the much more popular TCSPC, which has been probably related to the expensive costs of streak cameras in—unfortunate—combination with worse time resolution and lower S/N ratios compared to TCSPC. Streak cameras have continuously improved over the years though and recently started to enter the regimes of time resolutions less than 1 ps and single-photon detection, paralleled by an improved S/N, which makes them very powerful devices for full-spectrum TRF spectroscopy. Moreover, streak cameras have also become routinely used for transient absorption spectroscopy (*vide infra*)[379–381].

### 2.1.3. Transient UV/Vis Absorption Spectroscopy

As a complement to time-resolved fluorescence spectroscopy, also its ultrafast analogue in UV/Vis absorption, typically referred to as femtosecond transient absorption (fsTA) spectroscopy[382] is used in this work. Visible fsTA spectroscopy allows to monitor the dynamics and transient changes in the UV/Vis absorption spectrum, capturing spectral changes in both the electronic ground state and the electronically excited states. This ability to follow the transient absorption spectra makes TA a powerful

tool since many molecules do not fluoresce and hence cannot be studied using TRF spectroscopy to obtain information on the excited-state dynamics.

Ultrafast transient UV/Vis absorption spectroscopy is usually achieved in a pump–probe experiment[383]. First, the sample is initially excited by a (tunable) pump pulse, here from the UV/Vis range opting for electronic excitation. Then, the changes in absorption can be measured by using a second, delayed probe pulse, which consists here of a white-light continuum for probing the UV/Vis absorption. Similar to optical TRF, the delay between these two pulses is generated optically and usually controlled *via* a delay stage. The full time scale of interest is scanned by varying the delay $\tau$ between the pump and probe pulses, yielding the absorption difference

$$\Delta A(\tau, \lambda) = A(\tau, \lambda) - A(\tau < 0, \lambda) = -\log\left(\frac{I(\tau, \lambda)}{I(\tau < 0, \lambda)}\right) \tag{2.8}$$

where the right-hand side is obtained by applying the definition of the absorbance (cf. eq. (2.1)). This equation demonstrates that the absorption difference at a delay $\tau$ (and at a wavelength $\lambda$) is determined by the intensity of the probe pulse at time $\tau$ and the intensity prior to excitation, i.e., $\tau < 0$. Conveniently, $\Delta A(\tau, \lambda)$ is measured in practice as the intensity ratio of the probe pulse of the pumped (excited) and un-pumped (non-excited) sample since $I(\tau < 0, \lambda)$ corresponds to the intensity of the un-pumped sample.

As a pump–probe technique, (vis) fsTA is to some extent conceptually different from TRF spectroscopy since the focus on the (first) electronically excited state as the stage for monitoring chemical changes in fluorescence follows directly from the nature of fluorescence as being the radiative decay of the usually first excited singlet state, according to Kasha's rule[384] (exceptions are known[385] though). In contrast, the electronic excitation of molecules remains the initial step in TA spectroscopy as applied here, but because the focus is intentionally set to the photochemical reaction dynamics. In fact, also other forms of transient absorption spectroscopy exist. The initial excitation does not have to be electronically, i.e., the pump pulse does not need to be from the UV/Vis range, but could, for example, also excite a molecular vibration (using an mIR pulse)[386] or core electrons (using an X-ray pulse)[387]. Similarly, the probe pulse is not restricted to being a white-light continuum for probing the UV/Vis absorption, e.g., (broad-band or narrow-band) mIR pulses are used in transient mid-infrared spectroscopy to follow the changes in the vibrational spectrum[134,136]. The experimental setup used for UV/Vis TA spectroscopy in this work is shown in Fig. A.3 (Sec. A.2.1) for further reference.

Another important difference to TRF spectroscopy is that, with $\Delta A(\tau, \lambda)$ in eq. (2.8) as the central quantity in TA spectroscopy, the signals in a TA map can have different signs, i.e., both positive and negative. In contrast, the fluorescence intensity—time-resolved or steady-state—is always positive. The different signal contributions in TA are illustrated in Fig. 2.3 and summarized below:

- **Ground-state Bleach (GSB):** *Negative* signal arising from the missing ground-state molecules that have been initially excited by the pump pulse; typically recovers to zero if the molecule does not decompose or as long as the conversion into another species is reversible

- **Stimulated Emission (SE):** *Negative* signal arising from the emitted light in a stimulated emission process, i.e., the radiative relaxation of excited molecules due to the interaction with the probe pulse
- **Excited-state Absorption (ESA):** *Positive* signal arising from the additional absorption of excited molecules of the sample or other excited intermediates
- **Product Absorption (PA):** *Positive* signal arising from the additional absorption of the products that have been generated in photo reactions of the excited sample

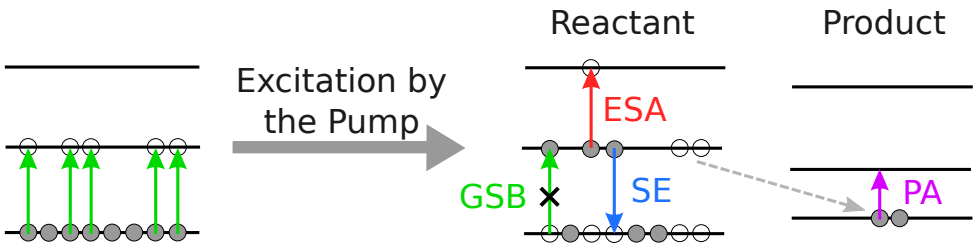



Figure 2.3.: **Signal contributions in TA spectroscopy.** After excitation by the pump pulse (left, green), four contributions are possible during interaction with the probe pulse (right): Ground-state bleach (GSB), stimulated emission (SE), excited-state absorption (ESA), and product absorption (PA). Note that each circle represents a molecule and not individual electrons. Figure reprinted with permission from Ref. 377.

Similarly to TRF, TA maps are also routinely analyzed within the framework of global lifetime analysis, i.e., using a multi-exponential model corresponding to a superposition of different (exponential) contributions for the various species. However, due to the different signs of the individual contributions (*vide supra*) and the additional contribution from dynamic solvatochromic shifts on the ultrafast (fs–ps) timescale, such analyses often becomes more complicated.

## 2.2. Computational Methods

This section will introduce the COSMO model (Sec. 2.2.1) as an efficient way to account for implicit solvent effects, in particular on the electronic excitation energies. Then, COSMO-RS—an extension of COSMO—will be presented (Sec. 2.2.2) that provides quantum-chemical access to thermodynamics in solution, which allows for the calculation of p$K_a$ values at a good compromise between accuracy and computational costs. Moreover, the combined use of COSMO and COSMO-RS allows for a consistent solvation treatment in this work. Finally, the underlying wavefunction-based methods MP2, ADC(2), and CC2 that have been used for geometry optimizations of ground-state and excited-state structures as well as for the computation of electronic excitation energies will be discussed (Sec. 2.2.3).

### 2.2.1. Continuum Solvation Using COSMO

#### Motivation—Scope of Solvent Models

Over the years, different solvation models have been developed to account for solvent effects, which are crucial for an accurate description of properties of molecules in solution. Regarding the scope of solvation, the two extremes on a scale of complexity are simple continuum models with a spherical cavity (e.g., the Onsager model[388,389]) on the lower end and molecular dynamics with a fully quantum-molecular description of the solvent (*ab initio* molecular dynamics, AIMD)[390,391] on the higher end, with various intermediate models in between (e.g., EC-RISM[392,393], frozen-density embedding[394,395], or polarizable embedding[396]). Implicit solvent models aim to describe bulk solvent effects without treating the solvent as explicit molecules, whereas explicit solvent models use a molecularly or atomically resolved structure of the solvent. A full, explicit solvation treatment—in principle—provides the most physically correct and thus most accurate description, but comes at considerable computational costs due to the high complexity. This involves the sampling over a statistically representative number of solvent configurations, but becomes even more severe in the case of electronic excitation energies (see Sec. 2.2.3). In contrast, Dielectric Continuum Solvent Models (DCSMs)[397], which are a special type of Continuum Solvent Models (CSMs)[398,399], have become highly popular and widely used owing to their computational efficiency and robustness. While *ab initio* molecular dynamics simulations for condensed phases are, because of the computational costs, limited to density functional theory or semi-empirical models, DCSMs can be readily combined with quantum-chemical methods, giving access to electronic excitation energies in solution[400] (see Sec. 2.2.3). The Polarizable Continuum Model (PCM)[401] is the most prominent CSM and many different formulations have been developed[329], including the Conductor-like Polarizable Continuum Model (C-PCM) as its DCSM variant[402,403]. Other examples of DCSMs include the Conductor-like Screening Model (COSMO)[362–364] or the SMx (x = 1-8[404], 12[405], D[406]) family of solvation models. The early Born model for ions (restricted to charges)[407], the Onsager model (restricted to electric dipoles)[388,389], and the Kirkwood–Onsager model (using a multi-pole extension)[408], which all use spherical cavities (i.e., only the radius as a parameter), are also classified as DCSMs. A major drawback of DCSMs is their limitation to

purely electrostatic interactions, thereby lacking the ability to describe specific solute–solvent interactions. To overcome this, explicit solvent is sometimes added to the implicitly solvated structures, giving rise to so-called hybrid implicit–explicit (or cluster continuum) approaches [409].

### Details on COSMO—An example of a DCSM

Common to all CSMs is that they treat the solute as being located within a cavity that is surrounded by the solvent, which is characterized by certain physical properties [398]. In the special case of DCSMs [397], the solvent is treated as a structure-less dielectric, i.e., it is described by a single physical quantity, the dielectric constant $\epsilon$. Such DCSMs then only consider purely electrostatic solute–solvent interactions *via* mutual polarization of the solute and the embedding dielectric continuum. The subsequent description of DCSMs and COSMO mainly follows the review on COSMO and COSMO-RS by Klamt [362] and the original publications on COSMO [363,364].

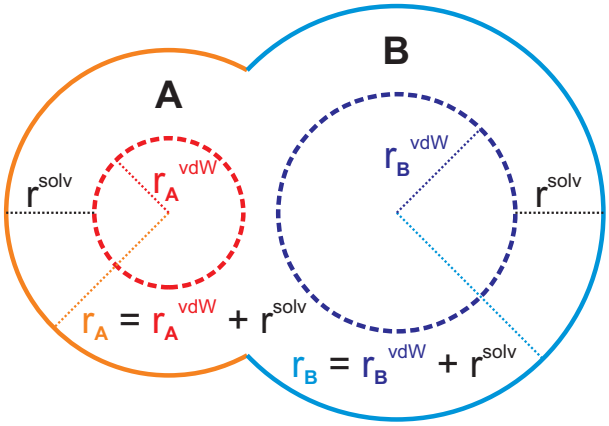



Figure 2.4.: **Two-dimensional schematic cavity construction for a diatomic molecule AB.** The solvent cavity is defined based on (outer) spheres with radii $r_\mathrm{A}$ and $r_\mathrm{B}$ for each atom that depend on atom-specific radii, e.g., the van-der-Waals radii ($r_\mathrm{A}^\mathrm{vdW}, r_\mathrm{B}^\mathrm{vdW}$) for the inner spheres as well as a global distance parameter $r^\mathrm{solv}$ to the outer solvent sphere. Note that such a radii-based cavity construction additionally requires smoothing at the intersections to avoid discontinuities, e.g., in derivatives. Figure adapted from Ref. 363.

Molecular-shaped cavities are known to give better results (e.g., compared to spherical cavities) and are hence frequently used for modern DCSMs [410]. Typically, the cavity is defined based on a set of atomic radii (see Fig. 2.4), although other construction schemes are possible (*vide infra*). In practice, the use of such molecule-specific cavities requires a discretization, which is achieved by subdividing the cavity into a set of $m$ surface segments with positions $\vec{r}_i$ and areas $s_i$. Then, the dielectric polarization of the continuum can be represented by apparent surface charges, collected in a vector $\vec{q} = (q_1, \ldots, q_m)$, that are located on these $m$ surface segments. In order to obtain these apparent surface charges, also referred to as screening charges, a set of linear equations needs to be solved:

$$\mathbf{A}\vec{q} + \mathbf{B}\vec{Q} = 0 \tag{2.9}$$

where $\vec{Q}$ contains the charge distribution of the solute, e.g., the nuclear charges and the electron density of the solute, and $\mathbf{A}$ and $\mathbf{B}$ are linear operators that implement a certain boundary condition. In the case of a dielectric continuum, these are given by:

$$\mathbf{A_D} = \mathbf{E}^{\perp} - \frac{4\pi\epsilon}{\epsilon - 1}\mathbf{S}^{-1} \quad \text{and} \quad \mathbf{B}_{\mathrm{D}} = \tilde{E}^{\perp} \tag{2.10}$$

where $\mathbf{E}^{\perp}$ is an $m \times m$ matrix that generates the normal component of the electric field on each surface segment caused by $\vec{q}$; $\mathbf{S}$ is the diagonal matrix of the surface segment areas; and $\tilde{E}^{\perp}$ is an operator that generates the normal component of the solute electric field on the surface segments based on the solute electron density and the nuclear charges.

Once eq. (2.9) has been solved for $\vec{q}$, the dielectric stabilization energy $E_{\mathrm{diel}}$, i.e., the energy gain due to the polarization of the continuum can be calculated as:

$$E_{\mathrm{diel}} = \frac{1}{2}\vec{\Phi}\vec{q}, \tag{2.11}$$

where $\vec{\Phi} = (\Phi_1, \ldots, \Phi_m)$ is the electrostatic potential generated by the solute's charge distribution at the positions of the charges $\vec{q}$ on the cavity. Important for the combination with quantum-chemical methods, the screening charges $\vec{q}$ enter in a subsequent iteration step of a self-consistent reaction field (SCRF)[411] procedure as external charges. Thereby, the solute and the embedding (solvent) continuum mutually polarize each other and an equilibration of the screening charges ($\vec{q}$) and the solute's charge distribution $\vec{Q}$ is realized by iteration until self-consistency.

The more complicated boundary condition for dielectric media typically prevents eq. (2.9) from directly being used in practice to solve for the screening charges, although this is possible and done, e.g., in the original formulation of PCM that is nowadays referred to as Dielectric PCM (D-PCM)[412]. For comparison, the boundary condition for the vanishing total potential of a conductor is more simple

$$\mathbf{A}\vec{q}^{\,*} + \vec{\Phi} = 0 \tag{2.12}$$

with the screening charges $\vec{q}^{\,*}$ in a real conductor (i.e., a dielectric with $\epsilon \to \infty$). Put another way, the matrices in the conductor case become:

$$\mathbf{A}_{\mathrm{C}} = \mathbf{V} \quad \text{and} \quad \mathbf{B}_{\mathrm{C}} = \tilde{V} \tag{2.13}$$

where $\mathbf{V}$ is a matrix that generates the electrostatic potential of each surface segment caused by $\vec{q}$ (i.e., a Coulomb matrix with non-zero diagonal elements), and $\tilde{V}$ is an operator that generates the electrostatic potential caused by the charge distribution of the solute on the cavity surface.

Motivated by this, COSMO introduces a conductor-like approximation for the solvent by using a scaled conductor boundary condition instead of the exact dielectric boundary condition [363]. Accordingly, within the COSMO approximation, the screening charges become

$$\vec{q} = f(\epsilon)\vec{q}^{\,*} \tag{2.14}$$

with the scaling factor

$$f(\epsilon) = \frac{\epsilon - 1}{\epsilon + x} \tag{2.15}$$

where $x$ is argued to be optimally set to 0.5 to obtain a reasonable estimate for the finite dielectric [363,403]. Based on eq. (2.14), eq. (2.12) simplifies within the COSMO approximation to

$$\mathbf{A}\vec{q} = -f(\epsilon)\vec{\Phi}, \tag{2.16}$$

which directly relates the screening charges to the solute potential (and thus to the charge density of the solute), and which can be (formally) solved by direct inversion.

According to eq. (2.15), $f(\epsilon) \to 1$ for $\epsilon \to \infty$, which means that the error of this conductor-like approximation decreases with increasing polarity of the solvent. This should not imply that COSMO can only be used for highly polar solvents because accurate results (with $x = 0.5$) can be obtained even down to $\epsilon = 2$ [403,413]. However, it should be recognized that DCSMs in general can have issues at both the low and high $\epsilon$ limits since the solute–solvent interaction for highly polar solvents (large $\epsilon$) often involves hydrogen bonding, whereas that for very apolar solvents (small $\epsilon$) often involves dispersion interactions, both of which are missing in DCSMs [360].

Note that COSMO and C-PCM are very closely related, basically only differing in this scaling factor, although they were developed independently. The use of a scaled conductor boundary condition turned out to significantly reduce the error from outlying-charge contributions [414], which motivated to also implement it in PCM, giving rise to C-PCM [402,403]. Later, the integral-equation-formalism version of PCM (IEF-PCM) [415] introduced a modified dielectric boundary condition that combines the dielectric exactness of D-PCM with the robustness regarding outlying charges of COSMO.

The cavity construction is a crucial factor for DCSMs in general to obtain robust and accurate results. Several construction schemes exist and, although the construction is rather empirical, two main concepts have been established [362]. The first and most widely used concept (and also the one used in this work) is the construction based on atom-centered spheres with specific radii. The second concept defines the cavity as an iso-electron-density surface of the solute, which is more complicated as the electron density of the solute depends on the polarization charges and thus the cavity, requiring a self-consist determination. The radii-based cavity construction can be further sub-divided into that using element-specific radii—as the COSMO implementation in TURBOMOLE [416,417] and COSMO*therm* [418]—and those using atom-type specific radii. Apart from the choice of radii, the smoothing between the intersecting spheres is another relevant factor for the performance.

Overall, compared to other DCSMs, COSMO has become a popular DCSM due to its algorithmic simplicity, numerical stability, and strong insensitivity with respect to outlying-charge errors. While combining COSMO with SCF methods like Hartree-Fock (HF) or density functional theory (DFT) is rather straightforward as it directly enters the SCF procedure (*vide supra*), the combination with post-SCF methods and particularly for the calculation of electronic excitation energies is more involved and requires more detailed considerations of different coupling schemes (cf. Sec. 2.2.3).

### 2.2.2. Accessing Thermodynamics via COSMO-RS

#### Motivation and General Remarks

The wide applications of DCSMs, particularly including COSMO, quickly revealed the clear limitations of the dielectric continuum solvation approach. For example, a main problem is the missing information on the molecular structure of the solvent, which prevents COSMO to distinguish between different solvents with similar dielectric constants. This has an important impact on the accuracy of Gibbs free energies of solvation[419,420]. With COSMO-RS, i.e., COSMO for Realistic Solvation, some substantial progress has been made in overcoming these inherent deficiencies of continuum solvation models[362]. COSMO-RS is an extension of COSMO that combines it with a statistical-thermodynamics treatment of interacting surfaces (*vide infra*) to improve the accuracy by reintroducing missing contributions from local, directional interactions (e.g., hydrogen bonds)[359–361]. By treating both the solute and the solvent on an equal footage, it provides a quantum-chemical access to the full thermodynamics in the fluid phase by predicting the chemical potential of any given species, at variable temperatures, and also in mixtures.

Owing to definition of the chemical potential $\mu_i$ of a compound $X_i$ in a system as

$$\mu_i := \left(\frac{\partial G}{\partial n_i}\right)_{T,p,n_{j\neq i}}, \tag{2.17}$$

i.e., as the partial derivative of the Gibbs free energy $G$ with respect to the chemical amount $n_i$ at constant temperature $T$, pressure $p$, and chemical amounts of the other compounds $n_{j\neq i}$, the chemical potential provides access to the total Gibbs free energy (in solution) and, in particular, Gibbs free energies of reactions. The scope of applications includes the prediction of activity coefficients, partition coefficients, vapor pressures, solubilities, solvation free energies, and many more[421–429]. Moreover, COSMO-RS has already been successfully applied to the prediction of p$K_\mathrm{a}$ values in water[365,366], DMSO[365], acetonitrile[367], and heptane[418]. In this work, it will be used to calculate p$K_\mathrm{a}$ values in acetone (*vide infra*).

Thereby, COSMO-RS is an approach to the fluid-phase thermodynamics that is almost second to none. To date, other quantum-chemical approaches to compute highly accurate solvation free energies—as the standard route to solution-phase free energies *via* thermodynamic cycles—mainly include SM12[405] and SMD[406] (from the SMx family) and IEF-PCM[415] (a variant of PCM). In this context, also the Analytical Linearized Poisson–Boltzmann (ALPB) method[430,431] reported by Grimme and co-workers

for density functional tight binding (DFTB) and their newly developed semi-empirical extended tight binding (GFN*n*-xTB)[432] and general force field (GFN-FF)[433] methods needs to be mentioned. ALPB was recently applied to p$K_a$ prediction in water using composite density functionals and the semi-empirical GFN2–xTB method; with an RMSD in prediction of 0.8-1.0 units (for the B97-3c functional)[434].

The original implementation of COSMO-RS had been developed by Klamt in 1999, as part of the COSMO*therm* program (commercially available by COSMO*logic*, now part of BIOVIA)[418]. Since then, several alternative implementations have emerged[435–440], which are claimed to (slightly) differ in their parameterization and to be less complete or detailed[362]. Very recently, also an open-source implementation of COSMO-RS has been reported[441].

#### Underlying Theory

The basic underlying idea behind COSMO-RS is to use the additional information on a given molecule that is contained in the cavity from a COSMO calculation (i.e., the topology) to determine its chemical potential ($\mu$) in solution. Instead of extracting just a single value, e.g., the dielectric stabilization energy, the COSMO cavity provides a whole distribution of charges on a surface. Similar to the derivation of COSMO, the state of reference for COSMO-RS is again a perfect conductor. This state is chosen since the electric field of a solute is perfectly screened by the screening charges $q_i = s_i\sigma_i$ (relating to the surface polarization charge densities $\sigma_i$) in a conductor and hence no intermolecular interactions between the solutes occur (providing that close contacts are avoided). It is furthermore assumed that (1) all parts of the COSMO surface can actually be in contact with each other (i.e., there are no hidden parts) and that (2) only pairwise interactions of the surface segments are allowed. The following description mainly follows the review by Klamt on COSMO and COSMO-RS[362].

Within the theory of COSMO-RS, energy expressions for the different solute–solvent interactions can then be derived by considering the pair-wise interaction of the segments (with screening charge densities $\sigma, \sigma'$) of two COSMO surfaces that are in contact with each other (e.g., see Ref. 359 for details). In general, such an energy contribution ($\Delta E_{\text{int},K}$) is given by

$$\Delta E_{\text{int},K} \simeq a_{\text{contact}} e_{\text{int},K}(\sigma, \sigma') \tag{2.18}$$

where $a_{\text{contact}}$ refers to the contact area of two surface segments and $e_{\text{int},K}(\sigma, \sigma')$ is a generic expression for the functional dependence on the charge densities $\sigma$ and $\sigma'$ for a given type of interaction ($K$). Moreover, when expressed in a (more) explicit form, $e_{\text{int},K}(\sigma, \sigma')$ will contain some parameters $a_{\text{int},K}$ that are later determined by fitting to thermochemical reference data.

A large contribution to the interaction energy arises from the electrostatic interaction that can be described (in first order) by the so-called MISFIT interaction of the polarization charge densities ($\sigma, \sigma'$) of the two charge surface segments that are in contact:

$$\Delta E_{\text{misfit}} \simeq a_{\text{contact}} e_{\text{misfit}}(\sigma, \sigma') = a_{\text{contact}} c_{\text{misfit}} \cdot (\sigma + \sigma')^2, \tag{2.19}$$

which increases with the squared net charge (i.e., $\sigma + \sigma'$).

If hydrogen-bonding is involved, i.e., if one of the two segments that are in contact is a HB donor and the other is a HB acceptor, another contribution arises that is described by

$$\Delta E_{\mathrm{HB}} \simeq a_{\mathrm{contact}} e_{\mathrm{HB}}(\sigma, \sigma') = a_{\mathrm{contact}} c_{\mathrm{HB}} \min(0, \sigma\sigma' - \sigma_{\mathrm{HB}}^2), \tag{2.20}$$

where the minimum criterion with the threshold $\sigma_{\mathrm{HB}}^2$ ensures that only sufficiently polar surface segments give rise to HB contributions to the interaction energy.

In addition, the van-der-Waals (vdW) contribution for dispersion interactions is approximated by

$$\mu_{\mathrm{vdW}}^X \simeq \sum_\alpha \gamma_\alpha A_\alpha^X \tag{2.21}$$

where the sum runs over all atoms $\alpha$ of a given solute $X$ with the exposed COSMO surface area $A_\alpha^X$ on an atom $\alpha$ and an element-specific pre-factor $\gamma_\alpha$. However, it is important to note that this vdW contribution is not part of the total interaction energy $\Delta E_{\mathrm{int}}$ defined as

$$\Delta E_{\mathrm{int}} \simeq a_{\mathrm{contact}} e_{\mathrm{int}}(\sigma, \sigma') = a_{\mathrm{contact}} \big( e_{\mathrm{misfit}}(\sigma, \sigma') + e_{\mathrm{HB}}(\sigma, \sigma') \big), \tag{2.22}$$

but $\mu_{\mathrm{vdW}}^X$ is directly added to the chemical potential (*vide infra*).

Under the above-mentioned assumptions and based on eq. (2.22), the total energy of a liquid ensemble $S$ of molecules compared to its conductor reference state can be expressed as the sum of interaction contributions over all surface contacts $k$:

$$E_{\mathrm{tot}}^S = \sum_k a_k e_{\mathrm{int}}(\sigma_k, \sigma_k') \simeq \sum_k a_{\mathrm{eff}} e_{\mathrm{int}}(\sigma_k, \sigma_k') \tag{2.23}$$

where the individual contact areas $a_k$ are additionally approximated by an effective contact area $a_{\mathrm{eff}}$ that takes over the role of averaging in this summation. Eq. (2.23) has converted the problem of calculating solvation energies into a problem of calculating the correct statistical-thermodynamic ensemble average of the total energy of a liquid that is subject to permanent fluctuations. Since it has been found that the explicit consideration of geometric constraints for the interactions is not necessary for an efficient evaluation of the thermodynamic average, neglecting these reduces the problem to finding the chemical potential $\mu_S(\sigma)$ of an effective surface segment with area $a_{\mathrm{eff}}$ and charge density $\sigma$ in the ensemble $S$:

$$\mu_S(\sigma) = -\frac{kT}{a_{\mathrm{eff}}} \ln \Big[ \int \mathrm{d}\sigma' p_S(\sigma') \exp\Big( - \frac{a_{\mathrm{eff}} e_{\mathrm{int}}(\sigma, \sigma') - \mu_S(\sigma')}{kT} \Big) \Big] \tag{2.24}$$

with

$$p_S(\sigma) = \sum_i x_i p^{X_i}(\sigma). \tag{2.25}$$

Thereby, $p_S(\sigma)$ represents the composition histogram of the ensemble $S$ with respect to the screening charge density $\sigma$ that relies on the mole fractions $x_i$ of the individual molecular components $X_i$ in the ensemble and the molecular histograms $p^{X_i}(\sigma)$ of each component. Note that $\mu_S(\sigma)$ and $p_S(\sigma)$ (or $p^{X_i}(\sigma)$) are often referred to as $\sigma$ potential and $\sigma$ profile, respectively. Since the $\sigma$ potential itself appears on the right-hand side of eq. (2.24), this equation needs to be solved iteratively.

Finally, the chemical potential of any molecule $X$ in the solvent $S$ can be computed by integrating $\mu_S(\sigma)$ in eq. (2.24) over the surface of the solute according to

$$\mu_S^X = \int \mathrm{d}\sigma p^X(\sigma)\mu_S(\sigma) + kT\ln(x + \gamma^X_{\mathrm{comb},S}) + \mu_{\mathrm{vdW}}. \tag{2.26}$$

The logarithmic term in eq. (2.26), sometimes referred to as combinatorial term, accounts for both the trivial dependence of $\mu_S^X$ on the mole fraction $x$ as well as for a correction $\gamma^X_{\mathrm{comb},S}$ for the relative sizes of the solute and solvent.

Information on different conformers of a molecule can be included in COSMO-RS, although it only matters if the conformers differ significantly in their $\sigma$ profiles. If this is the case, a Boltzmann average with respect to the Gibbs free energy in solution ($G_i^S = E_i^{\mathrm{COSMO}} + \mu_i^S$) can be performed[418]. In analogy to eq. (2.24), since the chemical potential $\mu_i^S$ of a given conformer depends itself on the populations in the ensemble $S$, the equations for the population must be solved self-consistently, additionally iterating in cycles over COSMO-RS calculations.

It is important to note that all molecular information that is needed for the evaluation of eq. (2.26), i.e., the $\sigma$ potentials and $\sigma$ profiles, are obtained from simple COSMO calculations of the respective species in the conductor reference state ($\epsilon \to \infty$). Moreover, apart from the COSMO surfaces, only very few parameters are needed that have been adjusted to experimental values of partition coefficients and vapor pressures of a wide range of neutral organic compounds[360]. This includes, as general parameters, the parameters for the interaction energies ($c_{\mathrm{misfit}}$, $c_{\mathrm{HB}}$, and $\sigma_{\mathrm{HB}}$) and one parameter for the effective contact area $a_{\mathrm{eff}}$, as well as one set of element-specific van-der-Waals parameters ($\gamma_\alpha$) for the dispersion interaction. This exclusive restriction to either general or element-specific parameters is a rather special feature of COSMO-RS that makes it different from other statistical-thermodynamics methods.

The parametrization for COSMO-RS in COSMO*therm* (in combination with TURBOMOLE) is available for three default methods[442,443]:

- **BP-SVP-AM1:** COSMO-BP-RI-DFT/def-SVP energy at AM1-COSMO/def-SVP geometry
- **BP-TZVP:** COSMO-BP-RI-DFT/def-TZVP energy at COSMO-BP-RI-DFT/def-TZVP geometry
- **BP-TZVPD-FINE:** COSMO-BP-RI-DFT/def2-TZVPD energy using a refined COSMO cavity[444] calculated at a COSMO-BP-RI-DFT/def-TZVP geometry

The BP-SVP-AM1 is only of lower quality and supposed to be used for screening a large number of compounds, while BP-TZVP is considered a 'good quality' method, and BP-TZVP-FINE the 'best

quality' method[418]. However, the prediction quality of COSMO-RS eventually refers to the quality of the COSMO surfaces, i.e., an accurate distribution of (correct) screening charges, and not on the underlying electronic-structure method *per se*. For example, also a parameterization with the higher-level MP2 has been reported, but no significant improvements over the BP DFT variants could be observed[443]. In this work, both the BP-TZVP and BP-TZVPD-FINE parameterizations are used for the p$K_\mathrm{a}$ prediction (*vide infra*).

Inherent limitations of COSMO-RS include its restriction (by construction) to the conductor reference state, which prevents a further application of COSMO-RS for response properties[445]. Moreover, the underlying electronic-structure method (i.e., basically BP DFT here) is a potential issue since it can become a limiting factor in the case of molecules for which it is no longer suitable[365]. Finally, since all information is eventually derived from the cavity, the cavity construction is a sensitive issue for COSMO-RS[444].

#### Application to the Prediction of Acidity Constants

For the prediction of acidity constants, the following dissociation equilibrium is considered:

$$\mathrm{HA}_{(\mathrm{soln.})} + \mathrm{S}_{(\mathrm{soln.})} \rightleftharpoons \mathrm{A}^-_{(\mathrm{soln.})} + \mathrm{SH}^+_{(\mathrm{soln.})} \tag{2.27}$$

where HA/A$^-$ and SH$^+$/S refer to the conjugate Brønsted acid–base pair of the acid HA and the solvent S, respectively. The acid dissociation constant $K_\mathrm{a}$ is defined based on the activities $a$ of all species as

$$K_\mathrm{a} := \frac{a(\mathrm{A}^-) \cdot a(\mathrm{SH}^+)}{a(\mathrm{HA}) \cdot a(\mathrm{S})} \tag{2.28}$$

and relates to the Gibbs free energy of dissociation $\Delta G_\mathrm{diss}$ *via* the fundamental relation

$$\Delta G_\mathrm{diss} = -RT \ln K_\mathrm{a} \tag{2.29}$$

with the ideal gas constant $R$ and the absolute temperature $T$. Based on the definition of p$K_\mathrm{a}$ as the negative decadic logarithm of $K_\mathrm{a}$, i.e.,

$$\mathrm{p}K_\mathrm{a} := -\lg K_\mathrm{a}, \tag{2.30}$$

the following exact relation is finally obtained by inserting eq. (2.29) into eq. (2.30) (and converting the logarithms):

$$\mathrm{p}K_\mathrm{a} = \frac{\Delta G_\mathrm{diss}}{RT \ln(10)}. \tag{2.31}$$

Furthermore, $\Delta G_\mathrm{diss}$ can be decomposed into

$$\Delta G_\mathrm{diss} = \big(G_\mathrm{soln.}(\mathrm{A}^-) + G_\mathrm{soln.}(\mathrm{SH}^+)\big) - \big(G_\mathrm{soln.}(\mathrm{HA}) + G_\mathrm{soln.}(\mathrm{S})\big), \tag{2.32}$$

meaning that $\Delta G_{\text{diss}}$ can be calculated based on the total Gibbs free energies (or the chemical potentials) of all species occurring in eq. (2.27). Since COSMO-RS allows to calculate the chemical potentials of all species in solution, it can be directly used to calculated the $\Delta G_{\text{diss}}$ based on eq. (2.32), which then could enter eq. (2.31) to obtain the p$K_{\text{a}}$. However, approaches to p$K_{\text{a}}$ using DCSMs—and also the implementation of COSMO-RS in COSMO*therm*[418]—typically use an empirical generalization of eq. (2.31) according to

$$\text{p}K_{\text{a}} = c_0 + c_1 \frac{\Delta G_{\text{diss}}}{RT \ln(10)} \tag{2.33}$$

instead of the exact thermodynamic relation, where ideally $c_0 = 0$ and $c_1 = 1$[321]. Eq. (2.33) resembles a linear free-energy relationship (LFER) that additionally includes a scaling factor (slope) $c_1$ and an offset (intercept) $c_0$ to introduce a higher flexibility, as the $\Delta G_{\text{diss}}$ based on DCSMs like PCM or COSMO usually suffer from systematic errors. Despite their inherent disadvantages, the use of DCSMs can be actually beneficial with respect to thermodynamic properties since the implicit solvation already accounts for a statistically averaged description[399]. The LFER parameters $c_0$ and $c_1$ are then obtained by using a molecular training set and fitting the calculated $\Delta G_{\text{diss}}$ values to the experimental p$K_{\text{a}}$ values according to eq. (2.33)[365–367].

In contrast to other DCSM-based approaches to p$K_{\text{a}}$, COSMO-RS can directly compute $\Delta G_{\text{diss}}$ (using the chemical potential in solution) and does not rely on an additional thermodynamic cycle to bypass this direct calculation and providing an alternative path. For example, the conceptually simplest thermodynamic (Born-Haber) cycle consists in formally shifting the dissociation reaction (eq. (2.27)) from the solution phase into the gas phase by first desolvating the reactants, next letting the gas-phase dissociation take place, and finally solvating the products[323]. In this way, $\Delta G_{\text{diss}}$ can be decomposed into contributions from the Gibbs free solvation energies ($\Delta G_{\text{solv}}$) of the involved species and the gas-phase reaction energy ($\Delta E$). However, it is important to note here that although the choice of the thermodynamic cycle is eventually arbitrary, as all cycles are in principle equivalent, different cycles may vary in performance in practice, e.g., due error compensation[356]. In fact, the direct thermodynamic cycle raises the problem of dealing with $\Delta G_{\text{solv}}$ of the proton, a quantity that is hard to theoretically predict, which then usually requires a value taken from experiments.

Although the direct thermodynamic cycle is not actually invoked by COSMO-RS, it is still reflected in the equation for $\Delta G_{\text{diss}}$ (eq. (2.32)) based on the dissociation reaction (eq. (2.27)) that is used. No efforts in improving the solvent-dependent contribution, $G_{\text{soln.}}(\text{SH}^+) - G_{\text{soln.}}(\text{S})$, are undertaken though, as any (constant) error in $\Delta G_{\text{diss}}$ will be absorbed in $c_0$ anyway. In fact, this can be used to motivate a further simplification of eq. (2.33) for COSMO-RS by incorporating this solvent-dependent contribution into a new intercept, yielding

$$\text{p}K_{\text{a}} = \tilde{c}_0 + \frac{c_1}{RT \ln(10)} \big( G_{\text{soln.}}(\text{A}^-) - G_{\text{soln.}}(\text{HA}) \big) \tag{2.34}$$

with

$$\tilde{c}_0 = c_0 + \frac{c_1}{RT\ln(10)}\big(G_{\text{soln.}}(\text{SH}^+) - G_{\text{soln.}}(\text{S})\big). \tag{2.35}$$

Eq. (2.35) directly correlates the difference in the Gibbs free energy in solution of $A^-$ and HA with the p$K_a$.

The accuracy in p$K_a$ prediction based on COSMO-RS and using a fit to the LFER between experimental p$K_a$ values and calculated $\Delta G_{\text{diss}}$ values, as described here, heavily relies on the quality of the experimental data. Further limitations can arise from the underlying electronic structure methods for COSMO-RS if these have an issue with a particular molecular class (*vide supra*). Perhaps a conceptual drawback is that this pragmatic approach to p$K_a$ will need a set of parameters for each solvent that is considered. In particular, this requires to determine these parameters if new solvents are about to be studied. Moreover, also a splitting of the molecular data set can appear, as observed for the p$K_a$ prediction in acetonitrile[367], indicating that method-dependent systematic errors with respect to different chemical classes can occur.

## 2.2.3. Electronic Structure Methods

### General Considerations on Post-HF Methods

To obtain reliable geometries and energies for the electronic ground and excited states, the post-HF methods MP2, ADC(2), and CC2 were used. The general idea behind these post-HF methods is to improve upon the Hartree-Fock (HF) result by accounting for dynamic electron–electron correlation *via* inclusion of excited determinants into the wavefunction ansatz, as done in Møller-Plesset Perturbation Theory (MPPT), Configuration Interaction (CI), and Coupled Cluster (CC) methods (e.g., see Ref. 446). However, it is important to remember that, being based on HF, these post-HF methods are only expected to give good results if HF itself is qualitatively correct. This implies that the electronic ground state must be described qualitatively correct by a single Slater determinant (or single configuration state function for restricted open-shell cases). In the following, it is assumed that the molecules have a closed-shell singlet ground state, which means that Restricted HF (RHF) can be applied. Here, the methods MP2 and CC2 are used for the electronic ground state, and ADC(2) and CC2 for the (first) electronically excited state.

### Second-Order Møller-Plesset Perturbation Theory (MP2)

Møller-Plesset Perturbation Theory (MPPT)[447,448] applies the general Rayleigh-Schrödinger Perturbation Theory (RSPT) to the problem of dynamic electron–electron correlation in a molecule with HF as the zeroth-order solution. The molecular electronic Hamiltonian $\hat{H}$ is split according to

$$\hat{H} = \hat{H}^{(0)} + \lambda\hat{V} \tag{2.36}$$

into the Hamiltonian of an unperturbed reference system $\hat{H}^{(0)}$ and the fluctuation potential $\hat{V}$. $\lambda$ denotes the perturbation strength (and is set to $\lambda = 1$ for evaluating the final equations). The solutions to the time-independent Schrödinger equation (TISE) of $\hat{H}^{(0)}$, i.e., the sets of eigenvalues $E_i^{(0)}$ and the

eigenfunctions $|\Psi_i^{(0)}\rangle$ are assumed to be known. The aim is then to express the solution of the TISE of the perturbed Hamiltonian ($\hat{H}$)

$$\hat{H}|\Psi_k\rangle = E_k|\Psi_k\rangle \tag{2.37}$$

in the eigenbasis of the unperturbed system ($\hat{H}^{(0)}$). Using a power expansion of the (ground-state) wave function $|\Psi_0\rangle$ of the perturbed system

$$|\Psi_0\rangle = \sum_{n=0}^{\infty} \lambda^n |\Psi_0^{(n)}\rangle \tag{2.38}$$

and a corresponding power expansion of the (ground-state) energy $E_0$

$$E_0 = \sum_{n=0}^{\infty} \lambda^n E_0^{(n)} \tag{2.39}$$

allows to derive equations for the various corrections to the wave function $|\Psi_0^{(n)}\rangle$ and the energy $E_0^{(n)}$ order by order.

In MPPT, the unperturbed Hamiltonian is set to the Fock operator $\hat{F}$

$$\hat{H}^{(0)} \equiv \hat{F} = \sum_{i=1}^{N} \hat{f}(i), \tag{2.40}$$

i.e., the sum of one-electron Fock operators $\hat{f}(i)$. The first correction to the HF energy ($E_{\mathrm{HF}}$) is only obtained in second-order MPPT (MP2) since, as usual in RSPT, the sum of the zeroth and first-order energy is equal to the expectation value of $\hat{H}$ taken over the unperturbed wavefunction:

$$E_{\mathrm{MP1}} = E_0^{(0)} + E_0^{(1)} = \langle \mathrm{HF}|\hat{H}|\mathrm{HF}\rangle = E_{\mathrm{HF}}. \tag{2.41}$$

The MP2 energy is given by

$$E_{\mathrm{MP2}} = E_0^{(0)} + E_0^{(1)} + E_0^{(2)} = E_{\mathrm{HF}} + E_0^{(2)} \tag{2.42}$$

with the second-order correction

$$E_0^{(2)} = \sum_{ia>jb} \frac{(\langle ij|r_{12}^{-1}|ab\rangle - \langle ij|r_{12}^{-1}|ba\rangle)^2}{\epsilon_i + \epsilon_j - \epsilon_a - \epsilon_b} = \frac{1}{4}\sum_{ia,jb} t_{ab}^{ij}\langle ij||ab\rangle \tag{2.43}$$

where $i$ and $j$ denote occupied and $a$ and $b$ virtual spin orbitals of the HF determinant, $\epsilon_k$ ($k = i, j, a, b$) are the corresponding orbital energies, and $\langle ij|r_{12}^{-1}|ab\rangle - \langle ij|r_{12}^{-1}|ba\rangle =: \langle ij||ab\rangle$ are four-center two-electron repulsion integrals. A more compact notation (RHS of eq. (2.43)) introduces the doubles amplitudes (cf. coupled cluster theory, *vide infra*)

$$t_{ab}^{ij} = \frac{\langle ij||ab\rangle}{\epsilon_i + \epsilon_j - \epsilon_a - \epsilon_b}. \tag{2.44}$$

Due to the Brillouin condition, singly excited Slater determinants do not contribute to $E_0^{(2)}$ and hence only doubly excited determinants appear in eq. (2.43). MP2 gives a significant improvement over HF by accounting for large parts of the correlation energy and benefits from a good error compensation. Therefore, MP2 energies as well as geometries are frequently used [449,450]. Higher orders of MPPT are not applied by default as the higher-order corrections often start to oscillate [451].

#### Approximate Coupled Cluster Singles and Doubles Method (CC2)

The approximate coupled cluster singles and doubles method (CC2) belongs to the Coupled Cluster (CC) family of methods (e.g., see Refs. 452–454 for recent reviews). These have in common that they utilize an exponential ansatz for the wave function

$$|\mathrm{CC}\rangle = \exp(\hat{T})|\mathrm{HF}\rangle, \tag{2.45}$$

with

$$\hat{T} = \sum_{i=1}^{N} \hat{T}_i = \hat{T}_1 + \hat{T}_2 + \ldots = \sum_{ai} t_{ai}\tau_{ai} + \sum_{ai>bj} t_{aibj}\tau_{ai}\tau_{bj} + \ldots = \sum_{i=1}^{N}\sum_{\mu_i} t_{\mu_i}\tau_{\mu_i}. \tag{2.46}$$

At each level, the cluster operator $\hat{T}$ corresponds to a certain excitation class, i.e., $\hat{T}_1$ for single excitations, $\hat{T}_2$ for double excitations, etc. Therefore, the operators $\hat{T}_i$ can be expressed as a product of cluster amplitudes ($t_{ai}, t_{aibj}, ...$) as coefficients and an $i$-fold product of excitation operators ($\tau_{ai}, \tau_{ai}\tau_{bj}, ...$), where an operator $\tau_{ai}$ promotes an electron from an occupied orbital $i$ into an virtual orbital $a$. Truncation of $\hat{T}$ at a given excitation level $N$ (i.e., at maximum the number of simultaneously excited electrons) yields the corresponding truncated CC methods, e.g., CC Singles (CCS; $N = 1$), CC Singles and Doubles (CCSD; $N = 2$), etc.

An equation for the CC energy ($E_{\mathrm{CC}}$) is obtained by inserting eq. (2.45) into the TISE (eq. (2.37)), multiplying by $\exp(-\hat{T})$ from the left, and projection onto the HF wave function:

$$E_{\mathrm{CC}}(t) = \langle \mathrm{HF}| \exp(-\hat{T})\hat{H}\exp(\hat{T})|\mathrm{HF}\rangle. \tag{2.47}$$

Similarly, a set of non-linear equations for the cluster amplitudes $t_{\mu_i}$ is obtained by a projection onto the excitation manifold $\{\langle\mu_i|\}$:

$$e_{\mu_i}(t) = \langle \mu_i| \exp(-\hat{T})\hat{H}\exp(\hat{T})|\mathrm{HF}\rangle = 0. \tag{2.48}$$

Two technical remarks shall be made here. First, the multiplication with $\exp(-\hat{T})$ prior to the projection matters in order to later exploit the Baker-Campbell-Hausdorff (BCH) expansion for the evaluation of the similarity-transformed Hamiltonian, $\tilde{H} = \exp(-\hat{T})\hat{H}\exp(\hat{T})$, as a series of commutators. Second, the non-variational nature of the CC equations in practice can be conveniently handled by using a variational CC Lagrangian, i.e., $L_{\mathrm{CC}}(t,\bar{t}) = E_{\mathrm{CC}}(t) + \bar{t}e(t)$, that additionally introduces Lagrangian multipliers $\bar{t}$ [455].

A special case are the approximate coupled cluster methods CC$n$ that build upon a CC method truncated at an excitation level $n$ and introduce further approximations to the $n$-tuple cluster equations.

The idea is to keep only those terms in the amplitude equation for the $n$-tuple excitation manifold that enter in lowest non-vanishing order (in MPPT), with the singles being considered in zeroth order, i.e., not being approximated. The latter is motivated by the special role of single excitations in response calculations, e.g. for excitations energies, for which the CC$n$ methods had been designed[456,457].

For example, CC2 is derived from CCSD (i.e., $\hat{T} = \hat{T}_1 + \hat{T}_2$), whose amplitude equations are given by

$$\langle \mu_i | \exp(-(\hat{T}_1 + \hat{T}_2)) \hat{H} \exp(\hat{T}_1 + \hat{T}_2) | \mathrm{HF} \rangle = 0, \quad (i = 1, 2) \tag{2.49}$$

which can be re-written using $\hat{T}_1$ similarity-transformed operators, $\tilde{O} = \exp(-\hat{T}_1) \hat{O} \exp(\hat{T}_1)$, as:

$$\langle \mu_1 | \tilde{H} + [\tilde{H}, \hat{T}_2] | \mathrm{HF} \rangle = 0 \tag{2.50}$$

$$\langle \mu_2 | \tilde{H} + [\tilde{H}, \hat{T}_2] + \frac{1}{2} [[\tilde{H}, \hat{T}_2], \hat{T}_2] | \mathrm{HF} \rangle = 0. \tag{2.51}$$

In the CC2 model, the singles equations are kept unchanged, while the doubles equations of CCSD are simplified such that they contain only terms to lowest non-vanishing (i.e., first) order[456]. Using the standard partitioning of the Hamiltonian $\hat{H} = \hat{F} + \hat{U}$ into a Fock operator $\hat{F}$ and a fluctuation potential $\hat{U}$ (cf. eq. (2.40)), the doubles equations for CC2 finally become

$$\langle \mu_2 | [\hat{F}, \hat{T}_2] + \tilde{H} | \mathrm{HF} \rangle = 0. \tag{2.52}$$

Since CC2 is based on CCSD and no approximations were made to the singles equations, CC2 is also termed a second-order method as it is correct up to second order (in MPPT) for singles excitations. The total CC2 energy is of MP2 quality and does not give a significant improvement beyond MP2 for ground-state energies[456]. However, unlike MP2, CC2 allows to calculate excitation energies and transition moments (i.e., spectra) within the framework of response theory (*vide infra*).

#### Linear Response Theory

Two main branches have emerged for the description of electronically excited states in quantum chemistry (e.g., see Ref. 458 for a recent review on excited-state coupled cluster methods). The first are state-specific approaches that explicitly optimize wave functions for each individual excited state[459]. The second is response theory that bypasses the need for an explicit treatment of excited-state wave functions by recovering information on the excited state through a perturbation of the ground state[460]. Thereby, response theory allows to extend an established electronic structure ground-state method to electronically excited states.

In a nutshell, this is accomplished by considering the interaction with light as a time-periodic perturbation $\hat{V}(t)$ to the unperturbed Hamiltonian ($\hat{H}^{(0)}$) of the molecular system

$$\hat{H}(t) = \hat{H}^{(0)} + \hat{V}(t) \tag{2.53}$$

with

$$\hat{V}(t) = \sum_k \exp(-i\omega_k t)\epsilon_k(\omega_k)\hat{Y}_k \tag{2.54}$$

where $\omega_k$ and $\epsilon_k(\omega_k)$ are the angular frequency and the amplitudes of the Fourier components of the (oscillating) light field and $\hat{Y}_k$ are operators that describe the interaction of the molecule with the field (e.g., the electric dipole operator for a homogeneous electric field). Then, the time-dependent expectation value of a given observable $X$ is expanded in orders of the perturbation strength

$$\langle\Psi_0(t)|\hat{X}|\Psi_0(t)\rangle = \langle\Psi_0|\hat{X}|\Psi_0\rangle + \sum_k \epsilon_k(\omega_k)\langle\langle X_0; X_k\rangle\rangle_{\omega_k} \exp(-i\omega_k t) + \ldots \tag{2.55}$$

which allows to identify the response functions as the central quantities in response theory; thus giving the theory its name. In first order, the linear response function can be identified which, for exact states, can be written in terms of the eigenbasis of the unperturbed Hamiltonian $\hat{H}$ as

$$\langle\langle X_0; X_k\rangle\rangle_{\omega_k} = \mathcal{P}^{X_0,X_k} \sum_{J\neq 0} \frac{\langle\Psi_0|\hat{X}_0|\Psi_J\rangle\langle\Psi_J|\hat{X}_k|\Psi_0\rangle}{\omega_k - \Delta\omega_{J0}} \tag{2.56}$$

where $\mathcal{P}^{X_0,X_k}$ is a permutation operator and $\Delta\omega_{J0} = \Delta E_{J0}/\hbar = (E_J - E_0)/\hbar$ refers to the excitation energy $\Delta E_{J0}$ for a transition from the ground state $(\Psi_0, E_0)$ to the $J$-th excited state $(\Psi_J, E_J)$. Important for response theory, eq. (2.56) demonstrates that the linear response function has poles at the excitation energies, i.e., when $\omega_k = \Delta\omega_{J0}$, and the corresponding residual $\langle\Psi_0|\hat{X}_0|\Psi_J\rangle\langle\Psi_J|\hat{X}_k|\Psi_0\rangle$ relates to the transition moment.

This brief motivation of the linear response function was only used here for illustration purposes. In general, a simple-minded derivation of response theory based on time-dependent perturbation theory is not suitable in practice (i.e., for numerical calculations). A more sound derivation of response theory and the response functions is given by partitioning the full time-dependent wavefunction into a phase-isolated wavefunction and an oscillating phase factor, and deriving a variational principle for time-periodic wave functions, with the so-called quasi energy taking over in the time-dependent formulation the role of the formerly time-independent energy[461]. A general approach to the response functions for non-variational methods (including the CC methods) then follows from derivatives of a (CC) quasi-energy Lagrangian.

An important implication of the formulation of response theory using a time-dependent variational principle and connecting the response functions to derivatives of the quasi-energy (or its Lagrangian) is that the excitation energies occur at the eigenvalues of the stability matrix of the Lagrangian,

$$(\mathbf{Q} - \omega_k\mathbf{S})\vec{c}^{(k)} = 0 \tag{2.57}$$

i.e., the electronic Hessian ($\mathbf{Q} = \mathbf{E}$) in case of variational methods or the electronic Jacobian ($\mathbf{Q} = \mathbf{A}$) in case of non-variational methods. $\mathbf{S}$ denotes the matrix for the metric.

#### Electronic Excitation Energies Using ADC(2) and CC2

As mentioned before, linear response theory now allows to extend the CC2 method to electronically excited states and, in particular, to the calculation of excitation energies based on eq. (2.57). A closely related second-order method is ADC(2), i.e., the Algebraic Diagrammatic Construction Scheme (for the Polarization Propagator) through second order, which also calculates electronic excitation energies as eigenvectors of its secular matrix. ADC(2) is not based on linear response theory of a corresponding ground-state method, but derived within the Polarization Propagator Approach (PPA) (e.g., see Ref. 462 for a recent review). However, based on rational design, the ground-state contribution to the excited-state ADC(2) energies is defined to be MP2.

Despite their different origins, an analysis of the structure of the respective secular matrix

$$A_{ij} = \left( \frac{\mathrm{d}L}{\mathrm{d}\bar{\lambda}_i \lambda_j} \right)_0 \tag{2.58}$$

allows to identify the similarities between ADC(2) and CC2 from a more pragmatic, technical perspective (see Ref. 463). Accordingly, if we consider the CC2 Jacobian ($\mathbf{A}^{\mathrm{CC2}}$) as a function of the ground-state singles ($T_1$) and doubles ($T_2$) amplitudes, i.e., $\mathbf{A}^{\mathrm{CC2}} = \mathbf{A}^{\mathrm{CC2}}(T_1, T_2)$, the ADC(2) Jacobian ($\mathbf{A}^{\mathrm{ADC(2)}}$) can be expressed as:

$$\mathbf{A}^{\mathrm{ADC(2)}} = \frac{1}{2}\big(\mathbf{A}^{\mathrm{CC2}}(0, T_2^{(1)}) + \mathbf{A}^{\mathrm{CC2}}(0, T_2^{(1)})^\dagger\big). \tag{2.59}$$

This analysis (eq. (2.59)) reveals two important differences between ADC(2) and CC2. First, the CC2 cluster amplitudes are replaced by those from first-order MPPT, i.e., the singles replacement part of $T_1$ vanishes (provided the Brillouin conditions is fulfilled) and $T_2$ is limited to $T_2^{(1)}$. Second, only the Hermitian part of this matrix is kept for the ADC(2) Jacobian.

Of these two differences, the missing ground-state singles contributions in ADC(2) are supposed to have a more relevant, potential effect on the excitation energies as these allow for a coupling of the ground and excited state. Instead, the additional hermitian nature of $\mathbf{A}^{\mathrm{ADC(2)}}$ is not supposed to significantly affect the excitation energy itself, but it leads to practical advantages (left and right eigenvectors become equivalent) and ensure a qualitatively correct behavior near conical intersections (in contrast to methods with a non-hermitian Jacobian)[463]. The typical deviation between CC2 and ADC(2) excitation energies are in the order of 0.01–0.03 eV for closed-shell organic molecules[464,465]. Larger deviations can occur if the singles contribute to a significant coupling between the electronic ground and excited states.

For excited states dominated by single excitations, ADC(2) and CC2 typically give quite similar results with an accuracy in the excitation energy of 0.1–0.2 eV based on vertical transitions compared to experiments[464–466]. For example, TDDFT has a typical accuracy of 0.2–0.4 eV[349]. In fact, CC2 typically yields for single excitations results of similar—or even better—quality compared to the more expensive CCSD, which is known to additionally suffer from less accurate ground-state geometries due to bad error compensation[466,467]. Therefore, in such cases, CC2 and ADC(2) are very attractive methods for excitation energies due to their good accuracy and medium computational costs based on a scaling of

$\mathcal{O}(\mathcal{N}^5)$ (compare CCSD: $\mathcal{O}(\mathcal{N}^6)$). For comparison, further significant improvements in the accuracy of excitation energies are then usually only obtained when moving to triples CC methods, e.g., with CC3 ($\mathcal{O}(\mathcal{N}^7)$), which come at drastically increased computational costs[467,468]. In this context, the second-order methods ADC(2) and CC2 have also established as important methods for the optimization of excited-state geometries[463,469].

#### Inclusion of implicit solvents effects via COSMO

The availability of accurate electronic-structure methods for the ground states (e.g., MP2 and CC2) and excited states (e.g., ADC(2) and CC2) is one important factor for electronic excitation energies, but the inclusion of solvent effects is another one. The implicit solvent model COSMO was already introduced in Section 2.2.1, where it was also mentioned that COSMO can be easily incorporated into the SCF procedure for HF and DFT[363,364]. However, for the post-SCF methods MP2 and ADC(2) as well as for CC2, the combination with COSMO is more involved since these methods use the orbitals from a preceding HF calculation without further optimization. Due to the close relation between MPPT and CC theory[455], MP2 and ADC(2) are considered CC-like in the following, and hence the inclusion of COSMO with either of these three methods is similar. In general, COSMO can be conveniently introduced into the CC Lagrangian, which eventually also allows to derive (analytic) expressions for energy gradients that are needed for geometry optimizations[458].

As mentioned before, electronic excitation energies can be either determined using linear response (LR) theory or through state-specific (SS) considerations. While both approaches are equivalent for an isolated system (for exact wave functions), this is no longer the case for a quantum mechanical (QM) system in a polarizable embedding. Within the linear response formalism, COSMO represents a simple case of an embedded system, i.e., the QM part (the molecule) needs to be coupled to a polarizable environment (the reaction field)[470,471]. This introduces a non-linearity to the Schrödinger equation, which then needs to be solved iteratively. Three main different coupling schemes are known (e.g., see Ref. 472):

1. The Perturbation to the Energy (PTE)[473,474],
2. the Perturbation to the Energy and Density (PTED)[475,476],
3. and the post-SCF scheme (originally implemented for PERI-CC2 excitation energies)[477,478].

PTE restricts to the reaction field obtained from the ground-state HF density and thus the environment cannot respond to changes due to electronic excitations. Importantly, this lacking response causes missing contributions to the coupling between the excitation in the QM system and the reaction field if the QM system is not chosen large enough. PTED makes the post-HF density self-consistent with the reaction field, which is usually achieved by a macro-iteration over the HF and post-HF calculations, and is thus the most expensive scheme. Although PTED can be considered most accurate, its state-specific contributions to the excitation energies (by relying on a reference state), make it unsuitable for exploring potential energy surfaces if states are not well separated since it leads to physically wrong shapes of

the potential energy surfaces in regions with avoided crossings or conical intersections. Additionally, the implementation of excited-state gradients for PTED is not straightforward and hence prevents an application to excited-state geometry optimizations. Lastly, the post-SCF scheme is characterized by evaluating the post-HF contributions to the reaction field with an approximate post-HF contribution to the density. Owing to this, the computational costs are comparable to that of the corresponding gas-phase calculation and the costly macro-iteration (as for PTED) is no longer needed.

Note that the choice for an SS, LR, or mixed approach (*vide supra*) enters through the coupling scheme that is used in the SCRF procedure. By construction, these differ in the individual contributions to the excitation energy. The LR contribution (from PTED) couples the transition moment to the polarization of the environment (referred to as *excitonic coupling*)[476], which matters if the transition density is large, i.e., typically if the oscillator strength of a transition is large. In contrast, SS accounts for all polarization effects exclusively through changes in the electron density itself. The transition density as such does not exist in SS, e.g., as expected for charge transfer excitations that typically have low oscillator strengths (i.e., small transition moments) and hence when excitonic coupling is less important. The post-SCF coupling scheme has been developed for LR, i.e., the excitonic coupling *via* the transition density is included, but SS contributions are missing[477,478]. It is possible to add SS corrections to post-SCF *via* corrected linear response (cLR) though[472,479].

Another important aspect of the post-SCF scheme is that it allows for a convenient derivation of expressions for energy gradients for both the ground and excited state[478,480], providing a promising path for COSMO-ADC(2) and COSMO-CC2 in excited-state geometry optimizations. The post-SCF coupling scheme is the one that is used here for the COSMO-MP2 and COSMO-CC2 calculations for the ground state and the COSMO-ADC(2) and COSMO-CC2 calculations for the excited state[478]. Currently, the excited-state geometries are limited to COSMO-ADC(2) though, as the corresponding COSMO-CC2 energy gradients for excited states are not yet implemented in TURBOMOLE[417].

# 3. ESPT in Acetone–Water Mixtures

The first sub-project combines steady-state UV/Vis absorption and fluorescence emission spectroscopy with streak-camera time-resolved fluorescence spectroscopy to examine the ESPT of the particularly strong photoacid **B** in acetone–water solvent mixtures. The elucidation of the precise reaction mechanism involving the identification of the intermediates and the determination of rate constants are at the center here. In the context of water as a possible contamination in acetone, this also poses the problem how to control or counteract efficiently its effect in these environments.

This part has been carried out under the supervision of Prof. Dr. Patrick Nürnberger and constitutes a continuation of my previous research within the scope of my Master thesis in his group[481]. Preliminary measurements had already been done at that time, but all data has been fully re-analyzed and the discussion was thoroughly revised since then. I am responsible for doing all measurements and the data analysis, as well as for writing the original draft of the manuscript which was further developed together with the co-authors. The correspondence with the editor and the reviewers has been collaboratively taken over by Patrick Nürnberger and me.

The following open-access publication is reprinted under the terms of CC BY-NC-ND 4.0 and with permission from: N. Sülzner, B. Geissler, A. Grandjean, G. Jung, and P. Nuernberger. Excited-State Proton Transfer Dynamics of a Super-Photoacid in Acetone-Water Mixtures. *ChemPhotoChem* **2022**, *6*, e202200041. **Copyright © 2022 The Authors. ChemPhotoChem published by Wiley-VCH GmbH.** The corresponding supporting information can be found in Section B.1. This publication is also available online: `https://doi.org/10.1002/cptc.202200041`.

ChemPhotoChem

Research Articles
doi.org/10.1002/cptc.202200041

Chemistry Europe
European Chemical Societies Publishing

www.chemphotochem.org

# Excited-State Proton Transfer Dynamics of a Super-Photoacid in Acetone-Water Mixtures

Niklas Sülzner,[a] Bastian Geissler,[b] Alexander Grandjean,[c] Gregor Jung,[c] and Patrick Nuernberger*[b]

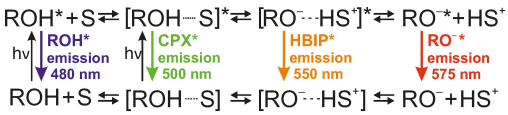
Super-photoacids, that is, photoacids with a negative p$K_a$ value in the electronically excited state, can trigger an excited-state proton transfer (ESPT) to the solvent. For the neutral pyranine-derived super-photoacid studied here, even indications for ESPT in acetoneous solution are reported. The characteristics of ESPT in this environment, that is, which intermediates exist and what the impact of cosolvents is, remain unsettled though. In this work, we study ESPT in acetone-water mixtures by steady-state and time-resolved fluorescence spectroscopy. Various effects are observed: First, the addition of water supports the formation of a hydrogen-bonded ground-state complex comprising one water molecule and the photoacid, whose excitation triggers the formation of a hydrogen-bonded ion pair on a sub-ns time scale. Second, water has an overall accelerating effect on the fluorescence dynamics of the involved emitting species, whose contributions are disentangled in a global analysis scheme, enabling the identification of emission from the free photoacid, a photoacid-water complex, a hydrogen-bonded ion pair, and the deprotonated photoacid. At least two water molecules are necessary for ESPT in the environment. Third, additional acidification thwarts an efficient ground-state complex formation of the photoacid and water. However, upon excitation, complexation may occur on a timescale faster than the photoacid's excited-state lifetime, so that emission from a nascent complex emerges.

## Introduction

Photoacids are molecules that exhibit an acidity increase upon irradiation, i.e., they are more acidic in an electronically excited state compared to the ground state.[1] This behavior is typical for aromatic alcohols such as phenols,[2–6] naphthols,[7,8] or hydroxyquinolines.[9] The prominent example, 8-hydroxypyrene-1,3,6-trisulfonate (pyranine, HPTS), is probably the most intensively studied photoacid of all.[10–17] Triggered by photoexcitation, a photoacid can transfer its acidic proton more easily to suitable acceptors such as solvent or base, which makes an instance of an excited-state proton transfer (ESPT).[18] Owing to the implementation of pulsed lasers, ultrafast time-resolved spectroscopy made it possible to monitor the ESPT process on its actual timescale.[19,20] Moreover, the study of photoacids in different molecular environments allows for elucidating mechanistic information on the ESPT process including the rate constants of the involved elementary reactions.[21,22] However, only exceptionally strong photoacids with a negative p$K_a$ value in the excited state, referred to as super-photoacids,[23,24] are capable of performing ESPT in non-aqueous[25,26] or aprotic solvents.[27]

The Förster cycle represents the simplest thermodynamic description of photoacidity, only taking into account the excited-state and ground-state species of the protonated and deprotonated photoacid.[28–30] More generally, the processes are described in a multi-step Eigen-Weller model[31,32] (see Scheme 1) which includes that, besides the emission from the isolated photoacid ROH* and the corresponding base $RO^-$*, further species can appear, namely a reaction complex (CPX) with a (co)solvent molecule S and a hydrogen-bonded ion pair (HBIP). Depending on the solvent's ability of separating ions, additional intermediates for the separation such as solvent-separated ion pairs (SSIPs) may also occur.

A few years ago, the Jung group introduced a promising, new class of pyranine-based photoacids that are substituted with strongly electron-withdrawing sulfonic ester groups.[33]




**Scheme 1.** Eigen-Weller model for the ESPT processes of the photoacid studied in this work. The wavelengths indicate the spectral position of the fluorescence of the excited-state species.

[a] N. Sülzner
Lehrstuhl für Theoretische Chemie
Ruhr-Universität Bochum, 44780 Bochum (Germany)
[b] Dr. B. Geissler, Prof. Dr. P. Nuernberger
Institut für Physikalische und Theoretische Chemie
Universität Regensburg, 93040 Regensburg (Germany)
E-mail: patrick.nuernberger@ur.de
[c] A. Grandjean, Prof. Dr. G. Jung
Biophysikalische Chemie, Universität des Saarlandes
66123 Saarbrücken (Germany)

Supporting information for this article is available on the WWW under https://doi.org/10.1002/cptc.202200041

© 2022 The Authors. ChemPhotoChem published by Wiley-VCH GmbH. This is an open access article under the terms of the Creative Commons Attribution Non-Commercial NoDerivs License, which permits use and distribution in any medium, provided the original work is properly cited, the use is non-commercial and no modifications or adaptations are made.



© 2022 The Authors. ChemPhotoChem published by Wiley-VCH GmbH

ChemPhotoChem | Research Articles
doi.org/10.1002/cptc.202200041
Chemistry Europe
European Chemical Societies Publishing

These substituents do not only drastically enhance the photoacidity but they also provide an effective way towards non-charged super-photoacids. All photoacids of this class are characterized by large fluorescence quantum yields, high photostability, and high solubility in organic solvents. One of these photoacids, tris(1,1,1,3,3,3-hexafluoropropan-2-yl)-8-hydroxypyrene-1,3,6-trisulfonate (Scheme 2), is particularly strong with the $pK_a$ dropping by more than eight orders of magnitude from 4.4 to −3.9.

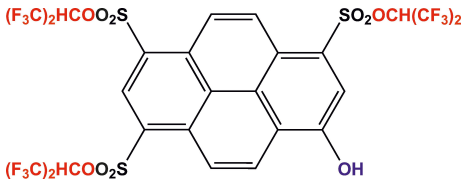
The solvatochromic effect of various solvents as well as the kinetic behavior in water, methanol, ethanol, and DMSO has been reported.[34,35] Recently, the dynamics and intermediate species in a strongly hydrogen-bonded complex with a trialkylphosphine oxide was elucidated.[36,37] Whereas most photoacids cannot transfer their proton to DMSO, the above-mentioned photoacid shows indications to do so even in the aprotic, weakly basic solvent acetone.[34] However, for such a rather poor proton acceptor as acetone, traces of protic solvent admixtures like water can interfere in the ESPT process as a competing proton acceptor.

In this work, we present a systematic study on the effect of water on the excited-state proton transfer of this photoacid in acetone-water mixtures. Steady-state and time-resolved fluorescence spectroscopy on the picosecond to nanosecond timescale are used to unravel the excited-state dynamics. We show that four emitting species have to be considered to explain the emission dynamics, which are sensitive to the amounts of water admixtures and additional acid. Systematic variations of the solvent composition allow disentangling the individual contributions of the involved species.

## Results and Discussion

### The effect of water on the ground-state equilibrium

To investigate the possibility of water causing deprotonation of the photoacid already in the ground state, we studied the effect of water on the ground-state proton-transfer equilibrium prior to the time-resolved measurements. The steady-state absorption spectra shown in Figure 1(a) refer to samples with increasing amounts of water. A neutral solution of the photoacid typically exhibits two absorption features in accordance with previous findings: one maximum around 445 nm ascribed to the protonated form (ROH), and another one at 575 nm being characteristic for the deprotonated form ($RO^-$).




**Scheme 2.** Molecular structure of the investigated photoacid with highlighted sulfonic ester moieties (red) and hydroxyl group (blue).

Two observations can be made as the concentration of water, $[H_2O]$, increases:

First, spectral shifts occur with changing solvent composition. The ROH peak reveals a redshift while the $RO^-$ peak undergoes a blueshift. Since in the acetone-water mixtures the polarity changes, this might be related to solvatochromism. The more water is present, the higher the polarity of the acetone-water solvent mixture[38] and hence the better stabilized are the more polar states. Depending on the relative polarity of the electronic ground and excited state, this can either increase or decrease the $S_0 - S_1$ energy gap, leading to bathochromic or hypsochromic shifts, respectively. Despite the existence of several polarity scales, even for solvent mixtures,[39] application of the Kamlet-Taft parameters appears especially appropriate to assign spectral shifts to specific solvent-solute interactions.[13,34] Our observations for the acetone-water mixtures are in accordance with the previous results on solvatochromic effects for ROH and $RO^-$ in polar solvents.[34]

Second, the ROH peak intensity slightly increases under $H_2O$ addition and, vice versa, the $RO^-$ peak intensity decreases. Since water-induced deprotonation would cause more $RO^-$, the $RO^-$ peak intensity decrease corroborates that ground-state deprotonation is negligible. Rather, the decrease can be rationalized by the formation of a photoacid-water complex in the ground state with slightly different spectroscopic properties (*vide infra*). Water-induced deprotonation starts to markedly affect the ground-state equilibrium only at water concentrations beyond 2 M (see Figure S1(a) in the Supporting Information).

Despite this rather high value before ground-state deprotonation sets in, we designed a new sample series using an initial amount of 6.5 mM of trifluoroacetic acid (TFA) to shift the ground-state protonation equilibrium to the protonated side. The steady-state absorption spectra in Figure 1(b) provide evidence that 6.5 mM of TFA is sufficient to shift the equilibrium completely to the protonated side due to the vanishing $RO^-$ absorption band at 575 nm. Moreover, the equilibrium seems unaffected by water under acidic conditions as the $RO^-$ signal does not reoccur with increasing $[H_2O]$ up to 1.09 M. The ROH absorption band reveals the same redshift as described before in combination with a weak decrease in absorbance. While there was only one reasonably defined isosbestic point for the spectra in neutral acetone (Figure 1(a)), there is an additional, yet still subtle one near 450 nm, i.e., in the ROH regime for acidic acetone. We note that solvatochromic shifts might be slightly different in the acidic environment compared to the neutral one, which could contribute to the observation of such an isosbestic feature. However, since also this one is substantially different from an isosbestic point corresponding to deprotonation (Figure S2), we assign the peak intensity changes of ROH also to the formation of a ground-state complex, in analogy to $RO^-$.


© 2022 The Authors. ChemPhotoChem published by Wiley-VCH GmbH

ChemPhotoChem
Research Articles
doi.org/10.1002/cptc.202200041
Chemistry Europe
European Chemical Societies Publishing

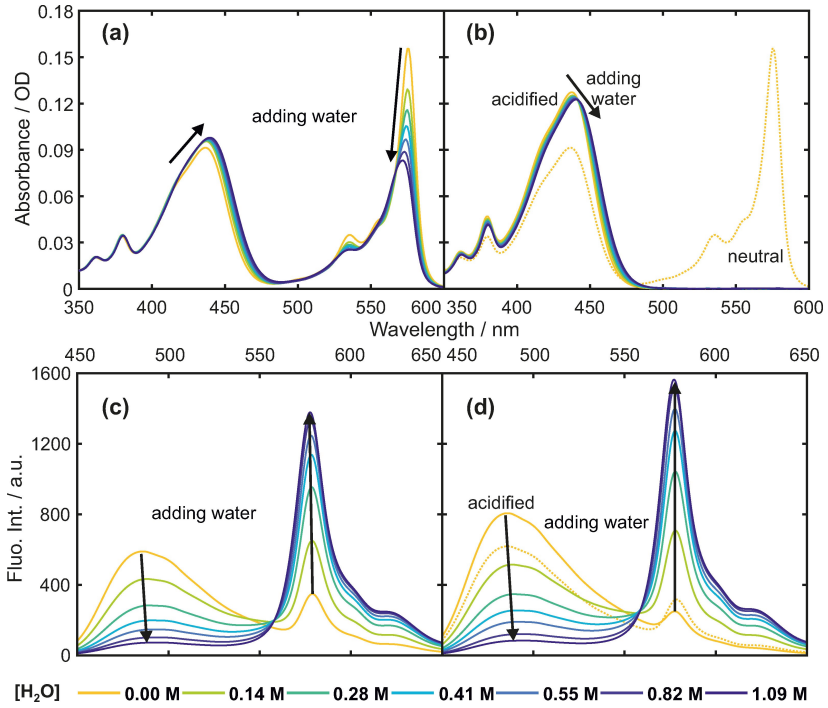



**Figure 1.** Steady-state characterization *via* UV/Vis absorption (top) and fluorescence emission (bottom) spectroscopy of samples with increasing concentration of water in neutral (left) and acidic (right) acetone solution. Fluorescence spectra (c, d) relate to 400 nm excitation. All samples refer to 20 μM photoacid while acidic solutions additionally contain 6.5 mM of TFA [with absorption spectra (a, b) being compensated accordingly to exclude dilution effects]. Concentrations of water are color-coded according to the legend. Arrows indicate the peak progressions upon the addition of water. The dotted lines in (b, d) refer to those neutral solutions in neat acetone without any additional water or acid from (a, c) as a reference.

### Ground-state complex formation

Adduct formation between hydroxyaromatic compounds and hydrogen-bond acceptors, including common solvent molecules, is widely known for both the excited state and the ground state.[40–43] With respect to ESPT in aprotic solvents, such hydrogen-bonded complexes (CPXs) between photoacids and additional bases have shown to affect the ESPT dynamics crucially because of the beneficial pre-coordination of the proton-accepting base. In fact, the CPX can represent the actual proton-transferring species of the photo-protolytic reaction cascade in aprotic environments, comprising two to three steps, as demonstrated for similarly strong photoacids in nitrile solution.[36,37,44,45] Transferred to our system and in view of the spectral changes discussed above, this implies that a photoacid-water complex ROH $\cdots$ $(H_2O)_n$ could be formed in acetone as well if water is present. We suppose that such a complex provides a path for modified ESPT dynamics compared to the free photoacid. Based on the observed changes in the absorption spectra (Figure 1) as a function of the water concentration, we determined *n*, the number of involved water molecules, *via* Benesi-Hildebrand analysis[46] represented by Eq. (1) (derivation given in the Supporting Information). According to

$$[H_2O]^{-n} = Kd\Delta\varepsilon[ROH]_0(\Delta A)^{-1} - K, \quad (1)$$

plotting $[H_2O]^{-n}$ against $(\Delta A)^{-1}$, where $\Delta A = A([H_2O]) - A(0)$ is the absorbance change at a given wavelength, should give a straight line. The intercept determines the association constant *K* of the complex, while the slope allows computing the difference attenuation coefficient $\Delta\varepsilon$ as a function of *K*, path length *d*, and initial ROH concentration $[ROH]_0$. The exponent *n* is obtained by finding the best linear behavior. Figure 2 illustrates the Benesi-Hildebrand plots referring to absorbance changes at 450 nm, characteristic of ROH, under neutral and acidic conditions, as well as for the changes of $RO^-$ at 580 nm. As can be seen, excellent agreement with the experimental data was found for $n = 1$. Based on that, we assume that neutral and acidic acetone solutions both contain the photoacid-water complex ROH $\cdots$ $OH_2$ if water is present. In neutral solution (Figure 2(a)), the value of $(2.15 \pm 0.06)\ M^{-1}$ for *K* suggests that already 23% of the photoacid is complexed after the first addition of water (0.14 M), while this fraction rises to 70% for 1.09 M of water. In contrast to this, the association


© 2022 The Authors. ChemPhotoChem published by Wiley-VCH GmbH

ChemPhotoChem | Research Articles
doi.org/10.1002/cptc.202200041
Chemistry Europe
European Chemical Societies Publishing

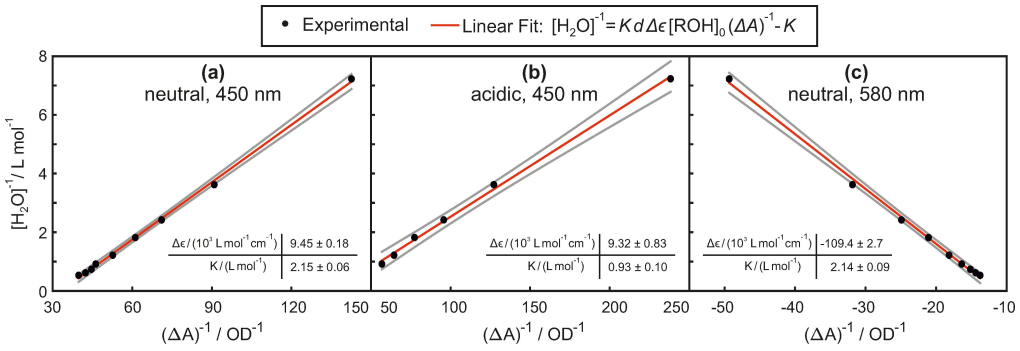



**Figure 2.** Benesi-Hildebrand plots ($[H_2O]^{-n}$ vs. $\Delta A^{-1}$) based on the dilution-corrected absorption spectra for the neutral (a) and acidic (b) water series (cf. Figure 1) monitored at 450 nm, and monitored at 580 nm (c) for the neutral water series. Best linear fits were obtained for $n = 1$ (shown in red), with the 99% confidence intervals shown by gray lines. The fit results (slope and intercept) are included in the tables as insets.

constant is much smaller in acidic solution [$(0.93 \pm 0.10)$ M$^{-1}$] predicting lower complex fractions of 12% to 47% for water concentrations of 0.14 M to 1.09 M, respectively. Despite differing $K$ values, the complexes can be considered equal because $\Delta\varepsilon$ was found to be about 9400 L mol$^{-1}$ cm$^{-1}$ (for $d = 0.2$ cm) under neutral ($[ROH]_0 = 16\ \mu$M) as well as acidic ($[ROH]_0 = 20\ \mu$M) conditions. Presumably, the complex ROH $\cdots$ OH$_2$ is less stable in an acidic environment because of complex cleavage upon acidification. Since it is reported that water forms clusters in acetone[47,48] and that the structure of water clusters changes upon protonation,[49] we conjecture that water molecules prefer to be in the vicinity of a TFA molecule, which is a stronger acid than the ground-state photoacid.

For the absorption changes of RO$^-$, the best fit was also found for $n = 1$ (Figure 2(c)), with an association constant that is similar to the one for ROH in neutral solution. However, the magnitude of $\Delta\varepsilon$ is much larger ($-109.4 \times 10^3$ L mol$^{-1}$ cm$^{-1}$) which directly reflects the higher attenuation coefficient of RO$^-$ compared to the one of ROH. In view of this, the aforementioned spectral shifts in Figure 1a and 1b comprise contributions from both solvatochromism and CPX formation.

### The impact of water on the steady-state fluorescence spectra

Figure 1c and 1d depict the steady-state fluorescence emission spectra upon 400 nm excitation of the neutral (c) and acidic (d) sample series. Each spectrum consists of two characteristic emission signals with maxima around 480 nm and 575 nm, originating from the excited protonated species (ROH*) and the excited deprotonated species (RO$^-$*), respectively. A direct comparison of 1c and 1d reveals no distinct differences between neutral and acidic conditions. Overall, the ROH* emission intensity is generally slightly higher in acidic solution at all values of $[H_2O]$ due to a higher concentration of initially excited ROH* by starting from a fully protonated system, as verified by the absorption spectra. For both sample series, the ROH* emission signal strongly diminishes with increasing $[H_2O]$, whereas the RO$^-$* signal rises. Only at concentrations larger than 2 M, the progression reverses and RO$^-$* intensity slightly decreases again (see Figure S1b). Moreover, the fluorescence spectra reveal an isoemissive point near 560 nm at both conditions, except for the spectra at 0 M water which behave differently.

We do not expect RO$^-$* emission after direct excitation of RO$^-$ with 400 nm due to the small absorption cross section[33] and the low concentrations of RO$^-$ under acidic conditions. Even though the weak RO$^-$* signal could be still due to some initially excited RO$^-$, the observed water-dependence suggests that RO$^-$* must be additionally produced by some other photochemical process. Taking both progressions of ROH* and RO$^-$* together, an excited-state proton transfer (ESPT) can be confirmed. Triggered by electronic excitation, ROH* becomes more acidic than ROH and can thus transfer the acidic proton more easily, generating RO$^-$*.

A closer look at the ROH* region also reveals that this emission signal is accompanied by a shoulder around 500 nm, causing a spectral broadening as a function of $[H_2O]$. Referring back to the complex formation in the ground state (*vide supra*), we assign this 500 nm feature to the excited photoacid-water complex CPX*. As $[H_2O]$ increases, the solution contains increasing initial concentrations of CPX* that start to dominate the ROH* emission region. Considering hydrogen bonding as the likely bonding interaction in the complex, such a redshift of the fluorescence emission of the excited complex CPX* relative to free ROH* is also anticipated and experimentally observed for other systems. However, no isoemissive point between 480 nm (ROH*) and 500 nm (CPX*) is present, which fits to the changing initial ROH* and CPX* populations as a function of $[H_2O]$. By contrast, the observed isoemissive point near 560 nm refers to a subsequent reaction step with an additional proton-transfer intermediate in the excited state, which we assign to a hydrogen-bonded ion pair (HBIP). Such hydrogen-bonded species typically lie spectrally in between the excited protonated and deprotonated forms.[50–52] To elucidate this, time-resolved fluorescence measurements were performed.


© 2022 The Authors. ChemPhotoChem published by Wiley-VCH GmbH

ChemPhotoChem
Research Articles
doi.org/10.1002/cptc.202200041
Chemistry Europe
European Chemical Societies Publishing

### The effect of water on the fluorescence dynamics

Time-resolved fluorescence maps were recorded for the samples of Figure 1, i.e., for 14 values of $[H_2O]$ under neutral and 7 values under acidic conditions, four of which are illustrated in Figure 3 (see SI for further fluorescence maps, Figure S4). The maps in Figure 3 exhibit two major spectral features in accordance with the steady-state spectra. The first is an emission signal centered at 480 nm that occurs directly after excitation at $t = 0$ ns ("time zero") and decays with a lifetime of about 4 ns at 0 M of $H_2O$. Concomitantly, another emission signal around 575 nm rises within about the same time constant (~ 4 ns) and decays with a longer lifetime (~ 6 ns). Both emission signals hence are kinetically correlated. When comparing the fluorescence maps for samples with increasing $[H_2O]$, it becomes apparent that water drastically alters the fluorescence kinetics. This can be followed by considering the kinetic traces taken at 480 nm and 575 nm, near the maximum positions, as shown in Figures 3(e) and 3(f). Thereby, the use of a logarithmic intensity scale allows testing for non-exponential decays since purely mono-exponential decays appear as straight lines in this representation.

On the one hand, the 480 nm signal referring to ROH* emission yields a straight line for the water-free sample, corresponding to a monoexponential decay. Having water initially added, the ROH* emission starts deviating from a monoexponential decay, which is reflected in a line curvature of the plots as indicated by the curved arrow in Figure 3(e). This effect becomes the more severe the more water is present. Evidently, a faster decay of ROH* that causes the more negative slope in the early time regime seems to superpose a slower decay represented by the less negative slope in the late time regime. Thus, the traces at 480 nm indicate a fluorescence decay becoming faster the more water is present.

On the other hand, the rise component of the 575 nm traces becomes steeper (in accordance with the corresponding shortened 480 nm decay), while the decay component remains almost unaffected, as demonstrated by the parallel lines in the late time regime of Figure 3(f). The combination of both eventually causes the intensity maximum at 575 nm to shift towards time zero, as indicated by the arrow.

The change caused by the first addition of water (0 M→ 0.14 M) behaves differently, as the 575 nm signal, referring to $RO^{-}$* emission, is very weak in water-free solution and hence constitutes a superposition of the actual $RO^{-}$* emission and the red tail of the ROH* decay, which is maximal at 480 nm but not zero at 575 nm. The possibility of two further processes in the water-free sample, namely the ESPT to acetone and the interference with a trifluoroacetate anion, will be discussed below.

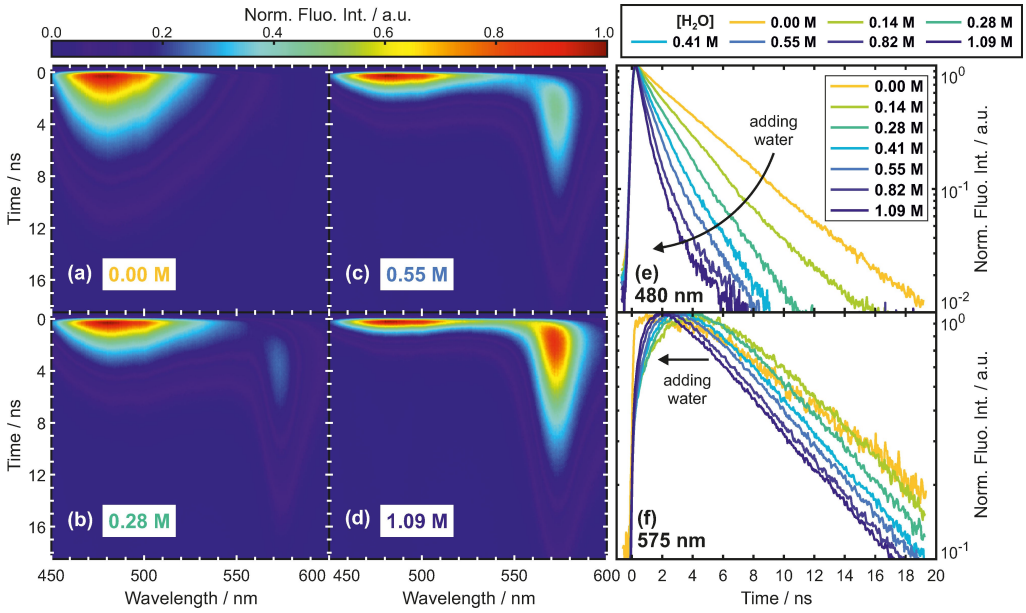



**Figure 3.** Normalized time-resolved fluorescence maps using 405 nm excitation for samples with increasing concentration of water (exemplarily (a) 0.00 M, (b) 0.28 M, (c) 0.55 M, (d) 1.09 M) in acidic solution (6.5 mM TFA) relating to Figure 1(d). All kinetic traces at 480 nm and 575 nm, taken from the maps, are compared on a logarithmic intensity scale in (e) and (f), respectively. Line colors refer to the concentrations as included in (e). Arrows indicate the progression when adding water.


© 2022 The Authors. ChemPhotoChem published by Wiley-VCH GmbH

ChemPhotoChem | Research Articles
doi.org/10.1002/cptc.202200041
Chemistry Europe
European Chemical Societies Publishing

### The kinetic model for global analysis

All time-resolved fluorescence data was further analyzed in the context of the Eigen-Weller model of Scheme 1. A complete, numerical modeling[53–55] with (diffusion-controlled) backreactions and equilibrations is very laborious and non-essential when the dynamic recombination is negligible, as indicated by the monoexponential decays in Figure 3(f).

In contrast to the trianion HPTS, the photoacid studied here is uncharged, so that diffusion contributions seem less relevant due to the weaker Coulomb attraction between the ions after ESPT. Moreover, Spies *et al.* demonstrated that the ESPT rates of this photoacid in $H_2O$, MeOH, and EtOH obtained from the exact, numerical solution to the Debye-Smoluchowski equation (DSE) are virtually identical to those determined by multi-exponential fitting.[35] Besides, further studies on ESPT of similarly strong photoacids in other polar-aprotic solvents also presented kinetic analyses being in accordance with the experimental results, without explicitly solving the DSE.[44,56–58]

Therefore, we apply a global analysis scheme[59–62] with three parallel exponential decays in order to disentangle the emission processes. Details on the model are given in the SI.

### Impact of water admixtures on the fluorescence dynamics

The results from the triexponential global analysis scheme for the water series in acidic solution are shown in Figure 4 (see corresponding residual maps in Figure S4 for assessing the fit quality), those in neutral solution are included in Figure S3 of the Supporting Information. Panels 4(a) to 4(c) display the decay-associated spectra (DAS), while the three rate constants are shown in Figure 4(d) as a function of the concentration of the water admixtures.

Similar to the steady-state fluorescence, the results for 0 M water differ from those with added water. We will thus first discuss those results after the first addition of water. At 0.14 M $H_2O$, the amplitude $A_1$ (Figure 4(a)) for the fastest component shows a large positive (decaying) contribution close to 475 nm, a negative (rising) contribution near 550 nm, and a small positive contribution at 575 nm. As $[H_2O]$ increases, the 475 nm feature shifts to the red (reaching 480 nm) and gains in intensity while becoming significantly broader. At the final water concentration of 1.09 M, a shoulder near 500 nm becomes clearly visible. Meanwhile, the 550 nm contribution is also red-shifted, but its amplitude passes through a minimum of −0.5 and then slightly increases again with increasing water concentration. In parallel to this, the 575 nm feature loses in intensity. For an interpretation of the different contributions, we confer Scheme 1 and the different species therein. For illustrative purposes, as insets in Figure 4, the composition of the individual DAS is mimicked by spectral components representing these species. The component peaking at 480 nm is connected to the free (i.e., uncomplexed) photoacid, while the one at 500 nm refers to the excited photoacid-water complex CPX*. The negative signal at 550 nm corresponds to the rise of the proton-transfer intermediate HBIP*. The putative

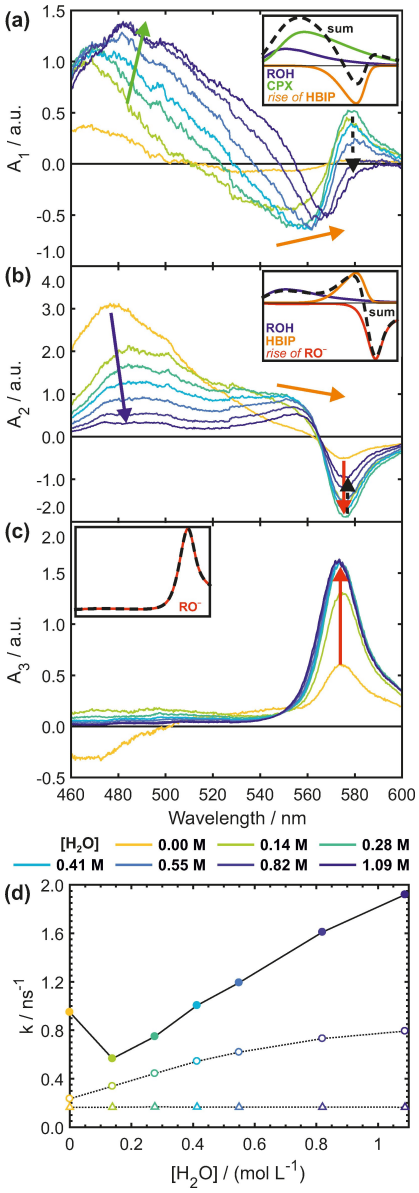



**Figure 4.** Results from a global analysis with three temporal components to the fluorescence intensity decay of the acidic sample series (Figure 3). Decay-associated spectra (DAS) relating to amplitudes $A_1$ (a), $A_2$ (b), and $A_3$ (c) are shown, together with a plot of the kinetic constants $k_1$ (filled circles), $k_2$ (open circles), and $k_3$ (open triangles), as a function of the concentration of water (d). The DAS comprise contributions from the four species ROH*, CPX*, HBIP*, and $RO^{-*}$ (Scheme 1). The insets of panels (a) to (c) provide a sketch to visualize the different contributions, which result in the overall DAS as indicated by the dashed black line. Note that the individual emission spectra change in shape and shift with an increase of the water concentration. This is indicated by the arrows whose colors correspond to the contribution given in the insets.


© 2022 The Authors. ChemPhotoChem published by Wiley-VCH GmbH

ChemPhotoChem
Research Articles
doi.org/10.1002/cptc.202200041
Chemistry Europe
European Chemical Societies Publishing

peak at 575 nm does not actually represent a decay contribution in the spectral region of the excited base, but is the result of a superposition of the ROH* (with decreasing contribution according to the steady-state complexation, see Figure 1), CPX*, and HBIP* (both with increasing contribution) spectra as indicated in the inset.

The corresponding rate $k_1$ (filled circles) shows an almost linear increase over the range from 0.14 M to 1.09 M with a slope of $\sim 1.5 \times 10^9$ $M^{-1}$ $s^{-1}$, as suggestive for bimolecular reaction kinetics. However, since $A_1$ has contributions from both the ROH* and the CPX* decay in varying amounts, a direct assignment of the increase of $k_1$ to an acceleration of a distinct reaction step is intricate because of such kinetic mixing. Along these lines, the observed progression for $k_1$ basically reflects that HBIP* formation via CPX* is faster at higher water concentrations, and at least the magnitude of the apparent bimolecular rate constant strongly supports a diffusion-controlled reaction mechanism, which is the involvement of a further water molecule. Furthermore, no unambiguous indication for excited-state formation of $RO^-$* is found along with this fastest process in acidified solution, in contrast to neutral solution (see Figure S3). The participation of a further water molecule may be rationalized by the necessity of stabilizing a hydronium cation in acetone, which is facilitated if it is part of a hydrogen-bonded water cluster.

The second kinetic component $A_2$ (Figure 4(b)) is closely related to $A_1$. Now, a strong positive contribution is observed, covering a broad range from 460 nm to 560 nm, that also shifts to the red during addition of water, but loses intensity in the spectral range of CPX*. Concomitantly, the amplitude peaks more and more around 560 nm, therefore adopting increasingly more CPX* and HBIP* decay character, in agreement with the complexation behavior. Furthermore, a negative contribution near 575 nm indicates that this component is coupled to the rise of $RO^-$*. Note that the overall spectra increase at 575 nm when water is added (black-dashed arrow in Figure 4(b)), but this is due to a superposition of the bathochromically shifting contribution of HBIP* (orange arrow in Figure 4(b)) and the increasingly negative feature of the $RO^-$* (red arrow). Therefore, we conclude that $A_2$ represents the time scale at which HBIP* turns into $RO^-$*, but also includes some contribution of emission from free ROH* on the short-wavelength side. A sketch of how the different species contribute is given in the inset of Figure 4(b).

The corresponding rate $k_2$ (open circles) increases with addition of water, initially in a linear fashion. This can be rationalized by the above-mentioned existence of water clusters in acetone, because for a HBIP to separate, the hydronium ion has to be stabilized, presumably via hydration in a water cluster, related to the long-standing debate of Zundel and Eigen complexes.[63] Therefore, adding water facilitates the formation of $RO^-$* from HBIP*, but if there are enough water complexes present, the effect should cease to increase, giving rise to a maximum value of $k_2$. Anyway, the observation that $k_2$ increases with a reaction order of $[H_2O]$ less than 1 suggests that higher oligomers ($n > 2$) are not mandatory for ESPT.

The amplitude $A_3$ of the slowest kinetic contribution only consists of a strong positive signal at 575 nm that is basically independent of the concentration of water. The corresponding rate constant $k_3$ (open triangles) does not change at all with water concentration. This can be understood given the assignment to the decay of $RO^-$*, a species which is not in contact with water cosolvent molecules and thus, may decay without a pronounced sensitivity on water concentration.

#### The instance of no water admixtures

The case of 0 M water behaves quite differently from the others. In the DASs, amplitude $A_1$ only has a comparably small 475 nm feature, but a rather broad negative contribution around 540 nm instead. The most pronounced DAS can be found for $A_2$, which consists of a positive signal originating from ROH* and a negative signal representing the rise of $RO^-$*. We note that the characteristic feature at 550 nm observed with water admixtures and attributed to HBIP* is not present without water (see yellow curve in Figure 4(b)). Despite no additional water, we observe the $RO^-$* signal at 575 nm in $A_3$. These three observations, (i) mainly ROH* in $A_1$, (ii) no pronounced HBIP* in $A_2$, and (iii) nonetheless $RO^-$* emission in $A_3$, lead us to infer that an ESPT is also possible without water admixtures. Whereas the presence of water traces cannot be fully excluded and hence a signal contribution nonetheless involving water is conceivable, the remarkably different DASs imply that a distinct further mechanism is operative. Due to the high photoacidity of ROH*, it is conceivable that acetone actually acts as proton acceptor, as previously argued by Finkler *et al.*[33] We note that the rate $k_2$ takes the value of 0.235 $ns^{-1}$, which is very close to the value of 0.234 $ns^{-1}$ for the decay of the excited methoxy analogue ROMe* which cannot transfer any proton (see Figure S5, ESI). Thus, if ESPT to acetone occurs, it has a much lower rate.

In addition, the slightly negative signal in $A_1$ together with the remaining positive signal in $A_3$, both around 540 nm, further indicate that some of the ROH* molecules might form a complex which is not capable of ESPT and thus emits in this wavelength range. This behavior might originate in part from the involvement of trifluoroacetate anions, but also the occurrence of ESPT to acetone in the absence of water may play a role. Finally, the negative part of $A_3$ is not due to a real signal, but is probably a fit artefact that emanates from the similarity of $k_2$ and $k_3$.

#### The impact of acid on the fluorescence spectra

As displayed in Figure 1, the addition of acid shifts the ground-state equilibrium towards ROH. Next, we aim to elicit whether there is a pronounced effect of acidification on the emission characteristics.

Starting with samples containing different amounts of water (for initial absorption spectra see Figure 1(b)), we added increasing amounts of TFA. Exemplarily, the steady-state


© 2022 The Authors. ChemPhotoChem published by Wiley-VCH GmbH

ChemPhotoChem | Research Articles
doi.org/10.1002/cptc.202200041
Chemistry Europe
European Chemical Societies Publishing

fluorescence spectra of three corresponding acidification series are illustrated in Figures 5(a-c). All spectra reveal the same progression with increasing [TFA] irrespective of the initial concentration of water, comprising a diminishing $RO^{-}$* emission (575 nm) coupled to an intensifying ROH* emission (480 nm). Depending on the initial concentration of water, TFA achieves within the employed concentration ranges no complete, but only a partial restoring of the ROH* emission intensity in water-free solution, as seen from the final spectrum of each series, i.e., those for highest [TFA]. It appears that the more water is present the more TFA is needed to restore the intensity referring to water-free solution.

Although a TFA excess suppresses the generation of $RO^{-}$*, the resulting spectra at high [TFA] do not fully resemble those in neutral or weakly acidic solution. Being most easily observable for the solution with highest [$H_2O$] in Figure 5(c), a new emission signal at 550 nm emerges (red asterisk), becoming only apparent in highly acidic solution, in which the $RO^{-}$* emission is close to vanishing. From comparison with Figure 4, the 550 nm signal is identified as emission from HBIP*. Thus, at high acid concentration, HBIP* emission prevails instead of $RO^{-}$*.

We assume that this originates from a preference of water to be located in the vicinity of the stronger acid. Since this is the TFA if there is no excited molecule, the amount of water being hydrogen-bonded to the photoacid is rather low. This has two implications. First, in case of an initial ground-state complex CPX, upon excitation CPX* can form HBIP*, but cannot further separate due to an insufficient number of water molecules to stabilize the separated ions. Second, in case of an initially isolated ROH, upon excitation ROH* may encounter water molecules by diffusion, leading to a delayed rise of HBIP* without further dissociation. To separate out the two contributions for HBIP* formation, time-resolved fluorescence maps for all acidification series have been recorded.

### The effect of acid on the fluorescence dynamics

Exemplarily, the corresponding kinetic traces at the emission maxima of ROH* at 480 nm and of $RO^{-}$* at 575 nm are displayed in Figures 5(d-f). As the concentration of water increases, a pronounced deviation from the mono-exponential decay found above for a water-free solution is found for ROH*, as is evident from the kink (black asterisk). Importantly, this kink disappears with increasing concentration of TFA, irrespective of the initial amount of water (as indicated by the curved black arrows). In contrast, the biphasic $RO^{-}$* signal is affected by TFA to a much lesser degree. Only the series for 0.14 M of water reveals a slight progression at 575 nm. For the others,

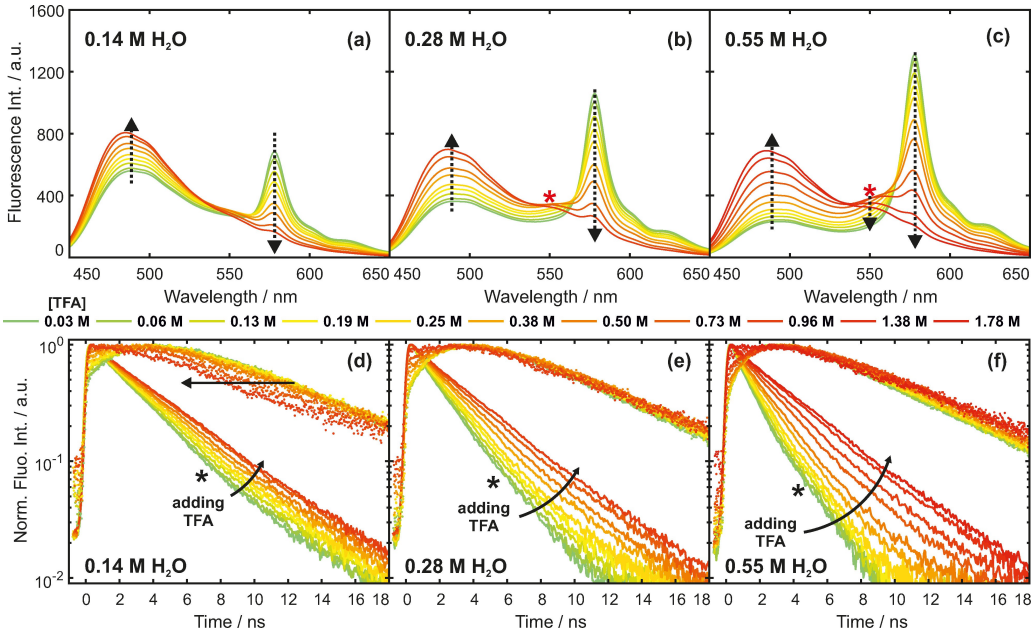



**Figure 5.** Emission from samples with increasing concentration of TFA after 400 nm **(a–c)** or 405 nm **(d–f)** excitation. Each column refers to a sample series with a specific concentration of water (0.14 M, 0.28 M, 0.55 M). Colors refer to the individual concentrations of TFA according to the legend. **Top row:** Steady-state fluorescence spectra. Black, dashed arrows indicate the peak progression with increasing TFA. Red asterisks highlight a new emission feature around 550 nm. **Bottom row**: Semi-logarithmic plots of selected kinetic traces at 480 nm (lower, solid lines) and 575 nm (upper, dotted lines) taken from the time-resolved maps of the samples with increasing concentration of TFA. Black asterisks indicate kinks in the profiles. Colors refer to the individual concentrations of TFA according to the legend. Solid arrows indicate the progression with increasing TFA.


© 2022 The Authors. ChemPhotoChem published by Wiley-VCH GmbH

ChemPhotoChem
Research Articles
doi.org/10.1002/cptc.202200041
Chemistry Europe
European Chemical Societies Publishing

merely the rise component vanishes, causing an overall shift of the maximum towards time zero, while the decay component remains mostly unaffected. These effects are mainly due to the spectral superposition of weak $RO^{-}$* emission (centered at 575 nm) to the red tail of the ROH* emission (extending to 575 nm).

In analogy to Figure 4, quantification of these effects on the fluorescence dynamics is accomplished by global analysis based on Eq. (S2) (SI), as displayed in Figure 6. The first row of

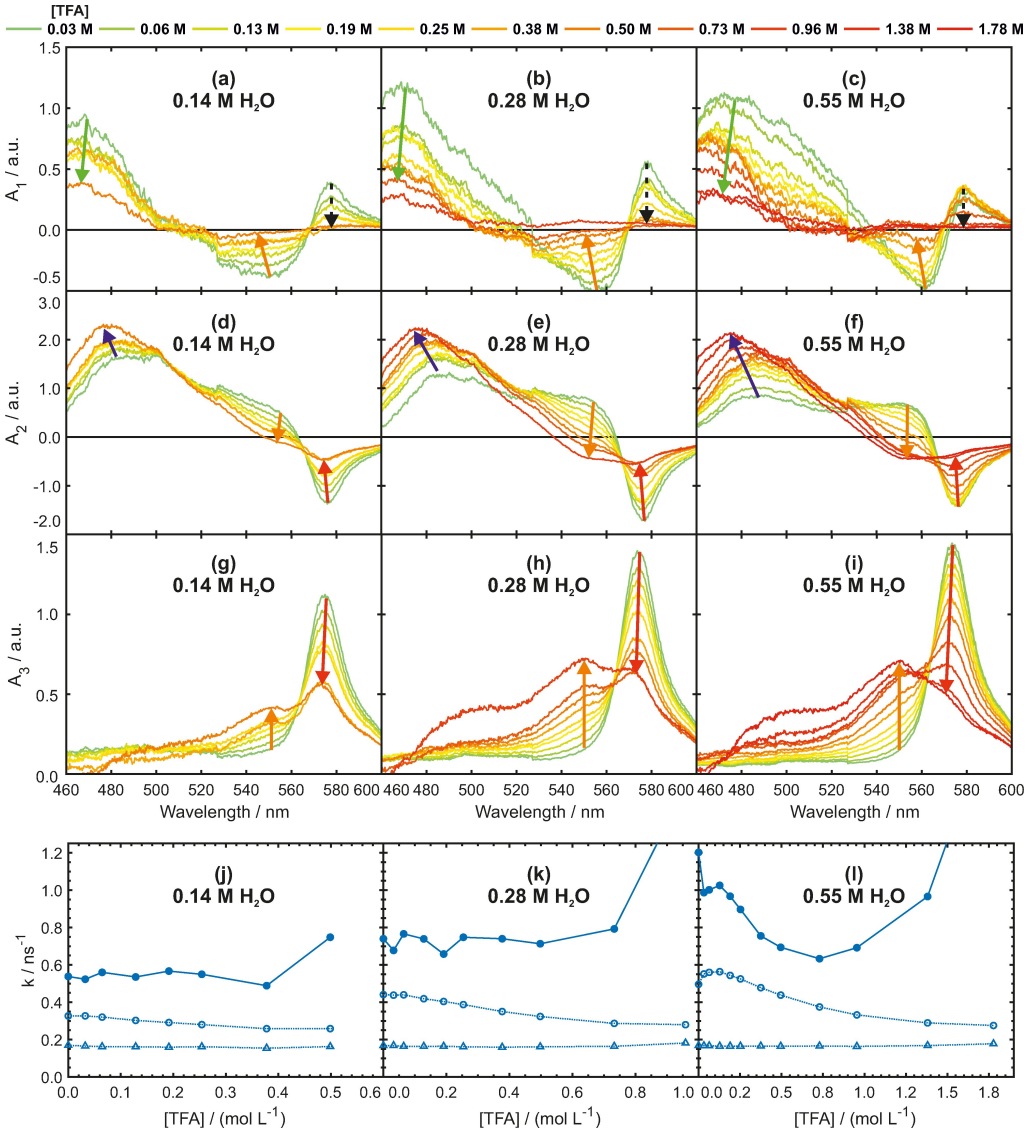



**Figure 6.** Results from a global analysis with three temporal components to the fluorescence intensity decay of the samples with increasing concentration of TFA (Figure 5). Each column refers to a sample series with a specific concentration of water (0.14 M, 0.28 M, 0.55 M). Colors refer to the individual concentrations of TFA according to the legend. Black, dashed arrows indicate the peak progression with increasing [TFA]. The peak progressions with increasing [TFA] are indicated by arrows whose colors refer to the contributing species, i.e., ROH* (blue), CPX* (green), HBIP* (orange), and $RO^{-}$* (red). **Upper three rows**: Decay-associated spectra (DAS) relating to amplitudes $A_1$ (a–c), $A_2$ (d–f), and $A_3$ (g–i). **Bottom row**: Plots (j–l) of the kinetic constants $k_1$ (filled circles), $k_2$ (open circles), and $k_3$ (open triangles) as a function of the concentration of TFA.


© 2022 The Authors. ChemPhotoChem published by Wiley-VCH GmbH

ChemPhotoChem | Research Articles
doi.org/10.1002/cptc.202200041
Chemistry Europe
European Chemical Societies Publishing

Figure 6 shows the effect of acidification on the DAS $A_1$ corresponding to the fastest dynamics. In the region below 520 nm and above 570 nm, the CPX* emission steadily decreases with increasing [TFA]. In the same manner, the negative signal observed in between, corresponding to HBIP* formation, decreases as well. This is in line with our interpretation that the water molecules gather around the strongest acid, i.e., around TFA rather than ROH, so that excitation yields the less CPX* the more TFA is present.

If this conclusion is appropriate, a decrease of CPX* should be accompanied by an increase of ROH* emission. This is indeed reflected in $A_2$ (Figure 6(d–f)) by the growth of the emission signal at 480 nm with increasing [TFA]. Moreover, the HBIP* emission around 550 nm in combination with the negative rise of $RO^{-}$* at 575 nm should also shrink, as is evident in these DASs. It seems that the addition of TFA, at least at low concentrations, reverses the effect of water addition, see the comparison of Figure 6(a-f) and Figure 4(a–b).

Remarkably, for the highest value of [TFA], the DAS $A_2$ even becomes negative in the spectral region around 550 nm. Thus, this signal indicates a rise of HBIP* emission that does not originate from a previous CPX*. Rather, we propose that a water molecule encounters an excited photoacid ROH* in a diffusive process, directly yielding HBIP*. This can be rationalized as ROH* now is the stronger acid than TFA, in contrast to the situation in the ground state.

Further in line with our interpretation, the $RO^{-}$* emission at 575 nm constantly diminishes with increasing [TFA], reflected in DAS $A_3$ in Figure 6(g–i). At high values of [TFA], $A_3$ starts to exhibit a positive contribution peaking at 550 nm and, for the highest TFA concentration, even a broad emission around 500 nm. This shows that HBIP* and even CPX* are formed more slowly and persist for a longer time compared to weakly acidic solution. Our explanation is again based on initial TFA-water complexes which encounter a ROH* molecule and can lead to HBIP* formation. Because this complex is already acidic, a full separation of HBIP* to yield $RO^{-}$* does not occur and, in the extreme case of very high [TFA], even HBIP* formation is hindered, giving rise to the emission signal of CPX*, persisting on the longest observed timescale. The putative formation of a [ROH···TFA]* complex under these conditions might further contribute.

The discussed processes are also reflected in the rate constants (Figure 6(j–l)). Corresponding to the fastest dynamics, $k_1$ describes the conversion of CPX* into HBIP* (*vide supra*). Since acidification only reduces the amount of CPX*, $A_1$ shrinks but $k_1$ stays almost constant. The actual value of $k_1$ depends on the water concentration (also compare to Figure 4(d)). The reason for the decrease of $k_1$ in Figure 6(l) is again rationalized by the proposed clustering of water around TFA, effectively reducing the amount of water in the vicinity of the photoacid, so that a value of $k_1$ is approached which would correspond to less water in the non-acidic case. In other words, TFA inhibits the formation of HBIP*, which shows signatures of diffusion-controlled reaction kinetics (cf. Figure 4(d)). We conjecture that this analogously affects $k_1$ in Figure 6(j–k), but to a lower extent. In the extreme case of strongly acidic conditions, there is basically no water close to the photoacid and hence, no CPX in the ground state. Consequently, there is also no initial CPX* after excitation and, in the global analysis, $k_1$ rather mimics the solvation dynamics of ROH*. This process occurs on ps timescales so that the actual value of $k_1$ is meaningless because of limited time resolution. Since the solvation dynamics lead to a bathochromic shift with time, the amplitude $A_1$ for the initial emission of ROH* is therefore still slightly blue-shifted with respect to the steady-state emission of ROH* (compare the maximum at 470 nm in the curves for highest acid concentration in Figure 6(a–c) vs. 480 nm as found in Figure 1(c–d)).

With increasing acidification, the rate constant $k_2$ undergoes a change from describing the HBIP*→$RO^{-}$* conversion to the diffusive HBIP* formation from ROH* with approaching water (see the sign change of the amplitude assigned to HBIP* in Figure 6). For large TFA excess, it appears that $k_2$ approaches the same value of about 0.27 $ns^{-1}$. We note that this is again close to the radiative decay rate of 0.234 $ns^{-1}$ for the methylated analog ROMe* (see Figure S5 in ESI), i.e., a situation where emission only originates from the initial species.

The rate constant $k_3$ takes the same value for all studied water concentrations (also see Figure 4(d)) and low [TFA], because it then solely represents the $RO^{-}$* emission, as already evident from the corresponding DAS $A_3$. Time-resolved studies using time-correlated single-photon counting (TCSPC) and fluorescence up-conversion report that $RO^{-}$* emission decays monoexponentially with a rate constant of 0.18 $ns^{-1}$ in DMSO,[33] 0.17 $ns^{-1}$ in water,[35] and 0.17 $ns^{-1}$ in MeOH and EtOH.[35] We find a value of 0.17 $ns^{-1}$, in very good agreement with these other studies. At high [TFA], further contributions from HBIP* and CPX* mix in as described before, causing a slight increase of $k_3$.

## Summary

Our experiments have investigated the emission characteristics of a super-photoacid ROH in acetone-water environments. For the dynamics, we found that global analysis with a tri-exponential model allows a comprehensive interpretation of the data. Our five main findings are:

**(1) ESPT even in neat acetone**

The observation of $RO^{-}$* emission without any water admixtures and the concomitant decay of ROH* with virtually the same rate as ROMe* implies that ESPT to acetone might also be possible, yet very inefficient. In steady-state fluorescence studies, this possibility has already been suggested[33] and is now supported by our time-resolved analysis.

**(2) CPX formation in the ground state upon water addition**

If water is used as a cosolvent, steady-state absorption and emission spectra reveal that a complex between the photoacid


© 2022 The Authors. ChemPhotoChem published by Wiley-VCH GmbH

ChemPhotoChem | Research Articles
doi.org/10.1002/cptc.202200041
Chemistry Europe
European Chemical Societies Publishing

and water is formed in the ground state. A Benesi-Hildebrand analysis disclosed that this complex CPX comprises one water molecule and the photoacid.

**(3) A three-step Eigen-Weller model can explain the fluorescence dynamics in the presence of water**

Excitation at 405 nm generates ROH* and, to an increasing degree with rising water concentration, CPX*. The latter subsequently transforms into HBIP*, which may further give rise to $RO^-$* (if there are sufficient water molecules, see finding (4)). Signatures of all four species involved in this three-step Eigen-Weller model can be clearly identified both in steady-state and time-resolved emission spectroscopy.

Excited contact ion pairs as the most prominent ESPT intermediates are commonly short-lived (few-ps) in water,[56,64,65] though this is not necessarily the case in polar-aprotic solvents. For experiments with our photoacid and trioctylphosphine oxide in nitriles, CPX* and HBIP* intermediates have been shown to be necessary as well to describe the emission characteristics adequately.[36,37] If ground-state dynamics are additionally monitored, as done by Vester *et al.*[51] in photon antibunching experiments for this photoacid in DMSO, a further solvent-separated ion pair needs to be taken into account.

Recently, Kumpulainen *et al.* reported that ESPT to DMSO of a 1,8-naphthalimide-based photoacid ($pK_a^* \sim -2$), which is similarly strong to ours, proceeds according to a two-step Eigen-Weller model *via* a contact ion pair that is generated by a fast, solvent-controlled initial proton-transfer equilibrium.[56] Further restraining proton dissociation by changing to even less polar solvents then gives rise to the need for complex formation with an additional base prior to the ESPT, overall requiring a description based on a three-step model.[57] Albeit it is a different photoacid, the employed model has great similarities to the one used by us.

**(4) More than one water molecule required for HBIP* separation**

By analyzing the titration series with water, it became apparent that HBIP* cannot separate if no further water molecules are in close vicinity. We conclude that a hydrogen-bonded network is necessary to stabilize the hydronium cation:

$$[RO^- \cdots H^+ \cdots OH_2]^* + n\ H_2O \rightarrow [RO^- \cdots H_2O \cdots H^+ \cdots (OH_2)_n]^*;\ n \geq 1$$

This observation has some analogy to the reactivity of diphenylcarbene (DPC) in methanol/acetonitrile mixtures,[66,67] in which, depending on the solvent composition, photogenerated singlet DPC can only abstract a proton from a methanol molecule if the generated methoxide anion is stabilized by hydrogen bonds to other methanol molecules.

**(5) Acidification of acetone-water mixtures reduces the local hydration of the photoacid**

TFA is a stronger acid than the ground-state photoacid. Thus, if TFA is added to an acetone-water mixture containing the photoacid, our data shows that the amount of water molecules adjacent to the photoacid declines, and in turn CPX*, HBIP*, and, finally, $RO^-$* is suppressed after excitation. It is known that water can form clusters in acetoneous environments,[47,48] which we assume to be located around TFA rather than ROH.

Under high concentration of TFA, there is hardly any CPX present in solution since all the water gathers around TFA. Photoexcitation thus initially leads to almost exclusively ROH* emission. However, HBIP* subsequently starts to emerge, but without preceding CPX* emission. In our interpretation, the HBIP* can be directly formed from ROH* and water which first have to encounter each other in a diffusive process. This effect is supposed to become the more distinct the more TFA is present, because then less ground-state complexation of the photoacid and water occurs. At large excess of TFA, even CPX* is observed which also originates from this diffusive mechanism.

## Outlook

The ESPT dynamics of the neutral super-photoacid employed here can vary significantly in acetone-water mixtures depending on the solvent composition and the acidification. This opens two perspectives. On the one hand, desired emission properties are attainable if the environmental conditions can be tuned in a controlled manner. On the other hand, recording the emission in a variable environment also allows to obtain information on the latter. These versatile properties could be further manipulated by employing solvent mixtures with perturbed hydrogen-bond dynamics,[68–74] applying high pressures[26,75–77] or spatially encapsulating the compound. The latter approach was demonstrated for other photoacids confined in small solvent droplets,[16] as e.g. also possible in (reverse) micelles,[24,78–86] or small container molecules,[87–89] which further alters the ESPT characteristics.

## *Acknowledgements*

*We thank Prof. Martina Havenith (Ruhr-Universität Bochum) for providing streak camera equipment and Dr. Anne Leutzgen (formerly Saarland University) for providing the photoacid. Different aspects of this work were supported by the Deutsche Forschungsgemeinschaft (DFG, German Research Foundation) within the Research Training Group "Confinement-controlled Chemistry" (Grant GRK2376, Project 331085229), under Germany's Excellence Strategy – EXC 2033 – 390677874 – RESOLV, and through Grant JU 650/8-1. Open Access funding enabled and organized by Projekt DEAL.*


© 2022 The Authors. ChemPhotoChem published by Wiley-VCH GmbH

ChemPhotoChem | Research Articles
doi.org/10.1002/cptc.202200041
Chemistry Europe
European Chemical Societies Publishing

### *Competing financial interests*

The authors declare no competing financial interests.

## Data Availability Statement

The data that support the findings of this study are available from the corresponding author upon reasonable request.

**Keywords:** Eigen-Weller model · excited-state proton transfer · photoacid · solvent effects · time-resolved spectroscopy

[1] E. Pines, Chapter 7 in "The Chemistry of Phenols", edited by Z. Rappoport; John Wiley & Sons, Ltd, **2003**, DOI: 10.1002/0470857277.ch7, part of *Patai's Chemistry of Functional Groups*.
[2] G. Granucci, J. T. Hynes, P. Millié, T.-H. Tran-Thi, *J. Am. Chem. Soc.* **2000**, *122*, 12243–12253.
[3] M. Lukeman, P. Wan, *J. Am. Chem. Soc.* **2002**, *124*, 9458–9464.
[4] N. Basarić, P. Wan, *Photochem. Photobiol. Sci.* **2006**, *5*, 656–664.
[5] M. K. Nayak, P. Wan, *Photochem. Photobiol. Sci.* **2008**, *7*, 1544–1554.
[6] S. Kaneko, S. Yotoriyama, H. Koda, S. Tobita, *J. Phys. Chem. A* **2009**, *113*, 3021–3028.
[7] E. Pines, D. Tepper, B.-Z. Magnes, D. Pines, T. Barak, *Ber. Bunsenges. Phys. Chem.* **1998**, *102*, 504–510.
[8] L. M. Tolbert, J. E. Haubrich, *J. Am. Chem. Soc.* **1990**, *112*, 8163–8165.
[9] T. G. Kim, M. R. Topp, *J. Phys. Chem. A* **2004**, *108*, 10060–10065.
[10] M. Rini, B.-Z. Magnes, E. Pines, E. T. J. Nibbering, *Science* **2003**, *301*, 349.
[11] O. F. Mohammed, D. Pines, J. Dreyer, E. Pines, E. T. J. Nibbering, *Science* **2005**, *310*, 83–86.
[12] E. T. J. Nibbering, H. Fidder, E. Pines, *Annu. Rev. Phys. Chem.* **2005**, *56*, 337–367.
[13] G. Jung, S. Gerharz, A. Schmitt, *Phys. Chem. Chem. Phys.* **2009**, *11*, 1416–1426.
[14] B. Cohen, C. Martin Álvarez, N. Alarcos Carmona, J. A. Organero, A. Douhal, *J. Phys. Chem. B* **2011**, *115*, 7637–7647.
[15] N. A. Carmona, B. Cohen, J. A. Organero, A. Douhal, *J. Photochem. Photobiol. A* **2012**, *234*, 3–11.
[16] N. Alarcos, B. Cohen, A. Douhal, *Phys. Chem. Chem. Phys.* **2016**, *18*, 2658–2671.
[17] C. Hoberg, T. Ockelmann, J. Shee, P. Balzerowski, D. DasMahanta, F. Novelli, M. Head-Gordon, M. Havenith, *ChemRxiv.* **2022**, DOI 10.33774/chemrxiv-2021-60zjv-v2.
[18] N. M. Trieff, B. R. Sundheim, *J. Phys. Chem.* **1965**, *69*, 2044–2059.
[19] R. Simkovitch, E. Kisin-Finfer, S. Shomer, R. Gepshtein, D. Shabat, D. Huppert, *J. Photochem. Photobiol. A* **2013**, *254*, 45–53.
[20] M. Premont-Schwarz, T. Barak, D. Pines, E. T. Nibbering, E. Pines, *J. Phys. Chem. B* **2013**, *117*, 4594–4603.
[21] N. Agmon, *J. Phys. Chem. A* **2005**, *109*, 13–35.
[22] R. Simkovitch, S. Shomer, R. Gepshtein, D. Huppert, *J. Phys. Chem. B* **2015**, *119*, 2253–2262.
[23] K. M. Solntsev, D. Huppert, N. Agmon, *J. Phys. Chem. A* **1999**, *103*, 6984–6997.
[24] L. M. Tolbert, K. M. Solntsev, *Acc. Chem. Res.* **2002**, *35*, 19–27.
[25] T. Nakagawa, S. Kohtani, M. Itoh, *J. Am. Chem. Soc.* **1995**, *117*, 7952–7957.
[26] N. Koifman, B. Cohen, D. Huppert, *J. Phys. Chem. A* **2002**, *106*, 4336–4344.
[27] Y. Guo, X. Li, J. Zheng, G.-l. Zhang, J. Liu, W. Chen, *Optoelectron. Lett.* **2006**, *2*, 115–117.
[28] T. Förster, *Naturwissenschaften* **1949**, *36*, 186–187.
[29] T. Förster, *Z. Elektrochem. Angew. Phys. Chem.* **1950**, *54*, 42–46.
[30] T. Förster, *Z. Elektrochem. Angew. Phys. Chem.* **1950**, *54*, 531–535.
[31] M. Eigen, *Angew. Chem. Int. Ed.* **1964**, *3*, 1–19; *Angew. Chem.* **1963**, *75*, 489–508.
[32] A. Weller, *Prog. React. Kinet.* **1961**, *1*, 187.
[33] B. Finkler, C. Spies, M. Vester, F. Walte, K. Omlor, I. Riemann, M. Zimmer, F. Stracke, M. Gerhards, G. Jung, *Photochem. Photobiol. Sci.* **2014**, *13*, 548–562.
[34] C. Spies, B. Finkler, N. Acar, G. Jung, *Phys. Chem. Chem. Phys.* **2013**, *15*, 19893–19905.
[35] C. Spies, S. Shomer, B. Finkler, D. Pines, E. Pines, G. Jung, D. Huppert, *Phys. Chem. Chem. Phys.* **2014**, *16*, 9104–9114.
[36] A. Grandjean, J. L. Pérez Lustres, S. Muth, D. Maus, G. Jung, *J. Phys. Chem. Lett.* **2021**, *12*, 1683–1689.
[37] A. Grandjean, J. L. Pérez Lustres, G. Jung, *ChemPhotoChem* **2021**, *5*, 1094–1105.
[38] J. Ortega, C. Rafols, E. Bosch, M. Roses, *J. Chem. Soc. Perkin Trans. 2* **1996**, 1497.
[39] C. Reichardt, T. Welton, *Solvents and Solvent Effects in Organic Chemistry*, 4th ed., Wiley-VCH, Weinheim, **2011**.
[40] H. Beens, K. H. Grellmann, M. Gurr, A. H. Weller, *Discuss. Faraday Soc.* **1965**, *39*, 183.
[41] C. A. Hasselbacher, E. Waxman, L. T. Galati, P. B. Contino, J. B. A. Ross, W. R. Laws, *J. Phys. Chem.* **1991**, *95*, 2995–3005.
[42] J. Juanos i Timoneda, J. T. Hynes, *J. Phys. Chem.* **1991**, *95*, 10431–10442.
[43] P. B. Bisht, G. C. Joshi, H. B. Tripathi, *Chem. Phys. Lett.* **1995**, *237*, 356–360.
[44] T. Kumpulainen, B. H. Bakker, M. Hilbers, A. M. Brouwer, *J. Phys. Chem. B* **2015**, *119*, 2515–2524.
[45] Y. M. Lee, S.-Y. Park, H. Kim, T. G. Kim, O.-H. Kwon, *Methods Appl. Fluoresc.* **2016**, *4*, 024004.
[46] R. L. Scott, *Recl. Trav. Chim. Pays-Bas* **1956**, *75*, 787–789.
[47] A. Perera, F. Sokolić, *J. Chem. Phys.* **2004**, *121*, 11272–11282.
[48] D. S. Venables, C. A. Schmuttenmaer, *J. Chem. Phys.* **2000**, *113*, 11222–11236.
[49] T. S. Zwier, *Science* **2004**, *304*, 1119–1120.
[50] R. Simkovitch, K. Akulov, S. Shomer, M. E. Roth, D. Shabat, T. Schwartz, D. Huppert, *J. Phys. Chem. A* **2014**, *118*, 4425–4443.
[51] M. Vester, A. Grueter, B. Finkler, R. Becker, G. Jung, *Phys. Chem. Chem. Phys.* **2016**, *18*, 10281–10288.
[52] M. Vester, T. Staut, J. Enderlein, G. Jung, *J. Phys. Chem. Lett.* **2015**, *6*, 1149–1154.
[53] E. Pines, D. Huppert, N. Agmon, *J. Chem. Phys.* **1988**, *88*, 5620–5630.
[54] N. Agmon, E. Pines, D. Huppert, *J. Chem. Phys.* **1988**, *88*, 5631–5638.
[55] D. Huppert, S. Y. Goldberg, A. Masad, N. Agmon, *Phys. Rev. Lett.* **1992**, *68*, 3932–3935.
[56] T. Kumpulainen, A. Rosspeintner, B. Dereka, E. Vauthey, *J. Phys. Chem. Lett.* **2017**, *8*, 4516–4521.
[57] T. Kumpulainen, B. H. Bakker, A. M. Brouwer, *Phys. Chem. Chem. Phys.* **2015**, *17*, 20715–20724.
[58] J. C. Penedo, M. Mosquera, F. Rodríguez-Prieto, *J. Phys. Chem. A* **2000**, *104*, 7429–7441.
[59] R. Ihaka, R. Gentleman, *J. Comput. Graph. Stat.* **1996**, *5*, 299–314.
[60] K. M. Mullen, I. H. van Stokkum, *J. Stat. Softw.* **2007**, *18(3)*, 1–46.
[61] J. J. Snellenburg, S. P. Laptenok, R. Seger, K. M. Mullen, I. H. M. van Stokkum, *J. Stat. Softw.* **2012**, *49(3)*,1–22.
[62] S. P. Laptenok, P. Nuernberger, A. Lukacs, M. H. Vos, *Methods Mol. Biol.* **2014**, *1076*, 321–336.
[63] D. Marx, M. E. Tuckerman, J. Hutter, M. Parrinello, *Nature* **1999**, *397*, 601–604.
[64] O. F. Mohammed, D. Pines, E. T. J. Nibbering, E. Pines, *Angew. Chem. Int. Ed.* **2007**, *46*, 1458–1461; *Angew. Chem.* **2007**, *119*, 1480–1483.
[65] A. Brenlla, M. Veiga Gutiérrez, M. C. Ríos Rodríguez, F. Rodríguez-Prieto, M. Mosquera, J. L. Pérez Lustres, *J. Phys. Chem. Lett.* **2014**, *5*, 989–994.
[66] J. Knorr, P. Sokkar, S. Schott, P. Costa, W. Thiel, W. Sander, E. Sanchez-Garcia, P. Nuernberger, *Nat. Commun.* **2016**, *7*, 12968.
[67] J. Knorr, P. Sokkar, P. Costa, W. Sander, E. Sanchez-Garcia, P. Nuernberger, *J. Org. Chem.* **2019**, *84*, 11450–11457.
[68] P. Jacques, *Chem. Phys. Lett.* **1990**, *171*, 353–356.
[69] S. Gupta, S. Rafiq, M. Kundu, P. Sen, *J. Phys. Chem. B* **2012**, *116*, 1345–1355.
[70] S. Gupta, S. Rafiq, P. Sen, *J. Phys. Chem. B* **2015**, *119*, 3135–3141.
[71] L. R. R. Santin, S. C. dos Santos, D. L. R. Novo, D. Bianchini, A. P. Gerola, G. Braga, W. Caetano, L. M. Moreira, E. L. Bastos, A. P. Romani, H. P. M. de Oliveira, *Dyes Pigm.* **2015**, *119*, 12–21.
[72] D. Das Mahanta, D. Rana, A. Patra, B. Mukherjee, R. K. Mitra, *Chem. Phys. Lett.* **2018**, *700*, 50–56.
[73] D. Das Mahanta, S. I. Islam, S. Choudhury, D. K. Das, R. K. Mitra, A. Barman, *J. Mol. Liq.* **2019**, *290*, 111194.
[74] S. Wortmann, S. Schloeglmann, P. Nuernberger, *J. Org. Chem.* **2022**, *87*, 1745–1755.
[75] M. Kondo, X. Li, M. Maroncelli, *J. Phys. Chem. B* **2013**, *117*, 12224–12233.


© 2022 The Authors. ChemPhotoChem published by Wiley-VCH GmbH

ChemPhotoChem
Research Articles
doi.org/10.1002/cptc.202200041
Chemistry Europe
European Chemical Societies Publishing

[76] L. Grimmelsmann, V. Schuabb, B. Tekin, R. Winter, P. Nuernberger, *Phys. Chem. Chem. Phys.* **2018**, *20*, 18169–18175.
[77] J. Schroeder, D. Schwarzer, J. Troe, P. Vöhringer, *Chem. Phys. Lett.* **1994**, *218*, 43–50.
[78] B. Cohen, D. Huppert, K. M. Solntsev, Y. Tsfadia, E. Nachliel, M. Gutman, *J. Am. Chem. Soc.* **2002**, *124*, 7539–7547.
[79] S.-Y. Park, O.-H. Kwon, T. G. Kim, D.-J. Jang, *J. Phys. Chem. C* **2009**, *113*, 16110–16115.
[80] K. J. Tielrooij, M. J. Cox, H. J. Bakker, *ChemPhysChem* **2009**, *10*, 245–251.
[81] T. Mondal, A. K. Das, D. K. Sasmal, K. Bhattacharyya, *J. Phys. Chem. B* **2010**, *114*, 13136–13142.
[82] M. D. Fayer, N. E. Levinger, *Annu. Rev. Anal. Chem.* **2010**, *3*, 89–107.
[83] C. Lawler, M. D. Fayer, *J. Phys. Chem. B* **2015**, *119*, 6024–6034.
[84] S. Panja, D. K. Khatua, P. Pramanik, M. Halder, *Chem. Phys.* **2018**, *510*, 1–9.
[85] A. Das, S. I. Islam, D. K. Das, R. K. Mitra, *ACS Omega* **2018**, *3*, 5715–5724.
[86] S. I. Islam, A. Das, R. K. Mitra, *J. Photochem. Photobiol. A* **2021**, *404*, 112928.
[87] R. Gepshtein, P. Leiderman, D. Huppert, E. Project, E. Nachliel, M. Gutman, *J. Phys. Chem. B* **2006**, *110*, 26354–26364.
[88] N. Basílio, C. A. T. Laia, F. Pina, *J. Phys. Chem. B* **2015**, *119*, 2749–2757.
[89] A. S. I. Amer, A. M. M. Alazaly, A. A. Abdel-Shafi, *J. Photochem. Photobiol. A* **2019**, *369*, 202–211.

Manuscript received: February 11, 2022
Revised manuscript received: April 13, 2022
Accepted manuscript online: April 14, 2022
Version of record online: May 16, 2022


© 2022 The Authors. ChemPhotoChem published by Wiley-VCH GmbH

# 4. ESPT in Neat Acetone

In view of the previous findings (Chap. 3), this part of the project extends the time-resolved spectroscopic measurements to neat acetone as the environment. Chapter 3 demonstrated that both a photoacid–base complex (CPX) and a hydrogen-bonded ion pair (HBIP) need to be considered as intermediates to describe the emission dynamics of photoacid **B** in acetone–water mixtures properly, but these intermediates were not specifically observed in neat acetone. Rather, the results indicated picosecond solvation dynamics and an ESPT that is described by a single time constant. These dynamics are elucidated using ultrafast transient absorption spectroscopy in combination with time-resolved fluorescence *via* TCSPC.

This part has been performed under the supervision of Prof. Dr. Patrick Nürnberger. The transient absorption has been measured by Dr. Johannes Knorr and the time-resolved emission by him together with Dr. Bastian Geißler. The anisotropy measurements have been performed by Dr. Roger Jan Kutta. My contribution consists in performing the data analysis, helping with the preparation of the figures, contributing ideas to the discussion, and finalizing the first draft of the manuscript (initially written by Dr. Johannes Knorr). Furthermore, I am responsible for a thorough revision of the whole manuscript and a complete re-analysis of the emission data (Fig. 1) during the publication process. I have also assisted Patrick Nürnberger in corresponding with the editor and the reviewers.

The following open-access publication is reprinted under the terms of CC BY-NC-ND 4.0 from: J. Knorr, N. Sülzner, B. Geissler, C. Spies, A. Grandjean, R. J. Kutta, G. Jung, and P. Nuernberger. Ultrafast transient absorption and solvation of a super-photoacid in acetoneous environments. *Photochem. Photobiol. Sci.* **2022** *21* (12), 2179–2192. **Copyright © The Authors 2022. Photochem. Photobiol. Sci. published by Springer.** This publication is also available online: `https://doi.org/10.1007/s43630-022-00287-z`.

Photochemical & Photobiological Sciences (2022) 21:2179–2192
https://doi.org/10.1007/s43630-022-00287-z

ORIGINAL PAPERS

# Ultrafast transient absorption and solvation of a super-photoacid in acetoneous environments

Johannes Knorr[4,5] · Niklas Sülzner[2,4] · Bastian Geissler[1,4] · Christian Spies[3,4] · Alexander Grandjean[3] · Roger Jan Kutta[1] · Gregor Jung[3] · Patrick Nuernberger[1,4]

Received: 11 May 2022 / Accepted: 8 August 2022 / Published online: 30 September 2022
© The Author(s) 2022

**Abstract**

The phenomenon of photoacidity, i.e., an increase in acidity by several orders of magnitude upon electronic excitation, is frequently encountered in aromatic alcohols capable of transferring a proton to a suitable acceptor. A promising new class of neutral super-photoacids based on pyranine derivatives has been shown to exhibit pronounced solvatochromic effects. To disclose the underlying mechanisms contributing to excited-state proton transfer (ESPT) and the temporal characteristics of solvation and ESPT, we scrutinize the associated ultrafast dynamics of the strongest photoacid of this class, namely tris(1,1,1,3,3,3-hexafluoropropan-2-yl)8-hydroxypyrene-1,3,6-trisulfonate, in acetoneous environment, thereby finding experimental evidence for ESPT even under these adverse conditions for proton transfer. Juxtaposing results from time-correlated single-photon counting and femtosecond transient absorption measurements combined with a complete decomposition of all signal components, i.e., absorption of ground and excited states as well as stimulated emission, we disclose dynamics of solvation, rotational diffusion, and radiative relaxation processes in acetone and identify the relevant steps of ESPT along with the associated time scales.

**Graphical abstract**




## 1 Introduction

Upon electronic excitation, so-called photoacids show a higher acidity, i.e., a higher tendency to release an acidic proton, caused by changes in the molecule's electronic

This article is dedicated to Prof. Dr. Silvia E. Braslavsky, a pioneer in photobiology and photobiophysics, on the occasion of her 80th birthday.

✉ Patrick Nuernberger
patrick.nuernberger@ur.de

[1] Institut für Physikalische und Theoretische Chemie, Universität Regensburg, Universitätsstraße 31, 95053 Regensburg, Germany

[2] Lehrstuhl für Theoretische Chemie, Ruhr-Universität Bochum, 44780 Bochum, Germany

[3] Biophysikalische Chemie, Universität des Saarlandes, 66123 Saarbrücken, Germany

[4] Physikalische Chemie II, Ruhr-Universität Bochum, 44780 Bochum, Germany

[5] Erlangen Graduate School in Advanced Optical Technologies (SAOT), Friedrich-Alexander-Universität Erlangen-Nürnberg (FAU), Paul-Gordan-Straße 6, 91052 Erlangen, Germany

distribution that in turn affect corresponding hydrogen bonds. In 1965, Trieff and Sundheim introduced the term excited-state proton transfer (ESPT) [1]. However, more than 30 years earlier, it was Weber who observed that changing the pH value in a solution containing 1,4-naphthylaminosulfonate leads to changes in the corresponding fluorescence spectrum, while leaving the absorption spectrum unaltered [2]. A few years later, Förster was able to assign this phenomenon to a difference in the protolytic equilibria in the molecular electronic ground and excited state, respectively. Consequently, he introduced the so-called Förster cycle which explains the basic processes occurring in photoacid systems [3, 4]. For these molecules, which are typically weak acids in their ROH form, electronic excitation decreases the p$K_a$ value by several orders of magnitude. The Förster cycle illustrates the existence of two different species in the excited state, namely the ROH* and the $RO^{-}$* species, whereby the asterisk denotes the excited state. Their different energetic positions give rise to two separate emission bands for relaxation back to the respective ground states. Given that the p$K_a$ value is known, the Förster cycle directly reveals the p$K_a$* value of the photoacid system. If the p$K_a$ value is unknown, however, still the change in acidity upon photoexcitation can be evaluated [5].

ESPT is always linked to the presence of a suitable acceptor such as a polar solvent molecule. Most studies on ESPT were conducted in aqueous environment which allows to study even weak photoacids due to its extraordinary good ability to stabilize a proton [6–9]. One special type of photoacids are so-called super-photoacids which are characterized by negative p$K_a$* values (in water) [10–12]. This class of molecules allows the study of ESPT in various polar solvents, because the photoacids are so strong that they are able to transfer the proton to less good acceptor molecules, e.g., dimethyl sulfoxide (DMSO) [12–18]. Many studies on super-photoacids have also been carried out in solvent mixtures, for instance in water–methanol mixtures [19], water–acetonitrile mixtures [20], or water–acetone mixtures [21]. Importantly, time-resolved experiments have made it possible to follow ESPT on its actual time scale [13, 22, 23].

We focus on previously synthesized and spectroscopically characterized neutral super-photoacids derived from pyranine (8-hydroxy-1,3,6-pyrenetrisulfonate, HPTS), a pH-sensitive fluorescent dye from the group of arylsulfonates, with the modified molecules differing in their substituents at the aromatic pyrene core [14–16]. HPTS and related photoacids with pyrene centers were extensively studied by different time-resolved spectroscopic techniques in various environments [24–48] and also with regard to aspects of proton transfer mechanisms to a co-solute base [49–61]. Recently, also the ultrafast dynamics of super-photobases have been reported. [62–64]

The neutral super-photoacids exhibit electronic transitions in the VIS spectral region, thus being promising candidates to study proton transfer on the single-molecule level [65, 66] where UV excitation light typically leads to unwanted background signals. Furthermore, the compounds combine high photostability and high solubility, thus making them applicable as pH sensors in biological systems just like HPTS [67, 68]. Steady-state measurements and solvatochromic analysis revealed that intramolecular charge transfer on the photoacid side correlates best with the observed photoacidity. The present study deals with ultrafast dynamics of the strongest photoacid out of this series [14–16], namely tris(1,1,1,3,3,3-hexafluoropropan-2-yl)8-hydroxypyrene-1,3,6-trisulfonate (molecular structure sketched in Fig. 1c), which exhibits a high fluorescence quantum yield (91% in DMSO) [15] and excellent photostability. Owing to the strongly electron withdrawing sulfonic ester groups, the molecule exhibits in water an increase in acidity in the excited state of eight logarithmic units, i.e., orders of magnitude, as is reflected in the reported values p$K_a$ = 4.4 and p$K_a$* = –3.9, respectively [14]. Hence, ESPT is also possible in solvents which exhibit a low polarity and are rather weak hydrogen-bonding acceptors. While many photoacids do not transfer a proton to the solvent DMSO upon excitation, the system investigated here does so even in acetone [14, 15, 21]. While previous studies have shown that a complex of the photoacid with a hydrogen-bond accepting molecule as well as a hydrogen-bonded ion pair have to be taken into account as intermediates to describe the emission dynamics conclusively [21, 69, 70], these intermediates are not identified in neat acetone; rather, analysis of emission data in neat acetone pointed towards solvation dynamics on the ps time scale and ESPT described by basically one time constant [21]. Here, we extend the time-resolved studies of this particularly strong super-photoacid to unravel the ultrafast dynamics in the aprotic solvent acetone by combining time-correlated single-photon counting (TCSPC) and femtosecond transient absorption (fsTA) data. In-depth analysis allows a conclusive description and an illustrative modeling within a reaction scheme considering proton-transfer dynamics in the ground and excited state.

## 2 Materials and methods

### 2.1 Sample preparation and basic spectroscopic characterization

The synthesis of tris(1,1,1,3,3,3-hexafluoropropan-2-yl)8-hydroxypyrene-1,3,6-trisulfonate and of the methylated analogue was performed according to References [14, 15]. For sample preparation, acetone (anhydrous and of spectrophotometric grade) and trifluoroacetic acid (TFA, 99%) were used as received. For the measurement of linear absorption spectra, a JASCO V-770 spectrophotometer was used. Absorption spectra shown in Fig. 1b were recorded in situ

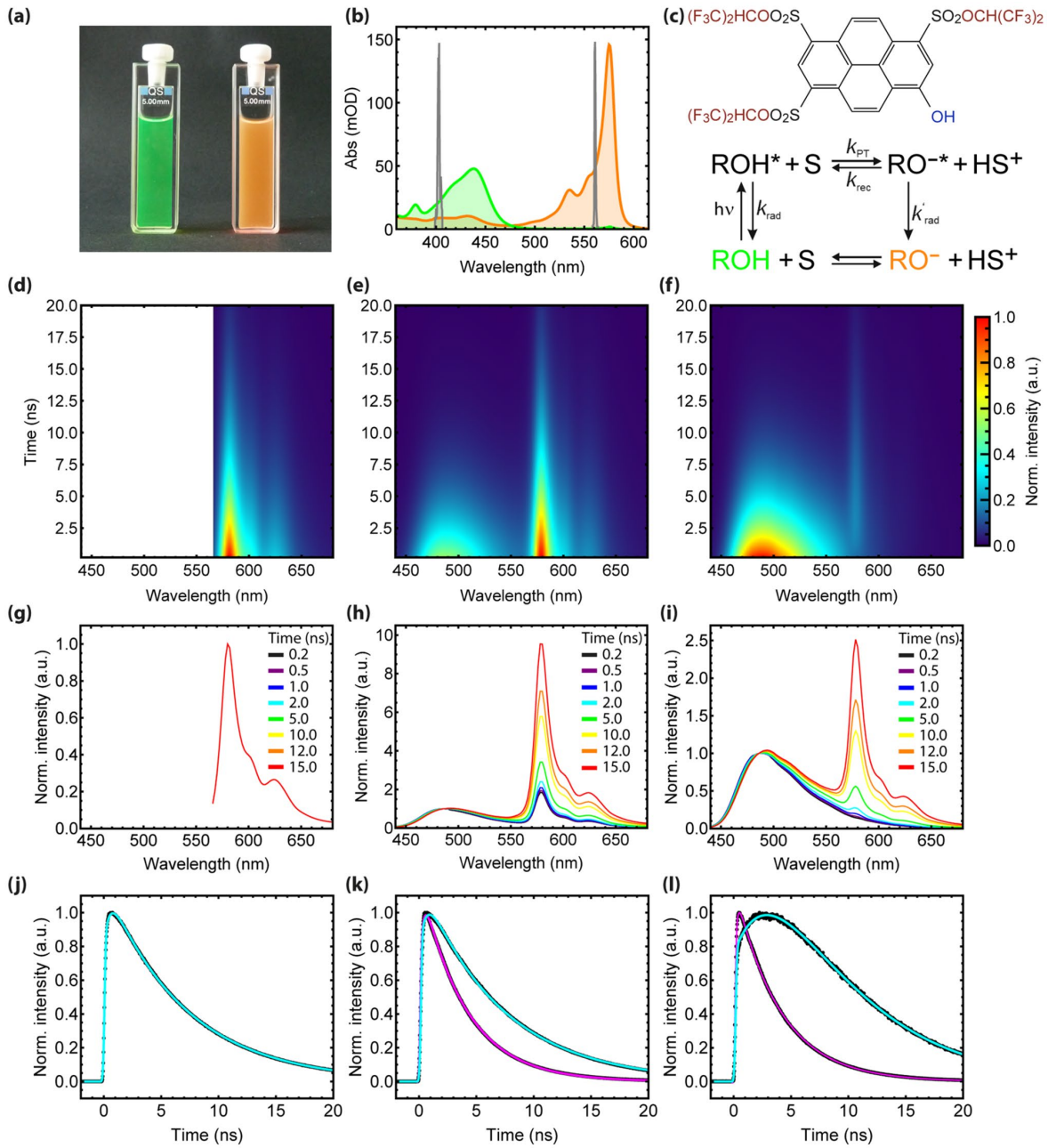



**Fig. 1** Fluorescence dynamics of the examined super-photoacid in acetoneous environment for two different acid-base equilibria. **a** Photograph of a neutral (orange) and an acidic (green) solution of the photoacid. **b** Absorption spectra of the neutral (orange) and acidic solution (green) used in the TCSPC experiments (note that spectra are corrected for solvent contributions). In addition, the emission spectra of the excitation laser diodes are indicated in gray. **c** Molecular structure of the investigated photoacid, with sulfonic ester moieties in red and hydroxyl group in blue, below, the one-step model used for fitting to the data. TCSPC data is displayed for: **d** neutral solution, excited at 561 nm; **e** neutral solution, excited at 405 nm; **f** acidic solution, excited at 405 nm. **g–i** Time-resolved emission spectra taken from graphs **d–f**. The spectra are normalized to the emission at 576 nm in the case of **g** or to the emission at 486 nm in the case of **h** and **i**, respectively; note that the individual curves in **g** are coinciding within experimental error. **j–l** Normalized temporal emission profiles at 480 nm (black, fit shown in magenta) and 576 nm (black, fit shown in cyan) taken from graphs **d–f**

in a 2 mm Suprasil cuvette before acquiring TCSPC data (see below).

### 2.2 Time-correlated single-photon counting (TCSPC)

Fluorescence lifetimes of the ROH* and $RO^-$* form were measured by TCSPC under magic-angle conditions [71, 72] in 90° geometry with a commercial setup (FluoTime 200 with a TimeHarp 260 correlation unit and a PMA-C-182-M photomultiplier detector assembly, Picoquant). For excitation, either a 405 nm (LDH-P–C-405) or a 561 nm (LDH-D-TA-560) pulsed diode laser (driven by a PDL-800-B oscillator module; Picoquant) was used at a repetition rate of 10 MHz. The optical density along the excitation path of the samples was well below 0.15 in order to minimize reabsorption of fluorescence photons. The instrument response function (IRF) was recorded by replacing the sample with a Ludox suspension revealing an overall time resolution of ca. 300 ps (FWHM) for both excitation wavelengths. Spectra were recorded in a cuvette with a pathlength of 2 mm. Lifetimes were determined using a custom-built Matlab fitting routine, taking into account the instrument response function and background.

### 2.3 Transient absorption spectroscopy

A regenerative Titanium:Sapphire (Ti:Sa) amplifier (Spitfire Ace; Spectra Physics: 1 kHz, 800 nm, 100 fs) was used to pump a commercial noncollinear optical parametric amplifier (NOPA, TOPAS White; Light Conversion). To selectively excite the ROH or the $RO^-$ form of the photoacid, the latter was tuned to generate 445 nm or 575 nm pump pulses having energies of 500 nJ or 350 nJ at the sample position, respectively. Supercontinuum probe pulses were generated in a linearly moving $CaF_2$ plate and used with polarization under magic angle (54.7°) with respect to the one of the pump pulses. Recording changes in optical density from pairs of subsequent laser shots was enabled by using a grating spectrograph (Acton SP2500i; Princeton Instruments) combined with a two-dimensional CCD camera (Pixis 2 K; Princeton Instruments) with an acquisition rate of 1 kHz and mechanically chopping every second pump pulse [73, 74]. When pumping at 445 nm, different absorbances of the investigated solutions were considered by globally scaling the dataset of the neutral solution with respect to the strength of the ground-state bleach signal observed for the acidic solution at 445 nm immediately after time zero. For measurements of anisotropy, a similar fsTA setup based on a Ti:Sa amplifier (Libra; Coherent: 1 kHz, 800 nm, 100 fs) was employed, using a collinear optical parametric amplifier (OPA, TOPAS-800-fs; Light Conversion) pumped at 800 nm as pump source and $CaF_2$ (5 mm) supercontinuum pumped at 800 nm as probe source. Two complementary high-speed spectrographs (EB Stresing) for signal and reference recording were used. Pump and probe polarizations were set to 0°, 54.7°, and 90°, respectively. Here, the pump energies at the sample position were 250 nJ or 400 nJ when using 405 nm or 575 nm, respectively.

The chirp of the supercontinuum probe was removed from fsTA data [71]. Due to high photostability and the characteristic time scales, exchanging the sample volume between subsequent pump pulses was not necessary. Hence, fsTA data were recorded in a sample cell with fixed volume (Suprasil, 200 µm or 1 mm path length). Photostability was verified by recording linear absorption spectra before and after the fsTA experiment without observing any change.

## 3 Results

For disclosing the ultrafast reaction dynamics, the photoacid is investigated with TCSPC and fsTA. With each technique, two solutions with differing ground-state equilibria are examined, whereby significantly lower sample concentrations are chosen for the TCSPC measurements to avoid reabsorption of fluorescence photons. For simplicity, the solutions are called "neutral" (without TFA, orange) or "acidic" (with additional TFA, green) in the following (see also Fig. 1a). To avoid confusion, we note that the neutral form of the photoacid predominates in the case of the "acidic" sample, because the nomenclature refers to the additional acidification of the solution.

### 3.1 TCSPC

The results from our TCSPC experiments are summarized in Fig. 1. The absorption spectra shown in Fig. 1b illustrate that acidification via addition of TFA shifts the photoacid's ground-state equilibrium from the $RO^-$ form (575 nm) towards the ROH form (445 nm). In other words, one observes a transition from a mainly deprotonated ensemble of ground state molecules (orange curve) to the ensemble of fully protonated molecules in the ground state (green curve). Both neutral and acidic solutions are studied upon excitation with 405 nm light, the former is furthermore studied with 561 nm excitation. For modeling the experimental findings, we use a simplified rate model based on the Förster cycle (Fig. 1c), in which both ROH and $RO^-$ can be directly excited. The model accounts for ROH* which either relaxes towards the ROH state with rate $k_{rad}$ or transfers a proton with rate $k_{PT}$ leading to $RO^-$* molecules which eventually can relax towards the $RO^-$ form with rate $k'_{rad}$. $RO^-$* can also be formed directly by excitation of $RO^-$ and decays back to the ground-state with $k'_{rad}$ as well. The individual populations right after excitation depend on both the pump

wavelength and the sample under study. Geminate recombination (rate $k_{rec}$) is omitted, the occurrence of ESPT is therefore reflected in the dynamics with rate $k_{rad}+k_{PT}$.

By illuminating the neutral solution with 561 nm light, only the $RO^-$ form is excited. The corresponding fluorescence originating solely from $RO^{-}*$ is recorded from 568 to 700 nm (Fig. 1d). When normalizing these time-resolved emission spectra (Fig. 1g), they exhibit an identical shape. Hence, there are no spectral shifts and identical dynamics are observed for all emission wavelengths, exemplarily shown in Fig. 1j for 576 nm. A mono-exponential fit to these data already yields a good agreement (adjusted $R^2=0.9982$). However, best results are obtained when an additional sub-ns exponential component is included (adjusted $R^2=0.9999$). While this is at the limit of the temporal resolution of the TCSPC device, it indicates that there are short-lived dynamics taking place as well, entailing subsequent investigations with fsTA (vide infra). For the ns decay time, a time constant of ${k'_{rad}}^{-1}=6.9$ ns is found.

Figures 1e, f display the fluorescence dynamics obtained after exciting the neutral or acidic solution with 405 nm light, respectively. Under these conditions, the excitation additionally confirms the existence of ROH* as a fluorescent species, whereby the anion's fluorescence (575 nm) is shifted towards longer wavelengths compared to the free photoacid (emitting in the spectral region around 480 nm). Again, the data are also visualized by time-resolved emission spectra (Fig. 1h, i), this time after normalizing each individual spectrum to the ROH* fluorescence at 486 nm. A comparison of these spectral profiles discloses that the ROH* fluorescence signal is higher relative to the one of $RO^{-}*$ when using a solution with a higher degree of acidification [21]. The normalized representation reveals that the emission in the region around 480 nm slightly red-shifts with time. On the one hand, this originates from the superposition with the $RO^{-}*$ emission and possible solvent rearrangement. On the other hand, the data of Fig. 1h, i also indicate the presence of ion-pair signals, since emission from ion pairs which have not separated completely usually appears in the spectral region around 550 nm for this photoacid (as e.g. observed in previous studies with water admixtures [21]), however, an identification of the involved cation is not possible from the data.

For both solutions under 405 nm excitation, the ROH* fluorescence signal appears within the time resolution of the experimental apparatus and decays in a mono-exponential manner with a time constant of 4.0 ns, as is evident from the emission at 486 nm (black data with magenta fit in Fig. 1k, l, adjusted $R^2=0.9983$ and 0.9995, respectively). Noteworthy, due to matching time constants for both solutions, putative traces of water seem negligible, as additional water has a more severe effect on the dynamics in neutral than in acidic solution [21]. In contrast, the temporal profiles associated with the $RO^{-}*$ emission monitored at 576 nm (cyan curves) are not identical (Fig. 1k, l). The total amount of fluorescing deprotonated molecules $[RO^{-}*](t)$ is given by the contributions of excited deprotonated molecules, which are formed by ESPT from ROH* ($[RO^{-}*]_{ESPT}$), and of directly excited $RO^-$ molecules ($[RO^{-}*]_{direct}$):

$$\left[RO^{-*}\right](t)=\frac{\left[RO^{-*}\right]_{ESPT}(k_{rad}+k_{PT})}{(k_{rad}+k_{PT})-k'_{rad}}\left(-e^{-(k_{rad}+k_{PT})t}+e^{-k'_{rad}t}\right)+\left[RO^{-*}\right]_{direct}e^{-k'_{rad}t}$$

where the rate constants correspond to those from Fig. 1c (with $k_{rec}$ set to zero). The first term thus describes a contribution that exhibits an exponential rise time $\tau=(k_{rad}+k_{PT})^{-1}\approx 4.0$ ns and a subsequent exponential decay with $k'^{-1}_{rad}$, whereas the second term describes a direct exponential decay with $k'^{-1}_{rad}$, resembling the direct $RO^{-}*$ emission displayed in Fig. 1j with $k'^{-1}_{rad}=6.9$ ns. The ratio $x=\left[RO^{-*}\right]_{ESPT}/\left[RO^{-*}\right]_{direct}$ of these two contributions, determined with the same fit model comprising fixed values of $(k_{rad}+k_{PT})^{-1}=4.0$ ns and $k'^{-1}_{rad}=6.9$ ns, is different for the data measured in neutral (Fig. 1k, x = 0.08, adjusted $R^2=0.9985$) and acidic (Fig. 1l, x = 1.44, adjusted $R^2=0.9995$) solution, respectively, as a consequence of the different initial concentrations of ROH or $RO^-$ in the two samples.

### 3.2 Transient absorption

The fsTA of the neutral solution after selective excitation of the $RO^-$ form with pulses spectrally centered at 575 nm is displayed in Fig. 2a. We observe negative signatures around 575 nm originating from the ground-state bleach (GSB) of the $RO^-$ absorption as well as stimulated emission (SE) of the $RO^{-}*$ form, and a positive signature centered around 450 nm reflecting the excited-state absorption (ESA) of the $RO^{-}*$ form. All signals are formed directly after time zero and decay with identical time constants. Importantly, the observed dynamics do not contain any spectral signatures of the ROH form, hence the excitable $RO^-$ are not in close proximity to a molecule that could transfer a proton (as, e.g., in the case of contact ion pairs in the electronic ground state).

Figure 2c illustrates the fsTA of the acidic solution after excitation at 445 nm. Negative signals originating from the GSB of the ROH absorption between 375 and 450 nm are observed, as well as two positive signatures appearing at 340 nm and 470 nm reflecting the ESA of the ROH* form (for a discourse on the latter signal, see Subsection "*Approach to Disassemble the fsTA Data*"). Since we do not observe any GSB signal at 575 nm directly after the pump interaction, we can infer that only the ROH form is excited

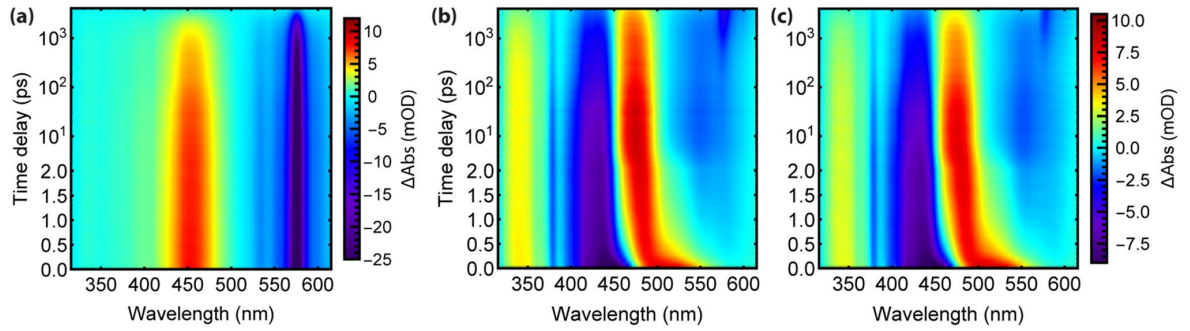



**Fig. 2** Transient absorption of the super-photoacid in acetoneous environment for two different acid-base equilibria. Data from fsTA experiments are shown for a pump–probe delay range of 4 ns; note the lin-log time axis (linear up to 2 ps, logarithmic afterwards) chosen to better visualize the characteristic time scales. **a** Neutral solution, excited at 575 nm; **b** neutral solution, excited at 445 nm; **c** acidic solution, excited at 445 nm [note that **b** and **c** have the same color scale]. The photoacid concentration was 616 µM, with 2 mM TFA added for **c**. The maximum optical density of the sample was 0.4

in this measurement. As observed in Fig. 2a when exciting the base form only, both ESA and GSB signals are formed directly after time zero and decay on the same time scale. Within the first few picoseconds, spectral shifts imprinted in the ESA signal and the GSB are present, after which a negative signal is observable around 550 nm. After several hundreds of picoseconds, a pronounced negative signal at 575 nm appears, and the ESA signal around 470 nm exhibits a blue shift on the same timescale. These dynamics evidence ESPT, as will be outlined below.

Figure 2b shows the fsTA of the neutral solution after exciting the non-dissociated ROH molecules, addressing the proton-transfer dynamics of the photoacid from a different ground-state equilibrium. At first glance, only minor differences compared to Fig. 2c appear, and hence we can infer that under neutral conditions mainly ROH rather than $RO^-$ is excited at 445 nm.

Generally, a global analysis [75] of photodynamic processes can be performed, with an exponential ansatz resulting in decay-associated difference spectra (DADS). If done for our data, the contributions in the ns regime resemble the findings in the TCSPC study (Fig. 1d). However, the dynamics for 445 nm excitation of both neutral and acidic solutions (Fig. 2b, c) exhibit pronounced spectral shifts during the first 100 ps. As the transient spectra themselves show a temporal behavior on these short timescales, global analysis with an exponential ansatz can only approximately describe these dynamics, giving rise to additional derivative-like DADS [76–80]. Recent studies have reported different advanced approaches to include spectral shifts in global analysis [81–84], however, we refrain from an analysis of DADS here and rather follow an alternative route to disentangle the dynamics, as outlined below.

## 4 Analysis and discussion

### 4.1 Dynamics after $RO^-$ excitation

When exciting the $RO^-$ form directly, no signature of the protonated solute is found, hence we infer that all transient absorption and emission signals originate from the deprotonated form. Specifically, we do not observe any indication of a re-protonation process. Besides energetic limitations, one would need to rationalize how a proton could approach an $RO^{-}$* anion after the photoexcitation. The following three scenarios all are unlikely for different reasons: (1) a proton is transferred from a methyl group of acetone; (2) a proton or a protonated acetone reaches the $RO^{-}$* (present for only a few ns) in a diffusion-controlled process; (3) ground-state ion pairs are present in solution, i.e., a $RO^-$ solute is not shielded by a solvent shell from a protonated acetone cation.

In the TCSPC data (Fig. 1d, g), the spectral shape does not change with time. Globally fitting the fsTA data yields a fast component (0.9 ps, see Fig. 3a) with which minor spectral shifts of a few nm are associated. We assign this behavior to solvation dynamics of the acetone environment as a reaction to the change in charge distribution in the solute upon photoexcitation. Maroncelli and coworkers report non-specific solvation dynamics of acetone to exhibit decay times of 0.187 ps and 1.09 ps; [85] while we could not explicitly deduce the former one, we identify them to correspond to the fastest time scale deduced from the fsTA data.

Steady-state spectra of $RO^-$ exhibit almost no significant Stokes shift in any solvent, indicating that predominantly the $v' = 0 \leftarrow v'' = 0$ vibronic transition is excited, but also that the reorganization energy for the solvation process must be small [85–87]. This implies that the solvation shells of

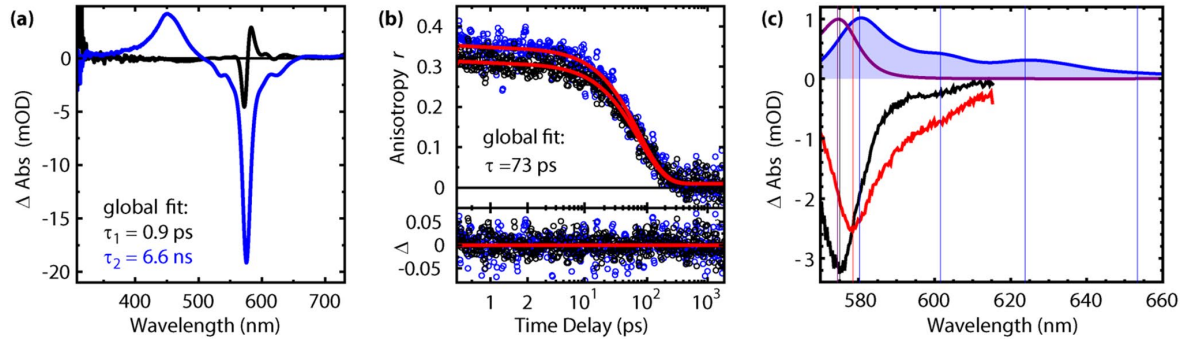



**Fig. 3** **a** Example of decay-associated difference spectra from global analysis of a fsTA data set of the super-photoacid in neutral aceteneous solution for 575 nm excitation, i.e., exciting $RO^-$. **b** Temporal decay of the anisotropy in the ESA (black, probe wavelength 450 nm) and SE/GSB region (blue, probe wavelength 580 nm) of $RO^-$*; note the logarithmic abscissa and the residuals as a measure of the fit quality. **c** Transient spectra at 4 ns pump–probe delay for the neutral solution after excitation at 575 nm (black) or 445 nm (red). For comparison, the SE profile of $RO^{-*}$ is shown in blue and the absorption spectrum of $RO^-$ is shown in purple. Vertical lines indicate the spectral positions of the maxima

the $RO^-$ and the $RO^{-}$* form are similar or at least that the rearrangement is not connected to large energetic changes, as can be rationalized since both the ground-state and the excited-state species are anionic.

HPTS and derivatives can exhibit a pronounced vibronic progression both in the absorption and the emission spectrum and both in the protonated and deprotonated form. Clear vibronic signatures are found in solvents with a low ability to donate a hydrogen bond, whereas the spectra are basically structureless if the solvent is a good hydrogen-bond donor [88]. In the low-energy part of the electronic absorption spectrum, two electronic states contribute which can mix significantly and may contribute differently to the vibronic structure [88]. In our data (Fig. 1d, g, and 2a), the decay dynamics (excluding the sub-100 ps contribution associated with solvation) are identical and mono-exponential with a time constant of around 6.9 ns for all emission/probe wavelengths (Fig. 3a).

Repetition of the experiments with different polarization conditions for the pump and probe beams has indicated further dynamics on the order of several tens of picoseconds. This behavior points towards rotational diffusion of the super-photoacid in the acetoneous environment. To clarify this point, measurements with parallel [signal intensity $I_{||}(t)$] and perpendicular [$I_{\perp}(t)$] pump and probe polarization directions have been performed and the anisotropy [72, 75, 89–98]

$$r(t) = \frac{I_{||}(t) - I_{\perp}(t)}{I_{||}(t) + 2I_{\perp}(t)}$$

was derived for the full spectral range covering all features. A global mono-exponential fit to the anisotropy data describes these sufficiently well with an optimized decay time constant of 73 ps (see transient anisotropy data at two exemplary probe wavelengths in Fig. 3b). This time constant is assigned to rotational diffusion, and under the approximation of a spherical solute (which is a simplification, but for instance an oblate rotor would already give rise to biexponential rotational behavior) [90] leads to an estimation of a molecular diameter of roughly 1.2 nm.

### 4.2 Population dynamics of ROH*

The emission signal of the excited photoacid ROH* observed at 480 nm (Fig. 1k, l) exhibits a mono-exponential decay with a time constant of 4.0 ns. Specifically, we do not observe a non-exponential contribution which would be characteristic of an excited-state geminate recombination process, i.e., that the proton is transferred to an acetone molecule but can come back to form ROH* again [16, 24, 25]. We thus omit the occurrence of excited-state geminate recombination and conclude that ROH* is depopulated with an overall rate $k_{rad}+k_{PT}=(4.0\ ns)^{-1}$ in acetoneous environment. The fsTA data (Fig. 2b, c) contains this information as well, further reflected not only in the SE but also in the ESA dynamics. The depopulation of ROH* is thus much slower than in water (ca. 3 ps) [16], methanol (0.12 ns) [16], ethanol (0.2 ns) [16], or DMSO (0.8 ns) [15], as a consequence of the reduced excited-state acidity in acetone, which is the reason why many photoacids will not perform an ESPT in acetone at all.

### 4.3 Differences in the $RO^-$ spectral region depending on pumped species

The pump wavelength determines which species are excited, but due to the ESPT, also the emergence of newly formed

transient signals depends on the excitation. We focus on the fsTA data in the spectral region from 560 to 700 nm and juxtapose in Fig. 3c the difference spectra for a time delay of 4 ns extracted from Fig. 2a, b to the steady-state absorption of $RO^-$ and the emission of $RO^{-}$* (converted from fluorescence to stimulated emission).

For the case of the neutral solution excited with 575 nm, no contribution from ROH* is expected and the difference spectrum (black curve in Fig. 3c) comprises both GSB of $RO^-$ and SE of $RO^{-}$*. Hence, the spectral peak position is not at the maximum emission wavelength of 575 nm but lower due to the GSB contribution. If the same solution is excited with 445 nm, the predominant signal originates from $RO^{-}$* molecules that were formed from ROH* by ESPT. These $RO^{-}$* molecules contribute an SE signal but no GSB signal. By contrast, when already relaxed to the ground state, a positive absorption caused by these newly formed $RO^-$ molecules is added, partially canceling the blue edge of the SE of the $RO^{-}$* molecules. Hence, the peak in the difference spectrum (red curve in Fig. 3c) is positioned further to the red and closer to the maximum of the $RO^{-}$* emission (blue curve in Fig. 3c). Furthermore, there is also a broad underlying contribution of SE from ROH* molecules reaching out to this spectral regime (compare Fig. 1b and Reference [21]).

### 4.4 Comparison to a methylated analogue

For assignment of the different signal contributions, it is advantageous to also study the methylated analogue tris(1,1,1,3,3,3-hexafluoropropan-2-yl)8-methoxypyrene-1,3,6-trisulfonate, i.e., where the hydroxy group is replaced by a methoxy group and therefore no ESPT is possible. Figure 4 shows the corresponding fsTA data, together with the temporal decay of the anisotropy and the quantum-chemically geometry-optimized structure. Besides solvation dynamics within the first few ps, long-lived signals are observed. The GSB is accompanied by two ESA signals, one at lower (ca. 350 nm) and one at higher (ca. 550 nm) wavelengths. These signals are analogous to those for ROH* in Fig. 2b, c, and the measurements corroborate that the latter are not related to any ESPT process. Nonetheless, also since the spectral positions of absorption and emission are blue-shifted for ROMe compared to ROH [21], the spectral position of the low-frequency ESA signal differs for ROH* and ROMe*, being centered towards 550 nm for ROMe* but below 500 nm for ROH* (see next section). Furthermore, a mono-exponential fit to the anisotropy data for ROMe* (Fig. 4b) yields a rotational diffusion time of 68 ps that matches within error the 73 ps obtained for $RO^{-}$* (Fig. 3b). We note that the slight difference might be associated with $RO^{-}$* being anionic, whereas ROMe* is not. Thus, we conclude that ROMe* and $RO^{-}$* (and probably also ROH*, for which anisotropy was not explicitly measured) behave alike in a fashion similar to a spherical rotor (Fig. 4c). In particular, for the case of $RO^{-}$*, no indications for a strongly bound counter ion or a solvent shell rotating with the solute are found.

### 4.5 Approach to disassemble the fsTA data

If several different species are involved and solvation is pronounced, global analysis is tedious and comprises several derivative-like features (as the black curve in Fig. 3a) to mimic spectral shifts [76–80]. Thus, instead of a global fit to the fsTA data for ROH excitation, we here do not want to

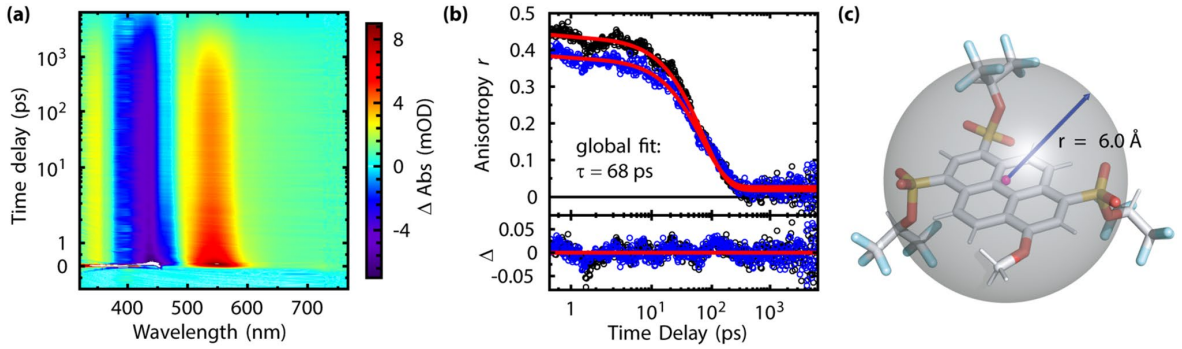



**Fig. 4** Studies for the methylated analogue ROMe [structure in panel **c**] in (neutral) acetoneous solution for 405 nm excitation. **a** Data from fsTA experiments; note the lin-log time axis (linear up to 2 ps, logarithmic afterwards) chosen to better visualize the characteristic time scales. **b** Temporal decay of the anisotropy in the ESA (blue, probe wavelength 548 nm) and SE/GSB region (black, probe wavelength 427 nm) of ROMe*; note the logarithmic abscissa and the residuals as a measure of the fit quality. **c** Geometry of ROMe, quantum-chemically optimized at the semi-empirical AM1 level of theory (carbons in grey, hydrogens in white, oxygens in red, sulfurs in yellow and fluorines in cyan). A sphere with a diameter of 1.2 nm, as deduced from the rotational diffusion time under the assumption of a spherical rotor, is plotted for comparison

fit but rather to reconstruct it systematically by separately addressing the different signal components and subsequently adding them up. For this, we have to identify how many components contribute and what the associated time scales and underlying processes (ESPT, solvation shift, ground-state refilling, etc.) are.

In the scheme derived from the original Förster cycle that we will also use here, there are just two excited-state species, ROH* and $RO^-$*, and the corresponding ground-state species, ROH and $RO^-$, respectively (Fig. 1c). To describe ESPT, population can go directly from ROH* to $RO^-$* with a characteristic rate. In literature, this picture was extended in analogy to the Eigen-Weller reaction scheme for bimolecular acid-base reactions to involve a contact ion pair, produced by an initial short-range proton transfer and composed of $RO^-$* and the dissociated proton in close proximity. Only in a second step, the ions separate via diffusion, which is why this model is called two-step model. Huppert and coworkers [32, 33] further augmented the two-step model by including an additional intermediate of the diffusive separation, a solvent-separated ion pair which is formed if only few solvent molecules have inserted in between the ions, still being held together by Coulombic interactions. Furthermore, if the photoacid and the proton acceptor are not in direct proximity prior to excitation, the (diffusive) formation of an encounter complex will constitute the first step. These models could well describe rather fast ESPT processes, and the individual intermediates could be identified in several experiments.

Here, we know that the photoacid under investigation is only of moderate strength in acetone and that ESPT occurs on the nanosecond time scale. Our previous study has clearly revealed the existence of complexes and hydrogen-bonded ion pairs with water molecules in the case of binary solvent environments of acetone and water, but also showed the distinctly different behavior for neat acetone [21]. Hence, we do not explicitly consider the ion separation step, nor do we have to take geminate recombination into account, as is corroborated by a mono-exponential emission decay rather than a non-exponential behavior [25]. Proton-induced quenching, as observed for instance in naphthols as another non-radiative process [10, 12, 22, 99–102], is unlikely to occur in the investigated system since the solvent is aprotic and the solute could only be quenched by a proton it has just transferred, a process that seems unlikely if even geminate recombination is marginal, an interpretation also supported by the high fluorescence yield. [15]

For modeling the fsTA of Fig. 2c, we thus take the model of Fig. 1c and identify six spectral contributions: the GSB of the ROH form ($RO^-$ is not present and hence not directly excited), the ESA and SE signals of ROH* and of $RO^-$* formed after ESPT, respectively, and the $RO^-$ ground-state absorption (GSA) from molecules formed from ROH via the ESPT pathway. In addition, the solvation shift is included by the characteristic time constants (0.187 ps and 1.09 ps) and relative amplitudes (0.565 and 0.435) reported in Reference [85].

We derive the individual absorption spectral profiles from the steady-state data (Fig. 1b), ESA signals are estimated from the fsTA data sets and approximated by Gaussians. As is known for pyranine and also evident from the data in Fig. 2, the ESA of the $RO^-$* is blue-shifted relative to the major ESA signal of ROH* [37, 44]. For the spectral SE profiles of the ROH* and $RO^-$* form, respectively, the emission spectrum after exciting ROH in an acidic solution is first interpolated, then divided into contributions from the ROH* and $RO^-$* form by subtracting, after reasonable rescaling, the spectrum of the base form excited at 561 nm (Fig. 1g), and finally transferred from fluorescence to SE profiles by applying the $\lambda^4$ correction related to the differences in the corresponding Einstein coefficients [103, 104]. These normalized spectral profiles are displayed in Fig. 5a. Importantly, these spectra are shown prior to putative spectral shifts, hence we assume that the spectral profile of the components does not change but spectrally shifts and grows/decreases with time. As a consequence, the SE signal of ROH* is shown with its maximum at the ROH absorption around 440 nm, i.e., mimicking SE from the Franck-Condon point directly after excitation, which will shift towards the center of the static ROH* fluorescence at 488 nm with the parameters of the solvation process. The same holds for the red-edge ESA signal which undergoes a solvation shift (in contrast to the blue-edge ESA or the ESA of the $RO^-$*, compare Fig. 2 and discussion below). The GSB dynamics remaining beyond the temporal window of the fsTA setup are estimated from the decay constant of the ESA of ROH* and the emission lifetime of ROMe* [21]. With the spectral profiles and determined time scales fixed, the amplitudes of the components are adjusted so that the fsTA data is adequately reproduced. The result is shown in Fig. 5, with the sum of all components (Fig. 5h) being in good accordance with the experiment (Fig. 2c, again plotted in Fig. 5i to allow a direct comparison).

While the spectral signatures of the individual components are already quite well separated for the super-photoacid, the advantage of this approach is that one can plot each contribution individually, as is done in panels b to g of Fig. 5. The analysis shows that the ESA and the SE of ROH* overlap and shift in opposite directions, as also reported for HPTA [30]. The shifts here are so pronounced that the two bands "shift through" each other, i.e. initially after excitation, SE is at shorter wavelengths than ESA, while it is the opposite on long time scales. After several nanoseconds, the signatures of $RO^-$* grow in, leading to the observed overall blue-shift of ESA in the spectral region 450–500 nm. In the spectral region above 560 nm, a decreasing SE signal of ROH* and a rising one from $RO^-$* contribute, overlapped

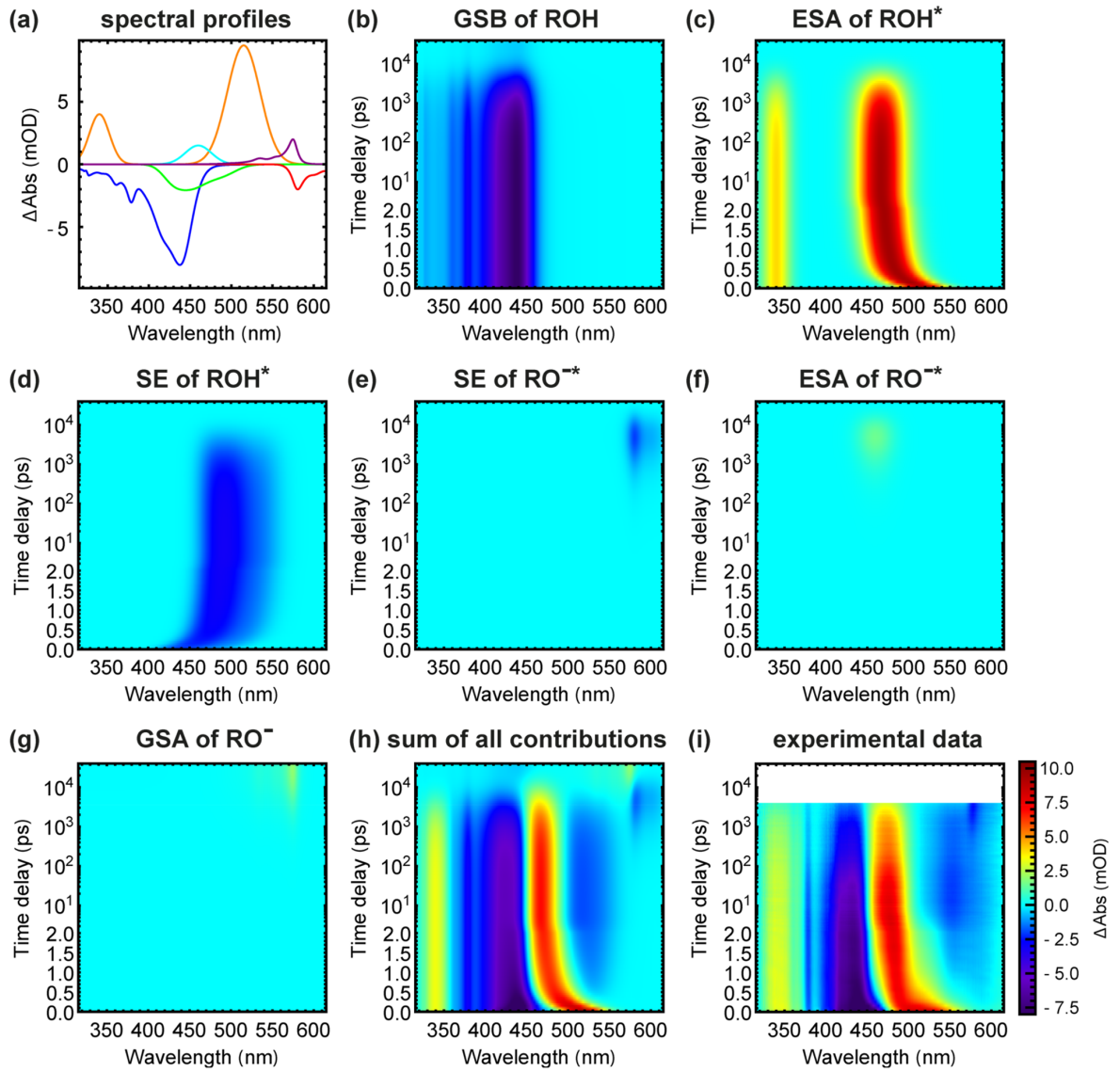



**Fig. 5** Modeling the fsTA data shown in Fig. 2c. **a** Individual spectral profiles comprising the GSB of ROH (blue), the ESA of ROH* (orange), the ESA of $RO^-$* (cyan), the SE of ROH* (green), the SE of $RO^-$* (red), and the GSA of $RO^-$ (purple). **b** GSB of ROH; **c** ESA of ROH*; **d** SE of ROH*; **e** SE of $RO^-$*; **f** ESA of $RO^-$*; **g** GSA of $RO^-$ (assuming re-protonation of $RO^-$ to ROH is negligible on the displayed time scale). **h** Modeled transient absorption data combining individual transient features shown in (b-g). **i** Experimental data from Fig. 2c for comparison. Note that the simulations go out to 40 ns, while the fsTA experiment only goes to 4 ns; the time delay axis is logarithmic from 2 ps to 40 ns

with an absorption signal of newly formed $RO^-$ molecules (which is not evident in the fsTA data of Fig. 5i as $RO^-$* rises with 4.0 ns and decays with 6.9 ns, but the fsTA data does not exceed delay times of 4 ns). Importantly, there is no contribution of GSB of $RO^-$, as none of these molecules were initially present in the acidic solution (as discussed above for Fig. 3c).

The ESA of ROH* (Fig. 5c) comprises two contributions, where only the one at the higher-wavelength shows a solvation shift. The ESA at lower wavelength behaves in analogy to the ESA of $RO^-$* (Fig. 3a), thus, is blue-shifted with respect to the GSB and does not show any solvation shift. From this, we conclude that the lower wavelength signal is the analogous ESA of ROH*. The presence of

corresponding ESA signals for ROMe* (Fig. 4a) corroborates this assignment.

The agreement between the modeled (Fig. 5h) and the experimental (Fig. 5i) data suggests that the main involved species and associated signals are covered, although our approach is not a fit but rather an adjusted qualitative model, yet the occurrence of pronounced signals from putative species not considered would become apparent. Hence, we conclude that during the ESPT dynamics in acetoneous environment, no intermediate species like ion pairs emerge to a conspicuous degree or at least do not cause pronounced transient signals. As these species can be identified when small amounts of water are added to the solution [21], their absence in the here reported experimental data support ESPT to acetone to a low extent.

## 5 Conclusion

This ultrafast spectroscopy study unveils the excited-state proton-transfer dynamics of an extraordinarily strong photoacid in the aprotic solvent acetone—an environment which, due to weaker proton-transfer capabilities of other photoacids, could not be investigated in most of the existing studies on photoacidity. Direct excitation of the anion $RO^-$ revealed that there are solvation dynamics on a ps time scale which are characteristic for acetoneous environments, and rotational diffusion occurs with a time constant of about 70 ps, suggesting a diameter of the solute of 1.2 nm. Elucidation of the dynamics after ROH excitation is realized by investigating neutral and acidic acetoneous solutions of the photoacid and comparison to the methylated analogue. Since various positive and negative signals superpose in the fsTA data, a decomposition into individual signal contributions was pursued in order to unravel the contributing components. These studies corroborate the potential of this particularly strong super-photoacid to be exploited as light-triggered proton donor in experimental conditions where this is unfeasible otherwise. Future studies will address ESPT dynamics under even harsher conditions, achievable with magic photoacids [105].

**Acknowledgements** We thank PicoQuant GmbH, Berlin, for the loan of the laser diode head LDH-D-TA-560. We furthermore thank Dr. Sebastian Goetz for providing the photographic images for Figure 1a and for the artwork of the graphical abstract. Different aspects of this work were supported by the Deutsche Forschungsgemeinschaft (DFG, German Research Foundation) within the Research Training Group "Confinement-controlled Chemistry" (Grant GRK2376, Project 331085229), through Grant JU 650/8-1, and under Germany's Excellence Strategy EXC 2033—390677874—RESOLV.

**Funding** Open Access funding enabled and organized by Projekt DEAL.

## Declarations

**Conflict of interest** The authors declare that there is no conflict of interest.

**Open Access** This article is licensed under a Creative Commons Attribution 4.0 International License, which permits use, sharing, adaptation, distribution and reproduction in any medium or format, as long as you give appropriate credit to the original author(s) and the source, provide a link to the Creative Commons licence, and indicate if changes were made. The images or other third party material in this article are included in the article's Creative Commons licence, unless indicated otherwise in a credit line to the material. If material is not included in the article's Creative Commons licence and your intended use is not permitted by statutory regulation or exceeds the permitted use, you will need to obtain permission directly from the copyright holder. To view a copy of this licence, visit http://creativecommons.org/licenses/by/4.0/.

## References

1. Trieff, N. M., & Sundheim, B. R. (1965). The effect of solvent on the acid-base kinetics of the excited state of β-naphthol. *The Journal of Physical Chemistry, 69*, 2044–2059.
2. Weber, K. (1931). Über die enge Beziehung der Fluorescenzauslöschung zur Hemmung photochemischer Reaktionen. *Zeitschrift für Physikalische Chemie, 15B*, 18–44.
3. Förster, T. (1949). Fluoreszenzspektrum und Wasserstoffionenkonzentration. *Naturwissenschaften 36*, 186–187.
4. Förster, T. (1950). Elektrolytische Dissoziation angeregter Moleküle. *Zeitschrift für Elektrochemie und angewandte physikalische Chemie, 54*, 42–46.
5. Braslavsky, S. E. (2007). Glossary of terms used in photochemistry, 3rd edition (IUPAC Recommendations 2006). *Pure and Applied Chemistry, 79*, 293–465.
6. Marx, D., Tuckerman, M. E., Hutter, J., & Parrinello, M. (1999). The nature of the hydrated excess proton in water. *Nature, 397*, 601–604.
7. Agmon, N. (1999). Proton solvation and proton mobility. *Israel Journal of Chemistry, 39*, 493–502.
8. Kornyshev, A. A., Kuznetsov, A. M., Spohr, E., & Ulstrup, J. (2003). Kinetics of proton transport in water. *The Journal of Physical Chemistry B, 107*, 3351–3366.
9. Knight, C., & Voth, G. A. (2012). The curious case of the hydrated proton. *Accounts of Chemical Research, 45*, 101–109.
10. Solntsev, K. M., Huppert, D., & Agmon, N. (1999). Photochemistry of "super"-photoacids. Solvent effects. *The Journal of Physical Chemistry A, 103*, 6984–6997.
11. Simkovitch, R., Shomer, S., Gepshtein, R., & Huppert, D. (2015). How fast can a proton-transfer reaction be beyond the solvent-control limit? *The Journal of Physical Chemistry B, 119*, 2253–2262.
12. Tolbert, L. M., & Solntsev, K. M. (2002). Excited-state proton transfer: From constrained systems to "super" photoacids to superfast proton transfer. *Accounts of Chemical Research, 35*, 19–27.
13. Simkovitch, R., et al. (2013). Ultrafast excited-state proton transfer from hydroxycoumarin-dipicolinium cyanine dyes. *Journal of Photochemistry and Photobiology A: Chemistry, 254*, 45–53.
14. Spies, C., Finkler, B., Acar, N., & Jung, G. (2013). Solvatochromism of pyranine-derived photoacids. *Physical Chemistry Chemical Physics, 15*, 19893–19905.

15. Finkler, B., et al. (2014). Highly photostable "super"-photoacids for ultrasensitive fluorescence spectroscopy. *Photochemical & Photobiological Sciences, 13*, 548–562.
16. Spies, C., et al. (2014). Solvent dependence of excited-state proton transfer from pyranine-derived photoacids. *Physical Chemistry Chemical Physics, 16*, 9104–9114.
17. Kumpulainen, T., Rosspeintner, A., Dereka, B., & Vauthey, E. (2017). Influence of solvent relaxation on ultrafast excited-state proton transfer to solvent. *The Journal of Physical Chemistry Letters, 8*, 4516–4521.
18. Verma, P., Rosspeintner, A., Dereka, B., Vauthey, E., & Kumpulainen, T. (2020). Broadband fluorescence reveals mechanistic differences in excited-state proton transfer to protic and aprotic solvents. *Chemical Science, 11*, 7963–7971.
19. Solntsev, K. M., Huppert, D., Agmon, N., & Tolbert, L. M. (2020). Photochemistry of "super" photoacids. 2. Excited-state proton transfer in methanol/water mixtures. *The Journal of Physical Chemistry A, 104*, 4658–4669.
20. Pérez-Lustres, J. L., et al. (2007). Ultrafast proton transfer to solvent: Molecularity and intermediates from solvation- and diffusion-controlled regimes. *Journal of the American Chemical Society, 129*, 5408–5418.
21. Sülzner, N., Geissler, B., Grandjean, A., Jung, G., & Nuernberger, P. (2022). Excited-state proton transfer dynamics of a super-photoacid in acetone-water mixtures. *ChemPhotoChem, 6*, e202200041.
22. Prémont-Schwarz, M., Barak, T., Pines, D., Nibbering, E. T. J., & Pines, E. (2013). Ultrafast excited-state proton-transfer reaction of 1-naphthol-3,6-disulfonate and several 5-substituted 1-naphthol derivatives. *The Journal of Physical Chemistry B, 117*, 4594–4603.
23. Corani, A., et al. (2013). Excited-state proton-transfer processes of DHICA resolved: From sub-picoseconds to nanoseconds. *Journal of Physical Chemistry Letters, 4*, 1383–1388.
24. Pines, E., & Huppert, D. (1986). Geminate recombination proton-transfer reactions. *Chemical Physics Letters, 126*, 88–91.
25. Pines, E., Huppert, D., & Agmon, N. (1988). Geminate recombination in excited-state proton-transfer reactions: Numerical solution of the Debye-Smoluchowski equation with backreaction and comparison with experimental results. *The Journal of Chemical Physics, 88*, 5620–5630.
26. Pines, E., & Huppert, D. (1989). Salt effect in photoacid quantum yield measurements: A demonstration of the geminate recombination role in deprotonation reactions. *Journal of the American Chemical Society, 111*, 4096–4097.
27. Tran-Thi, T.-H., Gustavsson, T., Prayer, C., Pommeret, S., & Hynes, J. T. (2000). Primary ultrafast events preceding the photoinduced proton transfer from pyranine to water. *Chemical Physics Letters, 329*, 421–430.
28. Tran-Thi, T.-H., Prayer, C., Millié, Ph., Uznanski, P., & Hynes, J. T. (2002). Substituent and solvent effects on the nature of the transitions of pyrenol and pyranine. Identification of an intermediate in the excited-state proton-transfer reaction. *The Journal of Physical Chemistry A, 106*, 2244–2255.
29. Mohammed, O. F., Dreyer, J., Magnes, B.-Z., Pines, E., & Nibbering, E. T. J. (2005). Solvent-dependent photoacidity state of pyranine monitored by transient mid-infrared spectroscopy. *ChemPhysChem, 6*, 625–636.
30. Pines, E., Pines, D., Ma, Y.-Z., & Fleming, G. R. (2004). Femtosecond pump-probe measurements of solvation by hydrogen-bonding interactions. *ChemPhysChem, 5*, 1315–1327.
31. Mondal, S. K., et al. (2005). Excited state proton transfer of pyranine in a γ-cyclodextrin cavity. *Chemical Physics Letters, 412*, 228–234.
32. Gepshtein, R., Leiderman, P., Genosar, L., & Huppert, D. (2005). Testing the three step excited state proton transfer model by the effect of an excess proton. *The Journal of Physical Chemistry A, 109*, 9674–9684.
33. Leiderman, P., Genosar, L., & Huppert, D. (2005). Excited-state proton transfer: Indication of three steps in the dissociation and recombination process. *The Journal of Physical Chemistry A, 109*, 5965–5977.
34. Mohammed, O. F., Pines, D., Nibbering, E. T., & Pines, E. (2007). Base-induced solvent switches in acid-base reactions. *Angewandte Chemie International Edition, 46*, 1458–1461.
35. Spry, D. B., Goun, A., Glusac, K., Moilanen, D. E., & Fayer, M. D. (2007). Proton transport and the water environment in nafion fuel cell membranes and AOT reverse micelles. *Journal of the American Chemical Society, 129*, 8122–8130.
36. Spry, D. B., Goun, A., & Fayer, M. D. (2007). Deprotonation dynamics and Stokes shift of pyranine (HPTS). *The Journal of Physical Chemistry A, 111*, 230–237.
37. Spry, D. B., & Fayer, M. D. (2007). Observation of slow charge redistribution preceding excited-state proton transfer. *The Journal of Chemical Physics, 127*, 204501.
38. Spry, D. B., & Fayer, M. D. (2008). Charge redistribution and photoacidity: Neutral versus cationic photoacids. *The Journal of Chemical Physics, 128*, 084508.
39. Tielrooij, K. J., Cox, M. J., & Bakker, H. J. (2009). Effect of confinement on proton-transfer reactions in water nanopools. *ChemPhysChem, 10*, 245–251.
40. Cohen, B., Martin Álvarez, C., Alarcos Carmona, N., Organero, J. A., & Douhal, A. (2011). Proton-transfer reaction dynamics within the human serum albumin protein. *The Journal of Physical Chemistry B, 115*, 7637–7647.
41. Carmona, N. A., Cohen, B., Organero, J. A., & Douhal, A. (2012). Excited state intermolecular proton and energy transfer of 1-hydroxypyrene interacting with the human serum albumin protein. *Journal of Photochemistry and Photobiology A: Chemistry, 234*, 3–11.
42. Wang, Y., et al. (2013). Early time excited-state structural evolution of pyranine in methanol revealed by femtosecond stimulated Raman spectroscopy. *The Journal of Physical Chemistry A, 117*, 6024–6042.
43. Han, F., Liu, W., & Fang, C. (2013). Excited-state proton transfer of photoexcited pyranine in water observed by femtosecond stimulated Raman spectroscopy. *Chemical Physics, 422*, 204–219.
44. Liu, W., et al. (2016). Panoramic portrait of primary molecular events preceding excited state proton transfer in water. *Chemical Science, 7*, 5484–5494.
45. Alarcos, N., Cohen, B., & Douhal, A. (2016). A slowing down of proton motion from HPTS to water adsorbed on the MCM-41 surface. *Physical Chemistry Chemical Physics, 18*, 2658–2671.
46. Agmon, N., et al. (2016). Protons and hydroxide ions in aqueous systems. *Chemical Reviews, 116*, 7642–7672.
47. Hoberg, C., et al. (2021). Caught in the act: Observation of the solvent response triggered by excited-state proton transfer in real time. *ChemRxiv*. https://doi.org/10.33774/chemrxiv-2021-60zjv
48. Eckert, S., et al. (2022). Electronic structure changes of an aromatic amine photoacid along the Förster cycle. *Angewandte Chemie International Edition, 67*, e202200709.
49. Pines, E., Magnes, B.-Z., Lang, M. J., & Fleming, G. R. (1997). Direct measurement of intrinsic proton transfer rates in diffusion-controlled reactions. *Chemical Physics Letters, 281*, 413–420.
50. Genosar, L., Cohen, B., & Huppert, D. (2000). Ultrafast direct photoacid−base reaction. *The Journal of Physical Chemistry A, 104*, 6689–6698.
51. Rini, M., Magnes, B.-Z., Pines, E., & Nibbering, E. T. J. (2003). Real-time observation of bimodal proton transfer in acid-base pairs in water. *Science, 301*, 349–352.

52. Rini, M., Pines, D., Magnes, B.-Z., Pines, E., & Nibbering, E. T. J. (2004). Bimodal proton transfer in acid-base reactions in water. *The Journal of Chemical Physics, 121*, 9593–9610.
53. Nibbering, E. T. J., Fidder, H., & Pines, E. (2005). Ultrafast chemistry: Using time-resolved vibrational spectroscopy for interrogation of structural dynamics. *Annual Review of Physical Chemistry, 56*, 337–367.
54. Mohammed, O. F., Pines, D., Dreyer, J., Pines, E., & Nibbering, E. T. J. (2005). Sequential proton transfer through water bridges in acid-base reactions. *Science, 310*, 83–86.
55. Pines, D., Nibbering, E. T. J., & Pines, E. (2007). Relaxation to equilibrium following photoacid dissociation in mineral acids and buffer solutions. *Journal of Physics: Condensed Matter, 19*, 065134.
56. Siwick, B. J., & Bakker, H. J. (2007). On the role of water in intermolecular proton-transfer reactions. *Journal of the American Chemical Society, 129*, 13412–13420.
57. Siwick, B. J., Cox, M. J., & Bakker, H. J. (2008). Long-range proton transfer in aqueous acid−base reactions. *The Journal of Physical Chemistry B, 112*, 378–389.
58. Cox, M. J., & Bakker, H. J. (2008). Parallel proton transfer pathways in aqueous acid-base reactions. *The Journal of Chemical Physics, 128*, 174501.
59. Cox, M. J., Timmer, R. L. A., Bakker, H. J., Park, S., & Agmon, N. (2009). Distance-dependent proton transfer along water wires connecting acid−base pairs. *The Journal of Physical Chemistry A, 113*, 6599–6606.
60. Liu, W., Han, F., Smith, C., & Fang, C. (2012). Ultrafast conformational dynamics of pyranine during excited state proton transfer in aqueous solution revealed by femtosecond stimulated Raman spectroscopy. *The Journal of Physical Chemistry B, 116*, 10535–10550.
61. Oscar, B. G., Liu, W., Rozanov, N. D., & Fang, C. (2016). Ultrafast intermolecular proton transfer to a proton scavenger in an organic solvent. *Physical Chemistry Chemical Physics, 18*, 26151–26160.
62. Sheng, W., et al. (2018). Ultrafast dynamics of a "Super" photobase. *Angewandte Chemie International Edition, 57*, 14742–14746.
63. Hunt, J. R., & Dawlaty, J. M. (2018). Photodriven deprotonation of alcohols by a quinoline photobase. *The Journal of Physical Chemistry A, 122*, 7931–7940.
64. Sittig, M., Tom, J. C., Elter, J. K., Schacher, F. H., & Dietzek, B. (2021). Quinoline photobasicity: Investigation within water-soluble light-responsive copolymers. *Chemistry–A European Journal, 27*, 1072–1079.
65. Vester, M., Grueter, A., Finkler, B., Becker, R., & Jung, G. (2016). Biexponential photon antibunching: Recombination kinetics within the Förster-cycle in DMSO. *Physical Chemistry Chemical Physics, 18*, 10281–10288.
66. Vester, M., Staut, T., Enderlein, J., & Jung, G. (2015). Photon antibunching in a cyclic chemical reaction scheme. *The Journal of Physical Chemistry Letters, 6*, 1149–1154.
67. Offenbacher, H., Wolfbeis, O. S., & Fürlinger, E. (1986). Fluorescence optical sensors for continuous determination of near-neutral pH values. *Sensors and Actuators, 9*, 73–84.
68. Clasen, A., et al. (2019). Kinetic and spectroscopic responses of pH-sensitive nanoparticles: Influence of the silica matrix. *RSC Advances, 9*, 35695–35705.
69. Grandjean, A., Pérez Lustres, J. L., Muth, S., Maus, D., & Jung, G. (2021). Steady-state spectroscopy to single out the contact ion pair in excited-state proton transfer. *The Journal of Physical Chemistry Letters, 12*, 1683–1689.
70. Grandjean, A., Pérez Lustres, J. L., & Jung, G. (2021). Solvent-controlled intermolecular proton-transfer follows an irreversible Eigen-Weller model from fs to ns. *ChemPhotoChem 5*, 1094–1105.
71. Megerle, U., Pugliesi, I., Schriever, C., Sailer, C. F., & Riedle, E. (2009). Sub-50 fs broadband absorption spectroscopy with tunable excitation: Putting the analysis of ultrafast molecular dynamics on solid ground. *Applied Physics B, 96*, 215–231.
72. Schott, S., Steinbacher, A., Buback, J., Nuernberger, P., & Brixner, T. (2014). Generalized magic angle for time-resolved spectroscopy with laser pulses of arbitrary ellipticity. *Journal of Physics B: Atomic, Molecular and Optical Physics, 47*, 124014.
73. Ruetzel, S., Kullmann, M., Buback, J., Nuernberger, P., & Brixner, T. (2013). Tracing the steps of photoinduced chemical reactions in organic molecules by coherent two-dimensional electronic spectroscopy using triggered exchange. *Physical Review Letters, 110*, 148305.
74. Selig, U., et al. (2013). Similarities and differences in the optical response of perylene-based hetero-bichromophores and their monomeric units. *ChemPhysChem, 14*, 1413–1422.
75. van Stokkum, I. H., Larsen, D. S., & van Grondelle, R. (2004). Global and target analysis of time-resolved spectra. *Biochimica et Biophysica Acta (BBA)-Bioenergetics, 1657*, 82–104.
76. Marciniak, H., & Lochbrunner, S. (2014). On the interpretation of decay associated spectra in the presence of time dependent spectral shifts. *Chemical Physics Letters, 609*, 184–188.
77. Consani, C., Berberich, M., Würthner, F., & Brixner, T. (2017). Ultrafast isomerization in a difluoroboryl-coordinated molecular switch. *Chemical Physics Letters, 683*, 83–90.
78. Bolze, T., Wree, J.-L., Kanal, F., Schleier, D., & Nuernberger, P. (2018). Ultrafast dynamics of a fluorescent tetrazolium compound in solution. *ChemPhysChem, 19*, 138–147.
79. Khah, A. M., Grimmelsmann, L., Knorr, J., Nuernberger, P., & Hättig, C. (2018). How a linear triazene photoisomerizes in a volume-conserving fashion. *Physical Chemistry Chemical Physics, 20*, 28075–28087.
80. Brandl, F., Bergwinkl, S., Allacher, C., & Dick, B. (2020). Consecutive photoinduced electron transfer (conPET): The mechanism of the photocatalyst rhodamine 6G. *Chemistry–A European Journal 26*, 7946–7954.
81. Schott, S., Ress, L., Hrušák, J., Nuernberger, P., & Brixner, T. (2016). Identification of photofragmentation patterns in trihalide anions by global analysis of vibrational wavepacket dynamics in broadband transient absorption data. *Physical Chemistry Chemical Physics, 18*, 33287–33302.
82. van Stokkum, I. H. M., et al. (2016). Estimation of damped oscillation associated spectra from ultrafast transient absorption spectra. *The Journal of Chemical Physics, 145*, 174201.
83. Braver, Y., Gelzinis, A., Chmeliov, J., & Valkunas, L. (2019). Application of decay- and evolution-associated spectra for molecular systems with spectral shifts or inherent inhomogeneities. *Chemical Physics, 525*, 110403.
84. Beckwith, J. S., Rumble, C. A., & Vauthey, E. (2020). Data analysis in transient electronic spectroscopy—an experimentalist's view. *International Reviews in Physical Chemistry, 39*, 135–216.
85. Horng, M. L., Gardecki, J. A., Papazyan, A., & Maroncelli, M. (1995). Subpicosecond measurements of polar solvation dynamics: Coumarin 153 revisited. *The Journal of Physical Chemistry, 99*, 17311–17337.
86. Dobryakov, A. L., Pérez Lustres, J. L., Kovalenko, S. A., & Ernsting, N. P. (2008). Femtosecond transient absorption with chirped pump and supercontinuum probe: Perturbative calculation of

transient spectra with general lineshape functions, and simplifications. *Chemical Physics, 347*, 127–138.
87. Kumpulainen, T., Lang, B., Rosspeintner, A., & Vauthey, E. (2017). Ultrafast elementary photochemical processes of organic molecules in liquid solution. *Chemical Reviews, 117*, 10826–10939.
88. Spry, D. B., Goun, A., Bell, C. B., & Fayer, M. D. (2006). Identification and properties of the $^1L_a$ and $^1L_b$ states of pyranine. *The Journal of Chemical Physics, 125*, 144514.
89. Lessing, H. E., & Von Jena, A. (1976). Separation of rotational diffusion and level kinetics in transient absorption spectroscopy. *Chemical Physics Letters, 42*, 213–217.
90. Fleming, G. R. (1986). *Chemical applications of ultrafast spectroscopy*. Oxford Univ. Press.
91. Jonas, D. M., Lang, M. J., Nagasawa, Y., Joo, T., & Fleming, G. R. (1996). Pump−probe polarization anisotropy study of femtosecond energy transfer within the photosynthetic reaction center of rhodobacter sphaeroides R26. *The Journal of Physical Chemistry, 100*, 12660–12673.
92. Arnett, D. C., Moser, C. C., Dutton, P. L., & Scherer, N. F. (1999). The first events in photosynthesis: Electronic coupling and energy transfer dynamics in the photosynthetic reaction center from rhodobacter sphaeroides. *The Journal of Physical Chemistry B, 103*, 2014–2032.
93. Shaw, G. B., Brown, C. L., & Papanikolas, J. M. (2002). Investigation of interligand electron transfer in polypyridyl complexes of Os(II) using femtosecond polarization anisotropy methods: Examination of $Os(bpy)_3^{2+}$ and $Os(bpy)_2(mab)^{2+}$. *The Journal of Physical Chemistry A, 106*, 1483–1495.
94. Nuernberger, P., Vogt, G., Gerber, G., Improta, R., & Santoro, F. (2006). Femtosecond study on the isomerization dynamics of NK88. I. Ground-state dynamics after photoexcitation. *The Journal of Chemical Physics 125*, 044512.
95. Theisen, M., et al. (2009). Femtosecond polarization resolved spectroscopy: A tool for determination of the three-dimensional orientation of electronic transition dipole moments and identification of configurational isomers. *The Journal of Chemical Physics, 131*, 124511.
96. Nuernberger, P., et al. (2011). Strong ligand-protein interactions revealed by ultrafast infrared spectroscopy of CO in the heme pocket of the oxygen sensor FixL. *Journal of the American Chemical Society, 133*, 17110–17113.
97. Kutta, R. J., Archipowa, N., & Scrutton, N. S. (2018). The sacrificial inactivation of the blue-light photosensor cryptochrome from Drosophila melanogaster. *Physical Chemistry Chemical Physics, 20*, 28767–28776.
98. Gera, R., Meloni, S. L., & Anna, J. M. (2019). Unraveling confined dynamics of guests trapped in self-assembled $Pd_6L_4$ nanocages by ultrafast mid-IR polarization-dependent spectroscopy. *The Journal of Physical Chemistry Letters, 10*, 413–418.
99. Shizuka, H. (1985). Excited-state proton-transfer reactions and proton-induced quenching of aromatic compounds. *Accounts of Chemical Research, 18*, 141–147.
100. Knochenmuss, R., Solntsev, K. M., & Tolbert, L. M. (2001). Molecular beam studies of the "Super" photoacid 5-cyano-2-naphthol in solvent clusters. *The Journal of Physical Chemistry A, 105*, 6393–6401.
101. Cohen, B., Segal, J., & Huppert, D. (2002). Proton transfer from photoacid to solvent. *The Journal of Physical Chemistry A, 106*, 7462–7467.
102. Clower, C., Solntsev, K. M., Kowalik, J., Tolbert, L. M., & Huppert, D. (2002). Photochemistry of "Super" photoacids. 3. Excited-state proton transfer from perfluoroalkylsulfonyl-substituted 2-Naphthols. *The Journal of Physical Chemistry A, 106*, 3114–3122.
103. Deshpande, A. V., Beidoun, A., Penzkofer, A., & Wagenblast, G. (1990). Absorption and emission spectroscopic investigation of cyanovinyldiethylaniline dye vapors. *Chemical Physics, 142*, 123–131.
104. Riedle, E., & Wenninger, M. Time resolved spectroscopy in photocatalysis. in *Chemical Photocatalysis* (ed. König, B.) (De Gruyter, 2013). doi:https://doi.org/10.1515/9783110269246.
105. Maus, D., Grandjean, A., & Jung, G. (2018). Toward magic photoacids: Proton transfer in concentrated sulfuric acid. *The Journal of Physical Chemistry A, 122*, 9025–9030.

# 5. Prediction of Ground-State p$K_a$ in Acetone

This sub-project marks the transition between the experimental part on the ESPT kinetics and the theoretical part on the ESPT thermodynamics of Jung's photoacids in acetone. As introduced before, this work aims at establishing a route to the excited-state p$K_a$ (p$K_a^*$) based on the Förster cycle and uses the ground-state p$K_a$ and the electronic excitation energies to determine p$K_a^*$. Here, to fulfill the first prerequisite, the existing quantum-chemical approach to p$K_a$ based on COSMO-RS (that is known for water, DMSO, and acetonitrile) is extended to acetone. From a technical perspective, this extension consists in determining the respective parameters for a linear free-energy relationship between the calculated $\Delta G_{diss}$ and the experimental p$K_a$ values of a training set. For this, I have collected experimental reference data from the (sparse) literature, computed the $\Delta G_{diss}$ values for each compound of this set using DFT and COSMO-RS calculations, and finally performed a linear regression to obtain the LFER parameters. The results are discussed in the context of the COSMO-RS-based p$K_a$ predictions in the other solvents, in particular with a focus on potentially combining all sub sets in the training set into a single set of compounds (i.e., obtaining generalized LFER parameters).

This part has been performed under the supervision of Prof. Dr. Christof Hättig, who also suggested the idea of using COSMO-RS for p$K_a$ prediction in acetone. Dr. Arnim Hellweg (from BIOVIA) has assisted with setting up the COSMO-RS calculations and resolving technical difficulties and participated in scientific discussions regarding the results. I am responsible for carrying out the calculations, analyzing the results, preparing the first draft of the manuscript (including all figures and tables), and for taking over the correspondence during the publication process. The calculations for the benzenesulfonamides have been performed under my supervision by Julia Haberhauer.

The following open-access publication is reprinted under the terms of CC BY-NC-ND 4.0 and with permission from: N. Sülzner, J. Haberhauer, C. Hättig, and A. Hellweg. Prediction of acid p$K_a$ values in the solvent acetone based on COSMO-RS. *J. Comput. Chem.* **2022**, *43* (15), 1011–1022. **Copyright © 2022 The Authors. *Journal of Computational Chemistry* published by Wiley Periodicals LLC.** The corresponding supporting information can be found in Section B.2. This publication is also available online: `https://doi.org/10.1002/jcc.26864`.

Received: 2 December 2021 | Revised: 25 March 2022 | Accepted: 29 March 2022

DOI: 10.1002/jcc.26864

RESEARCH ARTICLE

Journal of COMPUTATIONAL CHEMISTRY WILEY

# Prediction of acid p$K_a$ values in the solvent acetone based on COSMO-RS

Niklas Sülzner[1] | Julia Haberhauer[1] | Christof Hättig[1] | Arnim Hellweg[2]

[1]Lehrstuhl für Theoretische Chemie, Ruhr-Universität Bochum, Bochum, 44780, Germany

[2]Dassault Systèmes Deutschland GmbH, Am Kabellager 11-15, Köln, 51063, Germany

**Correspondence**
Niklas Sülzner, Lehrstuhl für Theoretische Chemie, Ruhr-Universität Bochum, 44780 Bochum, Germany.
Email: niklas.suelzner@rub.de

**Funding information**
Deutsche Forschungsgemeinschaft, Grant/Award Numbers: Germany's Excellence Strategy - EXC 2033 - 3906778, Project Ha 2588/8-1

## Abstract

In this contribution we extent the use of the conductor-like screening model for realistic solvation (COSMO-RS) to the prediction of p$K_a$ values in acetone, a commonly used dipolar aprotic solvent. For this, we calculated the Gibbs free energy of dissociation of 120 organic acids (nine acrylic acids, 87 benzoic acids, nine phenols, and 15 benzenesulfonamides) using COSMO-RS at the two levels BP-TZVP and BP-TZVPD-FINE and determined the parameters for a linear free energy relation for the p$K_a$ prediction by performing linear fits to experimental values. Our results suggest that the data set dissects into two groups, with the phenols being different from the other three subsets. The acrylic and benzoic acids and the sulfonamides can be treated together and yield an excellent linear correlation ($r^2 > 0.95$) with an RMSD of only ~0.3. The slope is found to be significantly smaller than the theoretical value ($1/RT\ln 10$), only 45% of it, which is in accordance with findings in the literature. The phenols, however, while similarly well correlated in their own subset with an RMSD of 1.7–1.9, exhibit a slope larger than one. We discuss both a higher uncertainty in the reference values as well as physical origins as possible reasons.

KEYWORDS

p$K_a$, acetone, acidity, COSMO-RS, proton transfer

## 1 | INTRODUCTION

Proton transfer is ubiquitous in chemistry and related fields.[1] Among countless examples, its involvement in catalytic[2] and enzymatic[3] reactions or the energy storage using fuel cells[4] are perhaps most noticeable at present. Reflecting this overall high importance, much work has been invested for a long time into the investigation of proton-transfer reactions in general,[5] and the determination of p$K_a$ values or their associated acid dissociation constants in particular.[6] Owing to its central role as the thermodynamic measure of Brønsted acidity, the p$K_a$ has gained widespread attention.

While p$K_a$ determination is nowadays standard in aqueous solution due to a broad variety of well-established experimental techniques for the solvent water,[7] the situation is very different in non-aqueous solution.[8,9] Especially for aprotic organic solvents, the acidity of a compound is usually severely reduced since an aprotic solvent cannot stabilize the corresponding base effectively due to its inherent lack of H-bond donation, which largely hinders the dissociation event. The resulting extremely low acid dissociation constants in combination with other complications such as low solubilities challenge the accuracy of experimental methods.[10] The non-trivial and relatively costly experimental determination is a major reason why

This is an open access article under the terms of the Creative Commons Attribution-NonCommercial-NoDerivs License, which permits use and distribution in any medium, provided the original work is properly cited, the use is non-commercial and no modifications or adaptations are made.
© 2022 The Authors. *Journal of Computational Chemistry* published by Wiley Periodicals LLC.

theoretical p$K_a$ predictions become much more important for solvents other than water.[11,12] Besides and independent from the solvent, computational methods also become crucial for such molecules, for example, reactive intermediates that elude the standard determination because of short lifetimes, difficult isolation, and so forth.

Several computational approaches for p$K_a$ predictions have been established in the literature (e.g., see Reference [12]), including quantum chemical approaches that avoid the costly direct sampling over a statistically representative number of solvent configurations, as done in molecular dynamics simulations with explicit solvent. These studies typically utilize the polarizable continuum model (PCM) to include implicit, that is, bulk solvation effects.[13] PCM belongs to the family of dielectric continuum solvation models (DCSMs, for an overview see, for example, Reference [14]) and is closely related to the conductor-like screening model (COSMO).[15–17] When applying DCSMs to p$K_a$ prediction, a linear free-energy relation (LFER) between the p$K_a$ value and the Gibbs free energy change of dissociation ($\Delta G_{diss}$) is usually employed

$$pK_a = c_1 \frac{\Delta G_{diss}}{RT\ln(10)} + c_0 \quad (1)$$

(with the ideal gas constant $R$, absolute temperature $T$, slope $c_1$ and intercept $c_0$), illustrating the need for accurate $\Delta G_{diss}$ values. One should note that this equation is an empirical generalization of the exact thermodynamic definition of p$K_a$, where ideally $c_0 = 1$ and $c_1 = -\lg[S]$ (with the solvent concentration $[S]$).[18] Although various, in principle equivalent, computational approaches for determining $\Delta G_{diss}$ exist, which only differ in the underlying thermodynamic cycle, they all have in common that the Gibbs free energy of solvation ($\Delta G_{solv}$) of all involved species must be accounted for.[19]

Despite their inherent disadvantages, for example, neglect of specific solute-solvent interactions or issues with short-range electrostatics, the use of DCSMs can be actually beneficial with respect to thermodynamic properties since the implicit solvation already accounts for a statistically averaged description.[17,20,21] Furthermore, these models and particularly COSMO have become widely used over the years owing to their computational efficiency and robustness. With COSMO-RS, that is, COSMO for realistic solvation, some substantial progress has been made in overcoming the inherent deficiencies of a continuum solvation model that is almost second to none. In order to improve the accuracy, this extension of COSMO reintroduces the missing contributions from local, directional interactions (e.g., H-bonds) by using an additional statistical-thermodynamics treatment of interacting surfaces (details given elsewhere).[20–23] Importantly, it was already successfully applied to the prediction of p$K_a$ values in water,[24,25] DMSO,[24] acetonitrile,[26] and heptane.[27]

Another common dipolar, aprotic organic solvent is acetone. Chemical reactions as well as analytics are examples of high practical importance where p$K_a$ values in acetone play a role. Only very few experimental results, for example, the compilation of p$K_a$ values in various organic solvents by Izutsu[28,29] or the later work by Ludwig et al.[30] and Pytela et al.,[31–34] but no theoretical studies were available as a reference though.

In the current study, we extend the parameterization for p$K_a$ calculations to acetone as an important aprotic solvent. Thereby, we followed closely the computational procedure described in References [24–26]. This is in particular of interest in light of recent studies of super photoacids in this solvent,[35,36] where previous implementations of COSMO excited-state energy gradients for efficient wave function-based methods[37,38] offer the possibility to employ these LFER parameters for COSMO in future applications on p$K_a^*$.

## 2 | METHODOLOGY

### 2.1 | Theoretical calculations

Our calculations of $\Delta G_{diss}$ in acetone assume the following model for the dissociation reaction

$$HA + S \rightleftharpoons A^- + HS^+, \quad (2)$$

where HA/$A^-$ and $HS^+$/S refer to the conjugate Brønsted acid–base pair of the target acids HA and the solvent acetone (with $S = (CH_3)_2O$), respectively. We adapted the workflow for p$K_a$ LFER parameterizations described in References [24–26] taking into account the recent guidelines proposed by Hellweg and Eckert.[39] Thus, the RI approximation[40] was routinely employed in all DFT[41] and COSMO-DFT[15] calculations and the conductor limit ($\epsilon = \infty$) was exclusively applied in all COSMO calculations. All quantum chemical (QC) calculations were done with the TURBOMOLE program package (version 7.3).[42] The default settings, in particular with respect to the COSMO cavity construction, were used unless stated differently.

To obtain best-quality results, we chose the recommended BP-TZVPD-FINE level (vide infra) of the COSMOtherm program[27,39] as the default for our calculations. Accordingly, the following steps were performed for each of the four species in Equation (2) to calculate the Gibbs free energy in solution:

1. Conformational analysis using the COSMOconf program (version 2020)[43] (with help of its GUI COSMOconfX [version 20.0.0]). COSMOconf automatically searches for all conformers of a given initial structure by generating a set of start structures and refining this set iteratively based on certain energetic and structural thresholds while optimizing the geometries.
2. Quantum chemical calculations for each conformer identified in step 1 at the following four different levels of theory using TURBOMOLE to generate the input required for the BP-TZVPD-FINE level of COSMOtherm (in step 3):
   a. Solution-phase geometry optimization using DFT with the BP86 functional[44,45] in combination with COSMO and the def-TZVP basis set.[46,47]
   b. A subsequent, more accurate single-point-energy calculation using the BP86 functional in combination with COSMO, in the

larger def2-TZVPD basis set,[48] and with a refined (i.e., smooth radii-based isosurface) cavity construction[49] at the COSMO-BP/TZVP geometry.

c. Gas-phase geometry optimization using the BP86 functional and the def-TZVP basis set.
d. A subsequent and more accurate single point energy calculation using the BP86 functional with the larger def2-TZVPD basis set at the BP/TZVP geometry.

3. A COSMO-RS calculation for the free energy in solution at 25°C (298.15 K) as implemented in the COSMOtherm program (version 2020)[27] for the complete conformer set. At the BP-TZVPD-FINE level, COSMO-RS uses the solution-phase refined-cavity information (step 2b) and the gas-phase energy (step 2d), both calculated with the larger TZVPD basis set. Since the results in the smaller TZVP basis are already obtained during the preceding geometry optimizations, the corresponding value at the BP-TZVP level of COSMOtherm can be additionally computed similarly without large effort (based on steps 2a and 2c).

Both calculations, those for the gas phase and those for the solution phase, are required by COSMO-RS to predict the $\Delta G_{solv}$ contributions to the total Gibbs free energies. To conveniently apply this workflow to all investigated acids HA, we used the BP-TZVPD-FINE-COSMO+GAS-18 template provided by COSMOconfX to run the conformer searches (cf. step 1) already at the desired QC levels (cf. step 2), which directly yielded the required input for COSMO-RS (cf. step 3). Supplementary information on the structures and energies of all conformers was made available in Reference [50]. We also exemplarily checked the results after step 2 and performed additional test calculations (e.g., potential energy scans or vibrational frequency calculations) if needed to ensure that only equilibrium structures, that is, minima on the potential energy surface were included. However, vibrational zero-point energies were not explicitly taken into account, following the assumption from the preceding COSMO-RS p$K_a$ predictions that the difference in zero-point energies between the acid and its conjugate base is generally small.[24–26] This assumption had been based on the observation that this difference was found to be fairly constant for molecules with the same functional group.[51,52] Therefore, the contribution from zero-point energies will be implicitly incorporated into the LFER parameters $c_0$ and $c_1$ of each compound class.

The effect of different conformations was taken care of by a Boltzmann average with respect to the Gibbs free energy in solution ($G_i^S = E_i^{COSMO} + \mu_i^S$) of the conformers. Since the chemical potential $\mu_i^S$ of a given conformer in the system S depends, at finite concentration, on the populations themselves, the equations for the population are solved self-consistently in the COSMOtherm program.[27] Symmetry factors, that is, conformer weights due to symmetry-degeneracies, were explicitly taken into account to avoid a biased description if only one enantiomer was included in the conformer set.

The central quantity $\Delta G_{diss}$ can be split according to

$$\begin{aligned}\Delta G_{diss} &= G_{tot}(A^-) + G_{tot}(HS^+) - (G_{tot}(HA) + G_{tot}(S)) \\ &= (G_{tot}(A^-) - G_{tot}(HA)) + (G_{tot}(HS^+) - G_{tot}(S))\end{aligned} \quad (3)$$

into a species-dependent contribution $G_{tot}(A^-) - G_{tot}(HA)$ and a constant solvent-specific contribution $G_{tot}(SH^+) - G_{tot}(S)$. Using the procedure described above, we obtain values of −1098.6 and −1103.9 kJ mol$^{-1}$ for $G_{tot}(SH^+) - G_{tot}(S)$ at the BP-TZVP and BP-TZVPD-FINE levels, respectively. These values are in line with estimates in the literature for the solvation enthalpy of the proton (in acetone) of −1051 kJ mol$^{-1}$ based on the DFT functional B3-LYP in combination with the IEF-PCM solvation model in the aug-cc-pVQZ basis set[53] or −1070 kJ mol$^{-1}$ in the smaller 6-311++G** basis set,[54] considering that (i) mere enthalpies do not include entropic contributions and (ii) our estimates differ by the proton's total Gibbs free energy in the gas phase (−26.3 kJ mol$^{-1}$)[55] from the full Gibbs free energy of solvation. Since $\Delta G_{diss}$ is subject to the linear free-energy relation in Equation (1), systematic errors due to the computational method (COSMO-RS, DFT functional, basis set, etc.) will change the LFER parameters $c_1$ and $c_0$, while the choice of the solvent species $HS^+$/S and the corresponding error will only affect the parameter $c_0$. Hence, regarding the LFER for p$K_a$ prediction, there is no point in improving this constant solvent-specific contribution, as any errors in it will be absorbed in $c_0$ anyway.

## 2.2 | Fit data set

To determine the LFER parameters in Equation (1), we used a set of 120 acids in the solvent acetone for which experimental reference data is available from the compilation of p$K_a$ values in organic solvents by Izutsu[28] that combines different sources. In addition, we included new results from Ludwig et al.,[30] Pytela et al.,[31,33,34] and Kulhánek et al.[32] Only those experimental values were chosen that fulfill the condition of representing true, thermodynamic dissociation constants (i.e., in the limit of infinite dilution or ionic strength). The obtained data set consists of 9 acrylic acids,[56] 87 benzoic acids (1 Parent, 18 ortho,[31] 16 meta,[30] 16 para,[30] 10 2,6-disubst.,[32] 16 3,4-disubst.,[33] and 10 3,5-disubst.[34] derivatives), 9 phenols,[57] and 15 benzenesulfonamides[58]; with halogen atoms and amino, nitro, methyl, or methoxy groups as typical substituents.

The reported p$K_a$ values are not directly comparable with each other due to the use of different reference values that have been used for calibration. The values for acrylic acids are given relative to a p$K_a$ value of 13.5[56] for benzoic acid, while the values for benzoic acids and sulfonamides refer to a corresponding value of 18.2.[30,58] In turn, the measurements for phenols used picric acid (2,4,6-trinitrophenol) with a p$K_a$ value of 6.3[57] as a reference, while the measurements on benzoic acids and sulfonamides refer to 9.2[30,58] for that compound. We prefer the values 18.2 and 9.2 over the others since (i) 18.2 for benzoic acid is both the more recent value and has later been reproduced by the same group[33] and (ii) 9.2 for picric acid has been

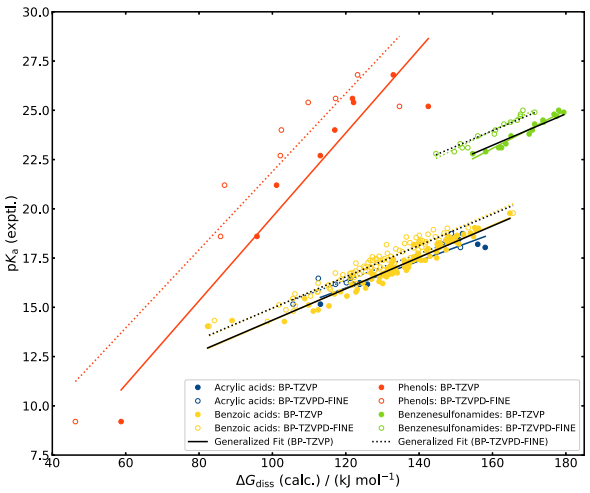



**FIGURE 1** (Shifted) Experimental p$K_a$ values [p$K_a$(exptl.)] plotted against calculated Gibbs free energies of dissociation [$\Delta G_{diss}$(calc.)] in the solvent acetone at the two computational levels BP-TZVP and BP-TZVPD-FINE. Each color represents a specific compound class and linear regression lines for each class are included in the respective color. Full lines refer to the BP-TZVP and dashed lines to the BP-TZVPD-FINE level. The LFER parameters and correlation coefficients for these class-specific fits are given in Table 2. In addition, also the results from a generalized fit that combines the different subsets (details given in the text) are included as black lines and the corresponding fit results can be found in Table 3

determined via two independent methods.[59] Furthermore, both values also appear much more reasonable in the light of recent p$K_a$ values in the solvent acetonitrile.[60,61]

Consequently, we shifted the p$K_a$ values of the acrylic acids up by 4.7 (benzoic acid as reference) and those for the phenols up by 2.9 (picric acid as reference) in order to account for these differences in the corresponding experimental reference values. The resulting shifted p$K_a$ values then range from 9.2 (picric acid) to 26.8 (2,6-dichlorophenol) and therefore span roughly 18 logarithmic units.

## 3 | RESULTS AND DISCUSSION

### 3.1 | Class-specific considerations

We begin our discussion with the pure $\Delta G_{diss}$ values and class-specific p$K_a$ values before moving on to those p$K_a$ values based on a generalized LFER. A direct comparison between the experimental p$K_a$ values and the calculated $\Delta G_{diss}$ values in Figure 1 reveals distinct differences between the molecular classes. To further illustrate this, we also calculated p$K_a$ values based on class-specific LFER parameter fits (cf. linear regression lines in Figure 1), referred to as $pK_a^{(calc.)}$ and given in Table 1. The corresponding LFER parameters are listed in Table 2.

At the BP-TZVP level, all compound classes show very good linear correlations between $pK_a^{(exptl.)}$ and $\Delta G_{diss}$ with squared correlation coefficients $r^2$ larger than 0.9, smallest for the acrylic acids (0.913) and largest for the benzenesulfonamides (0.963). The $r^2$ value for the benzoic acids is also very close (0.940). Despite their different experimental origins, the p$K_a$ values of the acrylic acids fit very well to those for the benzoic acids, demonstrating that a shift of the p$K_a$ scale is indeed justified in this case. Although the p$K_a$ values of the benzoic acids and sulfonamides have been determined by the same authors,[30–34,58] the latter do not match those for the carboxylic acids, but appear to be vertically shifted by a constant offset instead. Since a difference in the experimental reference values should not be the cause here, this behavior rather appears to have real, physical origin (vide infra). In addition, the phenols appear quite well linearly correlated ($r^2 > 0.91$), but characteristically different from the other classes.

The LFER parameter for the slope, $c_1$, is smallest for the acrylic acids (0.393), medium-large for the benzoic acids (0.460) and sulfonamides (0.555), and largest for the phenols (1.216). The statistical errors are largest for the acrylic acids and phenols (~10%), and decrease over the sulfonamides (~5%) toward the benzoic acids (~3%), reflecting the increasing numbers of compounds in the classes that increase the statistical significance. This flexibility in the slope is also reflected in the uncertainty of the intercepts, $c_0$. Their statistical errors amount to about 1 for the acrylic acids and sulfonamides, almost 3 for the phenols, but only 0.3 for the benzoic acids. Within these error bars, the overall agreement between the carboxylic acids and the sulfonamides is actually already fairly good. In analogy to the slope, the phenols also clearly differ from the other classes with respect to the intercept.

Largest deviations between the class-specific fits and the experimental data are observed for the phenols and benzoic acids, while the former will be discussed later. Still, due to the large number of benzoic acids, it is worthwhile to have a look at the most significant outliers. The largest absolute error is found for the ortho-SH derivative (1.130), followed by the ortho-COOH (0.884), and meta-$COCH_3$ (0.739) derivatives. If these compounds are excluded, the correlation further improves ($r^2 = 0.981$) and the regression results in the coefficients $c_0 = 5.106$ and $c_1 = 0.507$ at an RSMD of 0.044. The poor agreement for ortho-SH benzoic acid seems to be caused by a qualitatively wrong deprotonation at the SH group (i.e., proton exchange in the carboxylate), while for the ortho-COOH derivative the rather large proton delocalization involving intra-molecular hydrogen bonding might be the origin, as already indicated for dicarboxylic acids in acetonitrile.[26]

In general, similar observations are also made for the computational level BP-TZVPD-FINE, but the computed $\Delta G_{diss}$ values are systematically smaller, that is, horizontally shifted to the left compared to the BP-TZVP level. This shift is largest for the phenols and sulfonamides and much smaller for the carboxylic acids. We suspect that at least two factors contribute to this shift. First, we found a difference of about ~5 kJ mol$^{-1}$ between these two levels for the constant solvent-dependent term contributing to $\Delta G_{diss}$. Second, due to the negative charge, we anticipate a stronger energetic stabilization of the anionic bases relative to the neutral acids when moving to the higher computational level since the main difference lies in the larger basis

**TABLE 1** Comparison of experimental $pK_a$ values ($pK_a^{(exptl.)}$) and calculated $\Delta G_{diss}$ values of 120 acids in acetone using COSMO-RS at both the BP-TZVP and BP-TZVPD levels

| | | BP-TZVP | | | | | BP-TZVPD-FINE | | | | |
|---|---|---|---|---|---|---|---|---|---|---|---|
| | | | Class-specific | | Generalized | | | Class-specific | | Generalized | |
| Compound | $pK_a^{(exptl.)}$ | $\Delta G_{diss}$ | $pK_a^{(calc.)}$ | $\Delta pK_a$ | $pK_a^{(calc.)}$ | $\Delta pK_a$ | $\Delta G_{diss}$ | $pK_a^{(calc.)}$ | $\Delta pK_a$ | $pK_a^{(calc.)}$ | $\Delta pK_a$ |
| Acrylic acids | | | | | | | | | | | |
| Parent | 18.45 | 150.8 | 18.10 | 0.35 | 18.40 | 0.05 | 148.1 | 18.28 | 0.17 | 18.78 | −0.33 |
| 2-F | 16.17 | 125.9 | 16.39 | −0.22 | 16.41 | −0.24 | 123.8 | 16.62 | −0.45 | 16.85 | −0.68 |
| 2-Cl | 16.25 | 123.8 | 16.24 | 0.01 | 16.24 | 0.01 | 120.2 | 16.37 | −0.12 | 16.56 | −0.31 |
| 2-Br | 16.17 | 122.1 | 16.12 | 0.05 | 16.10 | 0.07 | 117.2 | 16.17 | 0.00 | 16.32 | −0.15 |
| 2-$CH_3$ | 18.74 | 151.8 | 18.17 | 0.57 | 18.48 | 0.26 | 148.8 | 18.33 | 0.41 | 18.84 | −0.10 |
| 3-$C_6H_5$ | 18.20 | 156.0 | 18.46 | −0.26 | 18.81 | −0.61 | 146.4 | 18.16 | 0.04 | 18.64 | −0.44 |
| 2-CN,3-$C_6H_5$ | 16.47 | 121.3 | 16.07 | 0.40 | 16.04 | 0.43 | 112.5 | 15.85 | 0.62 | 15.95 | 0.52 |
| 3-(2-Furyl) | 18.04 | 158.0 | 18.60 | −0.56 | 18.97 | −0.93 | 151.3 | 18.50 | −0.46 | 19.03 | −0.99 |
| 2,3-Dibromo-3-formyl | 15.16 | 113.1 | 15.50 | −0.34 | 15.39 | −0.23 | 105.6 | 15.38 | −0.22 | 15.40 | −0.24 |
| Benzoic acids | | | | | | | | | | | |
| Parent | 18.20 | 144.9 | 17.95 | 0.25 | 17.93 | 0.27 | 139.6 | 18.16 | 0.04 | 18.11 | 0.09 |
| 2-Substituted (ortho) | | | | | | | | | | | |
| 2-F | 17.44 | 139.9 | 17.54 | −0.10 | 17.52 | −0.08 | 133.0 | 17.62 | −0.18 | 17.58 | −0.14 |
| 2-Cl | 17.01 | 133.4 | 17.02 | −0.01 | 17.01 | 0.00 | 125.2 | 16.99 | 0.02 | 16.96 | 0.05 |
| 2-Br | 16.84 | 132.0 | 16.91 | −0.07 | 16.90 | −0.06 | 122.7 | 16.78 | 0.06 | 16.76 | 0.08 |
| 2-I | 16.98 | 131.4 | 16.86 | 0.12 | 16.85 | 0.13 | 123.7 | 16.87 | 0.11 | 16.84 | 0.14 |
| 2-$CH_3$ | 18.39 | 148.7 | 18.26 | 0.13 | 18.23 | 0.16 | 140.9 | 18.26 | 0.13 | 18.21 | 0.18 |
| 2-OH | 14.81 | 111.1 | 15.23 | −0.42 | 15.23 | −0.42 | 105.7 | 15.41 | −0.60 | 15.41 | −0.60 |
| 2-$OCH_3$ | 18.94 | 155.4 | 18.80 | 0.14 | 18.77 | 0.17 | 143.9 | 18.50 | 0.44 | 18.45 | 0.49 |
| 2-COOH | 14.33 | 89.0 | 13.45 | 0.88 | 13.47 | 0.86 | 84.2 | 13.67 | 0.66 | 13.70 | 0.63 |
| 2-$COOCH_3$ | 17.39 | 132.9 | 16.98 | 0.41 | 16.97 | 0.42 | 126.6 | 17.10 | 0.29 | 17.07 | 0.32 |
| 2-$OCOCH_3$ | 17.39 | 135.9 | 17.22 | 0.17 | 17.21 | 0.18 | 130.1 | 17.38 | 0.01 | 17.35 | 0.04 |
| 2-$NH_2$ | 18.58 | 148.0 | 18.20 | 0.38 | 18.18 | 0.40 | 144.4 | 18.55 | 0.03 | 18.49 | 0.09 |
| 2-$NHCH_3$ | 18.28 | 145.6 | 18.01 | 0.27 | 17.98 | 0.30 | 137.5 | 17.98 | 0.30 | 17.94 | 0.34 |
| 2-$NHCOCH_3$ | 15.79 | 118.6 | 15.83 | −0.04 | 15.83 | −0.04 | 112.4 | 15.95 | −0.16 | 15.94 | −0.15 |
| 2-$NO_2$ | 15.91 | 123.1 | 16.19 | −0.28 | 16.19 | −0.28 | 115.8 | 16.23 | −0.32 | 16.21 | −0.30 |
| 2-$SCH_3$ | 17.97 | 142.5 | 17.75 | 0.22 | 17.73 | 0.24 | 133.6 | 17.67 | 0.30 | 17.63 | 0.34 |
| 2-$SCOCH_3$ | 17.08 | 132.1 | 16.92 | 0.16 | 16.91 | 0.17 | 124.9 | 16.97 | 0.11 | 16.94 | 0.14 |
| 2-SH | 14.04 | 82.3 | 12.91 | 1.13 | 12.94 | 1.10 | 82.7 | 13.55 | 0.49 | 13.58 | 0.46 |
| 2-$SO_2NH_3$ | 15.44 | 108.8 | 15.04 | 0.40 | 15.05 | 0.39 | 105.6 | 15.40 | 0.04 | 15.40 | 0.04 |
| 3-Substituted (meta) | | | | | | | | | | | |
| 3-F | 17.40 | 138.5 | 17.44 | −0.04 | 17.42 | −0.02 | 131.7 | 17.52 | −0.12 | 17.48 | −0.08 |
| 3-Cl | 16.88 | 136.5 | 17.27 | −0.39 | 17.26 | −0.38 | 127.8 | 17.20 | −0.32 | 17.17 | −0.29 |
| 3-Br | 17.03 | 136.1 | 17.24 | −0.21 | 17.22 | −0.19 | 126.7 | 17.11 | −0.08 | 17.08 | −0.05 |
| 3-I | 17.27 | 136.0 | 17.23 | 0.04 | 17.22 | 0.05 | 126.1 | 17.06 | 0.21 | 17.03 | 0.24 |
| 3-CN | 16.69 | 131.9 | 16.90 | −0.21 | 16.89 | −0.20 | 123.9 | 16.88 | −0.19 | 16.85 | −0.16 |
| 3-$CH_3$ | 18.40 | 148.3 | 18.22 | 0.18 | 18.19 | 0.21 | 140.3 | 18.21 | 0.19 | 18.16 | 0.24 |
| 3-OH | 18.41 | 147.3 | 18.14 | 0.27 | 18.12 | 0.29 | 145.4 | 18.63 | −0.22 | 18.57 | −0.16 |
| 3-$OCH_3$ | 18.18 | 145.8 | 18.02 | 0.16 | 18.00 | 0.18 | 139.4 | 18.14 | 0.04 | 18.09 | 0.09 |
| 3-$OC_6H_5$ | 17.39 | 140.6 | 17.60 | −0.21 | 17.58 | −0.19 | 127.4 | 17.16 | 0.23 | 17.13 | 0.26 |
| 3-COOH | 17.24 | 137.4 | 17.35 | −0.11 | 17.33 | −0.09 | 133.2 | 17.64 | −0.40 | 17.60 | −0.36 |

(Continues)

**TABLE 1** (Continued)

| | | BP-TZVP | | | | | BP-TZVPD-FINE | | | | |
|---|---|---|---|---|---|---|---|---|---|---|---|
| | | | Class-specific | | Generalized | | | Class-specific | | Generalized | |
| 3-$COCH_3$ | 18.18 | 138.6 | 17.44 | 0.74 | 17.42 | 0.76 | 131.1 | 17.47 | 0.71 | 17.43 | 0.75 |
| 3-$NHCOCH_3$ | 18.05 | 145.6 | 18.01 | 0.04 | 17.98 | 0.07 | 140.7 | 18.24 | −0.19 | 18.19 | −0.14 |
| 3-$NO_2$ | 16.52 | 129.2 | 16.69 | −0.17 | 16.68 | −0.16 | 122.3 | 16.75 | −0.23 | 16.73 | −0.21 |
| 3-SH | 17.51 | 144.8 | 17.94 | −0.43 | 17.92 | −0.41 | 137.6 | 17.99 | −0.48 | 17.95 | −0.44 |
| 3-$SO_2CH_3$ | 16.75 | 134.0 | 17.07 | −0.32 | 17.06 | −0.31 | 128.8 | 17.28 | −0.53 | 17.25 | −0.50 |
| 3-$SO_2NH_2$ | 17.00 | 133.5 | 17.03 | −0.03 | 17.02 | −0.02 | 132.0 | 17.54 | −0.54 | 17.50 | −0.50 |
| 4-Substituted (para) | | | | | | | | | | | |
| 4-F | 17.89 | 142.0 | 17.72 | 0.17 | 17.70 | 0.19 | 134.6 | 17.75 | 0.14 | 17.71 | 0.18 |
| 4-Cl | 17.47 | 139.4 | 17.51 | −0.04 | 17.49 | −0.02 | 130.5 | 17.42 | 0.05 | 17.38 | 0.09 |
| 4-Br | 17.47 | 138.8 | 17.46 | 0.01 | 17.44 | 0.03 | 128.3 | 17.24 | 0.23 | 17.20 | 0.27 |
| 4-I | 17.56 | 138.6 | 17.44 | 0.12 | 17.42 | 0.14 | 127.3 | 17.15 | 0.41 | 17.12 | 0.44 |
| 4-CN | 16.74 | 130.5 | 16.79 | −0.05 | 16.78 | −0.04 | 121.4 | 16.68 | 0.06 | 16.66 | 0.08 |
| 4-$CH_3$ | 18.33 | 148.2 | 18.22 | 0.11 | 18.19 | 0.14 | 140.0 | 18.19 | 0.14 | 18.14 | 0.19 |
| 4-*tert*-Butyl | 18.57 | 149.9 | 18.35 | 0.22 | 18.33 | 0.24 | 136.5 | 17.90 | 0.67 | 17.86 | 0.71 |
| 4-OH | 19.04 | 155.2 | 18.77 | 0.27 | 18.75 | 0.29 | 153.4 | 19.27 | −0.23 | 19.20 | −0.16 |
| 4-$OCH_3$ | 18.77 | 154.0 | 18.68 | 0.09 | 18.65 | 0.12 | 146.8 | 18.74 | 0.03 | 18.68 | 0.09 |
| 4-$COCH_3$ | 17.28 | 137.2 | 17.33 | −0.05 | 17.31 | −0.03 | 128.7 | 17.27 | 0.01 | 17.24 | 0.04 |
| 4-$NH_2$ | 19.78 | 164.7 | 19.55 | 0.23 | 19.51 | 0.27 | 165.6 | 20.26 | −0.48 | 20.17 | −0.39 |
| 4-$NO_2$ | 16.43 | 127.0 | 16.51 | −0.08 | 16.50 | −0.07 | 118.7 | 16.46 | −0.03 | 16.45 | −0.02 |
| 4-SH | 17.92 | 147.4 | 18.15 | −0.23 | 18.12 | −0.20 | 139.8 | 18.17 | −0.25 | 18.12 | −0.20 |
| 4-$SCH_3$ | 18.22 | 150.8 | 18.42 | −0.20 | 18.40 | −0.18 | 141.7 | 18.32 | −0.10 | 18.27 | −0.05 |
| 4-$SO_2CH_3$ | 16.82 | 132.3 | 16.93 | −0.11 | 16.92 | −0.10 | 125.4 | 17.01 | −0.19 | 16.98 | −0.16 |
| 4-$SO_2NH_2$ | 16.90 | 133.6 | 17.04 | −0.14 | 17.02 | −0.12 | 130.2 | 17.39 | −0.49 | 17.36 | −0.46 |
| 2,6-Disubstituted | | | | | | | | | | | |
| 2-$CH_3$,6-$CH_3$ | 17.74 | 139.7 | 17.53 | 0.21 | 17.51 | 0.23 | 131.4 | 17.49 | 0.25 | 17.45 | 0.29 |
| 2-$CH_3$,6-Cl | 16.74 | 126.9 | 16.49 | 0.25 | 16.49 | 0.25 | 117.2 | 16.34 | 0.40 | 16.32 | 0.42 |
| 2-$CH_3$,6-$NO_2$ | 16.13 | 121.6 | 16.07 | 0.06 | 16.07 | 0.06 | 115.3 | 16.18 | −0.05 | 16.17 | −0.04 |
| 2-$CH_3$,6-$OCH_3$ | 18.24 | 145.1 | 17.97 | 0.27 | 17.95 | 0.29 | 136.0 | 17.87 | 0.37 | 17.82 | 0.42 |
| 2-Cl,6-$NO_2$ | 15.12 | 109.9 | 15.13 | −0.01 | 15.13 | −0.01 | 101.8 | 15.09 | 0.03 | 15.10 | 0.02 |
| 2-Cl,6-Cl | 15.68 | 116.9 | 15.69 | −0.01 | 15.69 | −0.01 | 106.1 | 15.45 | 0.23 | 15.45 | 0.23 |
| 2-$NO_2$,6-$NO_2$ | 14.28 | 103.3 | 14.60 | −0.32 | 14.61 | −0.33 | 98.7 | 14.84 | −0.56 | 14.85 | −0.57 |
| 2-$OCH_3$,6-Cl | 17.24 | 132.6 | 16.95 | 0.29 | 16.94 | 0.30 | 122.8 | 16.79 | 0.45 | 16.77 | 0.47 |
| 2-$OCH_3$,6-$NO_2$ | 16.65 | 127.6 | 16.55 | 0.10 | 16.54 | 0.11 | 119.2 | 16.50 | 0.15 | 16.48 | 0.17 |
| 2-$OCH_3$,6-$OCH_3$ | 18.65 | 150.4 | 18.39 | 0.26 | 18.36 | 0.29 | 140.1 | 18.19 | 0.46 | 18.14 | 0.51 |
| 3,4-Disubstituted | | | | | | | | | | | |
| 3-Br,4-$CH_3$ | 17.59 | 139.8 | 17.54 | 0.05 | 17.52 | 0.07 | 129.1 | 17.30 | 0.29 | 17.27 | 0.32 |
| 3-Br,4-$OCH_3$ | 17.82 | 144.7 | 17.93 | −0.11 | 17.91 | −0.09 | 135.4 | 17.81 | 0.01 | 17.77 | 0.05 |
| 3-$CH_3$,4-$CH_3$ | 18.71 | 152.1 | 18.53 | 0.18 | 18.50 | 0.21 | 142.4 | 18.38 | 0.33 | 18.33 | 0.38 |
| 3-$CH_3$,4-Cl | 17.59 | 142.9 | 17.79 | −0.20 | 17.77 | −0.18 | 132.2 | 17.56 | 0.03 | 17.52 | 0.07 |
| 3-$CH_3$,4-$NO_2$ | 16.55 | 131.1 | 16.84 | −0.29 | 16.83 | −0.28 | 121.3 | 16.67 | −0.12 | 16.65 | −0.10 |
| 3-$CH_3$,4-$OCH_3$ | 19.01 | 156.2 | 18.85 | 0.16 | 18.82 | 0.19 | 147.7 | 18.81 | 0.20 | 18.75 | 0.26 |
| 3-Cl,4-Cl | 16.70 | 132.7 | 16.96 | −0.26 | 16.95 | −0.25 | 121.1 | 16.66 | 0.04 | 16.63 | 0.07 |
| 3-Cl,4-$NO_2$ | 15.78 | 122.8 | 16.17 | −0.39 | 16.16 | −0.38 | 112.2 | 15.94 | −0.16 | 15.93 | −0.15 |
| 3-$NO_2$,4-$NO_2$ | 15.07 | 115.4 | 15.57 | −0.50 | 15.58 | −0.51 | 106.2 | 15.45 | −0.38 | 15.45 | −0.38 |
| 3-$NO_2$,4-$CH_3$ | 16.75 | 131.3 | 16.85 | −0.10 | 16.84 | −0.09 | 122.1 | 16.74 | 0.01 | 16.72 | 0.03 |

**TABLE 1** (Continued)

| | | BP-TZVP | | | | | BP-TZVPD-FINE | | | | |
|---|---|---|---|---|---|---|---|---|---|---|---|
| | | | Class-specific | | Generalized | | | Class-specific | | Generalized | |
| 3-$NO_2$,4-Cl | 15.98 | 125.4 | 16.38 | −0.40 | 16.37 | −0.39 | 115.5 | 16.20 | −0.22 | 16.19 | −0.21 |
| 3-$NO_2$,4-$OCH_3$ | 17.04 | 137.1 | 17.32 | −0.28 | 17.30 | −0.26 | 129.5 | 17.33 | −0.29 | 17.30 | −0.26 |
| 3-$OCH_3$,4-$OCH_3$ | 18.59 | 154.8 | 18.75 | −0.16 | 18.72 | −0.13 | 147.8 | 18.82 | −0.23 | 18.76 | −0.17 |
| 3-$OCH_3$,4-$CH_3$ | 18.32 | 150.1 | 18.37 | −0.05 | 18.35 | −0.03 | 141.9 | 18.34 | −0.02 | 18.29 | 0.03 |
| 3-$OCH_3$,4-Cl | 17.39 | 141.7 | 17.69 | −0.30 | 17.67 | −0.28 | 132.6 | 17.58 | −0.19 | 17.55 | −0.16 |
| 3-$OCH_3$,4-$NO_2$ | 16.21 | 130.1 | 16.75 | −0.54 | 16.74 | −0.53 | 122.8 | 16.80 | −0.59 | 16.77 | −0.56 |
| 3,5-Disubstituted | | | | | | | | | | | |
| 3-Br,5-Br | 16.23 | 124.7 | 16.32 | −0.09 | 16.31 | −0.08 | 112.5 | 15.96 | 0.27 | 15.95 | 0.28 |
| 3-Cl,5-$NO_2$ | 15.57 | 120.3 | 15.97 | −0.40 | 15.97 | −0.40 | 110.4 | 15.79 | −0.22 | 15.78 | −0.21 |
| 3-$CH_3$,5-$CH_3$ | 18.54 | 148.6 | 18.24 | 0.30 | 18.22 | 0.32 | 139.2 | 18.12 | 0.42 | 18.07 | 0.47 |
| 3-$CH_3$,5-Cl | 17.40 | 138.3 | 17.41 | −0.01 | 17.40 | 0.00 | 128.4 | 17.25 | 0.15 | 17.21 | 0.19 |
| 3-$CH_3$,5-$NO_2$ | 16.62 | 130.5 | 16.79 | −0.17 | 16.78 | −0.16 | 121.8 | 16.71 | −0.09 | 16.69 | −0.07 |
| 3-$CH_3$,5-$OCH_3$ | 18.26 | 147.8 | 18.18 | 0.08 | 18.16 | 0.10 | 140.0 | 18.19 | 0.07 | 18.14 | 0.12 |
| 3-$NO_2$,5-$NO_2$ | 14.87 | 112.5 | 15.33 | −0.46 | 15.34 | −0.47 | 103.7 | 15.25 | −0.38 | 15.25 | −0.38 |
| 3-$OCH_3$,5-$OCH_3$ | 18.02 | 145.2 | 17.97 | 0.05 | 17.95 | 0.07 | 138.5 | 18.06 | −0.04 | 18.01 | 0.01 |
| 3-$OCH_3$,5-Br | 17.03 | 136.2 | 17.25 | −0.22 | 17.23 | −0.20 | 127.0 | 17.13 | −0.10 | 17.10 | −0.07 |
| 3-$OCH_3$,5-$NO_2$ | 16.31 | 129.1 | 16.67 | −0.36 | 16.67 | −0.36 | 121.2 | 16.66 | −0.35 | 16.64 | −0.33 |
| Phenols | | | | | | | | | | | |
| o-Nitro | 25.20 | 142.5 | 28.64 | −3.44 | – | – | 134.6 | 28.76 | −3.56 | – | – |
| 2,4-Dinitro | 18.60 | 95.8 | 18.69 | −0.09 | – | – | 85.9 | 19.08 | −0.48 | – | – |
| 2,5-Dinitro | 22.70 | 113.1 | 22.37 | 0.33 | – | – | 102.2 | 22.32 | 0.38 | – | – |
| 2,5-Dinitro | 25.60 | 121.8 | 24.24 | 1.36 | – | – | 117.2 | 25.31 | 0.29 | – | – |
| 2,4,6-Trinitro | 9.20 | 58.8 | 10.81 | −1.61 | – | – | 46.3 | 11.23 | −2.03 | – | – |
| 2,6-Dichloro | 26.80 | 133.0 | 26.61 | 0.19 | – | – | 123.2 | 26.50 | 0.30 | – | – |
| 2,4,6-Trichloro | 25.40 | 122.1 | 24.30 | 1.10 | – | – | 109.8 | 23.83 | 1.57 | – | – |
| 2,4,6-Tribromo | 24.00 | 117.0 | 23.21 | 0.79 | – | – | 102.4 | 22.37 | 1.63 | – | – |
| Pentachloro | 21.20 | 101.1 | 19.83 | 1.37 | – | – | 87.0 | 19.30 | 1.90 | – | – |
| Benzenesulfonamides | | | | | | | | | | | |
| Parent | 24.50 | 173.8 | 24.40 | 0.10 | 24.32 | 0.18 | 166.7 | 24.58 | −0.08 | 24.50 | −0.00 |
| p-Fluoro | 24.30 | 171.5 | 24.18 | 0.12 | 24.14 | 0.16 | 163.1 | 24.25 | 0.05 | 24.21 | 0.09 |
| p-Chloro | 23.80 | 170.0 | 24.03 | −0.23 | 24.02 | −0.22 | 160.5 | 24.02 | −0.22 | 24.01 | −0.21 |
| p-Bromo | 24.00 | 170.9 | 24.12 | −0.12 | 24.09 | −0.09 | 160.8 | 24.04 | −0.04 | 24.03 | −0.03 |
| m-Chloro | 23.70 | 165.1 | 23.55 | 0.15 | 23.63 | 0.07 | 156.0 | 23.60 | 0.10 | 23.65 | 0.05 |
| 3.4-Dichloro | 23.10 | 162.5 | 23.30 | −0.20 | 23.42 | −0.32 | 151.8 | 23.21 | −0.11 | 23.31 | −0.21 |
| m-Cyano | 23.10 | 161.7 | 23.23 | −0.13 | 23.36 | −0.26 | 153.3 | 23.35 | −0.25 | 23.43 | −0.33 |
| m-Nitro | 22.90 | 158.2 | 22.88 | 0.02 | 23.07 | −0.17 | 149.6 | 23.01 | −0.11 | 23.14 | −0.24 |
| p-Nitro | 22.80 | 154.6 | 22.54 | 0.26 | 22.79 | 0.01 | 144.6 | 22.56 | 0.24 | 22.74 | 0.06 |
| p-Trifluoromethyl | 23.30 | 163.6 | 23.42 | −0.12 | 23.51 | −0.21 | 151.2 | 23.16 | 0.14 | 23.27 | 0.03 |
| p-Methoxy | 24.90 | 179.4 | 24.95 | −0.05 | 24.77 | 0.13 | 171.5 | 25.02 | −0.12 | 24.88 | 0.02 |
| m-Methoxy | 24.40 | 173.9 | 24.41 | −0.01 | 24.33 | 0.07 | 164.9 | 24.42 | −0.02 | 24.36 | 0.04 |
| p-Methyl | 24.80 | 176.8 | 24.70 | 0.10 | 24.56 | 0.24 | 167.6 | 24.67 | 0.13 | 24.57 | 0.23 |
| m-Methyl | 24.70 | 177.5 | 24.76 | −0.06 | 24.62 | 0.08 | 167.6 | 24.66 | 0.04 | 24.57 | 0.13 |
| o-Xylyl | 25.00 | 178.1 | 24.82 | 0.18 | 24.66 | 0.34 | 168.3 | 24.73 | 0.27 | 24.63 | 0.37 |

*Note*: Experimental values have been taken from References Ludwig (1986)[30]; Pytela (1994)[31]; Kulhánek (1997)[32]; Pytela (1994)[33,34]; Barabanov (1973)[56]; Nowak (1981)[57]; Ludwig (1986)[58] and were shifted as described in Section 2.2. The values $pK_a^{(calc.)}$ are based on LFER parameters that are either specifically fitted for each compound class, referred to as class-specific, or obtained from a generalized fit for a combined set, referred to as generalized, (see text for details). The errors $\Delta pK_a$, that is, the difference between $pK_a^{(exptl.)}$ and $pK_a^{(calc.)}$ are also included.

**TABLE 2** Class-specific p$K_a$ LFER parameters $c_1$ and $c_0$ with their standard deviations, squared correlation coefficient $r^2$, and root-mean-square deviation (RMSD) as obtained from linear regressions based on Equation (1) for each compound class at the two levels of theory

| | BP-TZVP | | | | BP-TZVPD-FINE | | | |
|---|---|---|---|---|---|---|---|---|
| Class | $c_0$ | $c_1$ | $r^2$ | RMSD | $c_0$ | $c_1$ | $r^2$ | RMSD |
| Acrylic acids | 7.708 ± 1.101 | 0.393 ± 0.046 | 0.913 | 0.357 | 8.154 ± 1.003 | 0.390 ± 0.044 | 0.920 | 0.343 |
| Benzoic acids | 6.279 ± 0.302 | 0.460 ± 0.013 | 0.940 | 0.288 | 6.853 ± 0.296 | 0.462 ± 0.013 | 0.935 | 0.298 |
| Phenols | −1.708 ± 2.788 | 1.216 ± 0.140 | 0.916 | 1.495 | 2.046 ± 2.732 | 1.133 ± 0.150 | 0.890 | 1.703 |
| Benzenesulfonamides | 7.511 ± 0.891 | 0.555 ± 0.030 | 0.963 | 0.142 | 9.329 ± 0.843 | 0.522 ± 0.030 | 0.959 | 0.151 |

**TABLE 3** Fit parameters $c_1$, $c_0^{(A)}$, and $c_0^{(B)}$ together with their error estimates as well as effective squared correlation coefficient $r^2$ and root-mean-square deviation (RMSD) as obtained from a generalized LFER fit according to Equation (4) for the combined data set consisting of the acrylic acids, benzoic acids, and sulfonamides at the two levels of theory

| Level | $c_1$ | $c_0^{(A)}$ | $c_0^{(B)}$ | $r^2$ | RMSD |
|---|---|---|---|---|---|
| BP-TZVP | 0.455 ± 0.012 | 6.369 ± 0.289 | 10.460 ± 0.363 | 0.960 | 0.291 |
| BP-TZVPD-FINE | 0.454 ± 0.013 | 7.009 ± 0.290 | 11.249 ± 0.364 | 0.953 | 0.308 |

set and anions are known to require more diffusive functions. Similar observations were already made during the prediction of total p$K_a$ values for substituted phenols in water using the CBS-QB3 method in combination with the C-PCM solvation model.[62] There is indeed an indication for this in our data as well since we observed a class-averaged difference in the Gibbs free energy in solution between the anion and the neutral acid for BP-TZVP and BP-TZVPD of about −4 kJ mol$^{-1}$ for the phenols and sulfonamides, but a distinct, almost vanishing difference for the carboxylic acids. This is also in perfect agreement with previous study on the absolute p$K_a$ values of carboxylic acids in water,[63] indicating that the size of the basis set has a much smaller affect for these compounds compared to the phenols.

Apart from that, the linear regressions still yield very similar results in terms of the LFER parameters and correlation coefficients. The slopes are generally slightly smaller at the BP-TZVPD-FINE level, with a decrease that is smallest for the acrylic acids (<1%) and largest for the sulfonamides and phenols (~6%), but overall virtually identical to those at the BP-TZVP level within the error bars. A one-to-one comparison of the intercepts is not meaningful though since this parameter is directly affected by changing the slope. However, the difference in the intercepts between the two levels can be indeed used to quantify the aforementioned horizontal shift in the $\Delta G_{diss}$ values by assuming identical slopes, which is a reasonable assumption in this case. Doing so, the shift can be estimated to be on average 6.8 kJ mol$^{-1}$ for the carboxylic acids and 18.3 kJ mol$^{-1}$ for the sulfonamides and phenols. Another important difference between the results for these two levels should also be noted: While the correlation slightly increases for the acrylic acids when moving to the BP-TZVPD-FINE level, it slightly decreases for the benzoic acids and sulfonamides, and noticeably for the phenols. This trend is also reflected in the fit quality as expressed by the root-mean-square deviation (RMSD). The RMSD decreases for the acrylic acids at the higher level, but increases for all other classes and the most for the phenols. In analogy to the BP-TZVP results, if the outliers observed for the linear regression of the benzoic acids are excluded again, we obtain a highly corrected data set ($r^2 = 0.979$) with regression coefficients $c_0 = 6.334$ and $c_1 = 0.484$ at an RMSD of 0.075.

## 3.2 | Combined data set

The class-specific considerations are useful for additional insights (vide infra), but only of limited use for p$K_a$ prediction for new compounds which should be based on a broad and chemically diverse molecular data set. Therefore, we aimed at a meaningful way to combine the four subsets. Regarding the carboxylic acids, this was easy since the acrylic and benzoic acids have comparable class-specific LFER parameters. Since we already noticed that the benzenesulfonamides mainly differ from the carboxylic acids by a constant offset (cf. Figure 1), which is reflected in a similar slope, including this subset was easily achieved by allowing for a shift in the p$K_a$ scale. However, due to the distinct qualitative difference between these three subsets and the phenols, for example, in terms of the slope $c_1$, we decided to not include the latter in the determination of generalized LFER parameters.

Thus, for combining the carboxylic acids and the sulfonamides, we performed a constraint linear regression that couples the two individual linear regressions for each class

$$pK_a^{(l)} = c_1^{(l)} \frac{\Delta G_{diss}}{RT\ln(10)} + c_0^{(l)}, \quad (4)$$

where $I = A$ for carboxylic acids and $I = B$ for sulfonamides, by requiring identical slopes, that is, $c_1^{(A)} = c_1^{(B)} = c_1$. Similar to the standard linear regression, this problem can be solved analytically and the solution for the slope $c_1$ and intercepts $c_0^{(I)}$ reads:

$$c_1 = \frac{N_A\left(\langle X_A Y_A\rangle - \langle X_A\rangle\langle Y_A\rangle\right) + N_B\left(\langle X_B Y_B\rangle - \langle X_B\rangle\langle Y_B\rangle\right)}{N_A\left(\langle X_A^2\rangle - \langle X_A\rangle^2\right) + N_B\left(\langle X_B^2\rangle - \langle X_B\rangle^2\right)}, \quad (5)$$

$$c_0^{(I)} = \langle Y_I\rangle - \langle X_I\rangle c_1, \quad (6)$$

where $N_I$ denotes the number of data points in the respective subset $I$, $X_I$ the subset of calculated $\frac{\Delta G_{diss}}{RT\ln(10)}$ values, and $Y_I$ the subset of experimental p$K_a$ values. Angle brackets $\langle Q\rangle$ represent the expectation value of a given quantity $Q$. The corresponding variances were calculated according to:

$$\Delta c_1 = \sqrt{\frac{N_A\sigma_A^2 s_{X_A}^2 + N_B\sigma_B^2 s_{X_B}^2}{\left(N_A s_{X_A}^2 + N_B s_{X_B}^2\right)^2}}, \quad (7)$$

$$\Delta c_0^{(I)} = \sqrt{\frac{\sigma_I^2}{N_I} + \langle X_I\rangle^2 (\Delta c_1)^2} \quad (8)$$

with the standard deviation $s_{X_I} = \sqrt{\langle X_I^2\rangle - \langle X_I\rangle^2}$ of $X_I$ and the estimated variance of the error $\sigma_I^2 = \sqrt{\frac{1}{N_I - 3}\sum_{i=0}^{N_I}\left(y_i^{(I)} - \left(c_0^{(I)} + c_1 x_i^{(I)}\right)\right)^2}$. $x_i^{(I)}$ and $y_i^{(I)}$ are the elements of the sets $X_I$ and $Y_I$, respectively.

The results for the generalized LFER parameters based on Equations (5–8) are given in Table 3, the fits are plotted in Figure 1 (black lines), and the corresponding calculated p$K_a$ values are listed in columns six and 11 together with their errors in columns seven and 12 of Table 1. Slopes of 0.45 that are identical within the error bars are obtained at both levels of theory, which fit well to that values already obtained in the class-specific LFER fits (cf. Table 2) and match our expectations. Due to the energetic shift in the $\Delta G_{diss}$ values between BP-TZVP and BP-TZVPD-FINE, the value for the intercepts $c_0^{(A)}$ and $c_0^{(B)}$ are larger for the latter level. As for the class-specific fits and due to almost identical slopes, the difference in the intercepts can be used to quantify this shift: 8.1 kJ mol$^{-1}$ for the carboxylic acids (using $c_0^{(A)}$) and 10.0 kJ mol$^{-1}$ for the sulfonamides (using $c_0^{(B)}$). These values lie in between the ones from the previous fits. The combined data set still yields an excellent overall correlation at both levels ($r^2 > 0.95$) with sufficiently small RMSDs of approximately only one third of a logarithmic unit on the p$K_a$ scale. The difference of the intercepts $c_0^{(A)} - c_0^{(B)}$ is 4.091 for BP-TZVP and 4.240 for BP-TZVPD-FINE, which are roughly the same considering the RMSDs or statistical errors of $c_0^{(A)}$ and $c_0^{(B)}$ of around 0.3. Thus, we can indeed use a common LFER parameter for the slope $c_1$ for the combined data set.

The shift in the intercept has two important possible interpretations. On the one hand, this deviation could simply have an experimental origin and be caused by a systematic error, for example, a different calibration with respect to the used p$K_a$ standard that leads to a constant offset on the p$K_a$ scale. However, as already stated before, this should not be the case here since the values for the benzoic acids and sulfonamides were determined by the same authors.[30–34,58] On the other hand, the difference in the intercepts can also reflect errors in the calculated values for $\Delta G_{diss}$ that depend mainly on the substance class, as discussed below.

Including the phenols in an even more general LFER parameter fit is not straightforward due to uncertainties for this subset. The main criterion for achieving a good overall correlation is a consistent slope throughout all subsets. In particular, the data points for 2-nitrophenol (p$K_a = 25.20$) and 2,4,6-trinitrophenol (p$K_a = 9.2$), which also roughly represent the two extremes on the phenol p$K_a$ scale, deviate substantially more from the class-specific linear regression line (cf. Table 1 and Figure 1). These values include the overall shift of 2.9 as explained in the Section 2.2. The non-shifted value of 6.3 for 2,4,6-trinitrophenol served as a reference point in the phenol studies and was originally measured conductometrically,[64] while the value of 22.3 for 2-nitrophenol was determined by potentiometry (glass electrode) as the other phenols. To test if the fit for the phenols is flawed by errors from these two outliers, we did for the BP-TZVP values three additional linear regressions: (i) one where 2-nitrophenol was excluded, (ii) one where we excluded 2,4,6-trinitrophenol, and (iii) one where both were excluded. The results from these restricted fits are plotted in Figure S1 and the obtained parameters are listed in Table S1 of the Supporting Information. Excluding 2,4,6-trinitrophenol from the fit decreases the slope from 1.216 to 0.887, which is closer to the value obtained for the carboxylic acids and benzenesulfonamides, but reduces the correlation parameter significantly from $r^2 = 0.916$ to 0.774. Excluding 2-nitrophenol, on the other hand, slightly improves the correlation ($r^2 = 0.987$) but further increases the slope to 1.398, which deviates even more from the slope for the other subsets. If, however, both data points are excluded, the results do not significantly differ from those for the unaltered fit that includes both points, while maintaining a good correlation (0.958). Hence, there is no clear indication that one of these two data points is more inaccurate than the remaining ones and we decided to continue with both included.

### 3.3 | Analysis of the LFER parameters

For a better comparison, we only refer to our values at the BP-TZVP level. This should also be a reasonable simplification since the results from the generalized fit of the combined data set were found almost identical for both levels of theory except for a constant shift in $\Delta G_{diss}$. We obtained a value of $6.369 \pm 0.289$ for the intercept, which is to some extent in qualitative agreement with the theoretical value of $\lg[S] = -1.134$. However, one should note that any method-dependent error leading to a constant shift in $G_{diss}$ will alter the intercept, hence complicating possible interpretations. Interestingly, we obtain for the LFER parameter for the slope, for the carboxylic acids

and sulfonamides, a value smaller than one ($c_1 \simeq 0.45$), whereas it is larger than and closer to one for the phenols ($c_1 \simeq 1.22$). In previous studies that used COSMO-RS, slopes of 0.58 (for acids)[24] and 0.75 (for bases)[25] were reported for aqueous solutions, while slopes of 0.70 (DMSO)[24] and 0.92 (acetonitrile)[26] were found in organic solvents. This deviation from the ideal slope, $c_1 = 1$, corresponds to an apparent, systematic overestimation of $\Delta G_{diss}$. This phenomenon is not unique to COSMO-RS, but occurs in all first-principles p$K_a$ predictions using simple DCSMs unless significant, but often physically questionable effort is taken to adjust the DCSM parameters (e.g., as pointed out by Chipman[65]). However, it has been argued that including a few explicit solvent molecules does not necessarily lead to better results in terms of increasing the slope toward one since this creates another bias from the exact configuration of these micro-solvated structures.[24] Such hybrid-solvation approaches typically lead to ambiguities and problems in practice: (i) especially for organic solvents, no obvious number of explicit solvent molecules in the solvation shell and (ii) optimization of the solute-solvent structure.[26] Also, the exact correspondence of the experimental p$K_a$ scales to the free energy of dissociation at infinite dilution had been questioned.[24,25]

Reference [26] discussed that the degree of deviation from the ideal behavior is largely solvent-dependent and has its main origin in the solvent's capability of solvating anions, which is also a relevant factor regarding the partitioning of data sets (vide infra). In water, which has the highest anion-solvating ability among the solvents studied with COSMO-RS, the slope has the lowest value (i.e., deviates most from the ideal case), it then increases for DMSO (with moderate stabilization), and finally reaches the largest and closest value for acetonitrile (with lowest stabilization). Precisely quantifying this anion-stabilization ability is difficult since it is a consequence of the overall solvent polarity, a concept that is vividly discussed in the literature.[66] However, we infer that the hydrogen-bond donation ability, for example, as described by the Kamlet-Taft solvent parameter[67] $\alpha$ and the relative dielectric constant $\epsilon_r$, entering the energy expression for Coulomb interactions, should have major effects. Values of $\alpha$ and $\epsilon_r$ are in the following taken from Reference [68]. Whereas water is clearly the most polar solvent in terms of both descriptors ($\alpha = 1.17$, $\epsilon_r = 78.3$), the two contributions show opposite trends for DMSO ($\alpha = 0.00$, $\epsilon_r = 46.5$) and acetonitrile ($\alpha = 0.19$, $\epsilon_r = 35.9$). The order of the solvents (water–DMSO–acetonitrile) as claimed by the authors would thus hint to the dielectric constant having the dominant effect as the more important property, which is reasonable considering the stabilization energy of ions.

Relating to this work, the current results seem to fall even below the water regime (slope of 0.58 for acids) based on our slope of 0.45 from the generalized fit for the combined data set that includes the carboxylic acids and benzenesulfonamides. In terms of the two polarity descriptors, acetone ($\alpha = 0.08$, $\epsilon_r = 20.56$) is expected to have an anion stabilization in between that of DMSO and acetonitrile. Assuming that $\epsilon_r$ is the dominant contribution, the stabilizing effect of acetone should be even smaller compared to that of acetonitrile. However, our results do not fit into this order, which indicates that also other factors seem to affect the slope.

In the current work, we observe a dissection of the molecular data set that at first may appear to be comparable to the observations made for acetonitrile in Reference [26]. The latter study also reported differences between LFER parameters for different molecular classes that could be dealt with by fixing the slope and adjusting a constant offset, and the physical origin was assigned to the degree of charge (de-)localization in the anions. More specifically, the data set reported in Reference [26] is dissected into compounds that newly form an aromatic system after deprotonation (i.e., CH acids) and those with ordinary acidic functional groups where the charge will remain more or less localized (e.g., phenols, carboxylic acids, sulfonic acids, etc.). This idea can also not fully explain the discrepancy observed in our study though since we identified the phenols, that is, strongly delocalized systems as the main exception here. In particular, the phenols are expected to behave very similarly compared to the benzoic acids in terms of charge delocalization via resonance stabilization. However, this idea might actually give us an explanation for the sulfonamides whose deviation from the carboxylic acids was indeed successfully accounted for by a constant shift in the p$K_a$ scale while retaining a common slope (vide supra). The sulfonamides are indeed structurally different from the carboxylic acids and the phenols since both the protonated and the deprotonated structures were found to be non-planar. Therefore, the negative charge of the deprotonated species cannot be stabilized via resonance and remains localized in a lone electron pair at the nitrogen atom of the functional group. Regarding the phenols, we also infer that the zero-point vibrational energy might have a larger contribution compared to the other classes, assuming that the degree of conjugation is much higher for the phenols and hence the vibrations would depend stronger on structural differences that are induced by the deprotonation.

### 3.4 | Special behavior of the phenol subset

For the phenols, it is unclear if the large deviation from the other subsets is due to a systematic error in the experimental data or has an actual physical origin. It does seem that they have a special role in this data set though. For them, the slope is closest to the theoretical value of one, but their results are also affected the most by changing the computational level. In this context, we note that this subset is also the one that covers the largest range of p$K_a$ values. Hence, the absolute differences are naturally much larger when comparing it to the other subsets with relatively smaller p$K_a$ ranges.

In a previous COSMO-RS study on aqueous p$K_a$, the underlying computational methods of the BP-TZVP level, that was also invoked in this work, were already suspected to be insufficient for describing the structural changes of the related compound 4-nitrophenol upon reorganization after deprotonation.[24] For that compound it was found that the deprotonated species adapts a chinoidal form as indicated by a pronounced shortening of the C—O bond lengths, which is accompanied by an overall stronger ionization. A chinoidal form is based on simple resonance considerations equally possible for the

2-nitrophenol and hence our observations might have indeed the same physical origin.

## 4 | CONCLUSIONS

For the 120 organic acids considered in the current work in the solvent acetone, class-specific LFER fits yield very good linear correlations between $\Delta G_{diss}$ computed with COSMO-RS and DFT and the experimental p$K_a$ values within each compound class. The acrylic and benzoic acids could be easily combined with the benzenesulfonamide subset by allowing for an additional offset in the experimental p$K_a$ scale. The resulting combined data set is still highly linearly correlated ($r^2 > 0.95$) and has the same slope of 0.45 at the two levels of theory BP-TZVP and BP-TZVPD-FINE, respectively. That this slope is below the ideal value of 1 is in agreement with previous observations made in the literature[24–26] for water, DMSO, and acetonitrile, although the values do not fit to an ordering of the solvents that would be expected if the deviations from the ideal value of 1 were solely determined by the dielectric constant or the hydrogen-bond donation ability. The constant shift in the p$K_a$ scale between the two subsets reaches at both levels ~4 within the standard deviation. Using these LFER parameters, the mean square deviation with respect to the experimental p$K_a$ values is only ~0.3.

In contrast to the carboxylic acids and benzenesulfonamides, the phenols revealed to be distinctly different. Especially the slope appeared to be larger than one and thus we did not find a natural way to combine this subset with the other ones. Moreover, there seems to be a higher uncertainty in this subset as the data points on the two extremes of the p$K_a$ scale (2-nitrophenol and 2,4,6-trinitrophenol) rather appear to have outlier character. Consequently, these points can affect the LFER parameters significantly if one or both of them are excluded from the fitting process. Having both included, the RMSD of p$K_a$ prediction amounts to 1.7–1.9 for the phenols (with $r^2 \sim 0.9$), which is still satisfying considering the broad range from 9.2 to 26.8. A substantial increase up to almost perfect linear correlation ($r^2 = 0.987$) indicates that excluding 2-nitrophenol from the data set might improve the fit quality. The bad performance of 2-nitrophenol seems to be comparable to problems with the related compound 4-nitrophenol in a preceding study[24] of p$K_a$ in water that was assigned to insufficient accuracy of the underlying electronic structure methods.

### ACKNOWLEDGMENTS

We are grateful to an unknown reviewer for pointing out to us References [30, 31, and 33]. We acknowlegde financial support by the Deutsche Forschungsgemeinschaft through project Ha 2588/8-1. Funded by the Deutsche Forschungsgemeinschaft (DFG, German Research Foundation) under Germany's Excellence Strategy - EXC 2033 - 390677874 - RESOLV. The authors declare the following competing financial interest: Arnim Hellweg is employee of Dassault Systèmes. Dassault Systèmes commercially distributes TURBOMOLE, COSMOtherm, and COSMOconf within the BIOVIA brand.

### DATA AVAILABILITY STATEMENT

The data that support the findings of this study are openly available on Zenodo at https://doi.org/10.5281/zenodo.5676011, reference number 5676011.

### ORCID

*Niklas Sülzner* https://orcid.org/0000-0002-8734-5807
*Julia Haberhauer* https://orcid.org/0000-0002-0100-1959
*Christof Hättig* https://orcid.org/0000-0002-5752-2710
*Arnim Hellweg* https://orcid.org/0000-0002-9508-4889

### REFERENCES

[1] S. Hammes-Schiffer, *J. Phys. Chem. B* **2021**, *125*, 3725.
[2] Y.-Y. Ren, S.-F. Zhu, Q.-L. Zhou, *Org. Biomol. Chem.* **2018**, *16*, 3087.
[3] P. A. Ash, R. Hidalgo, K. A. Vincent, *ACS Catal.* **2017**, *7*, 2471.
[4] M. Shabani, H. Younesi, M. Ponti, A. Rahimpour, M. Rahimnejad, A. A. Zinatizadeh, *J. Clean. Prod.* **2020**, *264*, 121446.
[5] E. F. Caldin, V. Gold, *Proton-Transfer Reactions*, Springer, Boston, MA **2013**.
[6] J. Reijenga, A. van Hoof, A. van Loon, B. Teunissen, *Anal. Chem. Insights* **2013**, *8*, ACI.S12304.
[7] B. Pathare, V. Tambe, V. Patil, *Int. J. Pharm. Pharm. Sci.* **2014**, *6*, 26.
[8] L. Barcza, Á. Buvári-Barcza, *J. Chem. Educ.* **2003**, *80*, 822.
[9] Á. Buvári-Barcza, L. Barcza, *Pharmazie* **2005**, *60*, 243.
[10] L. Soovali, I. Kaljurand, A. Kütt, I. Leito, *Anal. Chim. Acta* **2006**, *566*, 290.
[11] K. S. Alongi, G. C. Shields, in *Annual Reports in Computational Chemistry*, Vol. 6 (Ed: R. A. Wheeler), Elsevier, **2010**, p. 113.
[12] P. G. Seybold, G. C. Shields, *WIREs Comput. Mol. Sci.* **2015**, *5*, 290.
[13] B. Mennucci, *Wiley Interdiscip. Rev.: Comput. Mol. Sci.* **2012**, *2*, 386.
[14] J. Tomasi, B. Mennucci, R. Cammi, *Chem. Rev.* **2005**, *105*, 2999.
[15] A. Klamt, G. Schüürmann, *J. Chem. Soc., Perkin Trans. 2* **1993**, 799.
[16] A. Schäfer, A. Klamt, D. Sattel, J. C. Lohrenz, F. Eckert, *Phys. Chem. Chem. Phys.* **2000**, *2*, 2187.
[17] A. Klamt, *Wiley Interdiscip. Rev.: Comput. Mol. Sci.* **2011**, *1*, 699.
[18] J. R. Pliego, *Chem. Phys. Lett.* **2003**, *367*, 145.
[19] R. Casasnovas, J. Ortega-Castro, J. Frau, J. Donoso, F. Muoz, *Int. J. Quantum Chem.* **2014**, *114*, 1350.
[20] A. Klamt, *J. Phys. Chem.* **1995**, *99*, 2224.
[21] A. Klamt, V. Jonas, T. Bürger, J. C. Lohrenz, *Chem. A Eur. J.* **1998**, *102*, 5074.
[22] F. Eckert, A. Klamt, *AIChE J* **2002**, *48*, 369.
[23] A. Klamt, F. Eckert, W. Arlt, *Annu. Rev. Chem. Biomol. Eng.* **2010**, *1*, 101.
[24] A. Klamt, F. Eckert, M. Diedenhofen, M. E. Beck, *Chem. A Eur. J.* **2003**, *107*, 9380.
[25] F. Eckert, A. Klamt, *J. Comput. Chem.* **2006**, *27*, 11.
[26] F. Eckert, I. Leito, I. Kaljurand, A. Kütt, A. Klamt, M. Diedenhofen, *J. Comput. Chem.* **2009**, *30*, 799.
[27] BIOVIA COSMOtherm, Release **2020**; Dassault Systèmes. http://www.3ds.com.
[28] K. Izutsu, *Acid-base dissociation constants in dipolar aprotic solvents, 1st edn.* Blackwell Scientific Publications, Oxford. **1990**.
[29] A. M. Slater, *J. Comput. Aided Mol. Des.* **2014**, *28*, 1031.
[30] M. Ludwig, V. Baron, K. Kalfus, O. Pytela, M. Večeřa, *Collect. Czechoslov. Chem. Commun.* **1986**, *51*, 2135.
[31] O. Pytela, J. Liška, *Collect. Czechoslov. Chem. Commun.* **1994**, *59*, 2005.
[32] J. Kulhánek, O. Pytela, *Collect. Czechoslov. Chem. Commun.* **1997**, *62*, 913.
[33] O. Pytela, J. Kulhánek, M. Ludwig, V. Říha, *Collect. Czechoslov. Chem. Commun.* **1994**, *59*, 627.
[34] O. Pytela, J. Kulhánek, M. Ludwig, *Collect. Czechoslov. Chem. Commun.* **1994**, *59*, 1637.

[35] J. Knorr, N. Sülzner, B. Geissler, C. Spies, A. Grandjean, R. J. Kutta, G. Jung, and P. Nuernberger **2022**. In Press.
[36] N. Sülzner, B. Geissler, A. Grandjean, G. Jung, and P. Nuernberger (**2022**), https://doi.org/10.1002/cptc.202200041R2
[37] S. K. Khani, A. M. Khah, C. Hättig, *Phys. Chem. Chem. Phys.* **2018**, *20*, 16354.
[38] S. K. Khani, A. M. Khah, C. Hättig, *J. Chem. Theory Comput.* **2020**, *16*, 4554.
[39] A. Hellweg, F. Eckert, *AIChE J* **2017**, *63*, 3944.
[40] K. Eichkorn, O. Treutler, H. Öhm, M. Häser, R. Ahlrichs, *Chem. Phys. Lett.* **1995**, *240*, 283.
[41] O. Treutler, R. Ahlrichs, *J. Chem. Phys.* **1995**, *102*, 346.
[42] TURBOMOLE V7.3, A development of University of Karlsruhe and Forschungszentrum Karlsruhe GmbH, 1989–2007, TURBOMOLE GmbH 2007, **2018**; http://www.turbomole.com.
[43] BIOVIA COSMOconf, Release 2020; Dassault Systèmes. http://www.3ds.com.25
[44] A. D. Becke, *Phys. Rev. A* **1988**, *38*, 3098.
[45] J. P. Perdew, *Phys. Rev. B* **1986**, *33*, 8822.
[46] A. Schäfer, C. Huber, R. Ahlrichs, *J. Chem. Phys.* **1994**, *100*, 5829.
[47] K. Eichkorn, F. Weigend, O. Treutler, R. Ahlrichs, *Theor. Chem. Accounts* **1997**, *97*, 119.
[48] D. Rappoport, F. Furche, *J. Chem. Phys.* **2010**, *133*, 134105.
[49] A. Klamt, M. Diedenhofen, *J. Comput. Chem.* **2018**, *39*, 1648.
[50] N. Sülzner, J. Haberhauer, C. Hättig, and A. Hellweg, Raw Data to "Prediction of acid pKa values in the solvent acetone based on COSMO-RS" (**2022**), https://doi.org/10.5281/zenodo.5676011.
[51] J. J. Klicić, R. A. Friesner, S.-Y. Liu, W. C. Guida, *Chem. A Eur. J.* **2002**, *106*, 1327.
[52] F. Himo, L. Noodleman, M. R. A. Blomberg, P. E. M. Siegbahn, *Chem. A Eur. J.* **2002**, *106*, 8757.
[53] L. Rottmannová, P. Škorňa, J. Rimarčík, V. Lukeš, E. Klein, *Acta Chim. Slov.* **2013**, *6*, 60.
[54] J. Rimarčík, V. Lukeš, E. Klein, M. Ilčin, *J. Mol. Struct. THEOCHEM* **2010**, *952*, 25.
[55] I. A. Topol, G. J. Tawa, S. K. Burt, A. A. Rashin, *J. Chem. Phys.* **1999**, *111*, 10998.
[56] V. P. Barabanov, V. M. Tsentovskii, A. Y. Tret'yakova, *Russ. J. Phys. Chem.* **1973**, *47*, 1304.
[57] B. Nowak, Z. Pawlak, *Pol. J. Chem.* **1981**, *55*, 2407.
[58] M. Ludwig, O. Pytela, M. Večeřa, *Collect. Czechoslov. Chem. Commun.* **1986**, *51*, 1948.
[59] M. Foltin, P. Majer, *Collect. Czechoslov. Chem. Commun.* **1978**, *43*, 95.
[60] A. Kütt, I. Leito, I. Kaljurand, L. Sooväli, V. M. Vlasov, L. M. Yagupolskii, I. A. Koppel, *J. Org. Chem.* **2006**, *71*, 2829.
[61] A. Kütt, S. Tshepelevitsh, J. Saame, M. Lõkov, I. Kaljurand, S. Selberg, and I. Leito, *Eur. J. Org. Chem.* **2021**, 1407, *2021*.
[62] M. D. Liptak, K. C. Gross, P. G. Seybold, S. Feldgus, G. C. Shields, *J. Am. Chem. Soc.* **2002**, *124*, 6421.
[63] M. D. Liptak, G. C. Shields, *J. Am. Chem. Soc.* **2001**, *123*, 7314.
[64] C. French, I. Roe, *Trans. Faraday Soc.* **1953**, *49*, 314.
[65] D. M. Chipman, *Chem. A Eur. J.* **2002**, *106*, 7413.
[66] C. Reichardt, *Chem. Rev.* **1994**, *94*, 2319.
[67] M. J. Kamlet, J. L. M. Abboud, M. H. Abraham, R. Taft, *J. Org. Chem.* **1983**, *48*, 2877.
[68] C. Spies, B. Finkler, N. Acar, G. Jung, *Phys. Chem. Chem. Phys.* **2013**, *15*, 19893.

## SUPPORTING INFORMATION

Additional supporting information may be found in the online version of the article at the publisher's website.

**How to cite this article:** N. Sülzner, J. Haberhauer, C. Hättig, A. Hellweg, *J. Comput. Chem.* **2022**, *43*(15), 1011. https://doi.org/10.1002/jcc.26864

# 6. Theoretical Spectroscopy in DMSO

This sub-project now turns the focus to the electronic excitation energies that are needed as the other input quantities for calculating $pK_a^*$ based on the Förster cycle. In contrast to the experiments in Chapters 3–4 that have been done in acetone, this theoretical study is performed for the solvent DMSO, chosen for the following reasons: (i) Availability of experimental reference spectra and (ii) promising performance with the implicit solvent model COSMO. By choosing the implicit solvent model COSMO, the solvation treatment is restricted to purely electrostatic solute–solvent interactions. For computing the vertical electronic transition energies, the wavefunction-based methods ADC(2) and CC2 are chosen. Prior to productive calculations, a validation of the performance of these selected methods (with respect to the agreement with experimental reference data) has been necessary.

First, the effect of different methods and basis sets is studied to demonstrate that excitation energies using ADC(2) or CC2 in the aug-cc-pVDZ basis set calculated at COSMO-MP2/cc-pVDZ geometries give sufficiently accurate results. Second, energetic and structural contributions to the excitation energies are disentangled based on a detailed analysis of different combinations of COSMO, ADC(2), and CC2 for both the equilibrium geometries and excitation energies in the gas phase and in solution, as well as in the ground state and the excited state. Third, the selected methods are applied to the calculation of UV/Vis absorption and fluorescence emission spectra of Jung's photoacids, which gives access to $\Delta pK_a$. Finally, $\Delta pK_a$ in combination with COSMO-RS-based $pK_a$ is used to calculate $pK_a^*$. The results are discussed in terms of relative trends and differences between the individual photoacids. In addition, the electronic structure calculations allow for insights into the origin of photoacidity for these compounds and also reveal an interesting solvent dependence of $\Delta pK_a$.

This part has been performed under the supervision of Prof. Dr. Christof Hättig. The idea of validating our methods in DMSO was largely shaped by myself. I am responsible for carrying out the calculations, analyzing the results, and preparing the first draft of the manuscript which was further developed together with Prof. Dr. Christof Hättig. Moreover, I took over the correspondence during the publication process.

The following publication is reprinted with permission from: N. Sülzner and C. Hättig. Theoretical Study on the Photoacidity of Hydroxypyrene Derivatives in DMSO Using ADC(2) and CC2. *J. Phys. Chem. A* **2022**, *126* (35), 5911–5923. **Copyright © 2022 American Chemical Society**. The corresponding supporting information can be found in Section B.3. This publication is also available online: `https://doi.org/10.1021/acs.jpca.2c04436`.

THE JOURNAL OF PHYSICAL CHEMISTRY A
A JOURNAL OF THE AMERICAN CHEMICAL SOCIETY

pubs.acs.org/JPCA Article

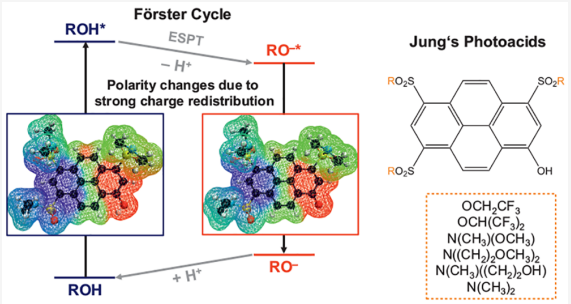
# Theoretical Study on the Photoacidity of Hydroxypyrene Derivatives in DMSO Using ADC(2) and CC2

Niklas Sülzner* and Christof Hättig

Cite This: J. Phys. Chem. A 2022, 126, 5911−5923 Read Online

ACCESS | Metrics & More | Article Recommendations | Supporting Information

**ABSTRACT:** This work applies the thermodynamic Förster cycle to theoretically investigate the $pK_a^*$, i.e., excited-state $pK_a$ values of pyranine-derived superphotoacids developed by Jung and co-workers. The latter photoacids are strong enough to transfer a proton to the aprotic solvent dimethyl sulfoxide (DMSO). The Förster cycle provides access to $pK_a^*$ via the ground-state $pK_a$ and the electronic excitation energies. We use the conductor-like screening model for real solvents (COSMO-RS) to compute the ground-state $pK_a$ and the correlated wavefunction-based methods ADC(2) and CC2 with the continuum solvation model COSMO to calculate the $pK_a$ change upon excitation. A comparison of the calculated UV/Vis absorption and fluorescence emission energies to the experimental results leads us to infer that this approach allows for a proper description of the electronic excitations. In particular, implicit solvation by means of the COSMO model appears to be sufficient for the treatment of these photoacids in DMSO. The calculations confirm the presumption that a charge redistribution from the hydroxy group to the aromatic ring and the electron-withdrawing substituents is the origin of photoacidity for these photoacids. Moreover, the calculations with the continuum solvation model predict that the $pK_a$ jump upon excitation decreases with increasing solvent polarity, as rationalized based on the Förster cycle.

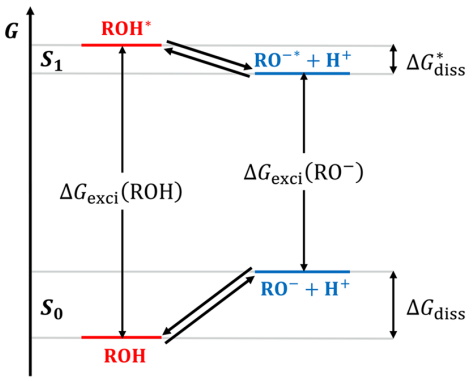



## INTRODUCTION

Proton transfer belongs to the most important elementary reactions taking part in various chemical, biochemical, and biological processes.[1−3] To elucidate the precise mechanisms of proton-transfer reactions, i.e., possible intermediates such as contact ion pairs and rate constants of the individual steps, so-called photoacids have proven particularly powerful tools.[4−22] These photoacids are molecules that exhibit an acidity increase, i.e., a decrease in $pK_a$, upon electronic excitation, which can trigger an excited-state proton transfer (ESPT) to a suitable proton acceptor.[23,24] Due to limited acid strengths, the use of most photoacids was restricted to the study of ESPT in water[4] or aqueous solutions containing either an additional base[5] or a cosolvent.[6−9] Only special photoacids, referred to as super-photoacids, are particularly strong and exhibit in water negative $pK_a$ values in the excited state,[25−28] which often also allows them to perform an ESPT in neat protic[10−12] or even aprotic solvents.[13−22]

Originally, it was Förster who pointed out that photoacidity can be explained by a thermodynamic cycle that includes the proton-transfer equilibria for the electronic ground and the excited state.[29,30] Based on this so-called Förster cycle (Scheme 1), the excited-state $pK_a$ value, from now on denoted $pK_a^*$, can be obtained from the ground-state $pK_a$ value and the Gibbs free energy differences between the ground and the excited state of the acid (ROH) and its conjugate base ($RO^-$):

**Scheme 1. Förster Cycle**




Received: June 27, 2022
Revised: August 3, 2022
Published: August 29, 2022



© 2022 The Authors. Published by American Chemical Society

$$pK_a^* = pK_a + \frac{\Delta G_{exci}(RO^-) - \Delta G_{exci}(ROH)}{RT \ln(10)} \quad (1)$$

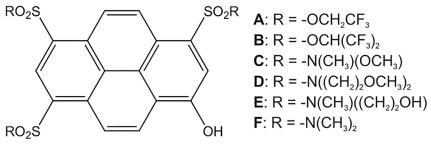
with the excitation Gibbs free energies $\Delta G_{exci}(ROH)$ and $\Delta G_{exci}(RO^-)$ of the two species, the ideal gas constant $R$, and the absolute temperature $T$. If used to calculate $pK_a^*$, the accuracy of the results thus depends on the accuracy of these input quantities. Nevertheless, it is the standard approach to determine $pK_a^*$ in experimental as well as in theoretical investigations since it is usually not possible to measure $pK_a^*$ as an equilibrium quantity.

Measurements of $pK_a$ values are in particular difficult in nonaqueous, aprotic solution.[31−33] For these solvents, theoretical $pK_a$ prediction tools are crucial.[34,35] Different methods are nowadays available,[36,37] including the conductor-like screening model for real solvents (COSMO-RS).[38−42] COSMO-RS is an extension of the conductor-like screening model (COSMO)[43,44] to reintroduce specific solute−solvent interactions and it has been already successfully applied to $pK_a$ calculations in water,[45,46] dimethyl sulfoxide (DMSO),[45] acetonitrile,[47] and acetone.[48]

Until today, only few examples of theoretical $pK_a^*$ predictions are reported in the literature, using quantum chemical calculations[49−56] as well as molecular dynamics (MD) simulations with hybrid quantum-mechanics/molecular-mechanics (QM/MM) techniques.[57−60] Some theoretical studies on photoacids also attempt to directly address the ESPT process by modeling its reaction mechanism or providing information on the molecular factors governing photoacidity, e.g., the electronic structure.[61−69] Recently, also the first *ab initio* (QM/MM) MD simulations on the excited-state dynamics of photoacids were reported, e.g., on the vibrational dynamics of 8-hydroxypyrene-1,3,6-trisulfonate (HTPS or pyranine) in neat water[70,71] or acetate-containing aqueous solution,[72,73] the ESPT dynamics of HPTS in 1-methylimidazole[74] or water,[75] and the ESPT dynamics of the superphotoacid quinone cyanine 9 (QCy9) in water.[76] However, all of these have in common that they are typically limited to time-dependent density functional theory (TDDFT) for the description of electronic excitations, which gives sometimes wrong shapes for the excited state potential energy curves.[77] Apart from the known deficiency of TDDFT regarding charge-transfer excitations, which could be avoided by using long-range-adapted functionals such as CAM-B3-LYP, the rather low accuracy in excitation energies still remains a problem. In the extreme, this can lead to qualitatively wrong results, e.g., a different order of the excited states as recently reported by Acharya et al. for the photoacid naphthol.[78] To the best of our knowledge, no comparable approach to the full $pK_a^*$ beyond TDDFT that uses accurate correlated wavefunction-based methods (e.g., the algebraic diagrammatic construction scheme through second order ADC(2) or the approximate coupled cluster singles and doubles method CC2) instead has yet been reported.

In this study, we focus on the non-charged HPTS derivatives introduced by Jung and co-workers (Scheme 2).[14] These are obtained by functionalizing the sulfonate groups with electron-withdrawing ester (**A**−**B**) and amide (**D**−**F**) moieties. The solvatochromic properties[15] as well as ESPT kinetics[14,16] have been studied experimentally in a variety of solvents including water, methanol, ethanol, and DMSO. Recently, the dynamics and ESPT intermediates of a strongly hydrogen-bonded complex of compound **A** with a trialkylphosphine oxide in nitrile solution were elucidated.[79,80] Furthermore, for the strongest superphotoacid **B** of that class, namely tris-(1,1,1,3,3,3-hexafluoropropan-2-yl)-8-hydroxypyrene-1,3,6-trisulfonate ($pK_a^* \approx -4$ in water),[14] the possibility of ESPT in acetone−water mixtures[81] and in neat acetone were demonstrated.[82] Despite the wealth of experimental knowledge regarding this photoacid, only limited information on the molecular origin of the exceptionally high photoacidity is yet available in the literature.

**Scheme 2. Molecular Structures of Jung's Photoacids A−F with the Different Substituents R**




Here we apply the Förster cycle to theoretically predict the $pK_a^*$ values of these pyranine-derived photoacids in the polar, aprotic solvent DMSO, which we choose because of the amount of experimental spectroscopic reference data for this class of photoacids in this solvent. Moreover, from a computational point of view, this solvent is a good compromise in accuracy for the implicit solvent model COSMO as it is both aprotic and polar. As a dielectric continuum solvation model, COSMO is restricted to purely electrostatic solute−solvent interactions and poorly describes specific interactions, e.g., hydrogen bonding. This approach provides access to $pK_a^*$ via the ground-state $pK_a$ and the electronic excitation energies. To the best of our knowledge, this is the first attempt that uses highly accurate wavefunction-based methods for $pK_a^*$ prediction.

First, a brief comparison of calculations at different levels of theory for the geometries and excitation energies is used to establish our defaults for computing electronic UV/Vis absorption and emission spectra. These tools are then used to thoroughly review the results for one selected photoacid with the methods ADC(2) and CC2 with and without COSMO to disentangle individual effects on the electronic excitation energies. Next, we compare the calculated UV/Vis absorption and fluorescence emission energies in DMSO with experimental spectra to quantify the accuracy of the results. Here, the focus will be on the differences between absorption and emission spectra, and between the protonated and deprotonated species. Finally, we compute $pK_a^*$ values of the photoacids in DMSO using the calculated results and analyze the individual contributions to and the solvent effect on this quantity.

## METHODS

All electronic structure calculations were done with the TURBOMOLE program package (version 7.4).[83,84] Second order Møller−Plesset perturbation theory (MP2), ADC(2), and CC2 calculations (with the ricc2 program) routinely used the resolution-of-the-identity (RI) approximation for the electron repulsion integrals and the frozen-core approximation for the 1s orbitals at C, N, O, F and the 1s2s2p orbitals at S. The integral screening threshold for the MO calculations ($scftol) was lowered to $10^{-15}$ to ensure convergence with diffuse basis functions. Solution-phase calculations refer to the solvent DMSO as described by the COSMO model with $\epsilon_r = 46.45$ for the (relative) dielectric constant and $n = 1.479$ for the refractive index. Default cavity parameters were used unless stated differently. For the calculation of electronic excitation



https://doi.org/10.1021/acs.jpca.2c04436
J. Phys. Chem. A 2022, 126, 5911−5923

**Table 1. Comparison of Vertical Electronic Excitation Energies in eV for the First Transition with Different Combinations of Equilibrium Structures for $S_0$ or $S_1$ (Rows) and Methods for the Calculation of the Electronic Excitation Energy (Columns) of the Protonated and Deprotonated Species of Photoacid F**

| | | excitation energies | | | |
|---|---|---|---|---|---|
| | geometries | ADC(2) | COSMO-ADC(2) | CC2 | COSMO-CC2 |
| | | | acid | | |
| $S_0$ | MP2 | 3.108 | 2.975 | 3.168 | 3.016 |
| | COSMO-MP2 | 3.096 | 2.957 | 3.156 | 2.999 |
| | CC2 | 3.067 | 2.929 | 3.130 | 2.975 |
| | COSMO-CC2 | 3.055 | 2.910 | 3.120 | 2.958 |
| $S_1$ | ADC(2) | 2.765 | 2.602 | 2.862 | 2.690 |
| | COSMO-ADC(2) | 2.733 | 2.547 | 2.844 | 2.655 |
| | CC2 | 2.759 | 2.599 | 2.852 | 2.683 |
| | | | base | | |
| $S_0$ | MP2 | 2.171 | 2.134 | 2.350 | 2.251 |
| | COSMO-MP2 | 2.160 | 2.174 | 2.350 | 2.283 |
| | CC2 | 2.143 | 2.107 | 2.329 | 2.229 |
| | COSMO-CC2 | 2.135 | 2.135 | 2.332 | 2.253 |
| $S_1$ | ADC(2) | 0.928 | 1.631 | 1.356 | 1.682 |
| | COSMO-ADC(2) | 1.999 | 2.001 | 2.219 | 2.129 |
| | CC2 | 1.953 | 1.989 | 2.178 | 2.102 |

energies with ADC(2) and CC2 in combination with COSMO, the post-SCF coupling scheme was used, as first introduced in ref 85 for the polarizable embedding model and later also combined with COSMO and compared in ref 86 to other reaction field coupling schemes. The notation A//B refers to an electronic excitation energy computed at a level A using a geometry optimized at a level B. For visualization of electronic excitations, natural transition orbitals (NTOs) were plotted at contour values of −0.05 (red) and +0.05 (blue). Further details on the individual calculations, e.g., the basis sets, are given below and in the Supporting Information. All structures together with their Hartree−Fock energies are available from ref 87.

For the calculation of p$K_a$, initial conformer searches were done to account for the conformational flexibility of the studied photoacids. This was taken care of by using COSMO*conf* (version 2021)[88] in combination with its BP-TZVPD-FINE-COSMO+GAS_18 template. Additional information on the results from the conformer search is given in the Supporting Information (see Tables S1 and S2). The full sets of conformers for both the protonated and deprotonated species of the photoacids were used for the calculation of p$K_a$, while only a single conformer was considered for the electronic excitation energies since the later are insensitive to conformational changes in the substituents at the sulfonate groups. COSMO-RS as implemented in COSMO*therm* (version 2021)[89] was used to calculate p$K_a$ in DMSO and water at the BP-TZVP and BP-TZVPD-FINE levels of theory (e.g., see ref 90 for further details). The main difference between these two is that the latter uses refined energies calculated in the larger def2-TZVPD basis set and with a smooth radii-based isosurface for COSMO.[91] At its core, COSMO*therm* uses a linear free-energy relationship (LFER) between p$K_a$ and the calculated Gibbs free energy difference in solution (soln.) between $RO^-$ and ROH, obtained with COSMO-RS,

$$pK_a = a + b(G_{soln.}(RO^-) - G_{soln.}(ROH)) \quad (2)$$

where $a$ and $b$ are the implemented LFER parameters that were originally derived from a linear fit to experimental p$K_a$ values in the given solvent.[89] $G_{soln.}(RO^-)$ and $G_{soln.}(ROH)$ were calculated according to the procedure described in refs 45−48. All calculations involving p$K_a$ refer to a temperature $T$ of 298.15 K (25 °C).

For investigating the importance of the ground-state singles amplitudes, i.e., the difference between MP2 or ADC(2) and CC2, and the role of direct and indirect solvent effects via the molecular structure on the lowest excitation energy, we performed a series of calculations on the protonated and deprotonated forms of compound **F** (compare Scheme 2). The ground-state geometries were optimized in the cc-pVDZ basis set[92,93] using MP2[94,95] or CC2[96] for the gas phase and in combination with COSMO, COSMO-MP2[97] and COSMO-CC2,[98] also for the solution phase. Similarly, the geometries for the first excited state were optimized in the cc-pVDZ basis set using ADC(2)[96] and CC2[99] for the gas phase and COSMO-ADC(2)[98] for the solution phase. The vertical electronic excitation energies were calculated in the larger aug-cc-pVDZ basis set[93,100] at the gas-phase ADC(2)[101] and CC2[102] as well as solution-phase COSMO-ADC(2)[98] and COSMO-CC2[98] levels. COSMO-CC2//COSMO-ADC(2) excitation energies for the excited state are used as estimates for the COSMO-CC2//COSMO-CC2 results. The obtained excitation energies for the first vertical transitions are given in Table 1.

## METHOD VALIDATION

Prior to a systematic study on the whole set of Jung's photoacids, we extensively tested our selected methods on the protonated (acid) and deprotonated (base) forms of compound **F** (cmp. Scheme 2). We studied the convergence of the ground-state geometries with the methods and basis sets, the convergence of the electronic excitation energies with the basis-set size, and the difference between ADC(2) and CC2 excitation energies. The corresponding results and further computational details are given in the Supporting Information, and only the main aspects will be briefly summarized here.

**Convergence of the Excitation Energies with the Ground-State Geometries and Basis Sets.** Geometry optimizations with different DFT functionals and MP2 with different basis sets (see Table S3) show that the method for the ground-state structure has only a small effect (≲0.1 eV) on the ADC(2)/aug-cc-pVDZ excitation energies. We thus decided to



https://doi.org/10.1021/acs.jpca.2c04436
J. Phys. Chem. A 2022, 126, 5911−5923

use—if nothing else is stated—MP2/cc-pVDZ as the method for the geometry optimizations because of two reasons: First, MP2 for the ground state will allow for a consistent description with ADC(2) for the excited-state later on. Second, when treating electronically excited states, we will be restricted to smaller basis sets such as cc-pVDZ due to the computational costs of the excited-state geometry optimizations.

We then compared the ADC(2) excitation energies for the first five vertical transitions in different basis sets (see Table S4). Based on the results, we chose the aug-cc-pVDZ basis as a compromise between accuracy and computational costs. The excitation energies for the lowest excited states obtained with this basis set deviate from the results in the aug-cc-pVQZ basis by ≈0.04 eV for the acid and by ≈0.03 eV for the base, which is considerably smaller than the methodical error of ≈0.1 eV for ADC(2) and CC2 (for $S_1$ in organic chromophores with single-reference ground states relative to the Full-CI limit). Besides, not the absolute excitation energies, but the acid−base energy difference will be of interest for the excited-state p$K_a$ prediction (*vide infra*). Here, we observe a difference between aug-cc-pVDZ and aug-cc-pVQZ for the acid−base difference of only 7 meV, which is probably an order of magnitude smaller than the error due to the electronic structure method and the solvation treatment. According to eq 1, such an error of less than 10 meV in excitation energy corresponds to an error of only 0.17 p$K_a$ units.

With ADC(2)/aug-cc-pVDZ for electronic excitation energies and MP2/cc-pVDZ for the geometry optimizations, we thus use a combination of closely related methods and basis sets. Moreover, aiming at a comparison of calculated and experimental spectra (*vide infra*), other sources of error, in particular regarding the solvation treatment, arise in any case and are expected to be larger than the remaining basis set errors.

**Difference between ADC(2) and CC2 Excitation Energies.** It turned out that for the lowest excited state in the pyranine-based photoacids the differences between ADC(2) and CC2 are not completely negligible. For the acid, a systematic blue shift of the CC2 compared to the ADC(2) excitation energies at identical geometries is observed. This shift is at the $S_0$ equilibrium structure in the gas phase about 60 meV and between 40 and 60 meV in solution. At the $S_1$ equilibrium structure, the differences are larger, between 80 and 110 meV (compare with Table 1). The largest difference between CC2 and ADC(2) is found at the COSMO-ADC(2) geometry for $S_1$, amounting to about 110 meV.

Also the differences in the equilibrium structures obtained with CC2 and MP2 ($S_0$) or ADC(2) ($S_1$) affect the excitation energies, as can be seen by comparing excitation energies for the same method but different geometries (columns in Table 1). The excitation energies obtained at the MP2 and COSMO-MP2 structures for $S_0$ are 35−60 meV higher compared to those at CC2 and COSMO-CC2. For the gas-phase $S_1$ equilibrium structures, this deviation is much smaller (≤10 meV) with almost coinciding excitation energies. Since excited-state gradients for COSMO-CC2 are not available, we could not optimize the $S_1$ structure at this level. The above result, however, gives us reason to assume that the corresponding excited-state structures in solution will be similar as well and hence that COSMO-CC2 excitation energies at the COSMO-ADC(2) geometries will be a good approximation for the COSMO-CC2 excitation energies at the COSMO-CC2 $S_1$ structure.

For the base, similar results are obtained, i.e.,

- a systematic, but considerably larger blue shift of CC2 vs ADC(2): ≈ 190 meV (gas phase) and ≈110 eV (solution phase) for $S_0$ and >200 meV (gas phase) and >110 meV (solution phase) for $S_1$;
- only minor differences between the excitation energies at the MP2 and CC2 ground-state geometries of only ≈20 meV (gas phase) and 20−30 meV (solution phase).

However, there are also distinct differences between the spectroscopic properties of the acid and the base. ADC(2) fails for the excited-state geometry optimization of the base in the gas phase, yielding a nonphysically small excitation energy in the near-infrared region (≫ 800 nm). Interestingly, this issue does not seem to occur in solution, i.e., in combination with COSMO. The COSMO-ADC(2) geometry results in excitation energies that are close to that for the CC2 equilibrium structure. The ADC(2) failure for the excited state in the gas phase is presumably related to the negative charge of the base, on which the solvent has a significant stabilizing effect. The main issue with ADC(2) in the gas phase seems to be a different order of the excited states in the different media: In the gas phase, the first excitation is no longer a HOMO−LUMO (*vide infra*) but a HOMO-3−LUMO transition, which occurs in solution only as the third excitation.

The general deviations between ADC(2) and CC2 excitation energies observed here for photoacid **F** are mainly due to missing contributions in the description of the electronic ground state for ADC(2) which is described as for MP2 using the first-order correction (MP1) to the wave function, including only double excitations out of the (closed-shell) Hartree−Fock reference determinant. Contributions from singly excited determinants to the ground state are missing. For the pyranine derivatives, the single excitation from the HOMO to the LUMO makes, however, a contribution to the correlated ground-state that is not completely negligible, which can be tested by checking the natural transition orbitals (NTOs) generated from the (ground-state) CC2 $T_1$ amplitudes (see Figure S1). For both the acid and base, the dominant NTO pair resembles that for the first excitation, $S_1$, especially the virtual NTO, indicating that these orbitals are already partially occupied in the ground state. Moreover, the weights of these NTOs are slightly larger for the base (14.2%) compared to the acid (11.3%); i.e., the need for the singles contribution for an accurate description of the ground state is more pronounced for the base. The neglect of these contributions in ADC(2) leads to an underestimation of the excitation energy for $S_1$.

## SOLVENT EFFECTS: DISENTANGLING ENERGETIC AND STRUCTURAL CONTRIBUTIONS TO THE EXCITATION ENERGIES

After having selected MP2/cc-pVDZ for the ground-state geometries and ADC(2)/aug-cc-pVDZ for excitation energies for our purposes, we turn our focus on the structural and energetic solvent contributions to the excitation energies of the protonated and deprotonated species of photoacid **F**.

**Limitations of Continuum Solvation with COSMO.** In general, the COSMO-related error in excitation energies typically varies over a broad range, depending on the polarity and proticity of the solvent. For the combinations of COSMO with ADC(2) or CC2 based on the post-SCF coupling scheme, we expect errors compared to experimental data of 0.05−0.07 eV in DMSO based on the reported errors in solvatochromic shifts in water and acetonitrile.[86] This error is significantly larger



https://doi.org/10.1021/acs.jpca.2c04436
J. Phys. Chem. A 2022, 126, 5911−5923

than the remaining basis set contributions and could amount to up to one p$K_a$ unit. While the COSMO error is generally larger for protic—and at the same time often strongly polar—solvents due to the lack of describing H-bond interactions between the solute and the solvent, the accuracy of COSMO is also for nonpolar solvents limited by the neglect of London dispersion and Pauli repulsion interactions. DMSO, as a polar and aprotic solvent, thus appears to be a suitable solvent for COSMO, with only the H-bond acceptance of the solvent missing in the description. Since DMSO is no significant H-bond donor, we expect the largest explicit solvation effects via specific interactions on the protonated, rather than the deprotonated species.

**Stokes and Solvatochromic Shifts of the Acid.** The Stokes shift, i.e., the difference in absorption and fluorescence emission energies of a given species, is of particular importance for photoacidity. Calculated absorption and emission energies refer to excitation energies at the ground-state ($S_0$) and excited-state ($S_1$) equilibrium geometries. From a comparison of the absorption and emission energies in Table 1, we obtain for the Stokes shifts values of 343 meV for ADC(2) and 278 meV for CC2 in the gas phase and, respectively, 410 and 303 meV in the solution phase. Hence, the Stokes shift of the acid appears to be larger in solution, but overall smaller for CC2.

Another interesting aspect are solvatochromic effects which can be determined from the gas-phase and solution-phase absorption and emission energies (diagonal elements of each $S_0$ and $S_1$ block in Table 1). Whereas bathochromic, i.e., solvatochromic red shifts of 151 and 172 meV are obtained for the vertical excitation energies at the ground-state structures for ADC(2) and CC2, respectively, the solvatochromic shifts are larger for the vertical transition energies at the excited-state structure rising to 218 and 197 meV. This finding is in accordance with a strong charge redistribution upon excitation of the photoacid, which increases the polarity (*vide infra*).

To separate structural and energetic effects on the excitation energy, we can compare COSMO-ADC(2)//MP2 (2.975 eV) with COSMO-ADC(2)//COSMO-MP2 (2.957 eV) energies which demonstrate that the ground-state solvatochromism is mainly due to a purely energetic effect on the excitation energy itself, rather than a structural effect. Only 18 meV are missing referring to the value in solution if the COSMO-ADC(2) excitation energy is calculated at the MP2 gas-phase geometry. Similar results are obtained for CC2: also COSMO-CC2//CC2 (2.975 eV) differs from COSMO-CC2//COSMO-CC2 (2.958 eV) by only 17 meV. For the excited-state solvatochromism, the largest contribution is again due to direct energetic effects, but the difference between COSMO-ADC(2)//ADC(2) and COSMO-ADC(2)//COSMO-ADC(2) is comparably larger (55 meV).

**Stokes and Solvatochromic Shifts of the Base.** For the base, the results for the Stokes shifts are in the gas phase 151 meV for CC2 and in the solution phase 173 meV for ADC(2) and 124 meV for CC2. For the solvatochromic shifts, we obtained −3 meV with ADC(2) and +76 meV with CC2 for the vertical transition at the ground-state structure and 49 meV with CC2 for the vertical transition at the excited-state equilibrium structure. The unreliable ADC(2) excited-state geometry prevents an analysis of structural similarities, Stokes shifts, and solvatochromic shifts for ADC(2) as consistently is done above for the acid. As a replacement for the ADC(2)//ADC(2) energy, either the ADC(2)//CC2 result, assuming structural similarities between the methods, or the ADC(2)//COSMO-ADC(2) result, assuming negligible solvent effects on the structures, could be used. Using the former result, as supported by the smaller energy deviation observed for excited-state acid, we can estimate the ADC(2) gas-phase Stokes shift to be 218 meV and the excited-state solvatochromic shift to be −48 meV. The Stokes shift hence again appears to be smaller in solution compared to the gas phase and smaller for CC2 compared to ADC(2), as observed for the acid.

Furthermore, both the ground-state and excited-state solvatochromism of the base do not show a clear trend at these levels since the shift is bathochromic for CC2, but hypsochromic for ADC(2). Still, both results are much smaller in magnitude compared to the acid, indicating that the polarity difference between the ground and excited state seems either less pronounced or even reversed. This is in accordance with the experiments where bathochromic shifts are observed for the protonated as well as methylated photoacids, whereas pronounced hypsochromic shifts are observed for the deprotonated species.[15] This bathochromism is furthermore known to increase linearly as a function of the Kamlet−Taft dipolarity and polarizability parameter $\pi^*$, while this hypsochromism increases as a function of the Kamlet−Taft parameter $\alpha$ for the hydrogen-bond donating ability of the solvent. While the latter is not well described by COSMO as it is a pure continuum solvation model, its effect in DMSO is still considered negligible due to the lacking H-bond donating ability ($\alpha$ = 0).[15] Rather, H-bonding interactions between the protonated photoacid acting as the donor and DMSO acting as the acceptor are anticipated to have a somewhat larger effect, e.g., as judged based on the large Kamlet−Taft H-bond accepting ability $\beta$ for DMSO (0.76),[15] although the correlation of excited-state acidity with $\beta$ is experimentally found to be less indicative compared to that for $\pi^*$.

Moreover, as for the acid also for the base, the solvent does not seem to affect the ground-state geometries significantly because the ADC(2) and CC2 energies (i.e., without COSMO) are almost identical at the equilibrium structures for the gas and the solution phase. Calculating solution-phase excitation energies at the corresponding gas-phase geometries, we obtain residuals of −40 meV (COSMO-ADC(2)//MP2) and 24 meV (COSMO-CC2//CC2), as well as −12 meV (COSMO-ADC(2)//ADC(2)) and 49 meV (COSMO-CC2//CC2) referring to the results at the actual ground-state and excited-state structures in solution, respectively.

These results show that (i) the solvent, as described by an implicit model, only has a minor effect on the molecular structure; (ii) the difference between the ADC(2) and CC2 result for the lowest energy is considerably larger for the base; (iii) ADC(2) fails in the excited-state geometry optimization for the base in the gas phase; and (iv) acid and base appear to have a different solvatochromic behavior.

## UV/VIS ABSORPTION AND FLUORESCENCE EMISSION SPECTRA

For a systematic study of Jung's photoacids and a comparison with the available experimental UV/Vis absorption and fluorescence emission spectra in DMSO, we did geometry optimizations in the cc-pVDZ basis set using COSMO-MP2 for the ground state and COSMO-ADC(2) for the first excited state. Ground-state structures were used for calculating the UV/Vis absorption spectra and excited-state structures for the fluorescence emission spectra. These calculations were done in solution phase using COSMO for the solvent DMSO. Because



https://doi.org/10.1021/acs.jpca.2c04436
J. Phys. Chem. A 2022, 126, 5911−5923

The Journal of Physical Chemistry A pubs.acs.org/JPCA Article

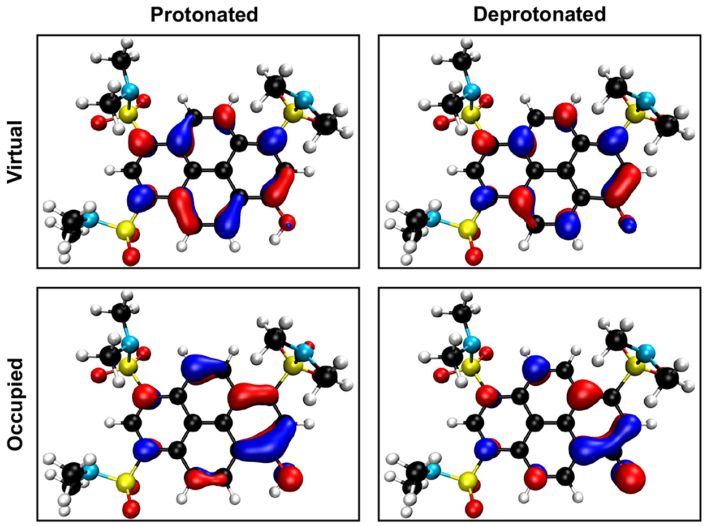



**Figure 1.** Comparison of the occupied and virtual NTOs for the first NTO pair of the first vertical electronic transition of the protonated and deprotonated species of photoacid **F**. Excitations are calculated with COSMO-ADC(2)/aug-cc-pVDZ at the COSMO-MP2/cc-pVDZ geometries, plotted at contour values of ±0.05 au. The weights of these NTOs are 97.4% (protonated) and 98.0% (deprotonated), respectively.

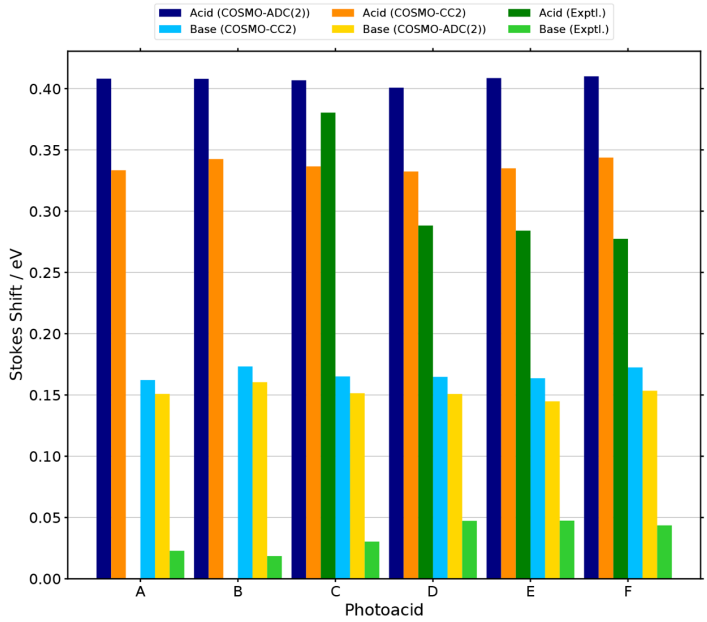



**Figure 2.** Comparison of calculated and experimental Stokes shifts of the acid and base forms of the photoacids **A**−**F** in the solvent DMSO. Stokes shifts based on the calculated absorption and emission energies of the first vertical transition at the COSMO-ADC(2) and COSMO-CC2 levels (cf. Table S9) as well as for the experimental values taken from ref 14. The corresponding numerical values of the Stokes shifts are given in Table S10.

no implementation of COSMO-CC2 excited-state gradients is yet available, COSMO-CC2 emission energies were estimated based on COSMO-CC2 excitation energies at the COSMO-ADC(2) geometries. All spectra, i.e., electronic excitation energies and oscillator strengths, were computed with COSMO-ADC(2) as well as with COSMO-CC2.

**Character of the First Excitation.** The first vertical electronic transition is most relevant since it defines the reference for comparison with experimental absorption ($S_0 \rightarrow S_1$) and emission ($S_1 \rightarrow S_0$). The corresponding natural transition orbitals (NTOs) relating to the first transition are exemplarily shown in Figure 1 for the protonated and deprotonated species of photoacid **F**. A full review of the NTOs for the first five vertical transitions of photoacid **F** is given in Tables S5 and S6 of the Supporting Information.

As can be seen in Figure 1, the first transition has for both species $\pi \rightarrow \pi^*$ character, which is typical for aromatic molecules. Moreover, comparison with the molecular orbitals



https://doi.org/10.1021/acs.jpca.2c04436
J. Phys. Chem. A 2022, 126, 5911−5923

revealed that these two excitations represent simple HOMO−LUMO transitions. The additional lone pair and larger negative charge at the O atom in the deprotonated species lead to a larger contribution from the p orbital at the O atom to the occupied NTO compared to the protonated form. Plots for the electron density difference between $S_1$ and $S_0$ (see Figure S2, SI) show that this electronic transition is associated with a large charge redistribution, i.e., an intramolecular charge transfer (ICT) which reduces the electron density at the −OH or $-O^-$ group, shifting it toward the electron-pulling sulfonic acid groups.

Due to the structural similarity, the character of the electronic transitions is basically identical for all pyranine derivatives studied here and, especially, the most relevant first transition remains unaltered, as verified by NTO analysis. For further reference, the NTOs for the first vertical transition of the protonated and deprotonated species of the photoacids **A**−**F** are shown in Tabs. S7 and S8. In particular, this first transition was always found to be bright, i.e., to have nonzero oscillator strengths. Therefore, it is sufficient to simply restrict the discussion to the excitation energies for this transition. The corresponding (de)excitation energies for the acid and base forms of the six photoacids **A**−**F** are listed in Table S9, at the two levels of theory and together with their experimental values.

**Comparison of Stokes and Substitution Shifts.** The direct comparison of the calculated absorption and emission energies in Table S9 to their experimental counterparts is significantly affected by the systematic errors arising from the limitations of the computational approach (*vide supra*). This includes the restriction to the second-order methods ADC(2) and CC2 and to purely electrostatic solute−solvent interactions, and importantly, that the experimental values refer to maximum positions in the experimental spectra, whereas the calculated results are vertical (de)excitation energies. In short, such a direct comparison reflects that the overall performance is largely affected by an error cancellation involving the inherent errors or ADC(2) or CC2, the (missing) solvation contributions, and the underestimation of fluorescence energies. As a result, best agreements between the calculated and experimental values are found for the emission energies of the acids and the absorption energies of the bases, both at the COSMO-CC2 level. In contrast, the absorption energies of the acids are systematically overestimated (≲0.15 eV), while the emission energies of the bases are underestimated (≲0.10 eV). Still, these errors appear to benefit from further compensation when including explicit solvent due to the experimentally observed solvatochromism, i.e., the bathochromic and hypsochromic behavior of the acid and base, respectively (*vide infra*).

To minimize the effect of systematic shifts, the comparison of relative energies is much more reasonable instead. One such quantity is the Stokes shift (see Figure 2 or Table S10). The results show that ADC(2) and CC2 both overestimate the Stokes shifts for the acids as well as for the bases: CC2 by 40−70 meV for the acids and 100−140 meV for the bases, ADC(2) by 110−130 meV for the acids and 120−150 meV for bases. One exception is photoacid **C**, where the experimental Stokes shift is between the CC2 and ADC(2) values. That the calculated results overestimate the experimental Stokes shifts might partially be due to the vertical approximation but, in particular for the bases, also due to the approximations in the COSMO solvation model.

The substitution shifts in Table 2 demonstrate an overall better performance of COSMO-CC2 over COSMO-ADC(2). In particular, almost quantitative agreement between the calculated and experimental results is obtained for the relative order of the absorption energies for the acids, with the exception of photoacid **D**. The calculated trends for the absorption energies of the bases are in good agreement with the experiments; only for the photoacids **B** and **D** the substutional shifts relative to **F** are overestimated somewhat. However, the deviations are in the order of only a few hundredths of an eV.

**Table 2. Substitutional Shifts in the UV/Vis Absorption and Fluorescence Emission Energies of Jungs's Photoacids in the Solvent DMSO[a]**

| | | photoacids | | | | | |
|---|---|---|---|---|---|---|---|
| | level | **A** | **B** | **C** | **D** | **E** | **F** |
| | | | | acid | | | |
| $S_0$ | COSMO-ADC(2) | −72 | −139 | −56 | −87 | 6 | 0 |
| | COSMO-CC2 | −61 | −117 | −53 | −78 | 7 | 0 |
| | experiment | −59 | −115 | −46 | 0 | 7 | 0 |
| $S_1$ | COSMO-ADC(2) | −70 | −137 | −53 | −77 | 8 | 0 |
| | COSMO-CC2 | −50 | −116 | −45 | −66 | 16 | 0 |
| | experiment | — | — | −149 | −11 | 0 | 0 |
| | | | | base | | | |
| $S_0$ | COSMO-ADC(2) | −68 | −150 | −72 | −67 | 15 | 0 |
| | COSMO-CC2 | −54 | −127 | −63 | −53 | 17 | 0 |
| | Experiment | −55 | −85 | −55 | −4 | 0 | 0 |
| $S_1$ | COSMO-ADC(2) | −58 | −151 | −65 | −60 | 24 | 0 |
| | COSMO-CC2 | −52 | −134 | −61 | −51 | 26 | 0 |
| | experiment | −34 | −60 | −42 | −8 | −4 | 0 |

[a]Comparison of differences in the vertical electronic excitation energies for the first transition taken from the calculations (cf. Table S9) and experimental results (from ref 14) of the photoacids **A**−**F** relative to photoacid **F**. Values are given in meV.

Due to nearly quantitative ESPT yield in DMSO, no experimental emission energies are available for the protonated species of photoacids **A** and **B**.[14] For the remaining photoacids, no clear difference between the results for the two species can be observed due to the reduced number of reference values. However, the deviations from the experimental shifts between the different substituents appear to be larger in emission compared to absorption. The underestimation of fluorescence emission energies is commonly known and originates from the discrepancy between the excited-state equilibrium structures used for the vertical approximation and those actually leading to the emission band maxima in experiments. In contrast to UV/Vis absorption spectroscopy, where the initial state is well-defined, the choice of the initial state in fluorescence is less clear. This is because the fluorescence (i.e., the radiative transition from the electronically excited state, usually $S_1$, to the electronic ground state) can take place at any geometry after vertical excitation, i.e., any structure in between the Franck−Condon point and the excited-state equilibrium. Also, the computational results for excited-state potential surfaces have larger uncertainties than for the ground-state surfaces.[103]

An important factor for the Stokes shift is the change in the equilibrium structure from the ground to the electronically excited state due to changes in the electronic structure. The larger Stokes shifts of the acids observed for the pyranine derivatives indicate stronger structural changes after electronic excitation which can be rationalized in terms of (anti)-aromaticity, as reviewed, e.g., by Agmon[23] or recently Wen et al.:[104] ROH is more aromatic compared to $RO^-$ in $S_0$ and, thus, experiences a larger loss in aromaticity upon excitation to $S_1$. As a consequence, the structural changes in the aromatic system from



https://doi.org/10.1021/acs.jpca.2c04436
J. Phys. Chem. A 2022, 126, 5911−5923

The Journal of Physical Chemistry A pubs.acs.org/JPCA Article

Table 3. Comparison of Calculated Ground-State and Excited-State Acidities of the Photoacids A−F in the Solvent DMSO[a]

| | | photoacids | | | | | |
|---|---|---|---|---|---|---|---|
| | level | A | B | C | D | E | F |
| p$K_a$ | COSMO-RS | 4.8 (3.2) | 3.9 (3.5) | 6.5 (4.9) | 7.9 (5.0) | 6.9 (6.4) | 7.2 (6.0) |
| | | | | absorption | | | |
| Δp$K_a$ | COSMO-ADC(2) | −13.2 | −13.4 | −13.5 | −12.9 | −13.1 | −13.2 |
| | COSMO-CC2 | −12.0 | −12.3 | −12.3 | −11.7 | −11.9 | −12.1 |
| | experimental | −10.7 | −10.3 | −11.0 | −10.9 | −10.9 | −10.8 |
| | | | | emission | | | |
| Δp$K_a$ | COSMO-ADC(2) | −9.0 | −9.5 | −9.4 | −8.9 | −8.9 | −9.2 |
| | COSMO-CC2 | −8.9 | −9.2 | −9.2 | −8.6 | −8.7 | −8.9 |
| | experimental | — | — | −5.0 | −6.8 | −6.9 | −6.8 |
| | | | | averaged | | | |
| Δp$K_a$ | COSMO-ADC(2) | −11.1 | −11.4 | −11.5 | −10.9 | −11.0 | −11.2 |
| | COSMO-CC2 | −10.4 | −10.7 | −10.7 | −10.2 | −10.3 | −10.5 |
| | experimental | — | — | −8.0 | −8.8 | −8.9 | −8.8 |
| | | | | averaged | | | |
| p$K_a^*$ | COSMO-ADC(2) | −6.3 (−7.9) | −7.5 (−7.9) | −5.0 (−6.6) | −3.0 (−5.9) | −4.1 (−4.7) | −4.0 (−5.2) |
| | COSMO-CC2 | −5.7 (−7.3) | −6.8 (−7.2) | −4.3 (−5.9) | −2.2 (−5.1) | −3.4 (−4.0) | −3.3 (−4.5) |

[a] p$K_a$ values using COSMO-RS at the BP-TZVP (BP-TZVPD-FINE) level. Δp$K_a$ based on the Förster cycle using either the absorption, emission, or averaged excitation energies at the COSMO-ADC(2), COSMO-CC2, and experimental levels. p$K_a^*$ using the BP-TZVP (BP-TZVPD-FINE) p$K_a$ and the averaged Förster cycle Δp$K_a$ values at the two levels COSMO-ADC(2) and COSMO-CC2. Experimental results are calculated based on ref 14, with no data for p$K_a^*$ due to missing experimental ground-state p$K_a$ in DMSO.

$S_0$ to $S_1$ are larger. This observation is also confirmed by the root-mean-square deviation for the C−C bond lengths in the pyrene ring between the $S_1$ and $S_0$ structures, e.g., 2.2 pm for the acid and 1.1 pm for the base of photoacid **F**.

## PREDICTION OF p$K_A^*$ IN DMSO

The calculated absorption and emission energies were used to compute Δp$K_a$ values for Jung's photoacids based on the Förster cycle, according to

$$\Delta pK_a = pK_a^* - pK_a = \frac{\Delta G_{exci}(RO^-) - \Delta G_{exci}(ROH)}{RT\ \ln(10)} \quad (3)$$

and p$K_a^*$ values (via eq 1) using the p$K_a$, calculated as described in the Computational Details section. The results for p$K_a$, Δp$K_a$, and p$K_a^*$ of the six photoacids in the solvent DMSO are summarized in Table 3.

**Ground-State Acidity.** Since no experimental p$K_a$ values are available for the photoacids **A**−**F** in DMSO, we additionally calculated the corresponding values in water (see Table S11), where experimental reference data for a comparison is available. The results in water demonstrate that the p$K_a$ values calculated at the BP-TZVP level of COSMO-RS are in much better agreement with the experimental values than the BP-TZVPD-FINE results, based on mean absolute errors of 0.4 and 0.8, respectively. In particular, the BP-TZVPD-FINE results are qualitatively wrong for the differences in acidity between the compounds **A**−**F**. This lead us to infer that the performance of BP-TZVP will be also better in the solvent DMSO.

Regarding the p$K_a$ values at the BP-TZVP level in DMSO (Table 3), a similar order of acidity as in water can be observed: Photoacid **B** is predicted to be most acidic (3.9) but close to **A** (4.8), whereas **D** (7.9) is least acidic, and **C**, **E**, and **F** have comparable acidities.

**Acidity Increase Upon Photoexcitation.** Computing Δp$K_a$, i.e. the change in p$K_a$ upon excitation into $S_1$, via the Förster cycle does not require the ground-state p$K_a$ values and could therefore be done with the experimental as well as the calculated absorption and emission energies. Moreover, also averaged Δp$K_a$ values using the mean absorption and emission energies were considered since these are frequently used in the experimental p$K_a^*$ determination. These mean energies represent an approximation to the true 0−0 transition energies that should be ideally inserted into the Förster equation. This implicitly assumes that the shapes (i.e., curvature) of the potential energy surfaces in the electronic ground and excited states are similar, so that the vibrational contributions to the vibronic 0−0 transition can effectively cancel out in the average.

Being based on the excitation energies in Table S9, the calculated Δp$K_a$ values reflect the trends and deviations that were discussed before. In detail, the trends in the excitation energies explain that (i) Δp$K_a$ is larger when calculated from absorption energies compared to the results obtained from the emission energies for both the theoretical and the experimental results, as rationalized by the Stokes shifts; (ii) the difference between the results for COSMO-ADC(2) and COSMO-CC2 is larger for absorption (≈ 1.2) compared to emission (≈ 0.2); and (iii) the difference between the calculated and experimental values is again smaller for absorption compared to emission (e.g., for COSMO-CC2, 1.3 and 2.9, respectively).

Considering the relative order of Δp$K_a$ at a specific level, we observe that the studied photoacids basically reveal the same experimental Δp$K_a$ in absorption (of approximately −11), largest for **C** and smallest for **B**. Similarly, this observations also holds for the calculated results, but with larger fluctuations and a noticeably overestimated result for photoacid **B**. In contrast, the experimental Δp$K_a$ in emission reveals a distinct difference between photoacid **C** and photoacids **D**−**F**, which cannot be reproduced by the calculations. Photoacid **E** gives the largest experimental Δp$K_a$, whereas it is again photoacid **B** in the calculations.

**Solvent Comparison and Origin of Photoacidity.** Due to the missing experimental emission energies for the acid forms of **A** and **B** in the solvent DMSO (cf. Table 2), no experimental Δp$K_a$ for emission and thus also no averaged values are available for these two compounds. Consequently, comparing the



https://doi.org/10.1021/acs.jpca.2c04436
J. Phys. Chem. A 2022, 126, 5911−5923

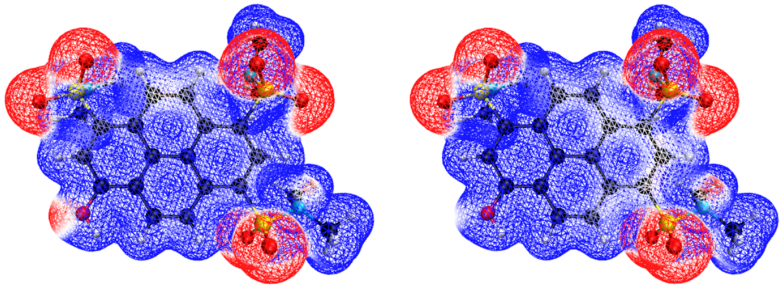



**Figure 3.** Electrostatic potential plotted in the range from −0.03 (red) to 0.03 (blue) [au] at the electron density isosurface (contour value: 0.01 au) of the electronic ground state $S_0$ (a) and excited state $S_1$ (b) of the protonated species of photoacid **F** in solution. Densities calculated at COSMO-MP2 for $S_0$ and COSMO-ADC(2) for $S_1$ in the aug-cc-pVDZ basis set using the COSMO-MP2/cc-pVDZ solution-phase geometry. The molecule is oriented such that the −OH group is located on the bottom left with the H atom pointing to the lower right.

averaged $\Delta pK_a$ is only of limited use in the special case of these photoacids. On the contrary, all of these results are known in water (see Table S11), allowing for a comparison of the two solvents. In water, the averaged experimental acidity change is smallest in magnitude for photoacids **D**−**F** (ca. − 6.5), slightly increases via **C** (− 6.8) and **A** (− 7.4), and reaches its maximum at **B** (− 8.3). A similar trend is found for our calculated averaged $\Delta pK_a$ values, but photoacids **B** and **C** are predicted to have the largest and most comparable changes. However, whereas the experimental $\Delta pK_a$ of photoacid **B** in water is dominated by the absorption contribution, the respective contributions in DMSO are quite similar for all photoacids studied here, as proven by both calculations and experiments.

Despite these slight deviations in the order of the photoacidity, the overall difference between the series for the two solvents allows for an interesting observation on its own: $\Delta pK_a$ is generally smaller in water, i.e., in the more polar solvent, compared to DMSO, the less polar solvent. This finding is supported by both the experimental and the calculated spectra and it can be rationalized on a simplified level by considering the solvent effects on each of the four species in the Förster cycle (cf. Scheme 1). Due to an intramolecular charge transfer (ICT) upon excitation, ROH* is more polar than ROH and hence stabilized more strongly by a polar solvent. This polarity change is exemplarily illustrated in Figure 3 for ROH and ROH* of photoacid **F** using the electrostatic potential. In analogy, the strong polarity of the $RO^-$ anion is reduced by a similar ICT, which causes $RO^-$* to be less polar (see Figure S3) and hence less strongly stabilized compared to $RO^-$.

This implies that ROH reveals a bathochromic and $RO^-$ a (more) hypsochromic shift, as indeed also observed in experiments. Moreover, the $\Delta pK_a$ is actually dominated by the energy gap between ROH* and $RO^-$ because both ROH and $RO^-$* are rather nonpolar. However, since $RO^-$ is an anion, its stabilization by a polar solvent is larger than that of the charge-neutral ROH* species, and thus $\Delta pK_a$ will decrease in magnitude with increasing solvent polarity. In line with this, the CC2 results for photoacid **F** (cf. Table 1) predict a $\Delta pK_a$ in the gas phase of −13.5 (absorption) and −11.4 (emission), i.e., −12.5 on average, which is even considerably more negative than the corresponding result in DMSO (−10.5).

**Excited-State Acidity.** From the $pK_a$ and $\Delta pK_a$, we computed the $pK_a^*$ values listed in Table 3. For the sake of brevity, only $pK_a^*$ values based on the averaged COSMO-CC2 $\Delta pK_a$ in combination with BP-TZVP $pK_a$ are considered. Our calculations predict compound **B** with a $pK_a^*$ of −6.8 to be the strongest photoacid in the solvent DMSO, followed by compounds **A** (−5.7), **C** (−4.3), **E** (−3.4), and **F** (−3.3) toward the weakest photoacid **D** (−2.2). Interestingly, this order exactly matches the one for the experimental Förster cycle $pK_a^*$ values in water.

Whereas in water the photoacids only span a range of three $pK_a$ units, this range is predicted to be larger in DMSO, covering almost five units. This is again due to the solvent effect causing the $\Delta pK_a$ contribution to decrease in magnitude with increasing solvent polarity (*vide supra*). However, the $pK_a$ jump upon excitation is comparable for these six structurally related photoacids and it is the ground-state $pK_a$ that decides which of these photoacids is the strongest.

Moreover, our calculations predict negative $pK_a^*$ values for all of these photoacids. Since the $pK_a$ values of any two given compounds (in the same solvent) determine the position of the corresponding proton-transfer equilibrium, the $pK_a^*$ of the photoacid and $pK_a$ of the protonated solvent decide to what extent protonation of the solvent is expected. A comparison with the $pK_a$ value for an isolated protonated DMSO molecule of 2.9 at the BP-TZVP level (or −0.71 at BP-TZVPD-FINE level) or with the ideal value[37] of $-\log[S] = -1.15$ (where $[S] = 14.08$ mol $L^{-1}$ is the solvent concentration[105]) reveals that the $pK_a^*$ values for all six studied photoacids are all considerably more negative. Thus, all six compounds are in the solvent DMSO true superphotoacids; i.e., they will be able to efficiently protonate the solvent.

## ■ CONCLUSIONS

This work applied the correlated wavefunction-based methods ADC(2) and CC2 in combination with the implicit solvent model COSMO to the theoretical spectroscopy of Jung's pyranine-derived photoacids in the solvent DMSO. Our calculated UV/Vis absorption and fluorescence emission energies are able to reproduce the experimental trends in the Stokes shifts as well as substitution shifts of the protonated and deprotonated species. In terms of trends, the calculations are typically in better agreement with the experiments for absorption compared to emission energies and for the protonated compared to the deprotonated species. In contrast, regarding absolute absorption and emission energies, we observe that COSMO-CC2 performs particularly better for the ROH emission and $RO^-$ absorption in comparison to ROH absorption and $RO^-$ emission. However, this performance



https://doi.org/10.1021/acs.jpca.2c04436
J. Phys. Chem. A 2022, 126, 5911−5923

should be considered the outcome of some beneficial error cancellation due to the combination of the method, solvation description, and the respective electronic state. An overestimation of the vertical absorption energies in the order of 0.1 eV is within the range of the typical errors observed for the second-order methods ADC(2) and CC2 in benchmarks relative to higher-order wavefunction methods.[106] Probably because of error compensation, the results for 0−0 energies are for these methods typically in better agreement with experiment.[107] For vertical emission energies, the single-reference methods ADC(2) and CC2 have probably a tendency to give too low results because of an overestimation of ground-state energies at distorted structures. For the comparison with band maxima in experimental fluorescence spectra, an additional error source is the assumption that the emission occurs from the fully relaxed excited-state structure at the minimum of the $S_1$ potential energy surface.

Despite being limited to purely electrostatic interactions, implicit solvent effects as described by COSMO appear to be sufficient for the solvation treatment of these photoacids in DMSO in first order. More precisely, for these photoacids, solvent effects on the electronic excitation energies occur mainly through the energetic contribution itself rather than structural effects on the geometries.

The strong photoacidity of these compounds originates from an intramolecular charge transfer upon electronic excitation from the −OH or $-O^-$ group to the aromatic ring system and the sulfonate groups in both the protonated and deprotonated species, causing the corresponding energy difference between the two species to change in favor of the deprotonated form in the excited state. Eventually, the relative energetic order of these species in the respective electronic states also explains the observed solvent effect: $\Delta pK_a$, the $pK_a$ jump during excitation, decreases with increasing polarity of the solvent due to a stronger stabilization of $RO^-$ relative to ROH*. For $\Delta pK_a$, we found that our calculated averaged results in DMSO are accurate within two $pK_a$ units. Moreover, this quantity serves as an excellent example to illustrate the need for having directly comparable computational and experimental results. For example, the experimental $\Delta pK_a$ values based on either absorption or emission energies differ by more than four $pK_a$ units. All studied photoacids are predicted to be actual superphotoacids in DMSO, i.e., to perform an efficient excited-state proton transfer to the solvent owing to negative $pK_a^*$, with compound **B** being the strongest among them. Careful analysis of the individual contributions to $pK_a^*$ revealed though that the exact order in excited-state acidity of these compounds is controlled by their ground-state $pK_a$, rather than by $\Delta pK_a$.

As our main difficulties encountered in this study, we identify the limitations due to the vertical approximation used during the calculation of excitation energies, which does not take into account vibronic effects and solvent-dependent broadening, as well as those due to the restriction to an implicit solvent model. Therefore, in order to obtain a better agreement with the experiments, going beyond implicit solvation and performing (*ab initio*) MD simulations with explicit solvent appears necessary. Unfortunately, for the rather large molecules studied here, this is rather difficult from a technical point-of-view, especially for the electronically excited states. These are required since the averaged absorption and fluorescence energies are typically used in the experimental calculation of $\Delta pK_a$, as pointed out before. *Ab initio* MD simulations are practically limited to TDDFT for the electronic structure, not allowing for CC2 MD in solution. Also, the large size of the molecules probably poses another problem because a large simulation box, i.e., a high number of solvent molecules, would be needed to avoid self-interactions in a setup that uses periodic boundary conditions.

## ■ ASSOCIATED CONTENT

### Supporting Information

The Supporting Information is available free of charge at https://pubs.acs.org/doi/10.1021/acs.jpca.2c04436.

Computational details and results for the convergence study of electronic excitation energies with different methods and basis sets; NTOs for the ground-state CC2 $T_1$ amplitudes, the first five electronic transitions of the acid and base of photoacid F, and the first transition for both species of all six photoacids A−F; plots of the difference electron density of the acid and base in the gas and solution phase; plots of the electrostatic potential of the base in $S_0$ and $S_1$; calculated absorption and emission energies of the acid and base of the six photoacids; details on the obtained conformer sets; and calculated $pK_a$ values of the six photoacids in water (PDF)

## ■ AUTHOR INFORMATION


### Corresponding Author

**Niklas Sülzner** − *Lehrstuhl für Theoretische Chemie, Ruhr-Universität Bochum, 44780 Bochum, Germany;* orcid.org/0000-0002-8734-5807; Phone: +49 (0)234 32-24250; Email: niklas.suelzner@rub.de; Fax: +49 (0)234 32-14045

### Author

**Christof Hättig** − *Lehrstuhl für Theoretische Chemie, Ruhr-Universität Bochum, 44780 Bochum, Germany;* orcid.org/0000-0002-5752-2710

Complete contact information is available at: https://pubs.acs.org/10.1021/acs.jpca.2c04436


### Notes

The authors declare no competing financial interest.

## ■ ACKNOWLEDGMENTS

We acknowledge financial support by the Deutsche Forschungsgemeinschaft through Project Ha 2588/8-1. This work was also funded by the Deutsche Forschungsgemeinschaft (DFG, German Research Foundation) under Germany's Excellence Strategy—EXC 2033−390677874−RESOLV.

## ■ REFERENCES


(1) Chou, P.-T.; Solntsev, K. M. Photoinduced Proton Transfer in Chemistry and Biology. *J. Phys. Chem. B* **2015**, *119*, 2089.

(2) Kagel, H.; Frohme, M.; Glökler, J. Photoacids in Biochemical Applications. *J. Cell. Biol.* **2018**, *4*, 23−30.

(3) Hammes-Schiffer, S. Virtual Issue on Proton Transfer. *J. Phys. Chem. B* **2021**, *125*, 3725−3726.

(4) Simkovitch, R.; Pines, D.; Agmon, N.; Pines, E.; Huppert, D. Reversible Excited-State Proton Geminate Recombination: Revisited. *J. Phys. Chem. B* **2016**, *120*, 12615−12632.

(5) Genosar, L.; Cohen, B.; Huppert, D. Ultrafast Direct Photoacid−Base Reaction. *J. Phys. Chem. A* **2000**, *104*, 6689−6698.

(6) Awasthi, A. A.; Singh, P. K. Proton Transfer Reaction Dynamics of Pyranine in DMSO/Water Mixtures. *ChemPhysChem* **2018**, *19*, 198−207.

(7) Gajst, O.; Pinto da Silva, L.; Esteves da Silva, J. C. G.; Huppert, D. Excited-State Proton Transfer from the Photoacid 2-Naphthol-8-sulfonate to Acetonitrile/Water Mixtures. *J. Phys. Chem. A* **2018**, *122*, 6166−6175.
(8) Gajst, O.; Pinto da Silva, L.; Esteves da Silva, J. C. G.; Huppert, D. Enhanced Excited-State Proton Transfer via a Mixed Methanol-Water Molecular Bridge of 1-Naphthol-3,6-disulfonate in Methanol−Water Mixtures. *J. Phys. Chem. A* **2019**, *123*, 48−58.
(9) Nandi, N.; Sahu, K. Analysis of Excited State Proton Transfer Dynamics of HPTS in Methanol-Water Mixtures from Time-Resolved Area-Normalised Emission Spectrum (TRANES). *J. Photochem. Photobiol., A* **2019**, *374*, 138−144.
(10) Pérez-Lustres, J. L.; Rodriguez-Prieto, F.; Mosquera, M.; Senyushkina, T. A.; Ernsting, N. P.; Kovalenko, S. A. Ultrafast Proton Transfer to Solvent: Molecularity and Intermediates from Solvation- and Diffusion-Controlled Regimes. *J. Am. Chem. Soc.* **2007**, *129*, 5408−5418.
(11) Solntsev, K. M.; Clower, C. E.; Tolbert, L. M.; Huppert, D. 6-Hydroxyquinoline-N-oxides: A New Class of "Super" Photoacids. *J. Am. Chem. Soc.* **2005**, *127*, 8534−8544.
(12) Simkovitch, R.; Shomer, S.; Gepshtein, R.; Roth, M. E.; Shabat, D.; Huppert, D. Comparison of the Rate of Excited-State Proton Transfer from Photoacids to Alcohols and Water. *J. Photochem. Photobiol., A* **2014**, *277*, 90−101.
(13) Simkovitch, R.; Shomer, S.; Gepshtein, R.; Shabat, D.; Huppert, D. Excited-State Proton Transfer from Quinone-Cyanine 9 to Protic Polar-Solvent Mixtures. *J. Phys. Chem. A* **2014**, *118*, 1832−1840.
(14) Finkler, B.; Spies, C.; Vester, M.; Walte, F.; Omlor, K.; Riemann, I.; Zimmer, M.; Stracke, F.; Gerhards, M.; Jung, G. Highly Photostable "Super"-Photoacids for Ultrasensitive Fluorescence Spectroscopy. *Photochem. Photobiol. Sci.* **2014**, *13*, 548−562.
(15) Spies, C.; Finkler, B.; Acar, N.; Jung, G. Solvatochromism of Pyranine-Derived Photoacids. *Phys. Chem. Chem. Phys.* **2013**, *15*, 19893−19905.
(16) Spies, C.; Shomer, S.; Finkler, B.; Pines, D.; Pines, E.; Jung, G.; Huppert, D. Solvent Dependence of Excited-State Proton Transfer from Pyranine-Derived Photoacids. *Phys. Chem. Chem. Phys.* **2014**, *16*, 9104−9114.
(17) Maus, D.; Grandjean, A.; Jung, G. Toward Magic Photoacids: Proton Transfer in Concentrated Sulfuric Acid. *J. Phys. Chem. A* **2018**, *122*, 9025−9030.
(18) Lee, Y. M.; Park, S.-Y.; Kim, H.; Kim, T. G.; Kwon, O.-H. Photoinduced Strong Acid−Weak Base Reactions in a Polar Aprotic Solvent. *Methods Appl. Fluoresc.* **2016**, *4*, 024004.
(19) Kumpulainen, T.; Bakker, B. H.; Hilbers, M.; Brouwer, A. M. Synthesis and Spectroscopic Characterization of 1,8-Naphthalimide Derived "Super" Photoacids. *J. Phys. Chem. B* **2015**, *119*, 2515−2524.
(20) Kumpulainen, T.; Bakker, B. H.; Brouwer, A. M. Complexes of a Naphthalimide Photoacid with Organic Bases, and their Excited-State Dynamics in Polar Aprotic Organic Solvents. *Phys. Chem. Chem. Phys.* **2015**, *17*, 20715−20724.
(21) Kumpulainen, T.; Rosspeintner, A.; Dereka, B.; Vauthey, E. Influence of Solvent Relaxation on Ultrafast Excited-State Proton Transfer to Solvent. *J. Phys. Chem. Lett.* **2017**, *8*, 4516−4521.
(22) Verma, P.; Rosspeintner, A.; Dereka, B.; Vauthey, E.; Kumpulainen, T. Broadband Fluorescence Reveals Mechanistic Differences in Excited-State Proton Transfer to Protic and Aprotic Solvents. *Chem. Sci.* **2020**, *11*, 7963−7971.
(23) Agmon, N. Elementary Steps in Excited-State Proton Transfer. *J. Phys. Chem. A* **2005**, *109*, 13−35.
(24) Simkovitch, R.; Shomer, S.; Gepshtein, R.; Huppert, D. How Fast Can a Proton-Transfer Reaction Be beyond the Solvent-Control Limit? *J. Phys. Chem. B* **2015**, *119*, 2253−2262.
(25) Solntsev, K. M.; Huppert, D.; Agmon, N. Photochemistry of "Super"-Photoacids. Solvent Effects. *J. Phys. Chem. A* **1999**, *103*, 6984−6997.
(26) Solntsev, K. M.; Huppert, D.; Agmon, N.; Tolbert, L. M. Photochemistry of "Super" Photoacids. 2. Excited-State Proton Transfer in Methanol/Water Mixtures. *J. Phys. Chem. A* **2000**, *104*, 4658−4669.
(27) Clower, C.; Solntsev, K. M.; Kowalik, J.; Tolbert, L. M.; Huppert, D. Photochemistry of "Super" Photoacids. 3. Excited-State Proton Transfer from Perfluoroalkylsulfonyl-Substituted 2-Naphthols. *J. Phys. Chem. A* **2002**, *106*, 3114−3122.
(28) Tolbert, L. M.; Solntsev, K. M. Excited-State Proton Transfer: From Constrained Systems to "Super" Photoacids to Superfast Proton Transfer. *Acc. Chem. Res.* **2002**, *35*, 19−27.
(29) Förster, T. Fluoreszenzspektrum und Wasserstoffionenkonzentration. *Naturwissenschaften* **1949**, *36*, 186−187.
(30) Förster, T. Elektrolytische dissoziation angeregter Moleküle. *Z. Elektrochem. Angew. Phys. Chem.* **1950**, *54*, 42−46.
(31) Barcza, L.; Buvári-Barcza, Á. Acid-Base Titrations in Nonaqueous Solvents and Solvent Mixtures. *J. Chem. Educ.* **2003**, *80*, 822.
(32) Buvári-Barcza, A.; Barcza, L. Problems in the Interpretation of Nonaqueous Titrations. *Die Pharmazie* **2005**, *60*, 243−246.
(33) Sooväli, L.; Kaljurand, I.; Kütt, A.; Leito, I. Uncertainty Estimation in Measurement of pKa Values in Nonaqueous Media: A Case Study on Basicity Scale in Acetonitrile Medium. *Anal. Chim. Acta* **2006**, *566*, 290−303.
(34) Alongi, K. S.; Shields, G. C. In *Annual Reports in Computational Chemistry*; Wheeler, R. A., Ed.; Elsevier: 2010; Vol. *6*; pp 113−138.
(35) Seybold, P. G.; Shields, G. C. Computational Estimation of pKa Values. *Wiley Interdiscip. Rev. Comput. Mol. Sci.* **2015**, *5*, 290−297.
(36) Casasnovas, R.; Ortega-Castro, J.; Frau, J.; Donoso, J.; Muñoz, F. Theoretical pKa Calculations with Continuum Model Solvents, Alternative Protocols to Thermodynamic Cycles. *Int. J. Quantum Chem.* **2014**, *114*, 1350−1363.
(37) Pliego, J. R. Thermodynamic Cycles and the Calculation of pKa. *Chem. Phys. Lett.* **2003**, *367*, 145−149.
(38) Klamt, A. Conductor-like Screening Model for Real Solvents: A New Approach to the Quantitative Calculation of Solvation Phenomena. *J. Phys. Chem.* **1995**, *99*, 2224−2235.
(39) Klamt, A.; Jonas, V.; Bürger, T.; Lohrenz, J. C. Refinement and Parametrization of COSMO-RS. *J. Phys. Chem. A* **1998**, *102*, 5074−5085.
(40) Eckert, F.; Klamt, A. Fast Solvent Screening via Quantum Chemistry: COSMO-RS Approach. *AIChE J.* **2002**, *48*, 369−385.
(41) Klamt, A.; Eckert, F.; Arlt, W. COSMO-RS: An Alternative to Simulation for Calculating Thermodynamic Properties of Liquid Mixtures. *Annu. Rev. Chem. Biomol. Eng.* **2010**, *1*, 101−122.
(42) Klamt, A. The COSMO and COSMO-RS Solvation Models. *Wiley Interdiscip. Rev. Comput. Mol. Sci.* **2011**, *1*, 699−709.
(43) Klamt, A.; Schüürmann, G. COSMO: A New Approach to Dielectric Screening in Solvents with Explicit Expressions for the Screening Energy and its Gradient. *J. Chem. Soc., Perkin Trans.* **1993**, *2*, 799−805.
(44) Schäfer, A.; Klamt, A.; Sattel, D.; Lohrenz, J. C.; Eckert, F. COSMO Implementation in TURBOMOLE: Extension of an Efficient Quantum Chemical Code towards Liquid Systems. *Phys. Chem. Chem. Phys.* **2000**, *2*, 2187−2193.
(45) Klamt, A.; Eckert, F.; Diedenhofen, M.; Beck, M. E. First Principles Calculations of Aqueous pKa Values for Organic and Inorganic Acids Using COSMO-RS Reveal an Inconsistency in the Slope of the pKa Scale. *J. Phys. Chem. A* **2003**, *107*, 9380−9386.
(46) Eckert, F.; Klamt, A. Accurate Prediction of Basicity in Aqueous Solution with COSMO-RS. *J. Comput. Chem.* **2006**, *27*, 11−19.
(47) Eckert, F.; Leito, I.; Kaljurand, I.; Kütt, A.; Klamt, A.; Diedenhofen, M. Prediction of Acidity in Acetonitrile Solution with COSMO-RS. *J. Comput. Chem.* **2009**, *30*, 799−810.
(48) Sülzner, N.; Haberhauer, J.; Hättig, C.; Hellweg, A. Prediction of Acid p$K_a$ Values in the Solvent Acetone based on COSMO-RS. *J. Comput. Chem.* **2022**, *43*, 1011−1022.
(49) Granucci, G.; Hynes, J. T.; Millié, P.; Tran-Thi, T.-H. A Theoretical Investigation of Excited-State Acidity of Phenol and Cyanophenols. *J. Am. Chem. Soc.* **2000**, *122*, 12243−12253.



https://doi.org/10.1021/acs.jpca.2c04436
*J. Phys. Chem. A* 2022, 126, 5911−5923

(50) Agmon, N.; Rettig, W.; Groth, C. Electronic Determinants of Photoacidity in Cyanonaphthols. *J. Am. Chem. Soc.* **2002**, *124*, 1089−1096.
(51) Jacquemin, D.; Perpète, E. A.; Ciofini, I.; Adamo, C. Fast and Reliable Theoretical Determination of p$K_a$* for Photoacids. *J. Phys. Chem. A* **2008**, *112*, 794−796.
(52) Le Bahers, T.; Adamo, C.; Ciofini, I. Photophysical Properties of 8-Hydroxyquinoline-5-sulfonic Acid as a Function of the pH: A TD-DFT Investigation. *J. Phys. Chem. A* **2010**, *114*, 5932−5939.
(53) Baranov, M. S.; Lukyanov, K. A.; Borissova, A. O.; Shamir, J.; Kosenkov, D.; Slipchenko, L. V.; Tolbert, L. M.; Yampolsky, I. V.; Solntsev, K. M. Conformationally Locked Chromophores as Models of Excited-State Proton Transfer in Fluorescent Proteins. *J. Am. Chem. Soc.* **2012**, *134*, 6025−6032.
(54) Brémond, É.; Alberto, M. E.; Russo, N.; Ricci, G.; Ciofini, I.; Adamo, C. Photophysical Properties of NIR-emitting Fluorescence Probes: Insights from TD-DFT. *Phys. Chem. Chem. Phys.* **2013**, *15*, 10019−10027.
(55) Houari, Y.; Jacquemin, D.; Laurent, A. D. Methodological Keys for Accurate Simulations. *Phys. Chem. Chem. Phys.* **2013**, *15*, 11875−11882.
(56) Houari, Y.; Jacquemin, D.; Laurent, A. D. TD-DFT study of the p$K_a$* for Coumarins. *Chem. Phys. Lett.* **2013**, *583*, 218−221.
(57) Gao, J.; Li, N.; Freindorf, M. Hybrid QM/MM Simulations Yield the Ground and Excited State p$K_a$ Difference: Phenol in Aqueous Solution. *J. Am. Chem. Soc.* **1996**, *118*, 4912−4913.
(58) Gao, J.; Byun, K. Solvent Effects on the n$\pi$* Transition of Pyrimidine in Aqueous Solution. *Theor. Chem. Acc.* **1997**, *96*, 151−156.
(59) Borg, O. A.; Durbeej, B. Relative Ground and Excited-State p$K_a$ Values of Phytochromobilin in the Photoactivation of Phytochrome: A Computational Study. *J. Phys. Chem. B* **2007**, *111*, 11554−11565.
(60) Anders Borg, O.; Durbeej, B. Which Factors Determine the Acidity of the Phytochromobilin Chromophore of Plant Phytochrome? *Phys. Chem. Chem. Phys.* **2008**, *10*, 2528−2537.
(61) Tran-Thi, T.-H.; Prayer, C.; Millié, P.; Uznanski, P.; Hynes, J. T. Substituent and Solvent Effects on the Nature of the Transitions of Pyrenol and Pyranine. Identification of an Intermediate in the Excited-State Proton-Transfer Reaction. *J. Phys. Chem. A* **2002**, *106*, 2244−2255.
(62) Savarese, M.; Netti, P. A.; Adamo, C.; Rega, N.; Ciofini, I. Exploring the Metric of Excited State Proton Transfer Reactions. *J. Phys. Chem. B* **2013**, *117*, 16165−16173.
(63) Savarese, M.; Netti, P. A.; Rega, N.; Adamo, C.; Ciofini, I. Intermolecular Proton Shuttling in Excited State Proton Transfer Reactions: Insights from Theory. *Phys. Chem. Chem. Phys.* **2014**, *16*, 8661−8666.
(64) Laurent, A. D.; Houari, Y.; Carvalho, P. H. P. R.; Neto, B. A. D.; Jacquemin, D. ESIPT or not ESIPT? Revisiting Recent Results on 2,1,3-Benzothiadiazole under the TD-DFT Light. *RSC Adv.* **2014**, *4*, 14189−14192.
(65) Houari, Y.; Chibani, S.; Jacquemin, D.; Laurent, A. D. TD-DFT Assessment of the Excited State Intramolecular Proton Transfer in Hydroxyphenylbenzimidazole (HBI) Dyes. *J. Phys. Chem. B* **2015**, *119*, 2180−2192.
(66) Raucci, U.; Savarese, M.; Adamo, C.; Ciofini, I.; Rega, N. Intrinsic and Dynamical Reaction Pathways of an Excited State Proton Transfer. *J. Phys. Chem. B* **2015**, *119*, 2650−2657.
(67) Zhao, J.; Yao, H.; Liu, J.; Hoffmann, M. R. New Excited-State Proton Transfer Mechanisms for 1,8-Dihydroxydibenzo[a,h]-phenazine. *J. Phys. Chem. A* **2015**, *119*, 681−688.
(68) Cimino, P.; Raucci, U.; Donati, G.; Chiariello, M. G.; Schiazza, M.; Coppola, F.; Rega, N. On the Different Strength of Photoacids. *Theor. Chem. Acc.* **2016**, *135*, 1−12.
(69) Zhou, P.; Han, K. Unraveling the Detailed Mechanism of Excited-State Proton Transfer. *Acc. Chem. Res.* **2018**, *51*, 1681−1690.
(70) Chiariello, M. G.; Rega, N. Exploring Nuclear Photorelaxation of Pyranine in Aqueous Solution: an Integrated Ab-Initio Molecular Dynamics and Time Resolved Vibrational Analysis Approach. *J. Phys. Chem. A* **2018**, *122*, 2884−2893.
(71) Chiariello, M. G.; Donati, G.; Rega, N. Time-Resolved Vibrational Analysis of Excited State Ab Initio Molecular Dynamics to Understand Photorelaxation: The Case of the Pyranine Photoacid in Aqueous Solution. *J. Chem. Theory Comput.* **2020**, *16*, 6007−6013.
(72) Chiariello, M. G.; Raucci, U.; Donati, G.; Rega, N. Water-Mediated Excited State Proton Transfer of Pyranine−Acetate in Aqueous Solution: Vibrational Fingerprints from Ab Initio Molecular Dynamics. *J. Phys. Chem. A* **2021**, *125*, 3569−3578.
(73) Chiariello, M. G.; Donati, G.; Raucci, U.; Perrella, F.; Rega, N. Structural Origin and Vibrational Fingerprints of the Ultrafast Excited State Proton Transfer of the Pyranine-Acetate Complex in Aqueous Solution. *J. Phys. Chem. B* **2021**, *125*, 10273−10281.
(74) Thomaz, J. E.; Walker, A. R.; Van Wyck, S. J.; Meisner, J.; Martinez, T. J.; Fayer, M. D. Proton Transfer Dynamics in the Aprotic Proton Accepting Solvent 1-Methylimidazole. *J. Phys. Chem. B* **2020**, *124*, 7897−7908.
(75) Walker, A. R.; Wu, B.; Meisner, J.; Fayer, M. D.; Martínez, T. J. Proton Transfer from a Photoacid to a Water Wire: First Principles Simulations and Fast Fluorescence Spectroscopy. *J. Phys. Chem. B* **2021**, *125*, 12539−12551.
(76) Raucci, U.; Chiariello, M. G.; Rega, N. Modeling Excited-State Proton Transfer to Solvent: A Dynamics Study of a Super Photoacid with a Hybrid Implicit/Explicit Solvent Model. *J. Chem. Theory Comput.* **2020**, *16*, 7033−7043.
(77) Sobolewski, A. L.; Domcke, W.; Hättig, C. Photophysics of Organic Photostabilizers. Ab Initio Study of the Excited-State Deactivation Mechanisms of 2-(2'-Hydroxyphenyl)benzotriazole. *J. Phys. Chem. A* **2006**, *110*, 6301−6306.
(78) Acharya, A.; Chaudhuri, S.; Batista, V. S. Can TDDFT Describe Excited Electronic States of Naphthol Photoacids? A Closer Look with EOM-CCSD. *J. Chem. Theory Comput.* **2018**, *14*, 867−876.
(79) Grandjean, A.; Pérez Lustres, J. L.; Muth, S.; Maus, D.; Jung, G. Steady-State Spectroscopy to Single Out the Contact Ion Pair in Excited-State Proton Transfer. *J. Phys. Chem. Lett.* **2021**, *12*, 1683−1689.
(80) Grandjean, A.; Pérez Lustres, J. L.; Jung, G. Solvent-Controlled Intermolecular Proton-Transfer Follows an Irreversible Eigen-Weller Model from fs to ns. *ChemPhotoChem.* **2021**, *5*, 1094−1105.
(81) Sülzner, N.; Geissler, B.; Grandjean, A.; Jung, G.; Nuernberger, P. Excited-State Proton Transfer Dynamics of a Super-Photoacid in Acetone-Water Mixtures. *ChemPhotoChem.* **2022**, *6*, No. e202200041.
(82) Knorr, J.; Sülzner, N.; Geissler, B.; Spies, C.; Finkler, B.; Jung, G.; Nuernberger, P. Ultrafast transient absorption and solvation of a super-photoacid in acetoneous environments. *Photochem. Photobiol. Sci.* **2022**, DOI: 10.1007/s43630-022-00287-z.
(83) *TURBOMOLE*, V7.4 2019, a development of University of Karlsruhe and Forschungszentrum Karlsruhe GmbH, 1989−2007, TURBOMOLE GmbH, since 2007; available from http://www.turbomole.com.
(84) Balasubramani, S. G.; Chen, G. P.; Coriani, S.; Diedenhofen, M.; Frank, M. S.; Franzke, Y. J.; Furche, F.; Grotjahn, R.; Harding, M. E.; Hättig, C.; et al. TURBOMOLE: Modular Program Suite for Ab Initio Quantum-Chemical and Condensed-Matter Simulations. *J. Chem. Phys.* **2020**, *152*, 184107.
(85) Schwabe, T.; Sneskov, K.; Haugaard Olsen, J. M.; Kongsted, J.; Christiansen, O.; Hättig, C. PERI−CC2: A Polarizable Embedded RI-CC2Method. *J. Chem. Theory Comput.* **2012**, *8*, 3274−3283.
(86) Karbalaei Khani, S.; Marefat Khah, A.; Hättig, C. Comparison of Reaction Field Schemes for Coupling Continuum Solvation Models with Wave Function Methods for Excitation Energies. *J. Chem. Theory Comput.* **2020**, *16*, 4554−4564.
(87) Sülzner, N.; Hättig, C. Raw Data to "Theoretical Study on the Photoacidity of Hydroxypyrene Derivatives in DMSO Using ADC(2) and CC2". *Zenodo* 2022, DOI: 10.5281/zenodo.6598713.
(88) *BIOVIA COSMOconf*, Release 2021; Dassault Systèmes. http://www.3ds.com.
(89) *BIOVIA COSMOtherm*, Release 2021; Dassault Systèmes. http://www.3ds.com.



https://doi.org/10.1021/acs.jpca.2c04436
J. Phys. Chem. A 2022, 126, 5911−5923

(90) Hellweg, A.; Eckert, F. Brick by Brick Computation of the Gibbs Free Energy of Reaction in Solution using Quantum Chemistry and COSMO-RS. *AIChE J.* **2017**, *63*, 3944−3954.
(91) Klamt, A.; Diedenhofen, M. A Refined Cavity Construction Algorithm for the Conductor-like Screening Model. *J. Comput. Chem.* **2018**, *39*, 1648−1655.
(92) Dunning, T. H. Gaussian Basis Sets for Tse in Correlated Molecular Calculations. I. The Atoms Boron through Neon and Hydrogen. *J. Chem. Phys.* **1989**, *90*, 1007−1023.
(93) Woon, D. E.; Dunning, T. H. Gaussian Basis Sets for Use in Correlated Molecular Calculations. III. The Atoms Aluminum through Argon. *J. Chem. Phys.* **1993**, *98*, 1358−1371.
(94) Weigend, F.; Häser, M. RI-MP2: First Derivatives and Global Consistency. *Theor. Chem. Acc.* **1997**, *97*, 331−340.
(95) Hättig, C.; Hellweg, A.; Köhn, A. Distributed Memory Parallel Implementation of Energies and Gradients for Second-Order Møller-Plesset Perturbation Theory with the Resolution-of-the-Identity Approximation. *Phys. Chem. Chem. Phys.* **2006**, *8*, 1159−1169.
(96) Hättig, C. Geometry Optimizations with the Coupled-Cluster Model CC2 using the Resolution-of-the-Identity Approximation. *J. Chem. Phys.* **2003**, *118*, 7751−7761.
(97) Cammi, R.; Mennucci, B.; Tomasi, J. Second-Order Møller-Plesset Analytical Derivatives for the Polarizable Continuum Model Using the Relaxed Density Approach. *J. Phys. Chem. A* **1999**, *103*, 9100−9108.
(98) Karbalaei Khani, S.; Marefat Khah, A.; Hättig, C. COSMO-RI-ADC(2) Excitation Energies and Excited State Gradients. *Phys. Chem. Chem. Phys.* **2018**, *20*, 16354−16363.
(99) Köhn, A.; Hättig, C. Analytic Gradients for Excited States in the Coupled-Cluster Model CC2 Employing the Resolution-of-the-Identity Approximation. *J. Chem. Phys.* **2003**, *119*, 5021−5036.
(100) Kendall, R. A.; Dunning, T. H.; Harrison, R. J. Electron Affinities of the First-Row Atoms Revisited. Systematic Basis Sets and Wave Functions. *J. Chem. Phys.* **1992**, *96*, 6796−6806.
(101) Hättig, C. In Response Theory and Molecular Properties (A Tribute to Jan Linderberg and Poul Jørgensen). *Adv. Quantum Chem.* **2005**, *50*, 37−60.
(102) Hättig, C.; Weigend, F. CC2 Excitation Energy Calculations on Large Molecules using the Resolution of the Identity Approximation. *J. Chem. Phys.* **2000**, *113*, 5154−5161.
(103) Jacquemin, D. What is the Key for Accurate Absorption and Emission Calculations, Energy or Geometry? *J. Chem. Theory Comput.* **2018**, *14*, 1534−1543.
(104) Wen, Z.; Karas, L. J.; Wu, C.-H.; Wu, J. I.-C. How does Excited-State Antiaromaticity Affect the Acidity Strengths of Photoacids? *Chem. Commun.* **2020**, *56*, 8380−8383.
(105) Haynes, W. M.; Lide, D. R.; Bruno, T. J. *CRC Handbook of Chemistry and Physics*, 97th ed.; CRC Press: Boca Raton, FL, 2016.
(106) Schreiber, M.; Silva-Junior, M. R.; Sauer, S. P. A.; Thiel, W. Benchmarks for Electronically Excited States: CASPT2, CC2, CCSD, and CC3. *J. Chem. Phys.* **2008**, *128*, 134110.
(107) Winter, N. O. C.; Graf, N. K.; Leutwyler, S.; Hättig, C. Benchmarks for 0−0 Transitions of Aromatic Organic Molecules: DFT/B3LYP, ADC(2), CC2, SOS-CC2 and SCS-CC2 Compared to High-Resolution Gas-Phase Data. *Phys. Chem. Chem. Phys.* **2013**, *15*, 6623−6630.

## Recommended by ACS

**A Theoretical Perspective on the Actinic Photochemistry of 2-Hydroperoxypropanal**
Emanuele Marsili, Basile F. E. Curchod, *et al.*
JULY 28, 2022
THE JOURNAL OF PHYSICAL CHEMISTRY A
READ

**Quantum Simulation of Molecules in Solution**
Davide Castaldo, Stefano Corni, *et al.*
NOVEMBER 09, 2022
JOURNAL OF CHEMICAL THEORY AND COMPUTATION
READ

**A Hessian-Free Method to Prevent Zero-Point Energy Leakage in Classical Trajectories**
Saikat Mukherjee and Mario Barbatti
JUNE 09, 2022
JOURNAL OF CHEMICAL THEORY AND COMPUTATION
READ

**Excited-State Barrier Controls $E \rightarrow Z$ Photoisomerization in *p*-Hydroxycinnamate Biochromophores**
Eleanor K. Ashworth, James N. Bull, *et al.*
SEPTEMBER 23, 2022
THE JOURNAL OF PHYSICAL CHEMISTRY LETTERS
READ

Get More Suggestions >



https://doi.org/10.1021/acs.jpca.2c04436
*J. Phys. Chem. A* 2022, 126, 5911−5923

# 7. Toward Explicit Solvent Effects and Specific Photoacid–Base Interactions

## 7.1. Introduction

The experimental study in acetone–water mixtures (Chapter 3) showed that a reaction complex between the photoacid and water—formed either already in the ground state or directly after excitation—becomes crucial for the ESPT dynamics of photoacid **B** (see Fig. 1.6 in Sec. 1.2.5) in these solvent mixtures. In particular, association constants could be determined from the changes in the UV/Vis absorption spectra, but more detailed spectroscopic information on such intermediates was not directly accessible. Similarly, the study in neat acetone (Chapter 4) did not fully answer the question regarding the actual proton acceptor, keeping the possibility of ESPT to acetone still unsettled. On the other side, our computational study of these photoacids in DMSO (Chapter 6) revealed some interesting insights into the origin of photoacidity of these systems, but fully remained within the implicit solvation picture, thus neglecting any explicit solvent effects.

This chapter will try to address these open questions from a computational perspective. First, the previous approach for the theoretical spectroscopy of the complete set of Jung's photoacids will be extended to the new target solvent acetone. The LFER parameters from Chapter 5 for the computation of $pK_a$ in acetone with COSMO-RS in combination with the $\Delta pK_a$ from the calculated spectra will give access to the excited-state $pK_a$ (i.e., $pK_a^*$) values of the photoacids **A**–**F** (cf. Fig. 1.6 in Sec. 1.2.5) in acetone. These will allow to judge and compare the thermodynamic possibility of ESPT of these different compounds in acetone. Second, the need to go beyond implicit solvation by incorporating explicit solvent molecules in the first solvation shells in different solvent environments will be investigated. Here, the focus will be set to the additional effect of explicit solvent on the electronic excitation energies which will also affect the calculated acidity increase upon excitation ($\Delta pK_a$). Finally, the role of acetone and water as proton acceptors (i.e., bases) in acetone solution will be briefly compared by providing additional spectroscopic information on possible reaction complexes to complement the experimental studies.

## 7.2. Computational Details

All quantum-chemical calculations were performed using the TURBOMOLE program package (development version V7-6-1323-gf7bfc1e)[416,482]. The resolution-of-the-identity (RI) approximation was used in all MP2, ADC(2), and CC2 calculations with the ricc2 module. In addition, the frozen-core approximation was applied for the 1*s* orbitals at C, N, O, F and the 1*s*2*s*2*p* orbitals at S. To ensure convergence with diffuse basis functions, the integral screening threshold for the MO calculations ($scftol) was lowered

to $10^{-15}$. Calculations in bulk solution refer to the implicit solvent model COSMO with values for the relative dielectric constant $\epsilon_r$ and refractive index $n$ for the respective solvents according to Tab. 7.1. Default COSMO parameters were used for the cavity construction. For the combination of COSMO with the methods ADC(2) and CC2 for electronic excitation energies, the post-SCF coupling scheme was used, as first introduced in Ref. 477 and later compared for COSMO[472] to other reaction schemes. The notation A//B is used for referring to an electronic excitation energy that was computed at a level A using a geometry optimized at a level B.

Table 7.1.: **COSMO Parameters.** Values for the relative dielectric constant $\epsilon_r$ and the refractive index $n$ of the solvents acetone, DMSO, and water (at 25 °C) used in this study; taken from Ref. 309.

| **Solvent** | $\boldsymbol{\epsilon_r}$ | $\boldsymbol{n}$ |
|---|---|---|
| Acetone | 20.56 | 1.359 |
| DMSO | 46.45 | 1.479 |
| Water | 78.30 | 1.333 |

Ground-state ($S_0$) equilibrium geometries were optimized in the cc-pVDZ basis set[483,484] using the methods MP2[485,486] or CC2[487] in the gas phase and COSMO-MP2[488] or COSMO-CC2[478] in solution. In analogy, geometries for the first excited state ($S_1$) were also optimized in the cc-pVDZ basis set, but using ADC(2)[487] or CC2[489] for the gas phase and only COSMO-ADC(2)[478] for the solution phase. If available, initial structures were taken from the previous calculations in DMSO (see Chapter 6; also available from Ref. 490) and re-optimized in the target solvent (mostly acetone). At the final geometries, vertical electronic excitation energies were then calculated in the larger aug-cc-pVDZ basis set[484,491] with the desired method(s) ADC(2)[463], CC2[492], COSMO-ADC(2)[478], or COSMO-CC2[478]. UV/Vis absorption was calculated at the $S_0$ equilibrium structures, while fluorescence emission was obtained at the $S_1$ equilibrium structures. The calculated absorption and emission energies were used to compute $\Delta pK_a$ values based on the Förster cycle (cf. Fig. 1.1 in Sec. 1.2.1), according to:

$$\Delta pK_a = pK_a^* - pK_a = \frac{\Delta G_{exci}(RO^-) - \Delta G_{exci}(ROH)}{RT \ln(10)}, \tag{7.1}$$

with the excitation Gibbs free energies $\Delta G_{exci}(ROH)$ and $\Delta G_{exci}(RO^-)$ of the two species, the ideal gas constant $R$, and the absolute temperature $T$. These $\Delta G_{exci}$ values were approximated by the corresponding experimental or calculated UV/Vis absorption and fluorescence emission energies.

Ground-state $pK_a$ values were calculated with COSMO-RS as implemented in COSMO*therm* (version 2021)[418] at the BP-TZVP and BP-TZVPD-FINE levels of theory. Details on COSMO-RS itself[359–362,428], the difference between these two levels[442], as well as the precise computational protocol for $pK_a$[365–367,493] can be found elsewhere. Multiple conformers for both the acid and base species of the photoacids **A**–**F** (defined in Fig. 1.6) were taken into account based on the conformer sets that were already determined during the previous study in DMSO[69]. Since the COSMO geometries used for COSMO-RS are based on $\epsilon \to \infty$, i.e., they are independent of the solvent, no additional changes were needed. For $pK_a$ in acetone, the parameters for COSMO-RS were taken from Ref. 493. Excited-state $pK_a^*$ values are then obtained

by adding the $\Delta pK_a$ from Eq. (7.1) to the COSMO-RS ground-state $pK_a$. All calculations refer to a temperature of 298.15 K (25 °C).

## 7.3. Theoretical Spectroscopy in Acetone with Implicit Solvation

Using the above-mentioned methods for the theoretical spectroscopy of these photoacids in DMSO (cf. Chapter 6), this approach was extended to acetone. After briefly reassessing the method performance for one selected photoacid, the results for the full set of photoacids **A**–**F** will be discussed and then used to predict their characteristic $\Delta pK_a$ values in acetone.

### 7.3.1. Re-Assessing the Method Performance for Photoacid B

First, the performance of the methods was validated, including the implicit solvent model COSMO, but this time with a focus on the photoacid **B** in acetone, as the center of the time-resolved experiments. The vertical (de-)excitation energies obtained with different combinations of methods for the geometry and for the electronic excitations are plotted in Fig. 7.1 and the numerical values can be found in Tab. C.1.

For the protonated form, referred to as ACID, a systematic deviation between ADC(2) and CC2 of $< 0.1$ eV is observed for the $S_0$ absorption energies (Fig. 7.1(a)), whereas a deviation $> 0.1$ eV is observed for the $S_1$ emission energies (Fig. 7.1(b)). These differences appear rather independent of the inclusion of implicit solvation effects *via* COSMO. However, the implicit solvent model COSMO does introduce a bathochromic (i.e, solvatochromic red) shift between the gas-phase (without COSMO) and solution-phase (with COSMO) excitation energies of $\sim 0.15$ eV at all geometries. Best agreement between the calculated and the experimental results is found for the COSMO-CC2//COSMO-CC2 level in absorption and COSMO-CC2//COSMO-ADC(2) in emission, differing only by 14 meV and 45 meV, respectively.

For the deprotonated form, referred to as BASE, the inherent ADC(2)–CC2 difference is significantly larger than for the acid in both absorption and emission. For $S_0$ (Fig. 7.1(c)) as well as $S_1$ (Fig. 7.1(d)), differences of $\sim 0.15$ eV with COSMO and $> 0.2$ eV without COSMO are observed. Implicit solvent effects as described by COSMO again cause a bathochromic shift of $\sim 0.1$ eV for CC2 and $< 0.1$ eV for ADC(2). Note that best agreement between the calculations and experiments is found in case of the base for absorption again with COSMO-CC2//COSMO-CC2 (differing by 6 meV) and for emission with CC2//COSMO-ADC(2) (differing by 9 meV). For comparison, the COSMO-CC2//COSMO-ADC(2) level, which gives the best result for the acid, underestimates the experimental emission energy of the base by $\sim 0.1$ eV.

The results for the base at the ADC(2) $S_1$ gas-phase geometry are not included in Fig. 7.1 as this geometry yields emission energies that are non-physically too small. Interestingly, this issue does neither occur with CC2 in the gas phase, nor with ADC(2) in combination with COSMO, suggesting that both the difference between ADC(2) and CC2 and implicit solvent effects could contribute. In general, the deviation between ADC(2) and CC2 is caused by a significant contribution of singly excited determinants

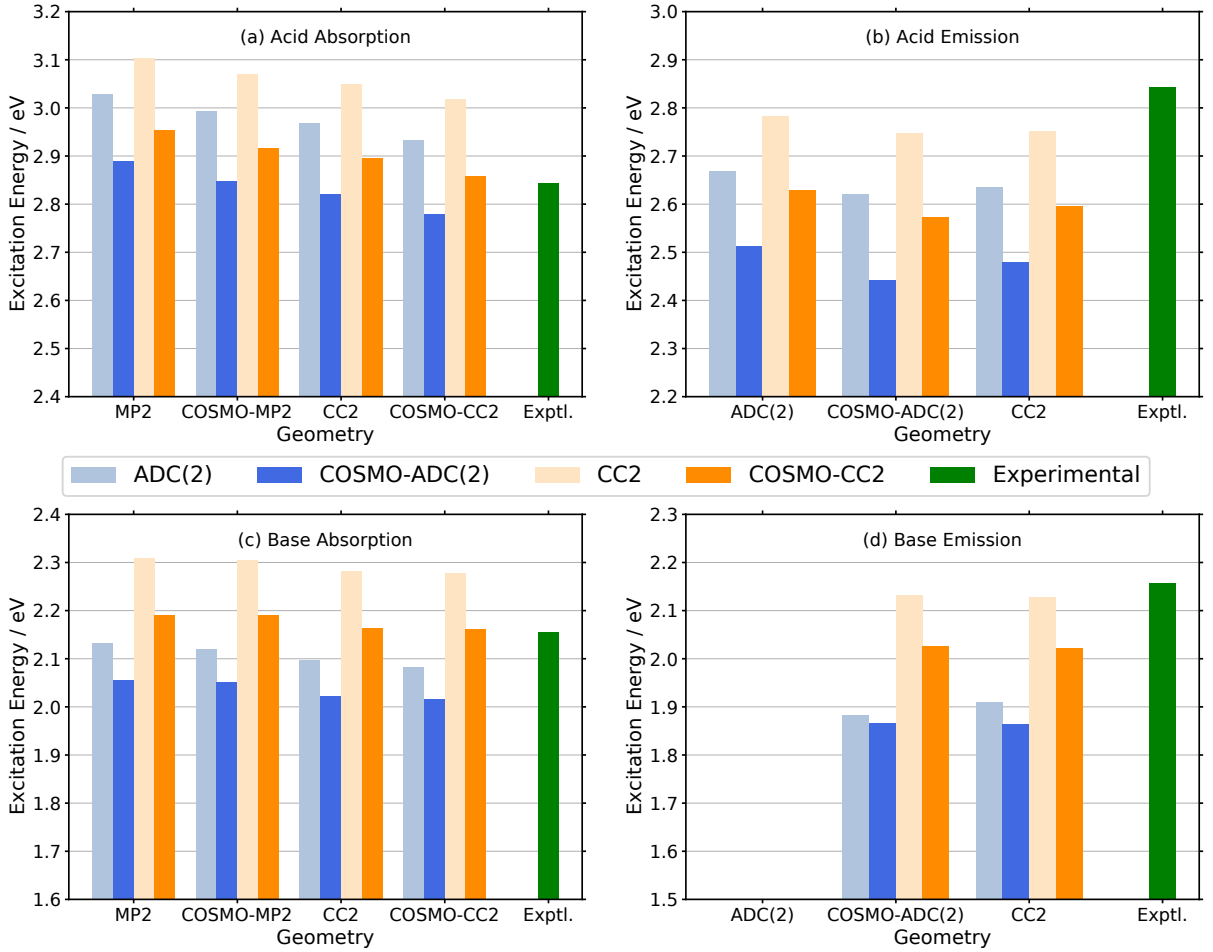



Figure 7.1.: **Disentangling structural and energetic effects of the solvent and methods on the electronic excitation energies.** Comparison of absorption (left) and emission (right) energies in eV at different combinations of methods for the equilibrium structures (horizontal axis; groups) and for the calculation of the electronic excitation energies (vertical axis; colored bars) of the acid (top) and base (bottom) species of photoacid **B**. Structures were optimized in the cc-pVDZ basis set and excitation energies were subsequently calculated in the aug-cc-pVDZ basis set. Experimental values taken from Ref. 494 are included for comparison. The results at the gas-phase ADC(2) $S_1$ geometry of the base in (d) are not included due to nonphysically low values.

to the ground-state wave function that is included in CC2, but missing in MP2 (as the ground-state analogue of ADC(2)). However, the negative charge of the (anionic) base also seems to play a role as ADC(2) works for the gas-phase $S_1$ geometry of the neutral acid just fine. As already observed and discussed in the previous study with DMSO as the solvent (cf. Chapter 6), this ADC(2) issue relates to a different order of the excited states in the gas phase and in solution, indicating that the solvent in fact has a stabilizing effect on the different excited states. These findings are also in agreement with the other observations that (i) the ADC(2)–CC2 deviation is larger for the base compared to the acid, pointing toward a higher need for singles contributions, and that (ii) the incorporation of implicit solvent effects seems to effectively reduce this need as reflected in a smaller ADC(2)–CC2 differences when COSMO is included. Another interesting observation is that the ADC(2)–CC2 deviation for the base is larger in $S_1$

compared to $S_0$ (see Tab. C.3), which might be a more general feature of such cases where ADC(2) and CC2 noticeably differ, posing a possible subject for more thorough investigations in the future.

Concluding on the reliability of the selected methods, the results for photoacid **B** in acetone are very similar to the previous results for photoacid **F** in DMSO. The absorption energies at the COSMO-CC2//COSMO-CC2 level are in excellent quantitative agreement with the experimental results, whereas the emission energies at the COSMO-CC2//COSMO-ADC(2) level underestimate them by 0.1–0.2 eV. For comparison, the mean absolute error of the methods ADC(2) and CC2 with respect to theoretical best estimates (mainly CC3/aug-cc-pVQZ) for vertical transition energies is also on the same order[467]. Therefore, except for the large deviation for the acid emission energy that is further analyzed later (*vide infra*), all results fall within the typical accuracy.

Being restricted to (solution-phase) COSMO-ADC(2) geometries in the excited state due to the missing availability of COSMO-CC2 for excited-state geometry optimizations argues for using the corresponding COSMO-MP2 geometries in the ground state to maintain a consistent description of both electronic states. This seems justified as the corresponding COSMO-CC2//COSMO-MP2 absorption energies likewise only differ slightly (50–70 meV) from the experiments. However, even independent of the method for the geometry, the use of COSMO-CC2 for the excitation energies clearly gives better results though and thus remains highly anticipated. Therefore, COSMO-CC2 excitation energies at COSMO-MP2 ($S_0$) or COSMO-ADC(2) ($S_1$) geometries are the default levels in this work.

For this photoacid, CC2 still yields geometries that give slightly smaller, which here means better, excitation energies. Particularly for the absorption of the acid, a monotonous decrease from the MP2, over the COSMO-MP2 and CC2, toward the COSMO-CC2 geometry is observed, independent of the method for the excitation energy. Besides, implicit solvation has a significant effect on the excitation energies, manifesting in the pronounced bathochromic shifts of 0.10–0.15 eV, but only a slight to no effect on the geometries (as probed by the excitation energies). Moreover, the effect through the geometry is actually larger for the acid compared to the base: Using the gas-phase geometry instead of the solution-phase geometry to calculate (solution-phase) excitation energies introduces an additional error of $\sim 50$ meV for the acid, while both geometries basically yield identical results for the base.

### 7.3.2. Comparison of Photoacids A–F in Implicit Acetone

In order to compare the $\Delta \mathrm{p}K_\mathrm{a}$ values of the different photoacids in acetone, the UV/Vis absorption and fluorescence emission energies of the compounds A–F were recalculated in acetone. In accordance with the results from the previous section and results of a previous study in DMSO, the geometries were optimized in the cc-pVDZ basis set using COSMO-MP2 for the ground state and COSMO-ADC(2) for the first excited state. UV/Vis absorption spectra were subsequently calculated at the ground-state equilibrium structures, while fluorescence emission spectra were calculated at the excited-state equilibrium structures. COSMO-ADC(2) as well as COSMO-CC2 were used for the calculation of electronic excitation energies and oscillator strengths in the aug-cc-pVDZ basis set. The COSMO-

CC2//COSMO-CC2 emission energies were estimated based on the COSMO-CC2//COSMO-ADC(2) results, i.e., COSMO-CC2 energies at the COSMO-ADC(2) excited-state geometries. Furthermore, the good performance of COSMO-CC2//COSMO-CC2 for the absorption energies of photoacid **B** in acetone—in parallel to revisiting the results in DMSO—motivated to additionally include these also for the other photoacids **A** and **C**–**F**.

### Agreement between Calculated and Experimental Excitation Energies

The calculated UV/Vis absorption and fluorescence emission energies are compared to the experimental results in Fig. 7.2 and the corresponding numerical values can be found in Tab. C.2. In addition, a statistical analysis of the errors is given in Tab. 7.2.

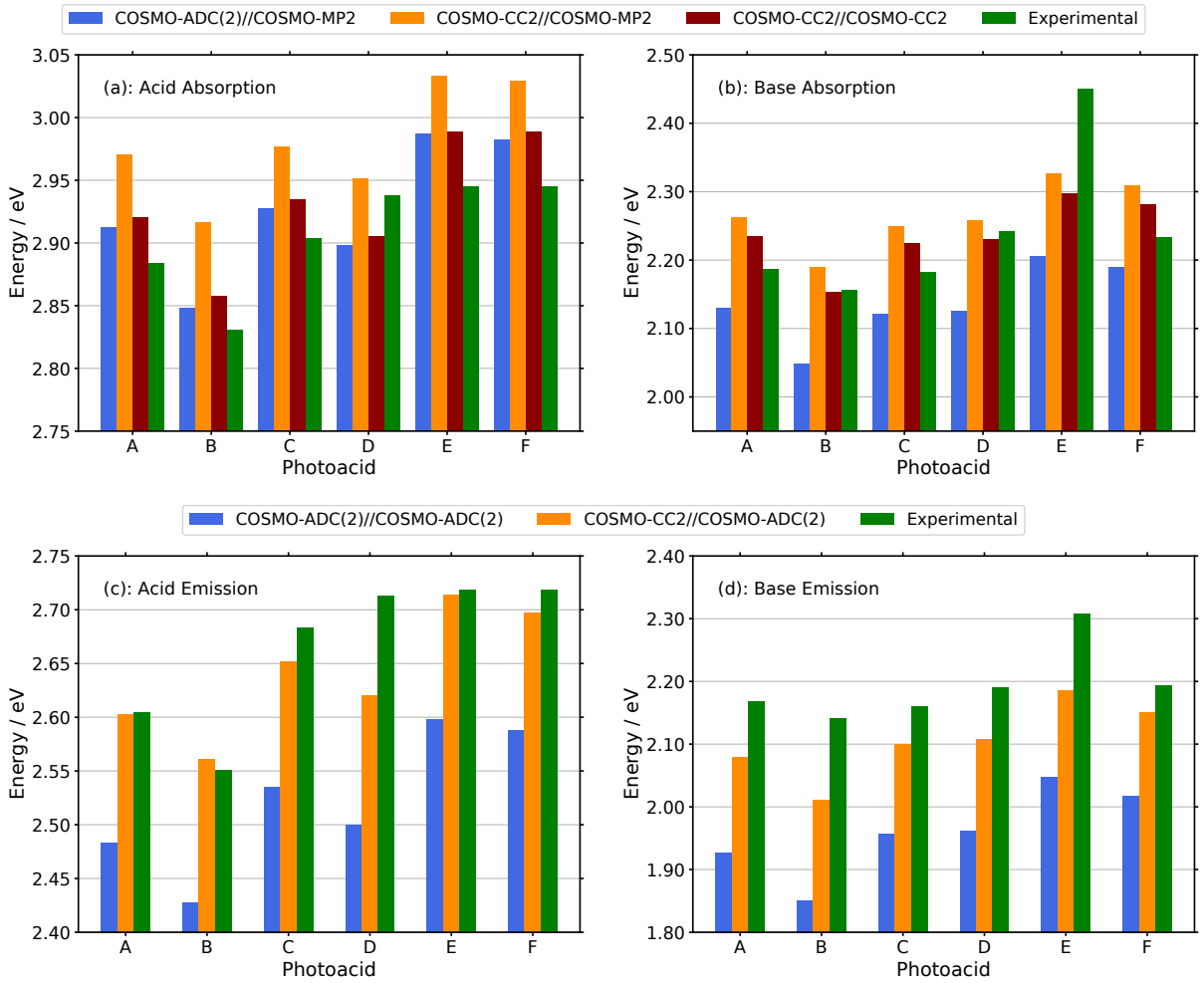



Figure 7.2.: **Theoretical spectroscopy of Jung's photoacids in acetone.** Comparison of calculated and experimental UV/Vis absorption (top row) and fluorescence emission (bottom row) energies in eV for the acid (left) and base (right) forms of the six photoacids **A**–**F** in acetone. Experimental values are taken from the original data from Ref. 309.

The results show that COSMO-CC2 does not only perform overall better than COSMO-ADC(2), but also very well in general based on mean absolute errors (MAEs) or root-mean-square errors (RMSEs) of

Table 7.2.: **Statistical error analysis of the UV/Vis absorption and fluorescence emission energies of the acid (ROH) and base ($RO^-$) species of photoacids A–F in acetone.** Mean error (ME), mean absolute error (MAE), maximum absolute error (maxAE), and root-mean-square error (RMSE) based on the calculated COSMO-ADC(2) and COSMO-CC2 excitation energies and experimental results (from Ref. 309) as shown in Fig. 7.2. An asterisk is used to differentiate absorption (ROH, $RO^-$) from emission ($ROH^*$, $RO^{-*}$) energies. Values are given in meV.

| | | **ME** | **MAE** | **maxAE** | **RMSE** |
|---|---|---|---|---|---|
| **ROH** | COSMO-ADC(2)//COSMO-MP2 | −18 | 32 | 42 (E) | 33 |
| | COSMO-CC2//COSMO-MP2 | −72 | 72 | 88 (E) | 77 |
| | COSMO-CC2//COSMO-CC2 | −25 | 36 | 44 (E) | 36 |
| **ROH*** | COSMO-ADC(2)//COSMO-ADC(2) | 143 | 143 | 213 (D) | 147 |
| | COSMO-CC2//COSMO-ADC(2) | 24 | 27 | 92 (D) | 41 |
| **$RO^-$** | COSMO-ADC(2)//COSMO-MP2 | 105 | 105 | 244 (E) | 125 |
| | COSMO-CC2//COSMO-MP2 | −24 | 65 | 124 (E) | 74 |
| | COSMO-CC2//COSMO-CC2 | 5 | 51 | 152 (E) | 70 |
| **$RO^{-*}$** | COSMO-ADC(2)//COSMO-ADC(2) | 233 | 233 | 290 (B) | 236 |
| | COSMO-CC2//COSMO-ADC(2) | 87 | 87 | 130 (B) | 93 |

$<$ 100 meV (i.e., better than the reported typical accuracy for excitation energies of organic closed-shell molecules in vacuum[466]). The only case where the COSMO-ADC(2) results happen to be closer to the experimental values are the absorption energies of the acid (Fig. 7.2(a)). The worst results are found for the COSMO-ADC(2) emission energies of the base (Fig. 7.2(d)), e.g., MAE of 233 meV and maximum absolute error (maxAE) of 290 meV, which appears the most demanding of these four cases due to multiple reasons. First, computational emission energies typically underestimate the experimental fluorescence energies (cf. ME mostly equal MAE for $S_1$ in Tab. 7.2) due to the assumption of a fully equilibrated excited-state geometry, which in the current study is also seen in the results for the emission energies of the acids. Second, ADC(2) has shown to be less accurate method for the bases of these photoacids due to missing contributions for a proper description of the electronic ground state (*vide supra*). Third, our calculated (de-)excitation energies refer to vertical transitions, whereas the experimental values denote maximum peak positions in UV/absorption or fluorescence emission spectra.

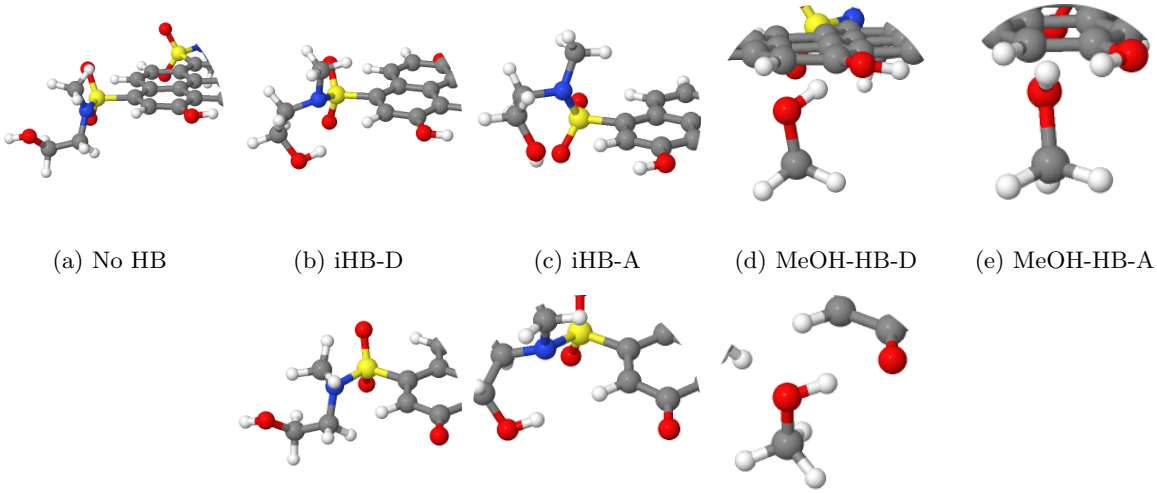
The fact that the COSMO-CC2//COSMO-MP2 results for the absorption energies of the acid agreed less well with the experimental results than those obtained with COSMO-ADC(2)//COSMO-MP2 served as a motivation to re-optimize the ground-state geometries at the COSMO-CC2 level and calculate COSMO-CC2//COSMO-CC2 absorption energies (red bars in Fig. 7.2(a-b)).

The COSMO-CC2 ground-state geometries generally give lower (COSMO-CC2) absorption energies compared to the COSMO-MP2 geometries for all compounds **A**–**F**, decreasing by ca. 0.05 eV for the acids and 0.025 eV for the bases. Note that the smaller effect of this energetic stabilization for the base compared to the acid is in line with the observations and discussion in Section 7.3.1. Resulting from this energy decrease, the accuracy increases with these COSMO-CC2 geometries. For the acid, MAE, maxAE, and RMSE are reduced by a factor of 2, while the improvement is much more subtle, yet still visible for the base. As demonstrated by an ME close to zero, COSMO-CC2//COSMO-CC2 reveals a good error compensation for the base absorption (MAE and RMSE are also slightly reduced), in contrast

to COSMO-CC2//COSMO-MP2 which consistently overestimated the energies. Only maxAE (photoacid **E**) has further increased owing to an underestimation of the experimental value already at the COSMO-MP2 geometry that further amplifies for the COSMO-CC2 geometry due to additional stabilization.

### Tracking the Error for the Outlier—Photoacid E

Apart from this improvement in accuracy, the deviation between the computed and the experimental results for the absorption energy of the base **E**, as the largest outlier, is not affected by changing the ground-state geometry, which motivated us to further investigate this particular photoacid. An important difference between this compound and the others are the additional OH groups in the side chains of the sulfonic acid amide moieties, which offer additional hydrogen-bonding sites. It turned out that compound **E** is not flexible enough to allow for intramolecular hydrogen bonding (HB) in either the acid (Fig. 7.3(b–c)) or base (Fig. 7.3(g)) that would explain the observed discrepancies, especially the huge underestimation of base absorption by $> 0.15$ eV. Thus, the absorption and emission energies obtained after geometry optimizations for such attempted structures are very similar to the original results (Fig. 7.3(a,f)) and, importantly, do not show any significant improvement with respect to the experiments (Tab. 7.3).



(a) No HB (b) iHB-D (c) iHB-A (d) MeOH-HB-D (e) MeOH-HB-A

(f) No HB (g) iHB-D (h) MeOH-HB-D

Figure 7.3.: **Intra and intermolecular hydrogen-bonding interactions for photoacid E.** Magnified acid (top) and base (bottom) structures without HB (No HB), for intramolecular HB (iHB) with the side-chain OH either acting as HB donor (D) or acceptor (A), and for intermolecular HB modeled by an interaction with MeOH acting as HB-D or HB-A. Only HB donation is relevant for the base. All structures have been optimized at the COSMO-MP2/cc-pVDZ level.

Next, self-association, i.e., *inter*molecular hydrogen bonding between the photoacid OH group of one molecule and an OH group in the side chain of another molecule was conjectured as the cause. To test this, first the effect of such hydrogen bonding on the base species was studied, i.e., the side-chain OH acting as the HB donor, which is assumed to have a stronger HB interaction (i.e., more negative bond

Table 7.3.: **Shifts induced for photoacid E by hydrogen bonding.** Comparison of calculated UV/Vis absorption and fluorescence emission energies (*) in eV of the acid (ROH) and base ($RO^-$) species of photoacid **E** for different intra and inter-molecular interactions: no interactions (No HB), intramolecular hydrogen bonding (iHB), and intermolecular hydrogen bonding due to self-association (MeOH). The HB role of the photoacid OH/$O^-$ is labeled with D (donor) and A (acceptor). The experimental results are taken from Ref. 309.

| | **No HB** | **iHB** | | **MeOH** | | **Experimental** |
|---|---|---|---|---|---|---|
| | | HB-D | HB-A | HB-D | HB-A | |
| **ROH** | 3.033 | 3.023 | 3.028 | 3.068 | 2.967 | 2.945 |
| **ROH*** | 2.714 | n.a. | n.a. | 2.737 | 2.649 | 2.719 |
| **$RO^-$** | 2.326 | 2.310 | — | 2.383 | — | 2.450 |
| **$RO^{-*}$** | 2.186 | n.a. | — | 2.224 | — | 2.309 |

energy) due to larger electrostatic contributions. Here, the second photoacid molecule was represented by methanol (MeOH) to decrease the computational costs of the model system (see Fig. 7.3(h)).

The results for photoacid **E** in Tab. 7.3 reveal a strong effect of intermolecular HB donation on $RO^-$ and $RO^{-*}$, consisting in blue shifts of $\sim 60$ meV and $\sim 40$ meV, respectively. These shifts almost reduce the errors by 50 %, changing from 0.12 meV to only 60–70 meV. Moreover, the results for $RO^-$ and $RO^{-*}$ both continue to underestimate the experimental value, which is in agreement with the explicit solvent effect of water on the $RO^-/RO^{-*}$ properties of photoacid **B** in water (see Section 7.4.3, Tab. 7.8). Since only one HB donor was considered, but each molecule of photoacid **E** has one OH group in each of the three substituents, additional blue shifts that would further compensate for that are anticipated.

In analogy, also the HB effect of MeOH, both as donor (Fig. 7.3(d)) and acceptor (Fig. 7.3(e)), on the acid species was studied. Regarding these two different HB scenarios, one should note that the aromatic OH group is only a weak HB acceptor, but a strong HB donor. For example, phenol—as a model for the pyrenol core of photoacid **E**—has Kamlet-Taft parameters of $\alpha = 1.65$ (HB donation) and $\beta = 0.30$ (HB acceptance), whereas ethanol—as a model for the side-chain OH group—has parameters $\alpha = 0.86$ and $\beta = 0.75$[495]. Consequently, such configurations with the aromatic OH group as the HB donor and the aliphatic side-chain OH as the acceptor should be more stable and hence be existent more frequently compared to the reverse scenario. For ROH, the previous result without HB interactions overestimated the experimental value by $\sim 90$ meV, which becomes significantly reduced by a red shift of $\sim 70$ meV in case of the HB acceptance of MeOH. In contrast, HB donation leads to a blue shift (35 meV) that does not further improve the result in this case. For $ROH^*$, similar red (65 meV) and blue (23 meV) shifts are found for MeOH acting as a HB acceptor or donor, respectively. However, these shifts do not markedly improve the error, as the result prior to any HB considerations was already—presumably accidentally due to beneficial error compensation—in excellent agreement with the experiment.

Still, these results for the model (Tab. 7.3) overall appeared convincing that such intermolecular HB interactions between the two or more photoacid molecules are the cause for the deviations of photoacid **E** observed in the results for the set of photoacid **A**–**F** (Fig. 7.2). Interestingly, no such distinct outlier character for photoacid **E** was found in the previous study in DMSO. This observation is assigned to the higher HB-acceptor strength of DMSO (as also discussed in Section 7.4.2) which binds the side-chain OH

groups more strongly and hence makes them less available for photoacid–photoacid interactions. This is also in line with the general description of DMSO as an HB breaker in the literature[496–498].

### Discussion of Acidity Increase Upon Excitation

Through the computational or experimental first electronic excitation energies (cf. Fig. 7.2), the $\Delta pK_a$ values, i.e., the change in $pK_a$ upon excitation can be computed based on the Förster cycle (Eq. (7.1)). The corresponding results have been collected in Tab. 7.4.

Table 7.4.: **Differences in the photo-induced acidity increase as quantified by $\Delta pK_a$ between the photoacids A–F in the solvent acetone.** $\Delta pK_a$ based on the Förster cycle (cf. Eq. (7.1)) using either absorption, emission, or averaged excitation energies calculated with COSMO-CC2 at the COSMO-MP2 ($S_0$) and COSMO-ADC(2) ($S_1$) geometries (taken from Tab. C.2) and the experimental results (taken from Ref. 309).

| | | Photoacids | | | | | |
|---|---|---|---|---|---|---|---|
| | **Level** | **A** | **B** | **C** | **D** | **E** | **F** |
| **Absorption** | COSMO-CC2 | −12.0 | −12.3 | −12.3 | −11.7 | −11.9 | −12.2 |
| | Experimental | −11.8 | −11.4 | −12.2 | −11.8 | −8.4 | −12.0 |
| **Emission** | COSMO-CC2 | −8.8 | −9.3 | −9.3 | −8.7 | −8.9 | −9.2 |
| | Experimental | −7.4 | −6.9 | −8.9 | −8.8 | −6.9 | −8.9 |
| **Averaged** | COSMO-CC2 | −10.4 | −10.8 | −10.8 | −10.2 | −10.4 | −10.7 |
| | Experimental | −9.6 | −9.2 | −10.5 | −10.3 | −7.6 | −10.4 |

Since the better performance of COSMO-CC2 over COSMO-ADC(2), as observed before, is also reflected in the $\Delta pK_a$ values of Tab. 7.4, we only focus on the COSMO-CC2 results in the following discussion. Moreover, the $\Delta pK_a$ values based on absorption energies are in better agreement with the experimental values compared to those based on emission energies. The reasons for this have already been discussed earlier. In particular, note that the more accurate COSMO-CC2 absorption energies at the COSMO-CC2 ground state geometries (see Tab. C.4) have overall increased the accuracy of $\Delta pK_a$ to an excellent agreement with the experimental results (except for **E**, *vide supra*).

That having said, the main focus is set—for brevity—to the $\Delta pK_a$ values that are averaged over absorption and emission energies. These are generally in very good agreement with the experimental data, differing by less than one $pK_a$ unit on average. The deviation is slightly larger for photoacids **A** (0.8) and **B** (1.6) and largest for **E** (2.8), with large deviations ($\sim 2$) for the emission contributions as the main error source. Note that the calculated values always overestimate $\Delta pK_a$ in magnitude, with the only exception of photoacid **D**.

In comparison to the previous results in DMSO (cf. Chapter 6), the calculated averaged COSMO-CC2 $\Delta pK_a$ values show a tendency to further decrease (i.e., increase in magnitude) in the less polar solvent acetone. This phenomenon was already observed before when comparing DMSO to water and can be explained based on the different stabilizing effect of the solvent polarity on the four different species (ROH, ROH$^*$, RO$^-$, RO$^{-*}$) involved in the Förster cycle. In the following, photoacid **E** is excluded since its calculated $\Delta pK_a$ are based on the results in Fig. 7.2, which revealed to be outliers (*vide supra*). Although the averaged computed $\Delta pK_a$ that is (additionally) averaged over the five remaining photoacids

**A**–**D** and **F** only differs slightly, i.e., −10.50 in DMSO vs. −10.58 in acetone, the same trend is already reflected in the experimental data. Unfortunately, a direct comparison of averaged experimental $\Delta pK_a$ values is prevented by missing experimental data on ROH$^*$ emission for **A** and **B** in DMSO. However, on average, the experimental $\Delta pK_a$ based on absorption in acetone (−11.84) compares to a value of −10.74 in DMSO. Similarly, this trend is also found in the $\Delta pK_a$ based on experimental emission energies which, averaged over compounds **C**, **D**, and **F**, yields values of −8.38 in acetone and −6.38 in DMSO.

In general, the agreement between the experimental and calculated results is overall better for acetone than for DMSO, in line with the weaker, specific solute–solvent interactions in the less polar solvent acetone and in view of the limitations of the implicit solvent model COSMO. The large deviations observed for compound **E**, when describing an isolated molecule in the solvent cavity, are most probably due to intermolecular interactions between two photoacid molecules (*vide supra*). For the photoacid–methanol complex as a model system, the following $\Delta pK_a$ values are obtained instead: −9.9 (absorption), −7.2 (emission), and −8.5 (averaged). These results demonstrate a significantly improved agreement with the experimental values by reducing the errors to only 1.5, 0.3, and 0.9 for absorption, emission, and on average, respectively. Compared to the COSMO-CC2 results without hydrogen bonding, the $\Delta pK_a$ in both absorption and emission have changed by roughly two $pK_a$ units, but slightly stronger in absorption. Since the deviation from the experimental $\Delta pK_a$ was already dominated by the absorption rather than the emission contribution, the results for the model system indeed reveal a stronger improvement *via* the absorption, in line with the larger effects on the ROH and RO$^-$ properties (Tab. 7.3).

#### Discussion of Ground and Excited-state Acidities

Table 7.5.: **Comparison of calculated ground-state and excited-state acidities of the photoacids A–F in the solvent acetone.** $pK_a$ values using COSMO-RS at the BP-TZVP (and BP-TZVPD-FINE) level, $\Delta pK_a$ based on the Förster cycle using the averaged excitation energies at the COSMO-CC2 level (taken from Tab. 7.4), and $pK_a^*$ based on these input quantities according to Eq. (1.1).

| | **Photoacids** | | | | | |
|---|---|---|---|---|---|---|
| | **A** | **B** | **C** | **D** | **E** | **F** |
| $\mathbf{pK_a}$ | 15.6 (15.4) | 14.2 (14.7) | 18.6 (18.5) | 20.9 (19.6) | 19.4 (20.6) | 19.9 (20.3) |
| $\mathbf{\Delta pK_a}$ | −10.4 | −10.8 | −10.8 | −10.2 | −10.4 | −10.7 |
| $\mathbf{pK_a^*}$ | 5.2 (5.0) | 3.4 (3.9) | 7.8 (7.7) | 10.7 (9.4) | 9.0 (10.2) | 9.2 (9.6) |

As can be seen in Tab. 7.5, the $pK_a$ at the two levels of theory are generally quite similar and, more importantly, share common characteristic features. For example, compound **B** is predicted to be the strongest ground-state acid at both levels and the same trends between compounds **A**–**D** are found. The largest deviations between the two levels are found for photoacids **D** (1.3) and **E** (1.2), which causes the overall trends for **A**–**F** to differ between these levels. **D** is the weakest at the BP-TZVP level, while it is **E** for BP-TZVPD-FINE. These general trends in the $pK_a$ values are governed by the electronic effect of the substituents. Photoacids **A** and **B** are the stronger acids owing to their strongly electron-withdrawing trifluoromethyl groups in the ester moieties, while **D**–**F** are the weaker acids due to their less electron-

withdrawing amide moieties that are either purely aliphatic (**F**) or carry only distal oxygen-containing functional groups (**D**, **E**). Compound **C** is of medium strength due to its amide substituents—amides are generally less electron-withdrawing compared to esters—that are directly substituted with strongly (inductively) electron-withdrawing methoxy groups.

The resulting $pK_a^*$, i.e., excited-state $pK_a$ values are also shown in Tab. 7.5. Since the acidity increase ($\Delta pK_a$) was found to be very similar for the compounds **A**–**F**, the relative order in $pK_a^*$ is mainly determined by the order in $pK_a$. As a result, photoacid **B** is predicted to be the strongest excited-state acid with a $pK_a^*$ (on average) around 3.6, followed by **A** (5.1), **C** (7.8), **E** (9.6) and **F** (9.4), leading to **D** (10.1) as the weakest acid in the excited state. These results are in line with those in the solvent DMSO. However, two main differences compared to DMSO should be noted. First, the $pK_a^*$ values cover a larger range in acetone (6.5) compared to DMSO (4.6) or water (3.1), which is due to the reduced $pK_a$ windows in these solvents. Second, all $pK_a^*$ values are strongly positive which indicates a much lower tendency for ESPT. This is due to the largely positive ground-state $pK_a$ values, as a consequence of the low bulk basicity of the solvent acetone. Thus all compounds **A**–**F** are expected to be weaker acids than the protonated solvent, which means that ESPT is thermodynamically unfavorable ($\Delta G_{\text{diss}} > 0$). Still, photoacid **B** is closest to these threshold values, thus suggesting the largest ESPT yield in acetone, which matches the experimental finding that ESPT to solvent is observed only for this compound [48].

## 7.4. Beyond Implicit Solvation

Compounds **B** and **E** are the photoacids for which the largest deviations between the COSMO-CC2 calculations and the experiments were observed. Photoacid **B** also revealed one of the largest deviations between the calculated and the experimental $\Delta pK_a$ values (cf. Tab. 7.4 in Section 7.3.2), especially regarding the emission energies. Furthermore, the experimental results show that specific molecular interactions between the photoacid **B** and the solvent or other proton acceptors become relevant in acetone solution (see Chapter 3). This motivated us to include explicit solvent molecules in the first solvation shell and to study their effect on the electronic excitation energies of photoacid **B**. Thereby, we focus on the local solvation of the OH and $O^-$ group of the acid (ROH) and base ($RO^-$), respectively.

It is important to note that the way of including explicit solvent that is followed here is purely based on chemical intuition and does not constitute an approach that aims at systematically improving the calculated results up to perfect agreement with the experiments, which would, e.g., require MD simulations to obtain representative solvation structures. Rather, micro-solvated structures for hydrogen-bonding configurations that appear most relevant based on the Kamlet-Taft parameters are considered (*vide infra*). In particular, a strict comparison of the absolute excitation energies with the experimental results is thus not meaningful, mainly because of two reasons: (i) an uncertainty due to the (larger) intrinsic errors compared to the observed (smaller) solvatochromic shifts induced by explicit solvent, and (ii) a possible overestimation of the solvatochromic shifts due to solvent fluctuation causing larger HB distances at the equilibrium structures compared to the thermodynamic ensemble average. Therefore,

the focus will be instead set to the differential effect (of explicit solvent) between the acid and base, i.e., the effect on $\Delta pK_a^*$, since large parts of these two errors are anticipated to cancel therein.

### 7.4.1. General Considerations

To compare the effect of explicit solvation on the spectral properties of the four fundamental photoacid species (ROH, ROH$^*$, RO$^-$, and RO$^{-*}$) in different environments, the solvents acetone, DMSO, and water were selected. This selection is chosen for best comparison with experiments since all three solvents were already part of experimental studies[48,309] and DMSO part of my previous work (Chapter 6).

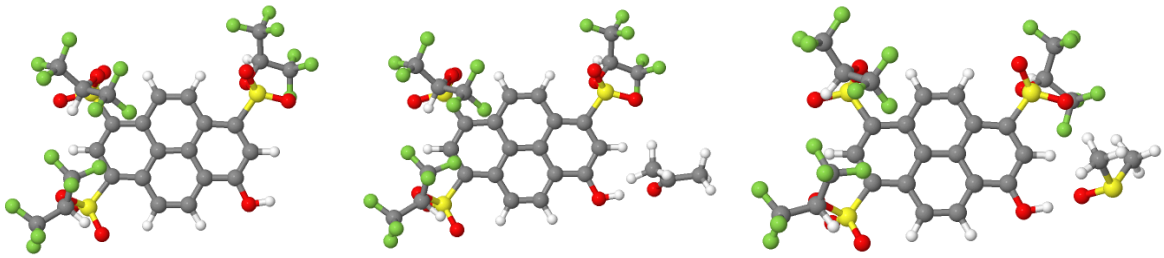
Before starting to include explicit solvent, it is worth to reconsider the H-bonding characteristics of these solvents and that of photoacid **B**. Per definition, acetone and DMSO have as *aprotic* solvents no or only a very small tendency to act as hydrogen-bond (HB) donors (HB-Ds) as quantified, e.g., by the Kamlet-Taft solvent parameter $\alpha$ (0.08 for acetone and 0.00 for DMSO)[495]. They mostly act as HB acceptors (HB-As) as quantified, e.g., by the Kamlet-Taft parameter $\beta$ (0.48 for acetone and 0.76 for DMSO). In contrast, water—as a dipolar *protic* solvent—can act as both a strong HB-D ($\alpha = 1.17$) and a moderate HB-A ($\beta = 0.47$). Thus, in this set of solvents, DMSO is the weakest HB-D and strongest HB-A, while water is the strongest HB-D, and water and acetone are both similarly the weakest HB-As. For photoacid **B** (referring to phenol as a model), the OH group can either act as a weak HB-A ($\alpha = 0.30$) or strong HB-D ($\beta = 1.65$), whereas the O$^-$ group can only accept hydrogen bonds from other solvent molecules.

Micro-solvated structures were generated by manually adding a given number of explicit solvent molecules according to the target HB configuration to the molecular structure of the implicitly solvated photoacid species and then re-optimizing the full structure embedded in a COSMO cavity. In particular, the $S_0$ equilibrium geometries, used for the calculation of ROH and RO$^-$ absorption energies, are optimized at the COSMO-MP2/cc-pVDZ level, whereas the $S_1$ equilibrium structures, used for the calculation of ROH$^*$ and RO$^{-*}$ emission energies, are optimized at the COSMO-ADC(2)/cc-pVDZ level. All excitation energies are typically calculated with COSMO-CC2/aug-cc-pVDZ.

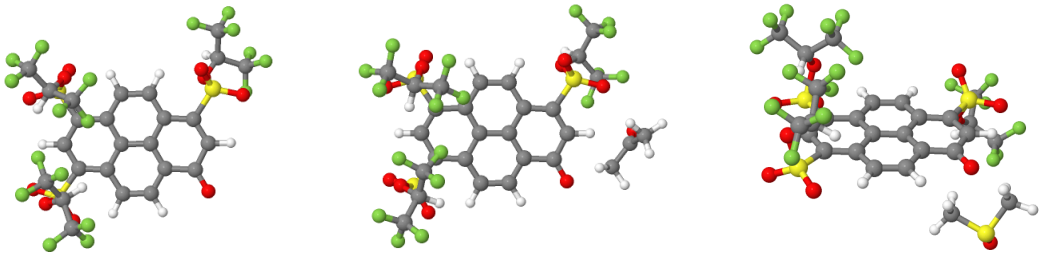
### 7.4.2. Explicit Solvent Effects in Acetone and DMSO

#### Local Solvation in Acetone and DMSO

Due to their similarity, the results for the solvents acetone and DMSO are discussed first. One explicit solvent molecule was included to locally solvate the OH or O$^-$ group. Resulting from our considerations regarding the HB characteristics of the different photoacid species as well as the solvents (*vide supra*), we chose the solvent to act as HB-A for ROH/ROH$^*$ (Fig. 7.4(b–c)) and to act as a HB-D for RO$^-$/RO$^{-*}$ (Fig. 7.4(e–f)). Due to the similarity between the $S_0$ and $S_1$ equilibrium structures, only those for $S_0$ are shown in Fig. 7.4. In Tab. 7.6, the excitation energies for these micro-solvated structures in both solvents are compared to those with the purely implicit solvent model COSMO and the experimental reference values.



(a) Acid: Purely implicit (b) Acid: Acetone (c) Acid: DMSO



(d) Base: Purely implicit (e) Base: Acetone (f) Base: DMSO

Figure 7.4.: **Implicitly solvated and micro-solvated structures of photoacid B in acetone and DMSO.** Acid (top) and base (bottom) structures without explicit solvent (purely implicit; left) and with one explicit acetone (middle) or DMSO (right) molecule. All structures have been optimized at the COSMO-MP2/cc-pVDZ level.

For both solvents, larger solvatochromic effects—due to the inclusion of explicit solvent—are found for the protonated species ROH and ROH$^*$: red shifts of roughly 80–90 meV in acetone and 110–170 meV in DMSO. In contrast, for $RO^-$ and $RO^{-*}$, the shifts fall below 10 meV, which is in agreement with the low HB-D ability of these solvents. Furthermore, the larger shifts for ROH and ROH$^*$ in DMSO compared to acetone emphasize the stronger HB acceptance of DMSO.

As mentioned before, a comparison of the absolute excitation energies with the experimental results has its issues. For example, the inclusion of one solvent molecule apparently improves the agreement with the experimental values in acetone for ROH (error $< 10$ meV), while it decreases for ROH$^*$ (error of 70 meV), and is hardly affected for $RO^-$ and $RO^{-*}$. One should note that these residual errors are much smaller than both the intrinsic error of CC2 and the error due to comparing (calculated) vertical excitation energies and (experimental) band maxima. Thus, it is not possible to directly infer from these results any reliable information on the main source of the remaining error, e.g., an incomplete solvation description. Instead, focusing on the explicit solvent effect on $\Delta pK_a^*$ appears a much more reliable way to use micro-solvated structures for tracking down the largest contributions of explicit solvation.

#### Effect on Acidity Increase in Acetone and DMSO

Using the excitation energies for the micro-solvated structures in acetone and DMSO (Tab. 7.6), the Förster-cycle $\Delta pK_a$ values *via* Eq. (7.1) were re-calculated, as given in Tab. 7.7. In accordance with the larger errors associated with the emission energies, the results in Tab. 7.7 show that the $\Delta pK_a$ in emission improves for both solvents more significantly compared to those in absorption. For example, we

Table 7.6.: **Solvatochromic shifts due to explicit solvent in the first solvation shell of photoacid B in the solvents acetone and DMSO.** Comparison of calculated UV/Vis absorption (ROH, $RO^-$) and fluorescence emission energies ($ROH^*$, $RO^{-*}$) in eV of the acid and base species of photoacid **B**. Results are given for the structures without explicit solvent in purely implicit solution and with one explicit solvent molecule. Experimental results are taken from Refs. 309 and 48 for acetone and DMSO, respectively.

| | **Acetone** | | | **DMSO** | | |
|---|---|---|---|---|---|---|
| | Implicit | Explicit | Experimental | Implicit | Explicit | Experimental |
| **ROH** | 2.916 | 2.837 | 2.831 | 2.882 | 2.769 | 2.761 |
| **ROH*** | 2.573 | 2.481 | 2.551 | 2.539 | 2.373 | — |
| **$RO^-$** | 2.191 | 2.187 | 2.156 | 2.155 | 2.164 | 2.153 |
| **$RO^{-*}$** | 2.027 | 2.020 | 2.141 | 1.995 | 1.997 | 2.134 |

find a change of 1.27 units in the absorption $\Delta pK_a$ for acetone that does not markedly affect the accuracy due a transition from over (0.84) to underestimation (0.43) (in magnitude), while the fluorescence $\Delta pK_a$ changes by 1.43 units, which drastically improves the error from $> 2$ (2.3) to $< 1$ (0.87).

Table 7.7.: **Effect of explicit solvent on the $\Delta pK_a$ of photoacid B in acetone and DMSO.** Calculated $\Delta pK_a$ based on the Förster cycle (cf. Eq. (7.1)) using absorption, emission, or averaged energies for implicitly as well as explicitly solvated structures of photoacid **B** (cf. Tab. 7.6) in comparison with the experimental $\Delta pK_a$ values (cf. Tab. 7.4) using the data from Refs. 48 and 309.

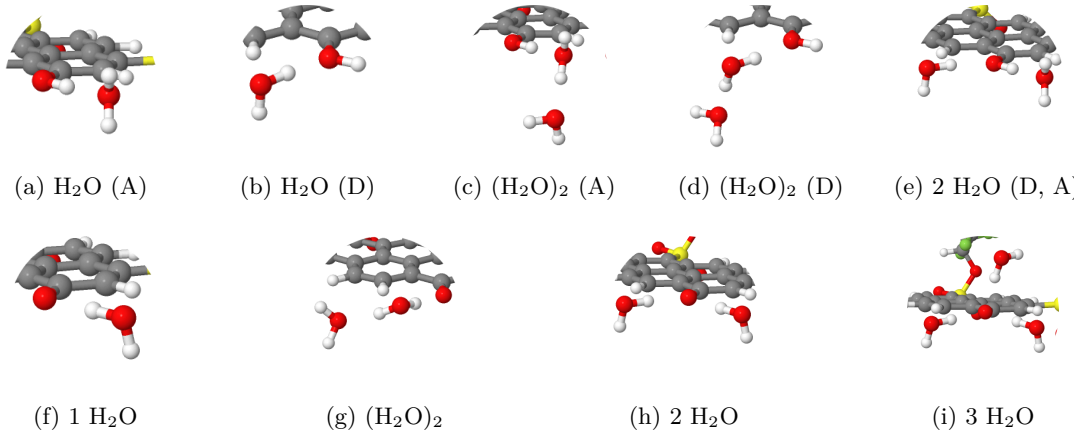
| | **Acetone** | | | **DMSO** | | |
|---|---|---|---|---|---|---|
| | Implicit | Explicit | Experimental | Implicit | Explicit | Experimental |
| **Absorption** | −12.26 | −10.99 | −11.42 | −12.29 | −10.23 | −10.28 |
| **Emission** | −9.23 | −7.80 | −6.93 | −9.20 | −6.36 | — |
| **Average** | −10.75 | −9.40 | −9.18 | −10.75 | −8.30 | — |

For DMSO, the absorption $\Delta pK_a$ strongly improves by almost 2 units, achieving an excellent agreement with the experiment (residual error of 0.1), whereas the fluorescence reveals an even more drastic change of $\sim$ 2.8 units. Unfortunately, no comparison with the experiment is possible due to the missing experimental fluorescence emission energy for $ROH^*$ in DMSO. However, the larger changes in both calculated absorption and emission $\Delta pK_a$ highlight the larger HB-acceptor ability of DMSO over acetone. In summary, we find some strong indications here that the largest contributions to the error with respect to experiment for the purely implicitly solvated photoacid in acetone and DMSO are missing HB interactions of the solvent with the photoacid OH group, especially the HB donation of $ROH^*$.

### 7.4.3. Explicit Solvent Effects in Water

#### Local Solvation in Water—One Explicit Water Molecule

Compared to the aprotic solvents acetone and DMSO, the situation in the protic solvent water is more complicated due to more extensive hydrogen bonding (see Fig. 7.5). The OH group of the photoacid can only donate one hydrogen bond, but accept up to two, i.e., two water molecules can act as HB donors in this case. Similarly, the $O^-$ group could in principle accept up to three hydrogen bonds. Therefore,



(a) $H_2O$ (A) (b) $H_2O$ (D) (c) $(H_2O)_2$ (A) (d) $(H_2O)_2$ (D) (e) 2 $H_2O$ (D, A)

(f) 1 $H_2O$ (g) $(H_2O)_2$ (h) 2 $H_2O$ (i) 3 $H_2O$

Figure 7.5.: **Micro-solvated structures of photoacid B in water for different numbers of explicit solvent molecules.** Magnified acid (top) and base (bottom) structures with up to three explicit water molecules, either as HB donors (D) or acceptors (A). Water exclusively acts as HB D for the base. All structures at the COSMO-MP2/cc-pVDZ level.

micro-solvated structures with varying numbers of water molecules and with different HB configurations need to be considered. This study is restricted to a maximum of three water molecules. Water can act as either a HB donor or acceptor in case of the acid, but only as a HB donor in case of the base. Like in section 7.4.2, the explicit solvent was added manually to the structures in implicit solution of the respective solvent and were subsequently re-optimized. The corresponding results for different structures are shown in Tab. 7.8. Due to the similarity between the $S_0$ and $S_1$ structures, only the former ones are displayed.

Table 7.8.: **Solvatochromic shifts due to explicit solvent in the first solvation shell of photoacid B in the solvent water.** Comparison of calculated UV/Vis absorption (ROH, $RO^-$) and fluorescence emission energies ($ROH^*$, $RO^{-*}$) of the acid and base species of photoacid **B**. Results are given for the structures without explicit solvent in purely implicit water and with up to three explicit water molecules as either HB donor (D) or acceptor (A). Experimental results are taken from Ref. 48.

| | **Water** | | | | | | | | |
|---|---|---|---|---|---|---|---|---|---|
| | Implicit | 1 $H_2O$ | | 2 $H_2O$ | | $(H_2O)_2$ | | 3 $H_2O$ | Experimental |
| | | HB-D | HB-A | HB-D HB-A | HB-D HB-D | HB-D | HB-A | HB-D | |
| **ROH** | 2.913 | 2.915 | 2.822 | 2.814 | — | 2.908 | 2.758 | — | 3.00 |
| **ROH*** | 2.562 | 2.602 | 2.477 | 2.502 | — | 2.604 | 2.435 | — | 2.53 |
| **$RO^-$** | 2.202 | 2.245 | — | — | 2.268 | 2.231 | — | 2.311 | 2.36 |
| **$RO^{-*}$** | 2.032 | 2.085 | — | — | 2.112 | 2.088 | — | 2.144 | 2.20 |

Comparing the results in Tab. 7.8 for the implicitly solvated species and those including one explicit water molecule (Fig. 7.5(a,b,f)) demonstrates that the specific hydrogen-bonding role of the solvent matters. When acting as a HB donor, explicit water causes a solvatochromic blue shift for all species: largest for $RO^{-*}$ (53 meV), slightly smaller for $RO^-$ (43 meV) and $ROH^*$ (40 meV), and almost zero for ROH (2 meV). In contrast, when acting as a HB acceptor, red shifts are observed: 91 meV for ROH and 85 meV for $ROH^*$. In comparison with the results for acetone and DMSO (Sec. 7.4.2), the solvatochromic

red shifts follow the order of the solvents in HB-acceptor strength ($\beta$): DMSO > acetone $\gtrsim$ water (cf. Sec. 7.4.1 for the $\beta$ values). Consistent blue shifts due to the solvent acting as the HB donor could only be observed for water since the HB-donating ability of acetone and DMSO are close to zero.

The trends that are observed here indicate that the excitation energies of the base are underestimated much more strongly compared to the acid. It is also physically plausible that for the negatively charge base more hydrogen bonds are relevant than for the acid. Therefore, we considered the addition of additional water molecules to the first solvation shell in the following.

#### Local Solvation in Water—Two (and More) Explicit Water Molecules

Perhaps not the most intuitive but a very simple case of adding two water molecules consists in its dimer, i.e., $(H_2O)_2$ (Fig. 7.5(c,d,g)) whose effect on the excitation energies is actually very similar to that of a single water molecule. In details, no pronounced effect for HB donation but a red shift of 155 meV for HB acceptance (larger than 1 $H_2O$) are found for ROH, whereas ROH$^*$ reveals a small blue shift of 42 meV (close to 1 $H_2O$) or a red shift of 127 meV (larger than 1 $H_2O$). Consequently, the HB donation of the dimer is comparable to that of the monomer, while the HB acceptance is enhanced—in line with a positive polarization of the oxygen of the water accepting the HB from the photoacid due to the HB donation of the second water molecule. In analogy, since only HB donation matters for the anion, blue shifts (very similar to 1 $H_2O$) of 29 meV and 56 meV are observed for $RO^-$ and $RO^{-*}$, respectively.

Apart from the dimer, also the interaction of two individual water molecules, i.e., non-hydrogen-bonded to themselves, with the photoacid OH ($O^-$) group was considered (Fig. 7.5 (e,h)), giving in theory three possible HB motifs: (i) both acting as HB donors, (ii) one acting as a HB donor and one as a HB acceptor, and (iii) both acting as HB acceptors. For the protonated form, scenario (i) was found to be unstable in the calculations (preferring intra-$H_2O$ HB) and (iii) is impossible (just one OH group for HB donation), leaving only (ii) to be considered; while (i) is the only relevant case for the deprotonated form. The mixed (HB-D, HB-A) motif (ii) yields a red shift of 99 meV for ROH, i.e., slightly larger compared to HB-D for 1 $H_2O$, and an overall red shift of 60 meV for ROH$^*$ that falls in between the HB-D and HB-A shifts for a single $H_2O$. This larger similarity in the ROH result to HB-D for 1 $H_2O$ reflects a more dominant effect of HB donation. Similarly, blue shifts of 66 meV ($RO^-$) and 80 meV ($RO^{-*}$) are found for the (HB-D, HB-D) case, which are larger than the results for 1 $H_2O$ and make a step in reducing the gap to the experimental value.

Finally, the case of micro-solvation with three water molecules was studied (Fig. 7.5(i)) for the $RO^-$ and $RO^{-*}$ species, mainly motivated by its negative charge. Here, each water acts as an HB donor (for the photoacid) and the structures were checked to lack HB between the water molecules. These results reveal even larger blue shifts of 124 meV for $RO^-$ and 112 meV for $RO^{-*}$, constituting in an apparent improvement with respect to the experiments. Although a detailed analysis of the actual residuals is less meaningful (*vide infra*), one should note that the underestimation of the results for $RO^-$ and $RO^{-*}$

shows a continuous progression from no explicit water to three water molecules with increasingly larger blue shifts.

#### Effect on Acidity Increase in Water

For water, studying the explicit solvent effect on $\Delta pK_a$ becomes more involved due to the larger number of possible solvent configurations. Based on the Kamlet-Taft parameters for phenol (cf. Sec. 7.4.1), as a model for hydroxyarenes, the following discussion is mainly restricted to the results for the most relevant micro-solvated structures in terms of the hydrogen bonding. This involves the configuration with one water molecule as the HB acceptor for the acid and the one with three water molecules as HB donors for the base. In addition, also the effect of water as a HB donor is studied in case of the acid (to illustrate the difference in the HB role), as well as the configuration with two water as HB donors for the base (to compare with the results for one and three water molecules). In all cases, the same number of water molecules and types of hydrogen bonds is present in both electronic states.

Table 7.9.: **Effect of explicit solvent on the $\Delta pK_a$ of photoacid B in water.** Calculated $\Delta pK_a$ based on the Förster cycle (Eq. (7.1)) using absorption, emission, or averaged energies for implicitly as well as explicitly solvated structures of photoacid **B** in comparison with the experimental $\Delta pK_a$ values using the data from Ref. 48 (cf. Tab. 7.8). Whereas the contribution for $RO^-$ and $RO^{-*}$ refers to the respective number of water molecules exclusively acting as HB donors, just one water molecule as either donor (HB-D) or acceptor (HB-A) is considered for ROH and $ROH^*$.

| | **Water** | | | | | |
|---|---|---|---|---|---|---|
| | Implicit | 1 $H_2O$ | | 2 $H_2O$ | 3 $H_2O$ | Explt. |
| | | HB-D | HB-A | | | |
| **Absorption** | −12.02 | −11.33 | −9.75 | −9.36 | −8.64 | −10.78 |
| **Emission** | −8.96 | −8.74 | −6.63 | −6.17 | −5.63 | −5.61 |
| **Average** | −10.49 | −10.04 | −8.19 | −7.77 | −7.14 | −8.20 |

For the results purely based on the implicit solvent model COSMO (Implicit in Tab. 7.9), the deviation from the experimental average $\Delta pK_a$ in water is dominated by the error from the emission contribution ($> 3$) rather than the absorption contribution ($\sim 1.2$), yielding an overall error of 2.3 $pK_a$ units. When including one explicit water molecule, the HB interaction with the photoacid as the HB donor and water as the HB acceptor is expected to be most relevant based on the Kamlet-Taft parameters. For this configuration (1 $H_2O$ (HB-A) in Tab 7.9), significant changes of $\sim 2.3$ units in both the $\Delta pK_a$ in absorption and in emission are observed, improving the agreement with the experimental results. In contrast, for the less relevant configuration with water as the HB donor (1 $H_2O$ (HB-D) in Tab 7.9), only a weak effect on $\Delta pK_a$ is found, reflecting the much smaller changes in the absolute energies for water as HB-D compared to HB-A (cf. Tab. 7.8). In fact, the $\Delta pK_a$ values with water as a HB donor for ROH and $ROH^*$ have larger contributions from the effect on $RO^-$ and $RO^{-*}$ instead. Thus, even if the (less relevant) HB donation of water occurs, the effect on $\Delta pK_a$ is much smaller. This comparison also shows that the calculated $\Delta pK_a$ in absorption switches (in magnitude) from an overestimation in implicit water

to an underestimation with one explicit water of the the experimental value, while for the emission only the error decreases but an underestimation remains.

Studying the effect of further solvation of the base with up to three water molecules as HB donors, the configuration for the acid with one water molecule (as HB acceptor) is retained in the following. In the progression 1 $H_2O \rightarrow 2\ H_2O \rightarrow 3\ H_2O$ at $RO^-$ and $RO^{-*}$, the previous trends in in the evolution of $\Delta pK_a$ continue. Both the absorption and the emission parts further decrease in magnitude by 0.4 and 0.7 as well as 0.5 and 0.7 units, respectively, enhancing the underestimation in absorption, but improving the agreement in emission. In fact, the $\Delta pK_a$ in emission apparently reaches an excellent agreement with the experiment. However, these results need to be interpreted carefully.

The strongest changes—and improvements—in $\Delta pK_a$ were observed upon inclusion of the first water molecule, which are dominated by the effect of water as a HB acceptor for both ROH and $ROH^*$, as discussed before. Therefore, the fact that the $\Delta pK_a$ in absorption starts to underestimate the experimental value already with one explicit water molecule (as HB acceptor for ROH/$ROH^*$), might refer to an overestimation of the red shifts of ROH and $ROH^*$ (with water as a HB acceptor) relative to the blue shifts of $RO^-$ and $RO^{-*}$ (with water as a HB donor). As pointed out before, such issues concerning solvatochromic shifts are common since the geometry-optimized micro-solvated structures will typically have shorter HB distances compared to the ensemble average. Apparently, this issue is more severe for the acid than the base, possibly due to the charges, i.e., a larger error due to a shorter HB distance in the micro-solvated structures of the non-charged acid compared to the negatively charged base. For comparison, $RO^-$ and $RO^{-*}$ also experience a systematic step-wise evolution in the absolute energies from 0 $H_2O$ (purely implicit) to 3 $H_2O$, while remaining underestimations of the experimental results (cf. Tab. 7.8), which seems a physically correct description.

In summary, this section has demonstrated that the largest contributions to the deviation between the $\Delta pK_a$ from calculations in implicit water and the experiments are due to the missing HB interactions of the OH group of the acid species as a HB donor and the $O^-$ group of the corresponding base as a HB acceptor.

### 7.4.4. Specific Photoacid–Base Interactions in Acetone–Water Mixtures

The previous section demonstrated that intermolecular interactions between the photoacid (as the solute) and the solvent are relevant already in acetone or DMSO, but even more so in the solvent water. Consequently, it is only natural to expect that such specific photoacid–co-solvent interactions also play a major role in the acetone–water mixtures that were studied experimentally (Chapter 3), in which acetone and water can compete with each other for the hydrogen-bonding sites of the photoacid. These specific photoacid–co-solvent interactions will be discussed in this section.

### Spectral Evolution in Bulk Acetone–Water Mixtures

The experimental UV/Vis absorption spectra of the protonated form of photoacid **B** revealed a noticeable peak progression with increasing water content in acetone–water mixtures (cf. Fig. 1 in Chapter 3). Moreover, it was also already inferred from the experimental data that a photoacid–water complex with the stoichiometry [ROH · $H_2O$] is formed under these conditions. To test if such as peak progression could be simply caused by a bulk electrostatic effect of changes in the solvent composition, we applied the calculation of electronic excitation energies with the continuum solvation model COSMO to these solvent mixtures. Due to the large similarity between the refractive indices of water (1.333) and acetone (1.359), only the effect through the relative dielectric constant ($\epsilon_r$) was considered, which is known to vary linearly in the weight fraction of water in acetone [499]. The UV/Vis absorption energies for the first transition calculated at the fixed COSMO-CC2/cc-pVDZ geometry optimized in acetone but using the $\epsilon_r$ value of the respective acetone-water mixtures for the COSMO-CC2/aug-cc-pVDZ excitation energy calculations are given in Tab. 7.10.

Table 7.10.: **Spectral evolution in acetone–water mixtures.** Comparison of the calculated UV/Vis absorption wavelength of the acid species (ROH) of photoacid **B** in different acetone–water mixtures as modeled by variation of the relative dielectric constant $\epsilon_r$. Each solvent mixture is characterized by its water content as expressed by the concentration $c(H_2O)$, molar fraction $x(H_2O)$, and weight fraction $w(H_2O)$, together with the associated $\epsilon_r$ value based on a linear interpolation ($R^2 = 0.999$) of the data from Ref. 499. For further reference, the results in bulk water ($\epsilon = 78.30$) are also included. Experimental values are taken from Ref. 494.

| $c(H_2O)$ / mol $L^{-1}$ | $x(H_2O)$ / % | $w(H_2O)$ / % | $\epsilon_r$ | $\lambda$ / nm | |
|---|---|---|---|---|---|
| | | | | Calc. | Exptl. |
| 0.0 | 0.0 | 0.0 | 20.56 | 433.89 | 436 |
| 0.8 | 5.8 | 1.9 | 21.64 | 433.94 | 438 |
| 1.6 | 11.0 | 3.7 | 22.68 | 434.00 | 439 |
| 2.4 | 15.6 | 5.4 | 23.68 | 434.05 | 440 |
| 3.1 | 19.7 | 7.1 | 24.65 | 434.09 | 440 |
| 4.1 | 24.7 | 9.2 | 25.89 | 434.15 | 441 |
| (55.6) | 100 | 100 | 78.30 | 434.88 | 414 |

A comparison of the calculated results in neat implicit acetone ($\epsilon_r = 20.56$) and water ($\epsilon_r = 78.30$) demonstrate that a very small $\epsilon_r$-related red shift between the two solvents is observed, from a wavelength of ca. 434 nm in acetone to a wavelength of ca. 435 nm in water. Since the experimental absorption maximum in water (414 nm) is actually blue-shifted relative to that in acetone (436 nm), the experimentally observed spectral changes cannot be a purely electrostatic bulk effect. Rather, these changes appear to be due to specific intermolecular interactions. This observation is in line with the calculations. While the solvent composition changes dramatically on a molecular level within a concentration range of 0.0 to 4.1 mol $L^{-1}$, reaching a final mole fraction of ca. 25 %, the changes in $\epsilon_r$ are much more subtle, increasing only from 20.56 to 25.89 due to the more weakly pronounced linear dependence in the volume fraction. The ROH absorption peak undergoes indeed a red shift from 436 nm to 441 nm in the experiments, but this is not equally reflected in the calculations that yield a more or less constant value of ca. 434 nm, despite a correct and yet very weak shift to the red.

### Specific Photoacid–Base Interactions

The addition of explicit water molecules has shown to cause distinct solvatochromic blue shifts when acting as HB donors. To study the effect of water molecules as competing HB partners in acetone, we re-calculated the UV/Vis absorption and fluorescence emission energies of the hydrogen-bonded complexes of the acid species. Absorption and emission energies were calculated using COSMO-CC2/aug-cc-pVDZ at the COSMO-MP2/cc-pVDZ and COSMO-ADC(2)/cc-pVDZ geometries, respectively. The corresponding results together with those for one explicit acetone molecule are compiled in Tab. 7.11. The results for acetone reproduce the values for one explicit solvent molecule (cf. Tab. 7.6), while those for $H_2O$ and $(H_2O)_2$ refer to the structures from Fig. 7.5 (and related results from Tab. 7.8), but repeated in acetone solution, i.e., using re-optimized geometries for calculating the excitation energies.

Table 7.11.: **Effect of specific photoacid-base interactions on the spectral properties of photoacid B in acetone.** Comparison of calculated UV/Vis absorption (ROH) and fluorescence emission energies ($ROH^*$) in eV for complexes of the protonated and deprotonated species of photoacid **B** with different bases. The HB role of the base is specified as acceptor (HB-A) or donor (HB-D).

| | **Acetone** | **$H_2O$** | | **$(H_2O)_2$** | |
|---|---|---|---|---|---|
| | (HB-A) | HB-D | HB-A | HB-D | HB-A |
| **ROH** | 2.837 | 2.915 | 2.786 | 2.913 | 2.759 |
| **$ROH^*$** | 2.481 | 2.602 | 2.479 | 2.604 | 2.450 |

A direct comparison of the results for the hydrogen-bonded photoacid–water complexes in acetone (Tab. 7.11) to the related micro-solvated structures in water (Tab. 7.8) shows little to no differences, in line with the large similarity between the two solvents when restricted to electrostatic interactions with the bulk surrounding. When exchanging the acetone by a water molecule as a HB acceptor in the [ROH·S] complex (where S represents the solvent), the associated solvatochromic red shift increases, matching the experimental peak progression in acetone–water mixtures upon addition of water. Moreover, the results for the water dimer even predict larger red shifts with a higher number of additional water molecules due to a cooperative effect. In a first approximation, the binding to the photoacid is for the water monomer ∼18 kJ/mol higher in energy relative to acetone, in line with the HB-acceptor strengths. However, this interaction already becomes slightly more favored (by ∼8 kJ/mol) for the dimer.

Moreover, water can also act as a HB donor. Despite of being the weaker interaction (disfavored by ∼26 kJ/mol compared to HB acceptor), this configuration would lead to a blue shift. Interestingly, the large experimental blue shift of the ROH absorption maximum in water (414 nm) with respect to the COSMO prediction in implicit water (435 nm) (cf. Tab. 7.10)—in view of the good agreement in acetone instead (434 nm calc. vs. 436 nm exptl.)—implies that the HB-D interaction will effectively take over at some critical water content. This means that there should be a two-step progression upon addition of water, i.e., first the observed red shift and second a counteracting blue shift, which was not yet experimentally observed due to the restriction to a maximum of ca. 4 M (25 %) water. Still, the

calculations lead us to infer that the experimental peak progression is indeed caused by the formation of photoacid–water complexes *via* a displacement of acetone molecules in the first coordination shell.

## 7.5. Conclusions

This chapter has extended the previous approach for the theoretical spectroscopy of Jung's photoacids using the implicit solvent model COSMO in combination with the wavefunction-based methods ADC(2) and CC2 to the solvent acetone. Revalidation of the methods demonstrated that COSMO-CC2/aug-cc-pVDZ excitation energies still achieve a (very) good agreement with the experimental UV/Vis absorption and fluorescence emission energies in acetone. However, the further improvement with COSMO-CC2 compared to COSMO-MP2 geometries motivated for a switch to COSMO-CC2/cc-pVDZ geometries, which is currently restricted in TURBOMOLE to the ground state due to the missing implementation of COSMO-CC2 excited-state gradients. Reasons for the inherent ADC(2)–CC2 deviations as well as different effects on the excitation energies were thoroughly discussed.

Regarding an absolute agreement between the calculated and experimental absorption and emission energies, COSMO-CC2 yields mean absolute errors and root-mean-square errors smaller than 0.1 eV for photoacids **A**–**F** in acetone. The agreement is generally slightly better for the acid compared to the base species and for absorption compared to emission. With COSMO-CC2 ground-state geometries, even an MAE of less than 0.05 eV is obtained. In most cases, photoacid **E** was found to be the largest outlier, which could be traced back to intermolecular hydrogen-bonding interactions between the photoacidic OH group (or $O^-$ after deprotonation) and the additional OH groups in the side chains, which in the calculations have been modeled by a photoacid–methanol complex.

The calculations using the implicit solvent model COSMO in combination with CC2 predict averaged (over absorption and emission) $\Delta pK_a$ values in the range of $-11$ to $-10$ for all the photoacids studied here, in good agreement with the experimental results. Moreover, the change in $\Delta pK_a$ when comparing the two solvents DMSO and acetone fits to the trend regarding the solvent polarity that was already observed and rationalized in our previous studies. Similar to the previous results in DMSO, the order in $pK_a^*$ is mainly determined by the order in $pK_a$ since $\Delta pK_a$ is virtually identical for all of these photoacids. However, due to their much weaker ground-state acidities in acetone, these photoacids have a much lesser tendency to protonate the solvent. Only photoacids **A** and **B** are expected to perform an efficient ESPT in acetone.

The strong deviations for photoacid **E** demonstrated that H-bonding interactions can significantly affect the spectral properties. Since any specific solute–solvent interaction had been completely neglected so far, we decided to further investigate the effect of explicit solvation based on micro-solvated structures for the solvents acetone, DMSO, and water. Following chemical intuition, the focus was set to the most relevant HB configurations according to Kamlet-Taft considerations and the analysis of the differential effect between ROH/ROH* and $RO^-/RO^{-*}$, i.e., $\Delta pK_a$. This hybrid approach appears to very efficiently capture the most important explicit solvent effects, as already one explicit solvent molecule (HB acceptor)

in the first solvation shell of the OH and $O^-$ group (HB donor) gives rise to a significant improvement in the calculated absorption and emission $\Delta pK_a$ of photoacid **B** for acetone and DMSO, reaching almost perfect agreement with the experiments. In contrast, a requirement for more than one solvent molecule is indicated for water, where the HB configurations become more involved. Kamlet-Taft considerations motivated one explicit water as HB acceptor at the OH group, which seems sufficient and already introduces an underestimation in the absorption part of $\Delta pK_a$, whereas the emission seems less effected. Increasing the number of water molecules at the $O^-$ group up to the chemically motivated number of three further decreases both the $\Delta pK_a$ in absorption and emission. In summary, by going beyond implicit solvation, it could be shown that the largest missing contributions to $\Delta pK_a$ are due to HB interactions of photoacid with solvent, i.e., solvent as the HB acceptor for protonated species and as the HB donor for the deprotonated species.

Closely related to the discussion of explicit solvent effects, also other specific photoacid–base interactions in acetone were studied. For the acetone–water mixtures from the experiments it was shown that the experimentally observed peak progression cannot be explained by a purely electrostatic bulk effect of the solvent with changing solvent composition. Instead, the calculations support that the spectral changes are due to a formation of photoacid–water complexes in acetone, i.e., the solvent molecules in the first solvation shell get replaced by water.

# 8. Conclusions and Outlook

This project presented a combined experimental–theoretical approach to study the ESPT kinetics and thermodynamics of Jung's pyrene-based photoacids **A**–**F** (cf. Fig. 1.6 in Sec. 1.2.5) in different environments, including acetoneous solution. Among these, compound **B** is the strongest photoacid, which is the reason why it received the largest attention in this work.

## 8.1. Conclusions from the Experimental Part

The first sub-project (Chapter 3) combined steady-state UV/Vis absorption and fluorescence emission spectroscopy with streak-camera time-resolved fluorescence spectroscopy to study the ESPT kinetics of the photoacid **B** in acetone–water mixtures. Water was found to have a significant effect in acetone leading upon its addition already in the ground state to the formation of a reaction complex (CPX) with the photoacid. With increasing amount of water in the mixtures, the molar fraction of CPX increases. This complex turned out to be a key intermediate in the ESPT mechanism as described by a three-step Eigen-Weller model. Due to spectral similarities, initial excitation near the ROH absorption band maximum produces both the excited free (i.e., uncomplexed) photoacid ($ROH^*$) and the excited complex ($CPX^*$) if present. Only $CPX^*$ can perform a short-range proton transfer yielding a hydrogen-bonded ion pair ($HBIP^*$), whereas $ROH^*$ first needs to find a water molecule in a diffusive process. Furthermore, as deduced from the concentration dependence of the rate constants, it seems that more than one additional water molecule is required for the subsequent $HBIP^*$ separation into the free excited corresponding base ($RO^{-*}$) and the proton (attached to its acceptor). Overall, the ESPT process is largely accelerated by the addition of water. However, even in neat acetone, i.e., without the addition of water, ESPT was observed, with acetone as the potential proton acceptor, but without a direct indication of contributions from a $HBIP^*$ as an intermediate on the pico to nanosecond timescale. Finally, acidification of these acetone–water mixtures revealed to be an efficient way to effectively counteract the effect of water since it reduces the local hydration of the photoacid.

Having identified acidic conditions as an effective way to deal with small residual amounts of water, the second sub-project (Chapter 4) could subsequently study the ESPT in neat acetone more thoroughly, with a particular focus on the ultrafast dynamics. Using a combination of time-resolved fluorescence *via* TCSPC and transient UV/Vis absorption spectroscopy, picosecond solvation dynamics and rotational diffusion ($\sim 70$ ps) were identified as important contributions. By comparing neutral and acidic solutions and the methylated analogue of the photoacid (that is not able to transfer a proton), the ROH dynamics could be elucidated. However, instead of following a global target analysis as for the fluorescence data in acetone–water mixtures, the complexity of the transient absorption data—especially dynamic spectral shifts—motivated to use a different decomposition scheme to unravel the contributing components. Six

relevant contributions to the transient spectra were identified: the ground-state bleach (GSB) of the ROH form, the excited-state absorption (ESA) and stimulated emission (SE) signals of $ROH^*$ and of $RO^{-*}$ formed after ESPT, respectively, and the $RO^-$ ground-state absorption (GSA) from molecules formed from ROH via the ESPT pathway.

These results, particularly the three-step Eigen-Weller model for the ESPT in acetone–water mixtures, are in agreement with the previous studies on photoacid **B** (cf. Sec. 1.2.5). The involvement of hydrogen-bonded species as proton-transfer intermediates was already observed by Vester *et al.* for the ground state dynamics[307,308]. In comparison to the other solvents that were previously studied by Finkler *et al.* and Spies *et al.*, including water ($3 \times 10^{11}$ $s^{-1}$)[302], methanol ($8 \times 10^9$ $s^{-1}$)[302], ethanol ($5 \times 10^9$ $s^{-1}$)[302], and DMSO ($1.25 \times 10^9$ $s^{-1}$)[48], the ESPT of photoacid **B** nicely fits into this progression as it is even slower in acetone ($0.25 \times 10^9$ $s^{-1}$), approaching the fluorescence lifetime. After the beginning of this project, two newer studies by Grandjean *et al.* on the ESPT of the related photoacid **A** in hydrogen-bonded complexes with tri-*n*-octylphosphine oxide (TOPO) in acetonitrile solution were reported[500,501], which considerably influenced the analysis of the data in acetone–water mixtures presented here. Using steady-state spectroscopy, the involvement of a reaction complex (CPX), comprising the photoacid **A** and TOPO, and a hydrogen-bonded ion pair (HBIP) as spectrally distinct species was derived from the fluorescence emission[500]. However, no distinction between a solvent-separated ion pair (SSIP)—as an additional intermediate—and the free ion pair (FIP) was possible. Time-resolved spectroscopy then allowed to identify an initial proton transfer within CPX on the sub-ps timescale, an excited-state equilibrium between CPX and the generated HBIP, an an irreversible dissociation of the HBIP on the nanosecond timescale[501].

Another important parallel is found in the work by Kumpulainen *et al.* on naphtalimide-based super-photoacids (cf. Sec. 1.2.3), which are similarly strong as Jung's pyrene-based photoacids, and capable of performing an ESPT in alcohols and DMSO[295]. Detailed kinetic studies revealed that in both water and DMSO the ESPT of these photoacids follows a two-step model involving a reversible short-range proton transfer under formation of a contact ion pair and followed by its diffusive separation[295,297,298]. Further restraining the proton transfer by changing to even less polar solvents, e.g., acetonitrile or benzonitrile, then gives rise to the need for complexes with an additional base prior to the ESPT, overall requiring a description based on a three-step model that takes into account hydrogen-bonded complexes and a solvent-separated ion pair as additional intermediates[296].

Similar observations for an initial, reversible proton-transfer step followed by an irreversible contact-ion pair splitting have also been made by Pérez-Lustres and co-workers for the cationic photoacids 2-(1'-hydroxy-2'-naphtyl)benzimidazolium[502] and $NM6HQ^+$[271] in aliphatic alcohols. The ESPT mechanism of these cationic photoacids in alcohols only consists of two steps, i.e., does not involve a CPX, which is still in line with the three-step model for Jung's photoacids **A** and **B** because a distinct hydrogen-bonded reaction complex is only needed as the true proton-transferring species in aprotic solvents, in contrast to the protic alcohols. Moreover, it was reported for the related photoacid $6HQ^+$ in water–

acetonitrile mixtures that an ultrafast solvent-controlled PT takes place that is followed by a bimolecular diffusion-controlled separation, whereas, in neat acetonitrile, only an intermediate PT state is formed, being ascribed to a 1:1 photoacid:water complex due to water impurities[270].

Furthermore, Kwon and co-workers demonstrated for $NM7HQ^+$, which is a similarly strong photoacid as compound **B**, that ESPT of this photoacid can only take place in the aprotic, weakly basic solvent acetonitrile in the presence of additional bases[272–274]. For weaker bases, it was found that the alcohols methanol and ethanol form ground-state complexes with a photoacid:base stoichiometry of 1:1, whereas water (as an impurity) forms 1:2 complexes. In the excited state, an additional alcohol molecule is then involved in the ESPT. Hence, the ESPT of $NM7HQ^+$ to alcohols and water in total requires two molecules (i.e., a dimer) that offers a small chain for the proton transfer. This preference for a hydrogen-bonded chain of two base molecules in the excited state was even observed for the stronger base *N*-methylbenzamide, despite the fact that it forms 1:1 complexes in the ground state[275]. In contrast, in case of the strong base DMSO, 1:1 complexes are formed in the ground state and no additional base molecule is required in the excited state, reflecting the deficiency of extensive HB for DMSO. These results are in line with the ESPT of photoacid **B** in acetone and acetone–water mixtures, for which also ground-state complexation with water and the involvement of an additional water molecule for the ESPT, more specifically the HBIP separation, are observed. A 1:1 photoacid:water stoichiometry is found in acetone though, which could be related to much higher basicity of acetone compared to acetonitrile and thus stronger HB interactions of acetone with the solutes, preventing the formation of larger aggregates.

For the even stronger super-photoacid CBCyP (cf. Sec. 1.2.3), Gajst *et al.* showed that the fluorescence dynamics in acetonitrile–water mixtures are bimodal due to a short-time contribution from the fast ESPT ($k_{PT} \geq 5 \times 10^{12}$ s$^{-1}$) of photoacid molecules that are hydrogen-bonded to water and a long-time contribution from those that are not[288]. Similarly to this work, the amplitude of the short-time contribution was found to depend on the water concentration. Importantly, Gajst *et al.* also inferred that the ESPT rate constant to water in acetonitrile–water mixtures depends only slightly on the water cluster size and structure surrounding the CBCyP molecule, as attributed to its large photoacidity and supported by DFT calculations. In contrast, the data on **B** in acetone–water mixtures displays a concentration dependence of the ESPT rate constant.

The experimental work shown here represents the first time-resolved study that investigated ESPT in acetone and acetone–water mixtures, demonstrating the strong photoacidity of Jung's HPTS derivatives. Importantly, since the ESPT of photoacid **B** in these mixtures varies significantly, this allows either tuning the emission properties by changing the environment or—*vice versa*—obtaining information on the environment by analyzing the emission. Moreover, the highlighted large potential of these photoacids as light-controlled proton sources in experiments can also motivate to study the ESPT under even harsher conditions in the future (e.g., magic photoacids in concentrated sulfuric acid[310]). However, for the current work, information on the actual protonated species in acetoneous environment is still missing since visible spectroscopy is not suited to monitor changes taking place during the proton at the acetone molecule.

Rather, apart from theoretical approaches (*vide infra*), transient mIR absorption (i.e., UV/Vis-pump–mIR-probe) spectroscopy on the ps–ns timescale could be used for this. From a technical perspective, such pump–probe measurements will require a setup with an additional pump laser (as visible source) that is used—in combination with a digital delay generator—to trigger in a time-controlled fashion the probe laser (as mIR source) if measurements on the larger ns–µs timescale are involved, due to the limitation of optical delay generation.

## 8.2. Conclusions from the Theoretical Part

The theoretical part of this project shifted the focus from the kinetics to the thermodynamics of the ESPT in acetone, as quantified by the $pK_a^*$ value. Based on the Förster cycle, calculation of $pK_a^*$ requires the ground-state $pK_a$ value and electronic excitation energies.

Therefore, the third sub-project (Chapter 5) followed a quantum chemical route to $pK_a$ based on COSMO-RS. Since acetone was not yet supported for $pK_a$ prediction due to missing LFER parameters, these needed to be determined for a molecular training set first. Izutsu's compilation of $pK_a$ values in organic solvents[503] was used as a starting point and newer results for the $pK_a$ in acetone from Refs. 504–509 were included, which resulted in a database of 120 compounds: 9 acrylic acids, 87 benzoic acids, 9 phenols, and 15 benzenesulfonamides. The Gibbs free energy of dissociation ($\Delta G_{diss}$) was calculated at the two levels BP-TZVP and BP-TZVPD-FINE with COSMO-RS and then subjected to a correlation with the experimental $pK_a$. Class-specific linear regressions revealed (squared) correlation coefficients of $r^2 \gg 0.9$ at both levels and an increase in $r^2$ when switching to the refined BP-TZVPD-FINE level for each class except for the phenols. In case of the phenols, the correlation slightly decreases at the higher level, which seemed to be an issue that is related to the COSMO surfaces of some phenols including *o*-nitrophenol. Still, both levels give overall very similar results in terms of the correlation and also for the LFER parameter for the slope, with only the parameter for the intercept differing due to a downshift in the calculated $\Delta G_{diss}$ of BP-TZVPD-FINE vs. BP-TZVP.

The data set splits into two groups that prevent a uniform description with a single set of LFER parameters. The carboxylic acids, i.e., the acrylic and benzoic acids, and the sulfonamides share the same slope of $\sim 0.45$, but an offset in the intercepts of $\sim 4$ units needs to be taken into account; with an overall excellent correlation ($r^2 > 0.95$) at both levels. Such splitting has been observed before for the $pK_a$ prediction with COSMO-RS in acetonitrile[367], where it was assigned to the degree of charge (de-) localization in the anions, which is in line with the shift between the carboxylic acids and sulfonamides in acetone. In contrast, the phenols must still be treated differently as their slope is larger than one and hence significantly differs for the other three classes. As discussed, this special role of the phenols could be either due to a higher uncertainty in the experimental $pK_a$ values or an insufficient description of the structural changes after deprotonation (if quinoidal structures are involved) with BP DFT as the electronic structure method. Importantly, the obtained LFER parameters, especially the slope, differ from their ideal values. The slope for the carboxylic acids and sulfonamides of $\sim 0.45$ is in accordance

with the literature, e.g., in view of the values in water (0.58 for acids and 0.75 for bases)[365,366], DMSO (0.70)[365], or acetonitrile (0.92)[367], and different reasons have been discussed. However, the order of these solvents according to their slopes does not reflect a simple order in, e.g., neither the dielectric constant $\epsilon$, nor the Kamlet-Taft parameter $\alpha$ for hydrogen-bond donation, which would be expected if the deviations from the ideal value of 1 were solely determined by electrostatic effects of HB interactions.

This study reported the first theoretical calculation of p$K_a$ in acetone by extending the applicability of COSMO-RS to this solvent, which is considered highly valuable for the determination of p$K_a$ in such non-aqueous environments in general. However, the dissection of the molecular data set also demonstrated the sensitivity of this model toward the molecular classes, i.e., the different characteristics of these acids. To further improve the p$K_a$ computation with COSMO-RS in acetone, different aspects could be addressed. First, the reliability of the experimental data, especially for the phenols, should be ideally validated, e.g., by performing p$K_a$ measurements (if possible). A pragmatic prediction method like COSMO-RS for p$K_a$ can only be as good as the experimental reference data. Second, the COSMO-RS results for $\Delta G_{\text{diss}}$ could be refined by including zero-point vibrational energies (ZPVEs) or higher-level calculations for the gas-phase contribution. These have not been included so far since the established protocol for p$K_a$ in the other solvents (water, DMSO, and acetonitrile) was followed without modifications. It is assumed though that the ZPVE will have an effect on $\Delta G_{\text{diss}}$, mainly because of the vibrational stretching mode of the acidic functional group that is missing for the corresponding base, hence introducing a—more or less—constant contribution for each molecular class. In general, higher levels of theory for the calculation of the gas-phase dissociation reaction could become crucial when aiming at the best accuracy (e.g., see Ref. 355). Third and more fundamentally, a different thermodynamic cycle for the p$K_a$ calculation could also be used. Although the approach described here does not actually use a thermodynamic cycle, as the Gibbs free energy in solution is calculated immediately with COSMO-RS, it implicitly relies on the direct cycle for the dissociation reaction of the acid in solution $\text{HA(solv.)} \rightarrow \text{A}^-\text{(solv.)} + \text{H}^+\text{(solv.)}$, which is known to suffer from dealing with the (solvated) proton and from small error cancellation between the anionic base and the neutral acid[322]. While the former does not matter in an approach to p$K_a$ that uses an LFER fit (since the proton contribution ends up in the intercept), the latter is still an issue here.

However, other thermodynamic cycles have been reviewed in the literature and, e.g., the proton-exchange method that uses a reference acid to avoid dealing with the (solvated) proton has shown best performance in terms of error cancellation[322,323,357]. Moreover, other studies typically directly predict the p$K_a$ without prior knowledge on an experimental test set, which then requires solvent-specific information on the Gibbs free energy of solvation of the proton ($\Delta G_{\text{solv.}}(\text{H}^+)$) in the respective solvent and the total Gibbs free energy of the proton in the gas phase ($G_{\text{gas}}(\text{H}^+)$). Whereas $G_{\text{gas}}(\text{H}^+)$ can be calculated based on statistical thermodynamics, $\Delta G_{\text{solv.}}(\text{H}^+)$ is more problematic and usually taken from experiments. Data on $\Delta G_{\text{solv.}}(\text{H}^+)$ is readily available in water, but typically unknown in organic solvents such as acetone. Therefore, if $\Delta G_{\text{solv.}}(\text{H}^+)$ would be involved in an alternative approach, still the pragmatic

approach of fitting this value to a test set could be followed. Lastly, instead of improving the COSMO-RS results, also different approaches to p$K_a$, e.g., recently based on neural networks could be invoked [510,511].

Apart from the ground-state p$K_a$, electronic excitation energies are needed to calculate p$K_a^*$ values based on the Förster cycle. The fourth sub-project (Chapter 6) investigated the performance of the correlated wavefunction-based methods ADC(2) and CC2 in combination with the implicit solvent model COSMO for the theoretical spectroscopy of Jung's photoacids **A**–**F** in the related solvent DMSO, prior to applying them to the target solvent acetone. It was found that the selected methods are sufficiently accurate to calculate the UV/Vis absorption and fluorescence emission energies of these photoacids in DMSO, reproducing the experimental trends in the Stokes shifts and substitution shifts. The calculations were typically in better agreement with the experiments for absorption compared to emission energies and for the protonated compared to the deprotonated species; with COSMO-CC2 generally outperforming COSMO-ADC(2) for the excitation energies. However, in terms of the total accuracy, no clear classification is possible as this appeared to crucially depend on error cancellation of contributions from the method, the solvation description, and differences between the electronic states. An overestimation of the vertical absorption energies on the order of 0.1 eV is within the error bar for ADC(2) and CC2 [466], whereas the underestimation of vertical emission energies can be caused by too large ground-state energies at distorted excited-state structures as well as the assumption of emission occurring from the fully relaxed excited-state geometry. Despite the limitation to purely electrostatic solute-solvent interactions, the COSMO model seems—in first order—sufficient to describe the solvent effects in DMSO.

An intramolecular charge transfer for the first electronic transition ($S_0 \rightarrow S_1$) was identified as the origin of photoacidity for these strong photoacids, involving a charge redistribution from the OH/$O^-$ group and along the aromatic ring toward the sulfonic acid groups. The corresponding acidity increase upon excitation ($\Delta$p$K_a$) was found to be similar for the photoacids **A**–**F**, e.g., approx. $-10.5$ for COSMO-CC2 energies averaged over absorption and emission. In addition, an interesting dependence of $\Delta$p$K_a$ on the solvent polarity (e.g., quantified by $\epsilon$) was observed: $\Delta$p$K_a$ decreases (in magnitude) with increasing solvent polarity, as rationalized based on the energetic effects on the different photoacid species. Another observation that has been made is that despite the virtually identical $\Delta$p$K_a$ values, the resulting p$K_a^*$ values of the photoacids **A**–**F** in DMSO differ, spanning a range of almost 5 units, and are modulated by the ground-state p$K_a$ that is—on its own—ruled by the substituent effects. For example, the strongly electron-withdrawing perfluoroalkyl substituents give photoacid **B** its exceptional strength. Owing to their negative p$K_a^*$ values, all compounds **A**–**F** can be truly classified as super-photoacids, i.e., they can perform an efficient ESPT to the solvent in DMSO.

To the best of my knowledge, this study still represents the first that applies ADC(2) and CC2 instead of TDDFT methods to the p$K_a^*$ prediction of photoacids. As basically the only other comparable reported studies so far, Aquino and co-workers investigated the photoacidity of pyranoanthocyanins [223,224,234] and other hydroxyflavylium cations [225,226] using TDDFT and ADC(2), but they only used TDDFT excitation energies for calculating p$K_a^*$ (in Ref. 234). Importantly for this project, the successful use of CC2 in

combination with COSMO for DMSO is fundamental to the later application in acetone. Regarding the origin of the photoacidity, other studies, e.g., the theoretical work by Agmon mention an intramolecular charge transfer (ICT) during the first electronic transition as the origin of photoacidity [37,110]. Importantly, an even stronger ICT is supposed to takes place for ROH than for $RO^-$ to lead to an energetic stabilization of $RO^-$ relative to ROH. Although this has been verified for weaker photoacids like HPTS [104,107,108,138] or naphthols [105], it is debated for stronger photoacids and super-photoacids where the situation becomes more complex [94,106]. In this work, no clear indication of a stronger ICT for $RO^-$ vs. ROH could be identified, which is even in agreement with the previous studies, e.g., steady-state measurements and solvatochromic analysis revealing that intramolecular charge transfer on the photoacid side correlates best with the observed photoacidity [309]. However, the larger Stokes shifts of the acid species of photoacids **A**–**F** observed in this computational study indicate stronger structural changes after electronic excitation, which are in line with the rationalization of photoacidity in terms of (anti)aromaticity (cf. Sec. 1.2.1).

The main difficulties encountered in this study are the limitations due to the vertical approximation for the calculation of excitation energies that neglects vibronic effects and solvent-dependent line broadening, and the restriction to an implicit solvent model. In order to further improve the agreement with the experiments, a more accurate description of the solvation appears most relevant, which requires *ab initio* MD simulations with explicit solvent for sampling the configuration space and finding representative structures. For best comparison with the experiments, both UV/Vis absorption and fluorescence emission energies are needed as usually an average of these two quantities is used to determine $\Delta \mathrm{p}K_\mathrm{a}$ experimentally. However, from a technical point of view, the rather large size of the photoacids as well as the solvent acetone studied here and the need to sample in the first electronically excited state are quite demanding. Classical MD is not an option since it provides no access to the fluorescence and also larger errors in absorption energies are anticipated when using quantum-chemical methods at force-field geometries. In turn, *ab initio* MD simulations are practically limited to TDDFT, which can have issues with the excitation energies of photoacids (cf. Sec. 1.2.6) and hence potentially with the excited-state dynamics. Accurate fluorescence emission energies that also take into account a finite lifetime could still be obtained using surface-hopping MD techniques for sampling the excited-state dynamics using a WFT method instead.

Motivated by the successful application of ADC(2) and CC2 in combination with COSMO for the theoretical spectroscopy of photoacids **A**–**F** in DMSO, the fifth sub-project (Chapter 7) extended this approach to acetone, as the target solvent of the experimental part. Since the experiments could not fully answer the question regarding the actual proton acceptor in acetone, one of the aims was to judge the thermodynamic possibility of ESPT to acetone based on calculated $\mathrm{p}K_\mathrm{a}^*$ values. First, after a careful re-validation, it was found that the selected computational methods still worked very well in acetone; or even slightly better than in DMSO. As for the study in DMSO, COSMO-CC2 excitation energies at COSMO-MP2 ($S_0$) or COSMO-ADC(2) ($S_1$) geometries performed good in terms of the total accuracy

(RMSD < 0.1 eV). In addition, an indication for switching to COSMO-CC2 geometries based on a further improved accuracy of the absorption energies (MAE of 0.05 eV) was also found.

Implicit solvation *via* COSMO still gave a sufficient description of the solvation in acetone, with only small effects on the geometry, but significant solvatochromic shifts in the excitation energies. Photoacid **E** turned out to be a special case since intermolecular hydrogen-bonding interactions—with the photoacid OH group as the HB donor and the side-chain OH group of another photoacid molecule as the HB acceptor—must be taken into account to achieve a good agreement with the experimental results. Similarly to DMSO, $\Delta \mathrm{p}K_\mathrm{a}$ was also nearly identical for the photoacids **A**–**F** in acetone (ca. −10.6), which is in line with the previously observed dependence of $\Delta \mathrm{p}K_\mathrm{a}$ on the solvent polarity since $\Delta \mathrm{p}K_\mathrm{a}$ is even slightly larger in magnitude in the less polar acetone. In contrast to DMSO, the acidity of compounds **A**–**F** is drastically reduced to $\mathrm{p}K_\mathrm{a}$ values between 14 and 21. Note that this range (7) is also larger than in DMSO (5), demonstrating the wider $\mathrm{p}K_\mathrm{a}$ window of acetone as the less basic solvent. Importantly, the weaker ground-state acidities ($\mathrm{p}K_\mathrm{a}$) also translate into weaker excited-state acidities ($\mathrm{p}K_\mathrm{a}^*$). Consequently, only photoacids **A** and **B** are expected to perform an efficient ESPT in acetone and none of the compounds **A**–**F** earns to be called a super-photoacid in this solvent.

Another focus was set to exceeding implicit solvation and accounting for explicit solvent effects by comparing the solvents acetone, DMSO, and water. For this, instead of performing MD simulations (*vide supra*), explicit solvent molecules in the first solvation shell of the photoacids were incorporated for the most relevant HB configurations, as judged based on the Kamlet-Taft parameters, to test if the largest contributions to the residual errors of the $\Delta \mathrm{p}K_\mathrm{a}$ values calculated with implicit solvent were due to explicit solvation. For the aprotic solvents acetone and DMSO, one explicit solvent molecule appeared sufficient, in agreement with the simplified HB interactions in these solvents. These solvents can only efficiently act as HB acceptors for the OH group of the acid species, leading to a bathochromic shift in the absorption and emission, but barely interact with the base species due to the lack of HB donation. In contrast, the situation was much more difficult in the protic solvent water, which can act as both a HB donor and acceptor. The additional HB interaction with the solvent as HB donor and the base species as HB acceptor was verified as another relevant interaction. Kamlet-Taft considerations motivated one explicit water as HB acceptor at the OH group, which seems sufficient and already introduces an underestimation in the absorption part of $\Delta \mathrm{p}K_\mathrm{a}$, whereas the emission seems less effected. Increasing the number of water molecules at the $\mathrm{O}^-$ group up to the chemically motivated number of three further decreases both the $\Delta \mathrm{p}K_\mathrm{a}$ in absorption and emission.

Finally, water and acetone were compared as complexation partners for photoacid **B** in acetoneous solution. The calculations provided supporting evidence that the experimentally observed spectral evolution in acetone–water mixtures is due to a specific molecular interaction (involving CPX formation), rather than a bulk effect. Interestingly, the experimental absorption maximum of the acid species is blue-shifted in water relative to acetone, although the initial peak progression upon addition of water consists in a red shift, indicating that water at very low concentrations is dominantly acting as HB acceptor,

but that at larger concentrations the effect HB donation dominates the solvent shift. This interesting observation provides a motivation to study acetone–water mixtures on the full range (0-100 %) of the water content to further investigate these changes. Particularly, at some critical water concentration, the progression is supposed to reverse in order to switch from the absorption maximum in neat acetone (436 nm) to that in neat water (414 nm). A related question is the molecular interpretation of this progression: Does this consist in a change in the (effective) HB role of water, as apparently the HB donation takes over?

The improved accuracy for the excitation energies at the COSMO-CC2 ground-state geometries (*vide supra*) and the generally rather large deviations between ADC(2) and CC2 for these photoacids highlight that these molecules are an interesting case for a closer inspection of the ADC(2)–CC2 difference. To date, this aspect has not been specifically addressed. Moreover, although adapting COSMO-CC2 as the default level for geometries is easily done for the ground state, it poses a problem for the excited state as the corresponding COSMO-CC2 excited-state energy gradients that are needed for the geometry optimizations are currently not available in the TURBOMOLE program package, which is the primary toolbox used in this project. Therefore and in order to investigate the different effects of COSMO-ADC(2) and COSMO-CC2 on the excited-state geometries, the implementation of COSMO-CC2 energy gradients for excited states within the framework of the existing post-SCF coupling scheme is considered a future task.

In view of the current state of research, this combined experimental–theoretical project illustrated advances in investigating the role of hydrogen bonding (HB), as an example of a specific molecular interaction, on the kinetics and thermodynamics of the ESPT process. On the one hand, the experiments revealed that HB has a dramatic effect on the ESPT in acetoneous solution as it leads to the formation of hydrogen-bonded complexes between the photoacid **B** and the co-solvent water, which become the dominant proton-transferring species. On the other hand, the calculations for the solvents DMSO and acetone using ADC(2) and CC2 demonstrated that the accuracy of the implicit solvent model COSMO is sufficient for reproducing the trends in the substitution shifts of Jung's photoacids **A**–**F** and for identifying photoacid **E** (with side-chain OH groups) as an outlier. Based on this accuracy, it can be assumed with a high probability that also the shifts for the micro-solvated structures are qualitatively correct. So far, no other similar theoretical studies have been reported.

# Bibliography


[1] Chou, P.-T.; Solntsev, K. M. Photoinduced Proton Transfer in Chemistry and Biology. *The Journal of Physical Chemistry B* **2015**, *119*, 2089–2089.

[2] Kagel, H.; Frohme, M.; Glökler, J. Photoacids in Biochemical Applications. *Journal of Cellular Biotechnology* **2018**, *4*, 23–30.

[3] Hammes-Schiffer, S. Virtual Issue on Proton Transfer. *The Journal of Physical Chemistry B* **2021**, *125*, 3725–3726.

[4] Eigen, M. Proton Transfer, Acid-Base Catalysis, and Enzymatic Hydrolysis. Part I: ELEMENTARY PROCESSES. *Angewandte Chemie International Edition* **1964**, *3*, 1–19.

[5] Hattori, H.; Ono, Y. In *Metal Oxides in Heterogeneous Catalysis*; Védrine, J. C., Ed.; Metal Oxides; Elsevier, 2018; pp 133–209.

[6] Shabani, M.; Younesi, H.; Pontié, M.; Rahimpour, A.; Rahimnejad, M.; Zinatizadeh, A. A. A critical review on recent proton exchange membranes applied in microbial fuel cells for renewable energy recovery. *Journal of Cleaner Production* **2020**, *264*, 121446.

[7] Petukh, M.; Stefl, S.; Alexov, E. The Role of Protonation States in Ligand–Receptor Recognition and Binding. *Current Pharmaceutical Design* **2013**, *19*, 4182–4190.

[8] Longo, G. S.; Pérez-Chávez, N. A.; Szleifer, I. How Protonation Modulates the Interaction Between Proteins and pH-responsive Hydrogel Films. *Current Opinion in Colloid & Interface Science* **2019**, *41*, 27–39.

[9] Neupane, P.; Bhuju, S.; Thapa, N.; Bhattarai, H. K. ATP Synthase: Structure, Function and Inhibition. *Biomolecular Concepts* **2019**, *10*, 1–10.

[10] Kirby, A. J. *Acid–Base Catalysis by Enzymes.* In *eLS*; John Wiley & Sons, Ltd, 2010.

[11] Ghosh, I.; Khan, S.; Banerjee, G.; Dziarski, A.; Vinyard, D. J.; Debus, R. J.; Brudvig, G. W. Insights into Proton-Transfer Pathways during Water Oxidation in Photosystem II. *The Journal of Physical Chemistry B* **2019**, *123*, 8195–8202.

[12] Leiderman, P.; Huppert, D.; Remington, S. J.; Tolbert, L. M.; Solntsev, K. M. The Effect of Pressure on the Excited-state Proton Transfer in the Wild-type Green Fluorescent Protein. *Chemical Physics Letters* **2008**, *455*, 303–306.

[13] Leiderman, P.; Gepshtein, R.; Tsimberov, I.; Huppert, D. Effect of Temperature on Excited-State Proton Tunneling in wt-Green Fluorescent Protein. *The Journal of Physical Chemistry B* **2008**, *112*, 1232–1239.

[14] Solntsev, K. M.; Poizat, O.; Dong, J.; Rehault, J.; Lou, Y.; Burda, C.; Tolbert, L. M. Meta and Para Effects in the Ultrafast Excited-State Dynamics of the Green Fluorescent Protein Chromophores. *The Journal of Physical Chemistry B* **2008**, *112*, 2700–2711.

[15] Chen, C.; Zhu, L.; Baranov, M. S.; Tang, L.; Baleeva, N. S.; Smirnov, A. Y.; Yampolsky, I. V.; Solntsev, K. M.; Fang, C. Photoinduced Proton Transfer of GFP-Inspired Fluorescent Superphotoacids: Principles and Design. *The Journal of Physical Chemistry B* **2019**, *123*, 3804–3821.

[16] Erez, Y.; Huppert, D. Excited-State Intermolecular Proton Transfer of the Firefly's Chromophore D-Luciferin. *The Journal of Physical Chemistry A* **2010**, *114*, 8075–8082.

[17] Presiado, I.; Erez, Y.; Huppert, D. Excited-State Intermolecular Proton Transfer of the Firefly's Chromophore D-Luciferin. 2. Water–Methanol Mixtures. *The Journal of Physical Chemistry A* **2010**, *114*, 9471–9479.

[18] Presiado, I.; Erez, Y.; Huppert, D. Excited-State Intermolecular Proton Transfer of Firefly Luciferin III. Proton Transfer to a Mild Base. *The Journal of Physical Chemistry A* **2010**, *114*, 13337–13346.

[19] Erez, Y.; Presiado, I.; Gepshtein, R.; Huppert, D. Excited-State Intermolecular Proton Transfer of Firefly Luciferin IV. Temperature and pH Dependence. *The Journal of Physical Chemistry A* **2011**, *115*, 1617–1626.

[20] Presiado, I.; Gepshtein, R.; Erez, Y.; Huppert, D. Excited-State Intermolecular Proton Transfer of Firefly Luciferin V. Direct Proton Transfer to Fluoride and Other Mild Bases. *The Journal of Physical Chemistry A* **2011**, *115*, 7591–7601.

[21] Kuchlyan, J.; Banik, D.; Roy, A.; Kundu, N.; Sarkar, N. Excited-State Proton Transfer Dynamics of Firefly's Chromophore D-Luciferin in DMSO–Water Binary Mixture. *The Journal of Physical Chemistry B* **2014**, *118*, 13946–13953.

[22] Kuchlyan, J.; Banik, D.; Kundu, N.; Ghosh, S.; Banerjee, C.; Sarkar, N. Effect of Confinement on Excited-State Proton Transfer of Firefly's Chromophore D-Luciferin in AOT Reverse Micelles. *The Journal of Physical Chemistry B* **2014**, *118*, 3401–3408.

[23] Silva, V. O.; Freitas, A. A.; Maçanita, A. L.; Quina, F. H. Chemistry and Photochemistry of Natural Plant Pigments: the Anthocyanins. *Journal of Physical Organic Chemistry* **2016**, *29*, 594–599.

[24] Quina, F. H.; Moreira, P. F.; Vautier-Giongo, C.; Rettori, D.; Rodrigues, R. F.; Freitas, A. A.; Silva, P. F.; Maçanita, A. L. Photochemistry of Anthocyanins and their Biological Role in Plant Tissues. *Pure and Applied Chemistry* **2009**, *81*, 1687–1694.

[25] Huynh, M. H. V.; Meyer, T. J. Proton-Coupled Electron Transfer. *Chemical Reviews* **2007**, *107*, 5004–5064.

[26] Hammes-Schiffer, S.; Soudackov, A. V. Proton-Coupled Electron Transfer in Solution, Proteins, and Electrochemistry. *The Journal of Physical Chemistry B* **2008**, *112*, 14108–14123.

[27] Weinberg, D. R.; Gagliardi, C. J.; Hull, J. F.; Murphy, C. F.; Kent, C. A.; Westlake, B. C.; Paul, A.; Ess, D. H.; McCafferty, D. G.; Meyer, T. J. Proton-Coupled Electron Transfer. *Chemical Reviews* **2012**, *112*, 4016–4093.

[28] Pines, D.; Pines, E. *Hydrogen-Transfer Reactions*; John Wiley & Sons, Ltd, 2006; pp 377–415.

[29] Caldin, E., Gold, V., Eds. *Proton-Transfer Reactions*; Springer US: Boston, MA, 1975.

[30] Reijenga, J.; van Hoof, A.; van Loon, A.; Teunissen, B. Development of Methods for the Determination of pKa Values. *Analytical Chemistry Insights* **2013**, *8*, ACI.S12304.

[31] Pathare, B.; Tambe, V.; Patil, V. A review on various analytical methods used in determination of dissociation constant. *International Journal of Pharmacy and Pharmaceutical Sciences* **2014**, *6*, 26–34.

[32] Barcza, L.; Buvári-Barcza, Á. Acid-Base Titrations in Nonaqueous Solvents and Solvent Mixtures. *Journal of Chemical Education* **2003**, *80*, 822.

[33] Buvári-Barcza, A.; Barcza, L. Problems in the Interpretation of Nonaqueous Titrations. *Die Pharmazie* **2005**, *60*, 243–246.

[34] Alongi, K. S.; Shields, G. C. In *Annual Reports in Computational Chemistry*; Wheeler, R. A., Ed.; Elsevier, 2010; Vol. 6; pp 113–138.

[35] Seybold, P. G.; Shields, G. C. Computational estimation of pKa values. *WIREs Computational Molecular Science* **2015**, *5*, 290–297.

[36] Ireland, J. F.; Wyatt, P. A. H. In *Advances in Physical Organic Chemistry*; Gold, V., Ed.; Academic Press, 1976; Vol. 12; pp 131–221.

[37] Agmon, N. Elementary Steps in Excited-State Proton Transfer. *The Journal of Physical Chemistry A* **2005**, *109*, 13–35.

[38] Trieff, N. M.; Sundheim, B. R. The Effect of Solvent on the Acid-Base Kinetics of the Excited State of $\beta$-Naphthol. *The Journal of Physical Chemistry* **1965**, *69*, 2044–2059.

[39] Arnaut, L. G.; Formosínho, S. J. Excited-state Proton Transfer Reactions I. Fundamentals and Intermolecular Reactions. *Journal of Photochemistry and Photobiology A: Chemistry* **1993**, *75*, 1–20.

[40] Formosínho, S. J.; Arnaut, L. G. Excited-state Proton Transfer Reactions II. Intramolecular Reactions. *Journal of Photochemistry and Photobiology A: Chemistry* **1993**, *75*, 21–48.

[41] Rini, M.; Magnes, B.-Z.; Pines, E.; Nibbering, E. T. J. Real-Time Observation of Bimodal Proton Transfer in Acid-Base Pairs in Water. *Science* **2003**, *301*, 349–352.

[42] Hoberg, C.; Talbot, J.; Shee, J.; Ockelmann, T.; DasMahanta, D.; Novelli, F.; Head-Gordon, M.; Havenith, M. Caught in the Act: Real-time Observation of the Solvent Response that Promotes Excited-state Proton Transfer in Pyranine. *ChemRxiv* **2022**,

[43] Wang, Y.; Liu, W.; Tang, L.; Oscar, B.; Han, F.; Fang, C. Early Time Excited-State Structural Evolution of Pyranine in Methanol Revealed by Femtosecond Stimulated Raman Spectroscopy. *The Journal of Physical Chemistry A* **2013**, *117*, 6024–6042.

[44] Saway, J.; Salem, Z. M.; Badillo, J. J. Recent Advances in Photoacid Catalysis for Organic Synthesis. *Synthesis* **2021**, *53*, 489–497.

[45] Wolfbeis, O. S.; Koller, E. Fluorimetric Assay of Hydrolases at Longwave Excitation and Emission Wavelengths with New Substrates Possessing Unique Water Solubility. *Analytical Biochemistry* **1983**, *129*, 365–370.

[46] Wolfbeis, O. S.; Fürlinger, E.; Kroneis, H.; Marsoner, H. Fluorimetric analysis. *Fresenius' Zeitschrift für Analytische Chemie* **1983**, *314*, 119–124.

[47] Zhujun, Z.; Seitz, W. R. A Fluorescence Sensor for Quantifying pH in the Range from 6.5 to 8.5. *Analytica Chimica Acta* **1984**, *160*, 47–55.

[48] Finkler, B.; Spies, C.; Vester, M.; Walte, F.; Omlor, K.; Riemann, I.; Zimmer, M.; Stracke, F.; Gerhards, M.; Jung, G. Highly Photostable "Super"-Photoacids for Ultrasensitive Fluorescence Spectroscopy. *Photochemical & Photobiological Sciences* **2014**, *13*, 548.

[49] Finkler, B.; Riemann, I.; Vester, M.; Grüter, A.; Stracke, F.; Jung, G. Monomolecular Pyrenol-Derivatives as Multi-Emissive Probes for Orthogonal Reactivities. *Photochemical & Photobiological Sciences* **2016**, *15*, 1544–1557.

[50] Menges, J. A.; Clasen, A.; Jourdain, M.; Beckmann, J.; Hoffmann, C.; König, J.; Jung, G. Surface Preparation for Single-Molecule Chemistry. *Langmuir* **2019**, *35*, 2506–2516.

[51] Menges, J. A.; Grandjean, A.; Clasen, A.; Jung, G. Kinetics of Palladium(0)-Allyl Interactions in the Tsuji-Trost Reaction, derived from Single-Molecule Fluorescence Microscopy. *ChemCatChem* **2020**, *12*, 2630–2637.

[52] Simkovitch, R.; Pines, D.; Agmon, N.; Pines, E.; Huppert, D. Reversible Excited-State Proton Geminate Recombination: Revisited. *The Journal of Physical Chemistry B* **2016**, *120*, 12615–12632.

[53] Simkovitch, R.; Rozenman, G. G.; Huppert, D. A fresh look into the time-resolved fluorescence of 8-hydroxy-1,3,6-pyrenetrisulfonate with the use of the fluorescence up-conversion technique. *Journal of Photochemistry and Photobiology A: Chemistry* **2017**, *344*, 15–27.

[54] Genosar, L.; Cohen, B.; Huppert, D. Ultrafast Direct Photoacid–Base Reaction. *The Journal of Physical Chemistry A* **2000**, *104*, 6689–6698.

[55] Awasthi, A. A.; Singh, P. K. Proton Transfer Reaction Dynamics of Pyranine in DMSO/Water Mixtures. *ChemPhysChem* **2018**, *19*, 198–207.

[56] Gajst, O.; Pinto da Silva, L.; Esteves da Silva, J. C. G.; Huppert, D. Excited-State Proton Transfer from the Photoacid 2-Naphthol-8-sulfonate to Acetonitrile/Water Mixtures. *The Journal of Physical Chemistry A* **2018**, *122*, 6166–6175.

[57] Gajst, O.; Pinto da Silva, L.; Esteves da Silva, J. C. G.; Huppert, D. Enhanced Excited-State Proton Transfer via a Mixed Water–Methanol Molecular Bridge of 1-Naphthol-5-Sulfonate in Methanol–Water Mixtures. *The Journal of Physical Chemistry A* **2018**, *122*, 4704–4716.

[58] Gajst, O.; Pinto da Silva, L.; Esteves da Silva, J. C. G.; Huppert, D. Enhanced Excited-State Proton Transfer via a Mixed Methanol–Water Molecular Bridge of 1-Naphthol-3,6-disulfonate in Methanol–Water Mixtures. *The Journal of Physical Chemistry A* **2019**, *123*, 48–58.

[59] Simkovitch, R.; Shomer, S.; Gepshtein, R.; Roth, M. E.; Shabat, D.; Huppert, D. Comparison of the rate of excited-state proton transfer from photoacids to alcohols and water. *Journal of Photochemistry and Photobiology A: Chemistry* **2014**, *277*, 90–101.

[60] Gajst, O.; Green, O.; Simkovitch, R.; Shabat, D.; Huppert, D. The photoacidity of phenol chloro benzoate cyanine picolinium salt photoacid in alkanols. *Journal of Photochemistry and Photobiology A: Chemistry* **2018**, *353*, 546–556.

[61] Gopich, I. V.; Solntsev, K. M.; Agmon, N. Excited-state reversible geminate reaction. I. Two different lifetimes. *The Journal of Chemical Physics* **1999**, *110*, 2164–2174.

[62] Weber, K. Über die enge Beziehung der Fluorescenzauslöschung zur Hemmung photochemischer Reaktionen. *Zeitschrift für Physikalische Chemie* **1932**, *15B*, 18–44.

[63] Terenin, A.; Kariakin, A. Proton Transfer between Organic Molecules Caused by Light. *Nature* **1947**, *159*, 881–882.

[64] Petersen, S. Organische Fluoreszenzfarbstoffe und ihre technische Verwendung Über die „optische Bleiche“. *Angewandte Chemie* **1949**, *61*, 17–19.

[65] Förster, T. Fluoreszenzspektrum und Wasserstoffionenkonzentration. *Naturwissenschaften* **1949**, *36*, 186–187.

[66] Förster, T. Elektrolytische Dissoziation angeregter Moleküle. *Zeitschrift für Elektrochemie und Angewandte Physikalische Chemie* **1950**, *54*, 42–46.

[67] Förster, T. Die pH-Abhängigkeit der Fluoreszenz von Naphthalinderivaten. *Zeitschrift für Elektrochemie und Angewandte Physikalische Chemie* **1950**, *54*, 531–535.

[68] Grabowski, Z. R.; Grabowska, A. The Förster Cycle Reconsidered. *Zeitschrift für Physikalische Chemie* **1976**, *101*, 197–208.

[69] Sülzner, N.; Hättig, C. Theoretical Study on the Photoacidity of Hydroxypyrene Derivatives in DMSO Using ADC(2) and CC2. *The Journal of Physical Chemistry A* **2022**, *126*, 5911–5923.

[70] Weller, A. Quantitative Untersuchungen der Fluoreszenzumwandlung bei Naphtholen. *Zeitschrift für Elektrochemie, Berichte der Bunsengesellschaft für physikalische Chemie* **1952**, *56*, 662–668.

[71] Weller, A. Allgemeine Basenkatalyse bei der elektrolytischen Dissoziation angeregter Naphthole. *Zeitschrift für Elektrochemie, Berichte der Bunsengesellschaft für physikalische Chemie* **1954**, *58*, 849–853.

[72] Weller, A. Protolytische Reaktionen angeregter Oxyverbindungen. *Zeitschrift für Physikalische Chemie* **1958**, *17*, 224–245.

[73] Schulman, S. G.; Rosenberg, L. S.; Vincent, W. R. Proton exchange in the lowest excited singlet state of 2-naphthol-6,8-disulfonate. Demonstration of the establishment of prototropic equilibrium in the excited state. *Journal of the American Chemical Society* **1979**, *101*, 139–142.

[74] Harris, C. M.; Selinger, B. K. Acid-base properties of 1-naphthol. Proton-induced fluorescence quenching. *The Journal of Physical Chemistry* **1980**, *84*, 1366–1371.

[75] Tsutsumi, K.; Shizuka, H. Proton Transfer and Acidity Constant in the Excited State of Naphthols by Dynamic Analyses. *Zeitschrift für Physikalische Chemie* **1980**, *122*, 129–142.

[76] Webb, S. P.; Philips, L. A.; Yeh, S. W.; Tolbert, L. M.; Clark, J. H. Picosecond kinetics of the excited-state, proton-transfer reaction of 1-naphthol in water. *The Journal of Physical Chemistry* **1986**, *90*, 5154–5164.

[77] Lee, S.-I.; Jang, D.-J. Proton Transfers of Aqueous 7-Hydroxyquinoline in the First Excited Singlet, Lowest Triplet, and Ground States. *The Journal of Physical Chemistry* **1995**, *99*, 7537–7541.

[78] Nakagawa, T.; Kohtani, S.; Itoh, M. Picosecond Fluorescence and Two-Step LIF Studies of the Excited-State Proton Transfer in Methanol Solutions of 7-Hydroxyquinoline and Methyl-Substituted 7-Hydroxyquinolines. *Journal of the American Chemical Society* **1995**, *117*, 7952–7957.

[79] Bardez, E.; Devol, I.; Larrey, B.; Valeur, B. Excited-State Processes in 8-Hydroxyquinoline: Photoinduced Tautomerization and Solvation Effects. *The Journal of Physical Chemistry B* **1997**, *101*, 7786–7793.

[80] Kim, T. G.; Topp, M. R. Ultrafast Excited-State Deprotonation and Electron Transfer in Hydroxyquinoline Derivatives. *The Journal of Physical Chemistry A* **2004**, *108*, 10060–10065.

[81] Ekimova, M.; Hoffmann, F.; Bekçioğlu-Neff, G.; Rafferty, A.; Kornilov, O.; Nibbering, E. T. J.; Sebastiani, D. Ultrafast Proton Transport between a Hydroxy Acid and a Nitrogen Base along Solvent Bridges Governed by the Hydroxide/Methoxide Transfer Mechanism. *Journal of the American Chemical Society* **2019**, *141*, 14581–14592.

[82] Fink, D. W.; Koehler, W. R. pH Effects on fluorescence of umbelliferone. *Analytical Chemistry* **1970**, *42*, 990–993.

[83] Yakatan, G. J.; Juneau, R. J.; Schulman, S. G. Phototautomerism in the lowest excited singlet state of 4-methylumbelliferone. *Analytical Chemistry* **1972**, *44*, 1044–1046.

[84] Schulman, S. G.; Rosenberg, L. S. Tautomerization kinetics of 7-hydroxy-4-methylcoumarin in the lowest excited singlet state. *The Journal of Physical Chemistry* **1979**, *83*, 447–451.

[85] Simkovitch, R.; Huppert, D. Photoprotolytic Processes of Umbelliferone and Proposed Function in Resistance to Fungal Infection. *The Journal of Physical Chemistry B* **2015**, *119*, 14683–14696.

[86] Sérgio Seixas de Melo, J.; Maçanita, A. L. Unveiling the Eigen-Weller Ion Pair from the Excited State Proton Transfer Kinetics of 3-Chloro-4-methyl-7-hydroxycoumarin. *The Journal of Physical Chemistry B* **2015**, *119*, 2604–2610.

[87] Simkovitch, R.; Pinto da Silva, L.; Esteves da Silva, J. C. G.; Huppert, D. Comparison of the Photoprotolytic Processes of Three 7-Hydroxycoumarins. *The Journal of Physical Chemistry B* **2016**, *120*, 10297–10310.

[88] Simkovitch, R.; Huppert, D. Photoprotolytic Processes of Lumazine. *The Journal of Physical Chemistry B* **2017**, *121*, 129–142.

[89] Pines, E.; Pines, D.; Ma, Y.-Z.; Fleming, G. R. Femtosecond Pump-Probe Measurements of Solvation by Hydrogen-Bonding Interactions. *ChemPhysChem* **2004**, *5*, 1315–1327.

[90] Lukeman, M.; Burns, M.-D.; Wan, P. Excited state intramolecular proton transfer in 1-hydroxypyrene. *Canadian Journal of Chemistry* **2011**, *89*, 433–440.

[91] Tsutsumi, K.; Shizuka, H. Excited state p$K_a^*$ values of naphthylamines: proton-induced fluorescence quenching. *Chemical Physics Letters* **1977**, *52*, 485–488.

[92] Shizuka, H.; Tsutsumi, K.; Takeuchi, H.; Tanaka, I. Proton transfer reactions in the excited state of 1-aminopyrene by picosecond/streak camera and nanosecond spectroscopy. *Chemical Physics* **1981**, *59*, 183–190.

[93] Pines, E.; Fleming, G. R. Proton transfer in mixed water-organic solvent solutions: correlation between rate, equilibrium constant, and the proton free energy of transfer. *The Journal of Physical Chemistry* **1991**, *95*, 10448–10457.

[94] Spry, D. B.; Fayer, M. D. Charge redistribution and photoacidity: Neutral versus cationic photoacids. *The Journal of Chemical Physics* **2008**, *128*, 084508.

[95] Wehry, E. L.; Rogers, L. B. Application of Linear Free Energy Relations to Electronically Excited States of Monosubstituted Phenols. *Journal of the American Chemical Society* **1965**, *87*, 4234–4238.

[96] Avigal, I.; Feitelson, J.; Ottolenghi, M. Dissociation Constants of Excited Phenols from Fluorescence Quenching Data. *The Journal of Chemical Physics* **1969**, *50*, 2614–2617.

[97] Schulman, S. G.; Vincent, W. R.; Underberg, W. J. M. Acidity of cyanophenols in the $S_1$ and $T_1$ states. The influence of substituent orientation. *The Journal of Physical Chemistry* **1981**, *85*, 4068–4071.

[98] Driscoll, E. W.; Hunt, J. R.; Dawlaty, J. M. Photobasicity in Quinolines: Origin and Tunability via the Substituents' Hammett Parameters. *The Journal of Physical Chemistry Letters* **2016**, *7*, 2093–2099.

[99] Driscoll, E. W.; Hunt, J. R.; Dawlaty, J. M. Proton Capture Dynamics in Quinoline Photobases: Substituent Effect and Involvement of Triplet States. *The Journal of Physical Chemistry A* **2017**, *121*, 7099–7107.

[100] Hunt, J. R.; Dawlaty, J. M. Photodriven Deprotonation of Alcohols by a Quinoline Photobase. *The Journal of Physical Chemistry A* **2018**, *122*, 7931–7940.

[101] Sheng, W.; Nairat, M.; Pawlaczyk, P. D.; Mroczka, E.; Farris, B.; Pines, E.; Geiger, J. H.; Borhan, B.; Dantus, M. Ultrafast Dynamics of a "Super" Photobase. *Angewandte Chemie International Edition* **2018**, *57*, 14742–14746.

[102] Sittig, M.; Tom, J. C.; Elter, J. K.; Schacher, F. H.; Dietzek, B. Quinoline Photobasicity: Investigation within Water-Soluble Light-Responsive Copolymers. *Chemistry – A European Journal* **2021**, *27*, 1072–1079.

[103] Shizuka, H. Excited-state proton-transfer reactions and proton-induced quenching of aromatic compounds. *Accounts of Chemical Research* **1985**, *18*, 141–147.

[104] Barrash-Shiftan, N.; Brauer, B. B.; Pines, E. Solvent dependence of pyranine fluorescence and UV-visible absorption spectra. *Journal of Physical Organic Chemistry* **1998**, *11*, 743–750.

[105] Solntsev, K. M.; Huppert, D.; Agmon, N. Solvatochromism of $\beta$-Naphthol. *The Journal of Physical Chemistry A* **1998**, *102*, 9599–9606.

[106] Solntsev, K. M.; Huppert, D.; Tolbert, L. M.; Agmon, N. Solvatochromic Shifts of "Super" Photoacids. *Journal of the American Chemical Society* **1998**, *120*, 7981–7982.

[107] Jung, G.; Gerharz, S.; Schmitt, A. Solvent-dependent steady-state fluorescence spectroscopy for searching ESPT-dyes: solvatochromism of HPTS revisited. *Physical Chemistry Chemical Physics* **2009**, *11*, 1416.

[108] Silverman, L. N.; Spry, D. B.; Boxer, S. G.; Fayer, M. D. Charge Transfer in Photoacids Observed by Stark Spectroscopy. *The Journal of Physical Chemistry A* **2008**, *112*, 10244–10249.

[109] Hückel, E. Quantentheoretische Beiträge zum Benzolproblem. *Zeitschrift für Physik* **1931**, *70*, 204–286.

[110] Agmon, N.; Rettig, W.; Groth, C. Electronic Determinants of Photoacidity in Cyanonaphthols. *Journal of the American Chemical Society* **2002**, *124*, 1089–1096.

[111] Wen, Z.; José Karas, L.; Wu, C.-H.; I-Chia Wu, J. How does excited-state antiaromaticity affect the acidity strengths of photoacids? *Chemical Communications* **2020**, *56*, 8380–8383.

[112] Rosenberg, M.; Dahlstrand, C.; Kilså, K.; Ottosson, H. Excited State Aromaticity and Antiaromaticity: Opportunities for Photophysical and Photochemical Rationalizations. *Chemical Reviews* **2014**, *114*, 5379–5425.

[113] Baird, N. C. Quantum organic photochemistry. II. Resonance and aromaticity in the lowest $^3\pi\pi^*$ state of cyclic hydrocarbons. *Journal of the American Chemical Society* **1972**, *94*, 4941–4948.

[114] Lampkin, B. J.; Nguyen, Y. H.; Karadakov, P. B.; VanVeller, B. Demonstration of Baird's rule complementarity in the singlet state with implications for excited-state intramolecular proton transfer. *Physical Chemistry Chemical Physics* **2019**, *21*, 11608–11614.

[115] Wu, C.-H.; Karas, L. J.; Ottosson, H.; Wu, J. I.-C. Excited-state proton transfer relieves antiaromaticity in molecules. *Proceedings of the National Academy of Sciences* **2019**, *116*, 20303–20308.

[116] Granucci, G.; Hynes, J. T.; Millié, P.; Tran-Thi, T.-H. A Theoretical Investigation of Excited-State Acidity of Phenol and Cyanophenols. *Journal of the American Chemical Society* **2000**, *122*, 12243–12253.

[117] Huppert, D.; Kolodney, E. Picosecond proton transfer studies in water-alcohols solutions. *Chemical Physics* **1981**, *63*, 401–410.

[118] Huppert, D.; Kolodney, E.; Gutman, M.; Nachliel, E. Effect of water activity on the rate of proton dissociation. *Journal of the American Chemical Society* **1982**, *104*, 6949–6953.

[119] Förster, T.; Völker, S. Kinetics of proton transfer reactions involving hydroxypyrene-trisulphonate in aqueous solution by nanosecond laser absorption spectroscopy. *Chemical Physics Letters* **1975**, *34*, 1–6.

[120] Pines, E.; Huppert, D. Observation of geminate recombination in excited state proton transfer. *The Journal of Chemical Physics* **1986**, *84*, 3576–3577.

[121] Pines, E.; Huppert, D. Geminate recombination proton-transfer reactions. *Chemical Physics Letters* **1986**, *126*, 88–91.

[122] Agmon, N.; Pines, E.; Huppert, D. Geminate recombination in proton-transfer reactions. II. Comparison of diffusional and kinetic schemes. *The Journal of Chemical Physics* **1988**, *88*, 5631–5638.

[123] Agmon, N. Geminate recombination in proton-transfer reactions. III. Kinetics and equilibrium inside a finite sphere. *The Journal of Chemical Physics* **1988**, *88*, 5639–5642.

[124] Agmon, N. Geminate recombination in proton-transfer reactions. IV. Ground-state yields. *The Journal of Chemical Physics* **1988**, *89*, 1524–1528.

[125] Pines, E.; Huppert, D.; Agmon, N. Geminate recombination in excited-state proton-transfer reactions: Numerical solution of the Debye–Smoluchowski equation with backreaction and comparison with experimental results. *The Journal of Chemical Physics* **1988**, *88*, 5620–5630.

[126] Huppert, D.; Pines, E.; Agmon, N. Long-time behavior of reversible geminate recombination reactions. *Journal of the Optical Society of America B* **1990**, *7*, 1545–1550.

[127] Huppert, D.; Goldberg, S. Y.; Masad, A.; Agmon, N. Experimental determination of the long-time behavior in reversible binary chemical reactions. *Physical Review Letters* **1992**, *68*, 3932–3935.

[128] Prayer, C.; Gustavsson, T.; Tran-Thi, T. What's new in the proton transfer reaction from pyranine to water? A femtosecond study of the proton transfer dynamics. *AIP Conference Proceedings* **1996**, *364*, 333–339.

[129] Tran-Thi, T. H.; Gustavsson, T.; Prayer, C.; Pommeret, S.; Hynes, J. T. Primary ultrafast events preceding the photoinduced proton transfer from pyranine to water. *Chemical Physics Letters* **2000**, *329*, 421–430.

[130] Hynes, J. T.; Tran-Thi, T.-H.; Granucci, G. Intermolecular photochemical proton transfer in solution: new insights and perspectives. *Journal of Photochemistry and Photobiology A: Chemistry* **2002**, *154*, 3–11.

[131] Tran-Thi, T.-H.; Prayer, C.; Millié, P.; Uznanski, P.; Hynes, J. T. Substituent and Solvent Effects on the Nature of the Transitions of Pyrenol and Pyranine. Identification of an Intermediate in the

Excited-State Proton-Transfer Reaction. *The Journal of Physical Chemistry A* **2002**, *106*, 2244–2255.

[132] Leiderman, P.; Genosar, L.; Huppert, D. Excited-State Proton Transfer: Indication of Three Steps in the Dissociation and Recombination Process. *The Journal of Physical Chemistry A* **2005**, *109*, 5965–5977.

[133] Gepshtein, R.; Leiderman, P.; Genosar, L.; Huppert, D. Testing the Three Step Excited State Proton Transfer Model by the Effect of an Excess Proton. *The Journal of Physical Chemistry A* **2005**, *109*, 9674–9684.

[134] Mohammed, O. F.; Pines, D.; Dreyer, J.; Pines, E.; Nibbering, E. T. J. Sequential Proton Transfer Through Water Bridges in Acid-Base Reactions. *Science* **2005**, *310*, 83–86.

[135] Mohammed, O. F.; Dreyer, J.; Magnes, B.-Z.; Pines, E.; Nibbering, E. T. J. Solvent-Dependent Photoacidity State of Pyranine Monitored by Transient Mid-Infrared Spectroscopy. *ChemPhysChem* **2005**, *6*, 625–636.

[136] Siwick, B. J.; Bakker, H. J. On the Role of Water in Intermolecular Proton-Transfer Reactions. *Journal of the American Chemical Society* **2007**, *129*, 13412–13420.

[137] Spry, D. B.; Goun, A.; Bell, C. B.; Fayer, M. D. Identification and properties of the $^1L_a$ and $^1L_b$ states of pyranine. *The Journal of Chemical Physics* **2006**, *125*, 144514.

[138] Spry, D. B.; Fayer, M. D. Observation of slow charge redistribution preceding excited-state proton transfer. *The Journal of Chemical Physics* **2007**, *127*, 204501.

[139] Han, F.; Liu, W.; Fang, C. Excited-state proton transfer of photoexcited pyranine in water observed by femtosecond stimulated Raman spectroscopy. *Chemical Physics* **2013**, *422*, 204–219.

[140] Liu, W.; Wang, Y.; Tang, L.; Oscar, B. G.; Zhu, L.; Fang, C. Panoramic portrait of primary molecular events preceding excited state proton transfer in water. *Chemical Science* **2016**, *7*, 5484–5494.

[141] Goldberg, S. Y.; Pines, E.; Huppert, D. Proton scavenging in photoacid geminate recombination processes. *Chemical Physics Letters* **1992**, *192*, 77–81.

[142] Pines, E.; Magnes, B.-Z.; Lang, M. J.; Fleming, G. R. Direct measurement of intrinsic proton transfer rates in diffusion-controlled reactions. *Chemical Physics Letters* **1997**, *281*, 413–420.

[143] Rini, M.; Pines, D.; Magnes, B.-Z.; Pines, E.; Nibbering, E. T. J. Bimodal proton transfer in acid-base reactions in water. *The Journal of Chemical Physics* **2004**, *121*, 9593–9610.

[144] Siwick, B. J.; Cox, M. J.; Bakker, H. J. Long-Range Proton Transfer in Aqueous Acid–Base Reactions. *The Journal of Physical Chemistry B* **2008**, *112*, 378–389.

[145] Cox, M. J.; Timmer, R. L. A.; Bakker, H. J.; Park, S.; Agmon, N. Distance-Dependent Proton Transfer along Water Wires Connecting Acid–Base Pairs. *The Journal of Physical Chemistry A* **2009**, *113*, 6599–6606.

[146] Liu, W.; Han, F.; Smith, C.; Fang, C. Ultrafast Conformational Dynamics of Pyranine during Excited State Proton Transfer in Aqueous Solution Revealed by Femtosecond Stimulated Raman Spectroscopy. *The Journal of Physical Chemistry B* **2012**, *116*, 10535–10550.

[147] Heo, W.; Uddin, N.; Park, J. W.; Rhee, Y. M.; Choi, C. H.; Joo, T. Coherent intermolecular proton transfer in the acid–base reaction of excited state pyranine. *Physical Chemistry Chemical Physics* **2017**, *19*, 18243–18251.

[148] Mohammed, O. F.; Pines, D.; Nibbering, E. T. J.; Pines, E. Base-Induced Solvent Switches in Acid–Base Reactions. *Angewandte Chemie* **2007**, *119*, 1480–1483.

[149] Mohammed, O. F.; Pines, D.; Pines, E.; Nibbering, E. T. J. Aqueous bimolecular proton transfer in acid–base neutralization. *Chemical Physics* **2007**, *341*, 240–257.

[150] Cox, M. J.; Bakker, H. J. Parallel proton transfer pathways in aqueous acid-base reactions. *The Journal of Chemical Physics* **2008**, *128*, 174501.

[151] Agmon, N.; Huppert, D.; Masad, A.; Pines, E. Excited-state proton transfer to methanol-water mixtures. *The Journal of Physical Chemistry* **1991**, *95*, 10407–10413.

[152] Leiderman, P.; Gepshtein, R.; Uritski, A.; Genosar, L.; Huppert, D. Effect of Electrolytes on the Excited-State Proton Transfer and Geminate Recombination. *The Journal of Physical Chemistry A* **2006**, *110*, 5573–5584.

[153] Oscar, B. G.; Liu, W.; Rozanov, N. D.; Fang, C. Ultrafast intermolecular proton transfer to a proton scavenger in an organic solvent. *Physical Chemistry Chemical Physics* **2016**, *18*, 26151–26160.

[154] Nandi, N.; Sahu, K. Analysis of excited state proton transfer dynamics of HPTS in methanol-water mixtures from time-resolved area-normalised emission spectrum (TRANES). *Journal of Photochemistry and Photobiology A: Chemistry* **2019**, *374*, 138–144.

[155] Schulman, S. G.; Kelly, R. N.; Gonzalez, N. J. Steady-state fluorimetric studies of proton-transfer kinetics of some photoexcited hydroxyaromatics in DMSO-water solutions. *Pure and Applied Chemistry* **1987**, *59*, 655–662.

[156] Pines, E.; Huppert, D. Salt effect in photoacid quantum yield measurements: a demonstration of the geminate recombination role in deprotonation reactions. *Journal of the American Chemical Society* **1989**, *111*, 4096–4097.

[157] Pines, E.; Huppert, D.; Agmon, N. Salt effects on steady-state quantum yields of ultrafast, diffusion-influenced, reversible photoacid dissociation reactions. *The Journal of Physical Chemistry* **1991**, *95*, 666–674.

[158] Agmon, N.; Goldberg, S. Y.; Huppert, D. Salt effect on transient proton transfer to solvent and microscopic proton mobility. *Journal of Molecular Liquids* **1995**, *64*, 161–195.

[159] Cox, M. J.; Siwick, B. J.; Bakker, H. J. Influence of Ions on Aqueous Acid-Base Reactions. *ChemPhysChem* **2009**, *10*, 236–244.

[160] Poles, E.; Cohen, B.; Huppert, D. Temperature Dependence of Excited-State Proton Transfer and Geminate Recombination Processes in Water and in Glycerol-Doped Ice. *Israel Journal of Chemistry* **1999**, *39*, 347–360.

[161] Leiderman, P.; Gepshtein, R.; Uritski, A.; Genosar, L.; Huppert, D. Temperature Dependence of Excited-State Proton Transfer in Water Electrolyte Solutions and Water–Methanol Solutions. *The Journal of Physical Chemistry A* **2006**, *110*, 9039–9050.

[162] Huppert, D. H.; Jayaraman, A.; Maines, R. G.; Steyert, D. W.; Rentzepis, P. M. Effect of pressure on proton transfer rate in aqueous solutions: A picosecond study. *The Journal of Chemical Physics* **1984**, *81*, 5596–5600.

[163] Pines, E.; Huppert, D. Kinetics of proton transfer in ice via the pH-jump method: Evaluation of the proton diffusion rate in polycrystalline doped ice. *Chemical Physics Letters* **1985**, *116*, 295–301.

[164] Uritski, A.; Leiderman, P.; Huppert, D. Electrolyte Screening Effect on the Photoprotolytic Cycle of Excited Photoacid in Ice. *The Journal of Physical Chemistry A* **2006**, *110*, 13686–13695.

[165] Uritski, A.; Leiderman, P.; Huppert, D. Proton Reaction with a Mild Base in Ice Studied by Proton–Photoacid Dynamics. *The Journal of Physical Chemistry C* **2007**, *111*, 8856–8865.

[166] Leiderman, P.; Uritski, A.; Huppert, D. Temperature Dependence of Excited State Proton Transfer in Ice. *The Journal of Physical Chemistry A* **2007**, *111*, 4998–5007.

[167] Uritski, A.; Huppert, D. Excited-State Proton Transfer in Methanol-Doped Ice in the Presence of KF. *The Journal of Physical Chemistry A* **2008**, *112*, 4415–4425.

[168] Uritski, A.; Presiado, I.; Erez, Y.; Gepshtein, R.; Huppert, D. Unusual Temperature Dependence of the Proton Transfer Rate from 8-Hydroxy-1,3,6-pyrenetrisulfonate Photoacid to Methanol-Doped Ice. *The Journal of Physical Chemistry C* **2009**, *113*, 17915–17926.

[169] Timmer, R. L. A.; Cox, M. J.; Bakker, H. J. Direct Observation of Proton Transfer in Ice Ih Using Femtosecond Spectroscopy. *The Journal of Physical Chemistry A* **2010**, *114*, 2091–2101.

[170] Spry, D. B.; Goun, A.; Glusac, K.; Moilanen, D. E.; Fayer, M. D. Proton Transport and the Water Environment in Nafion Fuel Cell Membranes and AOT Reverse Micelles. *Journal of the American Chemical Society* **2007**, *129*, 8122–8130.

[171] Tielrooij, K. J.; Cox, M. J.; Bakker, H. J. Effect of Confinement on Proton-Transfer Reactions in Water Nanopools. *ChemPhysChem* **2009**, *10*, 245–251.

[172] Mondal, T.; Das, A. K.; Sasmal, D. K.; Bhattacharyya, K. Excited State Proton Transfer in Ionic Liquid Mixed Micelles. *The Journal of Physical Chemistry B* **2010**, *114*, 13136–13142.

[173] Mandal, A. K.; Ghosh, S.; Das, A. K.; Mondal, T.; Bhattacharyya, K. Effect of NaCl on ESPT-Mediated FRET in a CTAC Micelle: A Femtosecond and FCS Study. *ChemPhysChem* **2013**, *14*, 788–796.

[174] Lawler, C.; Fayer, M. D. Proton Transfer in Ionic and Neutral Reverse Micelles. *The Journal of Physical Chemistry B* **2015**, *119*, 6024–6034.

[175] Spry, D. B.; Fayer, M. D. Proton Transfer and Proton Concentrations in Protonated Nafion Fuel Cell Membranes. *The Journal of Physical Chemistry B* **2009**, *113*, 10210–10221.

[176] Mondal, S. K.; Sahu, K.; Sen, P.; Roy, D.; Ghosh, S.; Bhattacharyya, K. Excited state proton transfer of pyranine in a $\gamma$-cyclodextrin cavity. *Chemical Physics Letters* **2005**, *412*, 228–234.

[177] Mondal, S. K.; Sahu, K.; Ghosh, S.; Sen, P.; Bhattacharyya, K. Excited-State Proton Transfer from Pyranine to Acetate in $\gamma$-Cyclodextrin and Hydroxypropyl $\gamma$-Cyclodextrin. *The Journal of Physical Chemistry A* **2006**, *110*, 13646–13652.

[178] Gepshtein, R.; Leiderman, P.; Huppert, D.; Project, E.; Nachliel, E.; Gutman, M. Proton Antenna Effect of the $\gamma$-Cyclodextrin Outer Surface, Measured by Excited State Proton Transfer. *The Journal of Physical Chemistry B* **2006**, *110*, 26354–26364.

[179] Ghosh, S.; Dey, S.; Mandal, U.; Adhikari, A.; Mondal, S. K.; Bhattacharyya, K. Ultrafast Proton Transfer of Pyranine in a Supramolecular Assembly: PEO–PPO–PEO Triblock Copolymer and CTAC. *The Journal of Physical Chemistry B* **2007**, *111*, 13504–13510.

[180] Amdursky, N.; Simkovitch, R.; Huppert, D. Excited-State Proton Transfer of Photoacids Adsorbed on Biomaterials. *The Journal of Physical Chemistry B* **2014**, *118*, 13859–13869.

[181] Chowdhury, R.; Saha, A.; Mandal, A. K.; Jana, B.; Ghosh, S.; Bhattacharyya, K. Excited State Proton Transfer in the Lysosome of Live Lung Cells: Normal and Cancer Cells. *The Journal of Physical Chemistry B* **2015**, *119*, 2149–2156.

[182] Simkovitch, R.; Huppert, D. Excited-State Proton Transfer of Weak Photoacids Adsorbed on Biomaterials: 8-Hydroxy-1,3,6-pyrenetrisulfonate on Chitin and Cellulose. *The Journal of Physical Chemistry A* **2015**, *119*, 1973–1982.

[183] Simkovitch, R.; Huppert, D. Excited-State Proton Transfer of Weak Photoacids Adsorbed on Biomaterials: Proton Transfer on Starch. *The Journal of Physical Chemistry B* **2015**, *119*, 9795–9804.

[184] Simkovitch, R.; Huppert, D. Excited-State Proton Transfer of Weak Photoacids Adsorbed on Biomaterials: Proton Transfer to Glucosamine of Chitosan. *The Journal of Physical Chemistry A* **2015**, *119*, 641–651.

[185] Peretz-Soroka, H.; Pevzner, A.; Davidi, G.; Naddaka, V.; Kwiat, M.; Huppert, D.; Patolsky, F. Manipulating and Monitoring On-Surface Biological Reactions by Light-Triggered Local pH Alterations. *Nano Letters* **2015**, *15*, 4758–4768.

[186] Amdursky, N.; Orbach, R.; Gazit, E.; Huppert, D. Probing the Inner Cavities of Hydrogels by Proton Diffusion. *The Journal of Physical Chemistry C* **2009**, *113*, 19500–19505.

[187] Simkovitch, R.; Gajst, O.; Zelinger, E.; Yarden, O.; Huppert, D. Irradiation by blue light in the presence of a photoacid confers changes to colony morphology of the plant pathogen Colletotrichum gloeosporioides. *Journal of Photochemistry and Photobiology B: Biology* **2017**, *174*, 1–9.

[188] Chakraborty, S.; Nandi, S.; Bhattacharyya, K.; Mukherjee, S. Time Evolution of Local pH Around a Photo-Acid in Water and a Polymer Hydrogel: Time Resolved Fluorescence Spectroscopy of Pyranine. *ChemPhysChem* **2019**, *20*, 3221–3227.

[189] Das, I.; Panja, S.; Halder, M. Modulation and Salt-Induced Reverse Modulation of the Excited-State Proton-Transfer Process of Lysozymized Pyranine: The Contrasting Scenario of the Ground-State Acid–Base Equilibrium of the Photoacid. *The Journal of Physical Chemistry B* **2016**, *120*, 7076–7087.

[190] Mojumdar, S. S.; Chowdhury, R.; Mandal, A. K.; Bhattacharyya, K. In what time scale proton transfer takes place in a live CHO cell? *The Journal of Chemical Physics* **2013**, *138*, 215102.

[191] Amin, M. A.; Nandi, S.; Mondal, P.; Mahata, T.; Ghosh, S.; Bhattacharyya, K. Physical chemistry in a single live cell: confocal microscopy. *Physical Chemistry Chemical Physics* **2017**, *19*, 12620–12627.

[192] Nandi, S.; Ghosh, S.; Bhattacharyya, K. Live Cell Microscopy: A Physical Chemistry Approach. *The Journal of Physical Chemistry B* **2018**, *122*, 3023–3036.

[193] Mondal, S. K.; Ghosh, S.; Sahu, K.; Sen, P.; Bhattacharyya, K. Excited-state proton transfer from pyranine to acetate in methanol. *Journal of Chemical Sciences* **2007**, *119*, 71–76.

[194] Sen Mojumdar, S.; Mondal, T.; Das, A. K.; Dey, S.; Bhattacharyya, K. Ultrafast and ultraslow proton transfer of pyranine in an ionic liquid microemulsion. *The Journal of Chemical Physics* **2010**, *132*, 194505.

[195] Maiti, S.; Mitra, S.; Johnson, C. A.; Gronborg, K. C.; Garrett-Roe, S.; Donaldson, P. M. pH-jumps in a Protic Ionic Liquid Proceed by Vehicular Proton Transport. 2022; `https://arxiv.org/abs/2205.06210`.

[196] Knochenmuss, R.; Solntsev, K. M.; Tolbert, L. M. Molecular Beam Studies of the "Super" Photoacid 5-Cyano-2-naphthol in Solvent Clusters. *The Journal of Physical Chemistry A* **2001**, *105*, 6393–6401.

[197] Knochenmuss, R.; Fischer, I. Excited-state proton transfer in naphthol/solvent clusters: the current state of affairs. *International Journal of Mass Spectrometry* **2002**, *220*, 343–357.

[198] Fleisher, A. J.; Morgan, P. J.; Pratt, D. W. Charge transfer by electronic excitation: Direct measurement by high resolution spectroscopy in the gas phase. *The Journal of Chemical Physics* **2009**, *131*, 211101.

[199] Melnichuk, A.; Bartlett, R. J. Gas phase solvatochromic effects of phenol and naphthol photoacids. *The Journal of Chemical Physics* **2011**, *134*, 244303.

[200] Lundy-Douglas, K.; Schelly, Z. A. Relaxation study of excited aqueous hydroxypyrenes. *Advances in Molecular Relaxation Processes* **1976**, *8*, 79–86.

[201] Gutman, M.; Huppert, D.; Pines, E. The pH jump: a rapid modulation of pH of aqueous solutions by a laser pulse. *Journal of the American Chemical Society* **1981**, *103*, 3709–3713.

[202] Pines, E.; Huppert, D. pH jump: a relaxational approach. *The Journal of Physical Chemistry* **1983**, *87*, 4471–4478.

[203] Smith, K. K.; Kaufmann, K. J.; Huppert, D.; Gutman, M. Picosecond proton ejection: an ultrafast pH jump. *Chemical Physics Letters* **1979**, *64*, 522–527.

[204] Shin, J.; Lim, C. H.; Lim, M. Photoacid-induced aqueous acid–base reactions probed by femtosecond infrared spectroscopy. *Photochemical & Photobiological Sciences* **2022**,

[205] Liu, W.; Tang, L.; Oscar, B. G.; Wang, Y.; Chen, C.; Fang, C. Tracking Ultrafast Vibrational Cooling during Excited-State Proton Transfer Reaction with Anti-Stokes and Stokes Femtosecond Stimulated Raman Spectroscopy. *The Journal of Physical Chemistry Letters* **2017**, *8*, 997–1003.

[206] Oscar, B. G.; Chen, C.; Liu, W.; Zhu, L.; Fang, C. Dynamic Raman Line Shapes on an Evolving Excited-State Landscape: Insights from Tunable Femtosecond Stimulated Raman Spectroscopy. *The Journal of Physical Chemistry A* **2017**, *121*, 5428–5441.

[207] Tang, L.; Wang, Y.; Zhu, L.; Lee, C.; Fang, C. Correlated Molecular Structural Motions for Photoprotection after Deep-UV Irradiation. *The Journal of Physical Chemistry Letters* **2018**, *9*, 2311–2319.

[208] Tang, L.; Zhu, L.; Wang, Y.; Fang, C. Uncovering the Hidden Excited State toward Fluorescence of an Intracellular pH Indicator. *The Journal of Physical Chemistry Letters* **2018**, *9*, 4969–4975.

[209] Eckert, S.; Winghart, M.-O.; Kleine, C.; Banerjee, A.; Ekimova, M.; Ludwig, J.; Harich, J.; Fondell, M.; Mitzner, R.; Pines, E.; Huse, N.; Wernet, P.; Odelius, M.; Nibbering, E. T. J. Electronic Structure Changes of an Aromatic Amine Photoacid along the Förster Cycle. *Angewandte Chemie International Edition* **2022**, *61*, e202200709.

[210] Cimino, P.; Raucci, U.; Donati, G.; Chiariello, M. G.; Schiazza, M.; Coppola, F.; Rega, N. On the different strength of photoacids. *Theoretical Chemistry Accounts* **2016**, *135*, 117.

[211] Savarese, M.; Netti, P. A.; Adamo, C.; Rega, N.; Ciofini, I. Exploring the Metric of Excited State Proton Transfer Reactions. *The Journal of Physical Chemistry B* **2013**, *117*, 16165–16173.

[212] Savarese, M.; Netti, P. A.; Rega, N.; Adamo, C.; Ciofini, I. Intermolecular proton shuttling in excited state proton transfer reactions: insights from theory. *Phys. Chem. Chem. Phys.* **2014**, *16*, 8661–8666.

[213] Laurent, A. D.; Houari, Y.; Carvalho, P. H. P. R.; Neto, B. A. D.; Jacquemin, D. ESIPT or not ESIPT? Revisiting recent results on 2,1,3-benzothiadiazole under the TD-DFT light. *RSC Advances* **2014**, *4*, 14189–14192.

[214] Houari, Y.; Chibani, S.; Jacquemin, D.; Laurent, A. D. TD-DFT Assessment of the Excited State Intramolecular Proton Transfer in Hydroxyphenylbenzimidazole (HBI) Dyes. *The Journal of Physical Chemistry B* **2015**, *119*, 2180–2192.

[215] Raucci, U.; Savarese, M.; Adamo, C.; Ciofini, I.; Rega, N. Intrinsic and Dynamical Reaction Pathways of an Excited State Proton Transfer. *The Journal of Physical Chemistry B* **2015**, *119*, 2650–2657.

[216] Zhao, J.; Yao, H.; Liu, J.; Hoffmann, M. R. New Excited-State Proton Transfer Mechanisms for 1,8-Dihydroxydibenzo[$a, h$]phenazine. *The Journal of Physical Chemistry A* **2015**, *119*, 681–688.

[217] Qu, Z.; Li, P.; Zhang, X.; Wang, E.; Wang, Y.; Zhou, P. Excited-state proton transfer of 4-hydroxyl-1, 8-naphthalimide derivatives: A combined experimental and theoretical investigation. *Journal of Luminescence* **2016**, *177*, 197–203.

[218] Savarese, M.; Raucci, U.; Fukuda, R.; Adamo, C.; Ehara, M.; Rega, N.; Ciofini, I. Comparing the performance of TD-DFT and SAC-CI methods in the description of excited states potential energy surfaces: An excited state proton transfer reaction as case study. *Journal of Computational Chemistry* **2017**, *38*, 1084–1092.

[219] Yang, D.; Zhao, J.; Jia, M.; Song, X. A theoretical study about the excited state intermolecular proton transfer mechanisms for 2-phenylimidazo[4,5-*b*]pyridine in methanol solvent. *RSC Advances* **2017**, *7*, 34034–34040.

[220] Krishnakumar, P.; Kar, R.; Maity, D. K. Microhydration of 2-Naphthol at Ground, First Excited Triplet, and First Excited Singlet States: A Case Study on Photo Acids. *The Journal of Physical Chemistry A* **2018**, *122*, 929–936.

[221] Zhou, P.; Han, K. Unraveling the Detailed Mechanism of Excited-State Proton Transfer. *Accounts of Chemical Research* **2018**, *51*, 1681–1690.

[222] Freitas, A. A.; Shimizu, K.; Dias, L. G.; Quina, F. H. A computational study of substituted flavylium salts and their quinonoidal conjugate-bases: $S_0 \rightarrow S_1$ electronic transition, absolute p$K_a$ and reduction potential calculations by DFT and semiempirical methods. *Journal of the Brazilian Chemical Society* **2007**, *18*, 1537–1546.

[223] Siddique, F.; Silva, C. P.; Silva, G. T. M.; Lischka, H.; Quina, F. H.; Aquino, A. J. A. The electronic transitions of analogs of red wine pyranoanthocyanin pigments. *Photochemical & Photobiological Sciences* **2019**, *18*, 45–53.

[224] Silva, C. P.; Silva, G. T. M.; Costa, T. d. S.; Carneiro, V. M. T.; Siddique, F.; Aquino, A. J. A.; Freitas, A. A.; Clark, J. A.; Espinoza, E. M.; Vullev, V. I.; Quina, F. H. Chromophores inspired by the colors of fruit, flowers and wine. *Pure and Applied Chemistry* **2020**, *92*, 255–263.

[225] He, J.; Li, X.; Silva, G. T. M.; Quina, F. H.; Aquino, A. J. A. Quantum Chemical Investigation of the Intramolecular Copigmentation Complex of an Acylated Anthocyanin. *Journal of the Brazilian Chemical Society* **2019**, *30*, 492–498.

[226] Silva, G. T. M.; Silva, C. P.; Silva, K. M.; Pioli, R. M.; Costa, T. S.; Marto, V. V.; Freitas, A. A.; Rozendo, J.; Martins, L. M. O. S.; Cavalcante, V. F.; Sun, L.; Aquino, A. J. A.; Carneiro, V. M. T.; Quina, F. H. Fluorescence and Phosphorescence of Flavylium Cation Analogues of Anthocyanins. *Photochem* **2022**, *2*, 423–434.

[227] Jacquemin, D.; Perpète, E. A.; Ciofini, I.; Adamo, C. Fast and Reliable Theoretical Determination of p$K_a^*$ for Photoacids. *The Journal of Physical Chemistry A* **2008**, *112*, 794–796.

[228] Le Bahers, T.; Adamo, C.; Ciofini, I. Photophysical Properties of 8-Hydroxyquinoline-5-sulfonic Acid as a Function of the pH: A TD-DFT Investigation. *The Journal of Physical Chemistry A* **2010**, *114*, 5932–5939.

[229] Baranov, M. S.; Lukyanov, K. A.; Borissova, A. O.; Shamir, J.; Kosenkov, D.; Slipchenko, L. V.; Tolbert, L. M.; Yampolsky, I. V.; Solntsev, K. M. Conformationally Locked Chromophores as Models of Excited-State Proton Transfer in Fluorescent Proteins. *Journal of the American Chemical Society* **2012**, *134*, 6025–6032.

[230] Brémond, É.; Alberto, M. E.; Russo, N.; Ricci, G.; Ciofini, I.; Adamo, C. Photophysical properties of NIR-emitting fluorescence probes: insights from TD-DFT. *Physical Chemistry Chemical Physics* **2013**, *15*, 10019.

[231] Houari, Y.; Jacquemin, D.; Laurent, A. D. Methodological keys for accurate simulations. *Physical Chemistry Chemical Physics* **2013**, *15*, 11875.

[232] Houari, Y.; Jacquemin, D.; Laurent, A. D. TD-DFT study of the for coumarins. *Chemical Physics Letters* **2013**, *583*, 218–221.

[233] Aqdas, A.; Siddique, F.; Nieman, R.; Quina, F. H.; Aquino, A. J. A. Photoacidity of the 7-Hydroxyflavylium Cation. *Photochemistry and Photobiology* **2019**, *95*, 1339–1344.

[234] Wang, J.; Siddique, F.; Freitas, A. A.; Silva, C. P.; Silva, G. T. M.; Quina, F. H.; Lischka, H.; Aquino, A. J. A. A computational study of the ground and excited state acidities of synthetic analogs of red wine pyranoanthocyanins. *Theoretical Chemistry Accounts* **2020**, *139*, 117.

[235] Cui, J.; Siddique, F.; Nieman, R.; Silva, G. T. M.; Quina, F. H.; Aquino, A. J. A. Quantum chemical investigation of the ground- and excited-state acidities of a dihydroxyfuranoflavylium cation. *Theoretical Chemistry Accounts* **2021**, *140*, 90.

[236] Chiariello, M. G.; Rega, N. Exploring Nuclear Photorelaxation of Pyranine in Aqueous Solution: an Integrated Ab-Initio Molecular Dynamics and Time Resolved Vibrational Analysis Approach. *The Journal of Physical Chemistry A* **2018**, *122*, 2884–2893.

[237] Chiariello, M. G.; Donati, G.; Rega, N. Time-Resolved Vibrational Analysis of Excited State Ab Initio Molecular Dynamics to Understand Photorelaxation: The Case of the Pyranine Photoacid in Aqueous Solution. *Journal of Chemical Theory and Computation* **2020**, *16*, 6007–6013.

[238] Chiariello, M. G.; Raucci, U.; Donati, G.; Rega, N. Water-Mediated Excited State Proton Transfer of Pyranine–Acetate in Aqueous Solution: Vibrational Fingerprints from Ab Initio Molecular Dynamics. *The Journal of Physical Chemistry A* **2021**, *125*, 3569–3578.

[239] Chiariello, M. G.; Donati, G.; Raucci, U.; Perrella, F.; Rega, N. Structural Origin and Vibrational Fingerprints of the Ultrafast Excited State Proton Transfer of the Pyranine-Acetate Complex in Aqueous Solution. *The Journal of Physical Chemistry B* **2021**, *125*, 10273–10281.

[240] Thomaz, J. E.; Walker, A. R.; Van Wyck, S. J.; Meisner, J.; Martinez, T. J.; Fayer, M. D. Proton Transfer Dynamics in the Aprotic Proton Accepting Solvent 1-Methylimidazole. *The Journal of Physical Chemistry B* **2020**, *124*, 7897–7908.

[241] Walker, A. R.; Wu, B.; Meisner, J.; Fayer, M. D.; Martínez, T. J. Proton Transfer from a Photoacid to a Water Wire: First Principles Simulations and Fast Fluorescence Spectroscopy. *The Journal of Physical Chemistry B* **2021**, *125*, 12539–12551.

[242] Raucci, U.; Chiariello, M. G.; Rega, N. Modeling Excited-State Proton Transfer to Solvent: A Dynamics Study of a Super Photoacid with a Hybrid Implicit/Explicit Solvent Model. *Journal of Chemical Theory and Computation* **2020**, *16*, 7033–7043.

[243] Masad, A.; Huppert, D. Geminate recombination of proton transfer reactions: time-resolved fluorescence study of 1-naphthol-3,6-disulfonate. *Chemical Physics Letters* **1991**, *180*, 409–415.

[244] Cox, M. J.; Bakker, H. J. Femtosecond Study of the Deuteron-Transfer Dynamics of Naphtol Salts in Water. *The Journal of Physical Chemistry A* **2010**, *114*, 10523–10530.

[245] Prémont-Schwarz, M.; Barak, T.; Pines, D.; Nibbering, E. T. J.; Pines, E. Ultrafast Excited-State Proton-Transfer Reaction of 1-Naphthol-3,6-Disulfonate and Several 5-Substituted 1-Naphthol Derivatives. *The Journal of Physical Chemistry B* **2013**, *117*, 4594–4603.

[246] Tolbert, L. M.; Haubrich, J. E. Enhanced photoacidities of cyanonaphthols. *Journal of the American Chemical Society* **1990**, *112*, 8163–8165.

[247] Shioya, Y.; Yagi, M.; Higuchi, J. A time-resolved electron spin resonance study of the triplet states of 1-nitronaphthalene and 1,4-dinitronaphthalene. *Chemical Physics Letters* **1989**, *154*, 25–28.

[248] Huppert, D.; Tolbert, L. M.; Linares-Samaniego, S. Ultrafast Excited-State Proton Transfer from Cyano-Substituted 2-Naphthols. *The Journal of Physical Chemistry A* **1997**, *101*, 4602–4605.

[249] Solntsev, K. M.; Huppert, D.; Agmon, N. Photochemistry of "Super"-Photoacids. Solvent Effects. *The Journal of Physical Chemistry A* **1999**, *103*, 6984–6997.

[250] Pines, E.; Pines, D.; Barak, T.; Magnes, B.-Z.; Tolbert, L. M.; Haubrich, J. E. Isotope and temperature effects in ultrafast proton-transfer from a strong excited-state acid. *Berichte der Bunsengesellschaft für Physikalische Chemie* **1998**, *102*, 511–517.

[251] Solntsev, K. M.; Agmon, N. Dual asymptotic behavior in geminate diffusion-influenced reaction. *Chemical Physics Letters* **2000**, *320*, 262–268.

[252] Solntsev, K. M.; Huppert, D.; Agmon, N.; Tolbert, L. M. Photochemistry of "Super" Photoacids. 2. Excited-State Proton Transfer in Methanol/Water Mixtures. *The Journal of Physical Chemistry A* **2000**, *104*, 4658–4669.

[253] Tolbert, L. M.; Haubrich, J. E. Photoexcited Proton Transfer from Enhanced Photoacids. *Journal of the American Chemical Society* **1994**, *116*, 10593–10600.

[254] Tolbert, L. M.; Solntsev, K. M. Excited-State Proton Transfer: From Constrained Systems to "Super" Photoacids to Superfast Proton Transfer. *Accounts of Chemical Research* **2002**, *35*, 19–27.

[255] Clower, C.; Solntsev, K. M.; Kowalik, J.; Tolbert, L. M.; Huppert, D. Photochemistry of "Super" Photoacids. 3. Excited-State Proton Transfer from Perfluoroalkylsulfonyl-Substituted 2-Naphthols. *The Journal of Physical Chemistry A* **2002**, *106*, 3114–3122.

[256] Carmeli, I.; Huppert, D.; Tolbert, L.; Haubrich, J. Ultrafast excited-state proton transfer from dicyano-naphthol. *Chemical Physics Letters* **1996**, *260*, 109–114.

[257] Cohen, B.; Huppert, D. Unusual Temperature Dependence of Excited State Proton Transfer Rates in Alcohols. *The Journal of Physical Chemistry A* **2000**, *104*, 2663–2667.

[258] Cohen, B.; Segal, J.; Huppert, D. Proton Transfer from Photoacid to Solvent. *The Journal of Physical Chemistry A* **2002**, *106*, 7462–7467.

[259] Koifman, N.; Cohen, B.; Huppert, D. Effect of Pressure on Proton-Transfer Rate from a Photoacid to Ethanol Solution. *The Journal of Physical Chemistry A* **2002**, *106*, 4336–4344.

[260] Cohen, B.; Leiderman, P.; Huppert, D. Effect of temperature and pressure on proton transfer rate from a photoacid to ethanol solution. *Journal of Luminescence* **2003**, *102–103*, 676–681.

[261] Genosar, L.; Leiderman, P.; Koifman, N.; Huppert, D. Effect of Pressure on the Proton-Transfer Rate from a Photoacid to a Solvent. 2. DCN2 in Propanol. *The Journal of Physical Chemistry A* **2004**, *108*, 309–319.

[262] Genosar, L.; Lasitza, T.; Gepshtein, R.; Leiderman, P.; Koifman, N.; Huppert, D. Effect of Pressure on the Proton Transfer Rate from a Photoacid to a Solvent. 4. Photoacids in Methanol. *The Journal of Physical Chemistry A* **2005**, *109*, 4852–4861.

[263] Nunes, R. M. D.; Arnaut, L. G.; Solntsev, K. M.; Tolbert, L. M.; Formosinho, S. J. Excited-State Proton Transfer in Gas-Expanded Liquids: The Roles of Pressure and Composition in Supercritical $CO_2$ /Methanol Mixtures. *Journal of the American Chemical Society* **2005**, *127*, 11890–11891.

[264] Kobayashi, I.; Terazima, M.; Kimura, Y. Study of the Excited-State Proton-Transfer Reaction of 5-Cyano-2-naphthol in Sub- and Supercritical Water. *The Journal of Physical Chemistry B* **2012**, *116*, 1043–1052.

[265] Fujii, K.; Aramaki, M.; Kimura, Y. Excited-State Proton Transfer of 5,8-Dicyano-2-naphthol in High-Temperature and High-Pressure Methanol: Effect of Solvent Polarity and Hydrogen Bonding Ability. *The Journal of Physical Chemistry B* **2018**, *122*, 12363–12374.

[266] Fujii, K.; Yasaka, Y.; Ueno, M.; Koyanagi, Y.; Kasuga, S.; Matano, Y.; Kimura, Y. Excited-State Proton Transfer of Cyanonaphthols in Protic Ionic Liquids: Appearance of a New Fluorescent Species. *The Journal of Physical Chemistry B* **2017**, *121*, 6042–6049.

[267] Popov, A. V.; Gould, E.-A.; Salvitti, M. A.; Hernandez, R.; Solntsev, K. M. Diffusional effects on the reversible excited-state proton transfer. From experiments to Brownian dynamics simulations. *Physical Chemistry Chemical Physics* **2011**, *13*, 14914.

[268] Gould, E.-A.; Popov, A. V.; Tolbert, L. M.; Presiado, I.; Erez, Y.; Huppert, D.; Solntsev, K. M. Excited-state proton transfer in *N*-methyl-6-hydroxyquinolinium salts: solvent and temperature effects. *Physical Chemistry Chemical Physics* **2012**, *14*, 8964.

[269] Pérez Lustres, J. L.; Kovalenko, S. A.; Mosquera, M.; Senyushkina, T.; Flasche, W.; Ernsting, N. P. Ultrafast Solvation of *N*-Methyl-6-quinolone Probes Local IR Spectrum. *Angewandte Chemie International Edition* **2005**, *44*, 5635–5639.

[270] Pérez-Lustres, J. L.; Rodriguez-Prieto, F.; Mosquera, M.; Senyushkina, T. A.; Ernsting, N. P.; Kovalenko, S. A. Ultrafast Proton Transfer to Solvent: Molecularity and Intermediates from Solvation- and Diffusion-Controlled Regimes. *Journal of the American Chemical Society* **2007**, *129*, 5408–5418.

[271] Veiga-Gutiérrez, M.; Brenlla, A.; Carreira Blanco, C.; Fernández, B.; Kovalenko, S. A.; Rodríguez-Prieto, F.; Mosquera, M.; Lustres, J. L. P. Dissociation of a Strong Acid in Neat Solvents: Diffusion Is Observed after Reversible Proton Ejection Inside the Solvent Shell. *The Journal of Physical Chemistry B* **2013**, *117*, 14065–14078.

[272] Lee, Y. M.; Park, S.-Y.; Kim, H.; Kim, T. G.; Kwon, O.-H. Photoinduced strong acid–weak base reactions in a polar aprotic solvent. *Methods and Applications in Fluorescence* **2016**, *4*, 024004.

[273] Park, S.-Y.; Kim, T. G.; Ajitha, M. J.; Kwac, K.; Lee, Y. M.; Kim, H.; Jung, Y.; Kwon, O.-H. The critical size of hydrogen-bonded alcohol clusters as effective Brønsted bases in solutions. *Physical Chemistry Chemical Physics* **2016**, *18*, 24880–24889.

[274] Park, S.-Y.; Lee, Y. M.; Kwac, K.; Jung, Y.; Kwon, O.-H. Alcohol Dimer is Requisite to Form an Alkyl Oxonium Ion in the Proton Transfer of a Strong (Photo)Acid to Alcohol. *Chemistry - A European Journal* **2016**, *22*, 4340–4344.

[275] Choi, Y.; Kim, H.; Kwon, O. Acid–base reaction of a super-photoacid with a cooperative amide hydrogen-bonded chain. *Bulletin of the Korean Chemical Society* **2022**, *43*, 501–507.

[276] Solntsev, K. M.; Clower, C. E.; Tolbert, L. M.; Huppert, D. 6-Hydroxyquinoline-*N*-oxides: A New Class of "Super" Photoacids. *Journal of the American Chemical Society* **2005**, *127*, 8534–8544.

[277] Karton-Lifshin, N.; Segal, E.; Omer, L.; Portnoy, M.; Satchi-Fainaro, R.; Shabat, D. A Unique Paradigm for a Turn-ON Near-Infrared Cyanine-Based Probe: Noninvasive Intravital Optical Imaging of Hydrogen Peroxide. *Journal of the American Chemical Society* **2011**, *133*, 10960–10965.

[278] Karton-Lifshin, N.; Albertazzi, L.; Bendikov, M.; Baran, P. S.; Shabat, D. "Donor–Two-Acceptor" Dye Design: A Distinct Gateway to NIR Fluorescence. *Journal of the American Chemical Society* **2012**, *134*, 20412–20420.

[279] Karton-Lifshin, N.; Presiado, I.; Erez, Y.; Gepshtein, R.; Shabat, D.; Huppert, D. Ultrafast Excited-State Intermolecular Proton Transfer of Cyanine Fluorochrome Dyes. *The Journal of Physical Chemistry A* **2012**, *116*, 85–92.

[280] Simkovitch, R.; Karton-Lifshin, N.; Shomer, S.; Shabat, D.; Huppert, D. Ultrafast Excited-State Proton Transfer to the Solvent Occurs on a Hundred-Femtosecond Time-Scale. *The Journal of Physical Chemistry A* **2013**, *117*, 3405–3413.

[281] Simkovitch, R.; Shomer, S.; Gepshtein, R.; Shabat, D.; Huppert, D. Temperature Dependence of the Excited-State Proton-Transfer Reaction of Quinone-cyanine-7. *The Journal of Physical Chemistry A* **2013**, *117*, 3925–3934.

[282] Simkovitch, R.; Akulov, K.; Shomer, S.; Roth, M. E.; Shabat, D.; Schwartz, T.; Huppert, D. Comprehensive Study of Ultrafast Excited-State Proton Transfer in Water and $D_2O$ Providing the Missing $RO^- \cdots H^+$ Ion-Pair Fingerprint. *The Journal of Physical Chemistry A* **2014**, *118*, 4425–4443.

[283] Simkovitch, R.; Shomer, S.; Gepshtein, R.; Shabat, D.; Huppert, D. Excited-State Proton Transfer from Quinone-Cyanine 9 to Protic Polar-Solvent Mixtures. *The Journal of Physical Chemistry A* **2014**, *118*, 1832–1840.

[284] Green, O.; Simkovitch, R.; Pinto da Silva, L.; Esteves da Silva, J. C. G.; Shabat, D.; Huppert, D. Excited-State Proton Transfer and Formation of the Excited Tautomer of 3-Hydroxypyridine-Dipicolinium Cyanine Dye. *The Journal of Physical Chemistry A* **2016**, *120*, 6184–6199.

[285] Pinto da Silva, L.; Green, O.; Gajst, O.; Simkovitch, R.; Shabat, D.; Esteves da Silva, J. C. G.; Huppert, D. Excited-State Proton Transfer of Phenol Cyanine Picolinium Photoacid. *ACS Omega* **2018**, *3*, 2058–2073.

[286] Green, O.; Gajst, O.; Simkovitch, R.; Shabat, D.; Huppert, D. Chloro benzoate cyanine picolinium photoacid excited-state proton transfer to water. *Journal of Photochemistry and Photobiology A: Chemistry* **2017**, *349*, 230–237.

[287] Green, O.; Gajst, O.; Simkovitch, R.; Shabat, D.; Huppert, D. New Phenol Benzoate Cyanine Picolinium Salt Photoacid Excited-State Proton Transfer. *The Journal of Physical Chemistry A* **2017**, *121*, 3079–3087.

[288] Gajst, O.; Green, O.; Pinto da Silva, L.; Esteves da Silva, J. C. G.; Shabat, D.; Huppert, D. Excited-State Proton Transfer to $H_2O$ in Mixtures of $CH_3CN$–$H_2O$ of a Superphotoacid, Chlorobenzoate Phenol Cyanine Picolinium (CBCyP). *The Journal of Physical Chemistry A* **2018**, *122*, 8126–8135.

[289] Li, Z.; Yang, Q.; Chang, R.; Ma, G.; Chen, M.; Zhang, W. N-Heteroaryl-1,8-naphthalimide fluorescent sensor for water: Molecular design, synthesis and properties. *Dyes and Pigments* **2011**, *88*, 307–314.

[290] Zhu, B.; Gao, C.; Zhao, Y.; Liu, C.; Li, Y.; Wei, Q.; Ma, Z.; Du, B.; Zhang, X. A 4-hydroxynaphthalimide-derived ratiometric fluorescent chemodosimeter for imaging palladium in living cells. *Chemical Communications* **2011**, *47*, 8656–8658.

[291] Luo, Z.; Yang, B.; Zhong, C.; Tang, F.; Yuan, M.; Xue, Y.; Yao, G.; Zhang, J.; Zhang, Y. A dual-channel probe for selective fluoride determination and application in live cell imaging. *Dyes and Pigments* **2013**, *97*, 52–57.

[292] Biczók, L.; Valat, P.; Wintgens, V. Effect of molecular structure and hydrogen bonding on the fluorescence of hydroxy-substituted naphthalimides. *Physical Chemistry Chemical Physics* **1999**, *1*, 4759–4766.

[293] Biczók, L.; Valat, P.; Wintgens, V. Ion pair formation via photoinduced proton transfer in excited hydroxynaphthalimide-N-methylimidazole hydrogen bonded complex: effect of temperature and viscosity on dual fluorescence. *Physical Chemistry Chemical Physics* **2001**, *3*, 1459–1464.

[294] Biczók, L.; Valat, P.; Wintgens, V. Solvent and temperature effects on the deactivation pathways of excited ion pairs produced via photoinduced proton transfer. *Photochemical & Photobiological Sciences* **2003**, *2*, 230–235.

[295] Kumpulainen, T.; Bakker, B. H.; Hilbers, M.; Brouwer, A. M. Synthesis and Spectroscopic Characterization of 1,8-Naphthalimide Derived "Super" Photoacids. *The Journal of Physical Chemistry B* **2015**, *119*, 2515–2524.

[296] Kumpulainen, T.; Bakker, B. H.; Brouwer, A. M. Complexes of a naphthalimide photoacid with organic bases, and their excited-state dynamics in polar aprotic organic solvents. *Physical Chemistry Chemical Physics* **2015**, *17*, 20715–20724.

[297] Kumpulainen, T.; Rosspeintner, A.; Dereka, B.; Vauthey, E. Influence of Solvent Relaxation on Ultrafast Excited-State Proton Transfer to Solvent. *The Journal of Physical Chemistry Letters* **2017**, *8*, 4516–4521.

[298] Verma, P.; Rosspeintner, A.; Dereka, B.; Vauthey, E.; Kumpulainen, T. Broadband fluorescence reveals mechanistic differences in excited-state proton transfer to protic and aprotic solvents. *Chemical Science* **2020**, *11*, 7963–7971.

[299] Simkovitch, R.; Shomer, S.; Gepshtein, R.; Huppert, D. How Fast Can a Proton-Transfer Reaction Be beyond the Solvent-Control Limit? *The Journal of Physical Chemistry B* **2015**, *119*, 2253–2262.

[300] Eigen, M.; De Maeyer, L. Untersuchungen über die Kinetik der Neutralisation. I. *Zeitschrift für Elektrochemie, Berichte der Bunsengesellschaft für Physikalische Chemie* **1955**, *59*, 986–993.

[301] Eigen, M.; Kruse, W.; Maass, G.; Demaeyer, L. Rate Constants of Protolytic Reactions in Aqueous Solution. *Progress in Reaction Kinetics and Mechanism* **1964**, *2*, 287–318.

[302] Spies, C.; Shomer, S.; Finkler, B.; Pines, D.; Pines, E.; Jung, G.; Huppert, D. Solvent dependence of excited-state proton transfer from pyranine-derived photoacids. *Physical Chemistry Chemical Physics* **2014**, *16*, 9104.

[303] Agmon, N. Excited-state reversible geminate reaction. II. Contact geminate quenching. *The Journal of Chemical Physics* **1999**, *110*, 2175–2180.

[304] Gopich, I. V.; Agmon, N. Excited-state reversible geminate reaction. III. Exact solution for noninteracting partners. *The Journal of Chemical Physics* **1999**, *110*, 10433–10444.

[305] Agmon, N.; Gopich, I. V. Kinetic transition in excited-state reversible reactions. *Chemical Physics Letters* **1999**, *302*, 399–404.

[306] Solntsev, K. M.; Huppert, D.; Agmon, N. Experimental Evidence for a Kinetic Transition in Reversible Reactions. *Physical Review Letters* **2001**, *86*, 3427–3430.

[307] Vester, M.; Staut, T.; Enderlein, J.; Jung, G. Photon Antibunching in a Cyclic Chemical Reaction Scheme. *The Journal of Physical Chemistry Letters* **2015**, *6*, 1149–1154.

[308] Vester, M.; Grueter, A.; Finkler, B.; Becker, R.; Jung, G. Biexponential photon antibunching: recombination kinetics within the Förster-cycle in DMSO. *Physical Chemistry Chemical Physics* **2016**, *18*, 10281–10288.

[309] Spies, C.; Finkler, B.; Acar, N.; Jung, G. Solvatochromism of pyranine-derived photoacids. *Physical Chemistry Chemical Physics* **2013**, *15*, 19893.

[310] Maus, D.; Grandjean, A.; Jung, G. Toward Magic Photoacids: Proton Transfer in Concentrated Sulfuric Acid. *The Journal of Physical Chemistry A* **2018**, *122*, 9025–9030.

[311] Szczepanik, B. Protolytic dissociation of cyano derivatives of naphthol, biphenyl and phenol in the excited state: A review. *Journal of Molecular Structure* **2015**, *1099*, 209–214.

[312] Davidson, E. R.; Jarzęcki, A. A. Zero point corrections to vertical excitation energies. *Chemical Physics Letters* **1998**, *285*, 155–159.

[313] Weller, A. Fast Reactions of Excited Molecules. *Progress in Reaction Kinetics and Mechanism* **1961**, *1*, 187–214.

[314] Schulman, S.; Fernando, Q. Excited state prototropic equilibria of some quinolinols. *Tetrahedron* **1968**, *24*, 1777–1783.

[315] Himmel, D.; Goll, S. K.; Leito, I.; Krossing, I. A Unified pH Scale for All Phases. *Angewandte Chemie International Edition* **2010**, *49*, 6885–6888.

[316] Bastkowski, F. et al. In *Messunsicherheit praxisgerecht bestimmen – Prüfprozesse in der industriellen Praxis 2021*; VDI Wissensforum GmbH„ Ed.; VDI Verlag, 2021; pp 13–22.

[317] Deleebeeck, L.; Snedden, A.; Nagy, D.; Szilágyi Nagyné, Z.; Roziková, M.; Vičarová, M.; Heering, A.; Bastkowski, F.; Leito, I.; Quendera, R.; Cabral, V.; Stoica, D. Unified pH Measurements of Ethanol, Methanol, and Acetonitrile, and Their Mixtures with Water. *Sensors* **2021**, *21*, 3935.

[318] Radtke, V. et al. A unified pH scale for all solvents: part I – intention and reasoning (IUPAC Technical Report). *Pure and Applied Chemistry* **2021**, *93*, 1049–1060.

[319] Solntsev, K. M.; Huppert, D.; Agmon, N. Challenge in Accurate Measurement of Fast Reversible Bimolecular Reaction. *The Journal of Physical Chemistry A* **2001**, *105*, 5868–5876.

[320] Liptak, M. D.; Shields, G. C. Experimentation with different thermodynamic cycles used for p$K_a$ calculations on carboxylic acids using complete basis set and Gaussian-n models combined with CPCM continuum solvation methods. *International Journal of Quantum Chemistry* **2001**, *85*, 727–741.

[321] Pliego, J. R. Thermodynamic cycles and the calculation of p$K_a$. *Chemical Physics Letters* **2003**, *367*, 145–149.

[322] Ho, J.; Coote, M. L. A universal approach for continuum solvent p$K_a$ calculations: are we there yet? *Theoretical Chemistry Accounts* **2009**, *125*, 3.

[323] Casasnovas, R.; Ortega-Castro, J.; Frau, J.; Donoso, J.; Muñoz, F. Theoretical p$K_a$ calculations with continuum model solvents, alternative protocols to thermodynamic cycles. *International Journal of Quantum Chemistry* **2014**, *114*, 1350–1363.

[324] Topol, I. A.; Tawa, G. J.; Burt, S. K.; Rashin, A. A. On the structure and thermodynamics of solvated monoatomic ions using a hybrid solvation model. *The Journal of Chemical Physics* **1999**, *111*, 10998–11014.

[325] Liptak, M. D.; Shields, G. C. Accurate p$K_a$ Calculations for Carboxylic Acids Using Complete Basis Set and Gaussian-n Models Combined with CPCM Continuum Solvation Methods. *Journal of the American Chemical Society* **2001**, *123*, 7314–7319.

[326] Toth, A. M.; Liptak, M. D.; Phillips, D. L.; Shields, G. C. Accurate relative p$K_a$ calculations for carboxylic acids using complete basis set and Gaussian-n models combined with continuum solvation methods. *The Journal of Chemical Physics* **2001**, *114*, 4595–4606.

[327] Liptak, M. D.; Gross, K. C.; Seybold, P. G.; Feldgus, S.; Shields, G. C. Absolute p$K_a$ Determinations for Substituted Phenols. *Journal of the American Chemical Society* **2002**, *124*, 6421–6427.

[328] Gao, J.; Li, N.; Freindorf, M. Hybrid QM/MM Simulations Yield the Ground and Excited State p$K_a$ Difference: Phenol in Aqueous Solution. *Journal of the American Chemical Society* **1996**, *118*, 4912–4913.

[329] Mennucci, B. Polarizable continuum model. *WIREs Computational Molecular Science* **2012**, *2*, 386–404.

[330] Gao, J.; Byun, K. Solvent effects on the $n \rightarrow \pi^*$ transition of pyrimidine in aqueous solution. *Theoretical Chemistry Accounts* **1997**, *96*, 151–156.

[331] Borg, O. A.; Durbeej, B. Relative Ground and Excited-State p$K_a$ Values of Phytochromobilin in the Photoactivation of Phytochrome: A Computational Study. *The Journal of Physical Chemistry B* **2007**, *111*, 11554–11565.

[332] Anders Borg, O.; Durbeej, B. Which factors determine the acidity of the phytochromobilin chromophore of plant phytochrome? *Physical Chemistry Chemical Physics* **2008**, *10*, 2528.

[333] Jacquemin, D.; Adamo, C. In *Density-Functional Methods for Excited States*; Ferré, N., Filatov, M., Huix-Rotllant, M., Eds.; Topics in Current Chemistry; Springer International Publishing: Cham, 2016; pp 347–375.

[334] Jacquemin, D.; Mennucci, B.; Adamo, C. Excited-state calculations with TD-DFT: from benchmarks to simulations in complex environments. *Physical Chemistry Chemical Physics* **2011**, *13*, 16987–16998.

[335] Brémond, E.; Savarese, M.; Adamo, C.; Jacquemin, D. Accuracy of TD-DFT Geometries: A Fresh Look. *Journal of Chemical Theory and Computation* **2018**, *14*, 3715–3727.

[336] Loos, P.-F.; Scemama, A.; Jacquemin, D. The Quest for Highly Accurate Excitation Energies: A Computational Perspective. *The Journal of Physical Chemistry Letters* **2020**, *11*, 2374–2383.

[337] Jacquemin, D.; Perpète, E. A.; Ciofini, I.; Adamo, C. Accurate Simulation of Optical Properties in Dyes. *Accounts of Chemical Research* **2009**, *42*, 326–334.

[338] Jacquemin, D.; Wathelet, V.; Perpète, E. A.; Adamo, C. Extensive TD-DFT Benchmark: Singlet-Excited States of Organic Molecules. *Journal of Chemical Theory and Computation* **2009**, *5*, 2420–2435.

[339] Jacquemin, D.; Perpète, E. A.; Scalmani, G.; Ciofini, I.; Peltier, C.; Adamo, C. Absorption and emission spectra of 1,8-naphthalimide fluorophores: A PCM-TD-DFT investigation. *Chemical Physics* **2010**, *372*, 61–66.

[340] Graef, E. L.; Martins, J. B. L. Analysis of lowest energy transitions at TD-DFT of pyrene in vacuum and solvent. *Journal of Molecular Modeling* **2019**, *25*, 183.

[341] Lee, C.; Chung, S.; Song, H.; Rhee, Y. M.; Lee, E.; Joo, T. Excited State Proton Transfer of Quinone Cyanine 9: Implications on the Origin of Super-Photoacidity. *ChemPhotoChem* **2021**, *5*, 245–252.

[342] Jacquemin, D.; Duchemin, I.; Blase, X. Is the Bethe–Salpeter Formalism Accurate for Excitation Energies? Comparisons with TD-DFT, CASPT2, and EOM-CCSD. *The Journal of Physical Chemistry Letters* **2017**, *8*, 1524–1529.

[343] Guido, C. A.; Mennucci, B.; Scalmani, G.; Jacquemin, D. Excited State Dipole Moments in Solution: Comparison between State-Specific and Linear-Response TD-DFT Values. *Journal of Chemical Theory and Computation* **2018**, *14*, 1544–1553.

[344] Sarkar, R.; Boggio-Pasqua, M.; Loos, P.-F.; Jacquemin, D. Benchmarking TD-DFT and Wave Function Methods for Oscillator Strengths and Excited-State Dipole Moments. *Journal of Chemical Theory and Computation* **2021**, *17*, 1117–1132.

[345] Laurent, A. D.; Jacquemin, D. TD-DFT benchmarks: A review. *International Journal of Quantum Chemistry* **2013**, *113*, 2019–2039.

[346] Adamo, C.; Jacquemin, D. The calculations of excited-state properties with Time-Dependent Density Functional Theory. *Chemical Society Reviews* **2013**, *42*, 845–856.

[347] Jacquemin, D.; Perpète, E. A.; Scuseria, G. E.; Ciofini, I.; Adamo, C. TD-DFT Performance for the Visible Absorption Spectra of Organic Dyes: Conventional versus Long-Range Hybrids. *Journal of Chemical Theory and Computation* **2008**, *4*, 123–135.

[348] Sobolewski, A. L.; Domcke, W.; Hättig, C. Photophysics of Organic Photostabilizers. Ab Initio Study of the Excited-State Deactivation Mechanisms of 2-(2'-Hydroxyphenyl)benzotriazole. *The Journal of Physical Chemistry A* **2006**, *110*, 6301–6306.

[349] Suellen, C.; Freitas, R. G.; Loos, P.-F.; Jacquemin, D. Cross-Comparisons between Experiment, TD-DFT, CC, and ADC for Transition Energies. *Journal of Chemical Theory and Computation* **2019**, *15*, 4581–4590.

[350] Platt, J. R. Classification of Spectra of Cata-Condensed Hydrocarbons. *The Journal of Chemical Physics* **1949**, *17*, 484–495.

[351] Guidez, E. B.; Aikens, C. M. Origin and TDDFT Benchmarking of the Plasmon Resonance in Acenes. *The Journal of Physical Chemistry C* **2013**, *117*, 21466–21475.

[352] Acharya, A.; Chaudhuri, S.; Batista, V. S. Can TDDFT Describe Excited Electronic States of Naphthol Photoacids? A Closer Look with EOM-CCSD. *Journal of Chemical Theory and Computation* **2018**, *14*, 867–876.

[353] Grimme, S.; Parac, M. Substantial Errors from Time-Dependent Density Functional Theory for the Calculation of Excited States of Large $\pi$ Systems. *ChemPhysChem* **2003**, *4*, 292–295.

[354] Prlj, A.; Sandoval-Salinas, M. E.; Casanova, D.; Jacquemin, D.; Corminboeuf, C. Low-Lying $\pi\pi^*$ States of Heteroaromatic Molecules: A Challenge for Excited State Methods. *Journal of Chemical Theory and Computation* **2016**, *12*, 2652–2660.

[355] Ho, J.; Coote, M. L. First-principles prediction of acidities in the gas and solution phase. *WIREs Computational Molecular Science* **2011**, *1*, 649–660.

[356] Ho, J. Predicting p$K_a$ in Implicit Solvents: Current Status and Future Directions. *Australian Journal of Chemistry* **2014**, *67*, 1441–1460.

[357] Sutton, C. C. R.; Franks, G. V.; da Silva, G. First Principles p$K_a$ Calculations on Carboxylic Acids Using the SMD Solvation Model: Effect of Thermodynamic Cycle, Model Chemistry, and Explicit Solvent Molecules. *The Journal of Physical Chemistry B* **2012**, *116*, 11999–12006.

[358] Saracino, G. A. A.; Improta, R.; Barone, V. Absolute p$K_a$ determination for carboxylic acids using density functional theory and the polarizable continuum model. *Chemical Physics Letters* **2003**, *373*, 411–415.

[359] Klamt, A. Conductor-like Screening Model for Real Solvents: A New Approach to the Quantitative Calculation of Solvation Phenomena. *The Journal of Physical Chemistry* **1995**, *99*, 2224–2235.

[360] Klamt, A.; Jonas, V.; Bürger, T.; Lohrenz, J. C. W. Refinement and Parametrization of COSMO-RS. *The Journal of Physical Chemistry A* **1998**, *102*, 5074–5085.

[361] Eckert, F.; Klamt, A. Fast solvent screening via quantum chemistry: COSMO-RS approach. *AIChE Journal* **2002**, *48*, 369–385.

[362] Klamt, A. The COSMO and COSMO-RS solvation models. *WIREs Computational Molecular Science* **2011**, *1*, 699–709.

[363] Klamt, A.; Schüürmann, G. COSMO: a new approach to dielectric screening in solvents with explicit expressions for the screening energy and its gradient. *Journal of the Chemical Society, Perkin Transactions 2* **1993**, 799–805.

[364] Schäfer, A.; Klamt, A.; Sattel, D.; Lohrenz, J. C. W.; Eckert, F. COSMO Implementation in TURBOMOLE: Extension of an efficient quantum chemical code towards liquid systems. *Physical Chemistry Chemical Physics* **2000**, *2*, 2187–2193.

[365] Klamt, A.; Eckert, F.; Diedenhofen, M.; Beck, M. E. First Principles Calculations of Aqueous p$K_a$ Values for Organic and Inorganic Acids Using COSMO–RS Reveal an Inconsistency in the Slope of the pKa Scale. *The Journal of Physical Chemistry A* **2003**, *107*, 9380–9386.

[366] Eckert, F.; Klamt, A. Accurate prediction of basicity in aqueous solution with COSMO-RS. *Journal of Computational Chemistry* **2006**, *27*, 11–19.

[367] Eckert, F.; Leito, I.; Kaljurand, I.; Kütt, A.; Klamt, A.; Diedenhofen, M. Prediction of acidity in acetonitrile solution with COSMO-RS. *Journal of Computational Chemistry* **2009**, *30*, 799–810.

[368] Mullen, K. M.; Stokkum, I. H. M. v. TIMP: An R Package for Modeling Multi-way Spectroscopic Measurements. *Journal of Statistical Software* **2007**, *18*, 1–46.

[369] Snellenburg, J. J.; Laptenok, S.; Seger, R.; Mullen, K. M.; Stokkum, I. H. M. v. Glotaran: A Java-Based Graphical User Interface for the R Package TIMP. *Journal of Statistical Software* **2012**, *49*, 1–22.

[370] Becker, W. *Advanced Time-Correlated Single Photon Counting Techniques*; Springer Science & Business Media, 2005.

[371] Nordlund, T. M. In *Topics in Fluorescence Spectroscopy: Techniques*; Lakowicz, J. R., Ed.; Springer US: Boston, MA, 1999; pp 183–260.

[372] Shah, J. Ultrafast luminescence spectroscopy using sum frequency generation. *IEEE Journal of Quantum Electronics* **1988**, *24*, 276–288.

[373] Laptenok, S. P.; Nuernberger, P.; Lukacs, A.; Vos, M. H. In *Fluorescence Spectroscopy and Microscopy: Methods and Protocols*; Engelborghs, Y., Visser, A. J., Eds.; Methods in Molecular Biology; Humana Press: Totowa, NJ, 2014; Vol. 1076; pp 321–336.

[374] Gerecke, M.; Bierhance, G.; Gutmann, M.; Ernsting, N. P.; Rosspeintner, A. Femtosecond broadband fluorescence upconversion spectroscopy: Spectral coverage versus efficiency. *Review of Scientific Instruments* **2016**, *87*, 053115.

[375] Kemnitz, K.; Pfeifer, L.; Paul, R.; Fink, F. In *Laser in Forschung und Technik / Laser in Research and Engineering: Vorträge des 12. Internationalen Kongresses. Proceedings of the 12th International Congress. Laser 95*; Waidelich, W., Hügel, H., Opower, H., Tiziani, H., Wallenstein, R., Zinth, W., Eds.; Springer Berlin Heidelberg: Berlin, Heidelberg, 1996; pp 118–119.

[376] Lakowicz, J. R., Ed. *Principles of Fluorescence Spectroscopy*; Springer US: Boston, MA, 2006.

[377] Geißler, B. Time-Resolved Spectroscopy for the Analysis of Halogen-Bonded Ion Pairs in the Liquid Phase. Ph.D. thesis, Ruhr-Universität Bochum, Bochum, Germany, 2021.

[378] Guide to Streak Cameras. Hamamatsu Photonics KK, 2008.

[379] Kutta, R.-J.; Langenbacher, T.; Kensy, U.; Dick, B. Setup and performance of a streak camera apparatus for transient absorption measurements in the ns to ms range. *Applied Physics B* **2013**, *111*, 203–216.

[380] Li, X.; Kutta, R. J.; Jandl, C.; Bauer, A.; Nuernberger, P.; Bach, T. Photochemically Induced Ring Opening of Spirocyclopropyl Oxindoles: Evidence for a Triplet 1,3-Diradical Intermediate and Deracemization by a Chiral Sensitizer. *Angewandte Chemie International Edition* **2020**, *59*, 21640–21647.

[381] Wortmann, S.; Kutta, R. J.; Nuernberger, P. Monitoring the photochemistry of a formazan over 15 orders of magnitude in time. *Frontiers in Chemistry* **2022**, *10*.

[382] Berera, R.; van Grondelle, R.; Kennis, J. T. M. Ultrafast transient absorption spectroscopy: principles and application to photosynthetic systems. *Photosynthesis Research* **2009**, *101*, 105–118.

[383] Fushitani, M. Applications of pump-probe spectroscopy. *Annual Reports Section "C" (Physical Chemistry)* **2008**, *104*, 272–297.

[384] Kasha, M. Characterization of electronic transitions in complex molecules. *Discussions of the Faraday Society* **1950**, *9*, 14–19.

[385] Mondal, J. A.; Ghosh, H. N.; Mukherjee, T.; Palit, D. K. S2 Fluorescence and Ultrafast Relaxation Dynamics of the S2 and S1 States of a Ketocyanine Dye. *The Journal of Physical Chemistry A* **2005**, *109*, 6836–6846.

[386] Banno, M.; Ohta, K.; Yamaguchi, S.; Hirai, S.; Tominaga, K. Vibrational Dynamics of Hydrogen-Bonded Complexes in Solutions Studied with Ultrafast Infrared Pump–Probe Spectroscopy. *Accounts of Chemical Research* **2009**, *42*, 1259–1269.

[387] Inoue, I.; Inubushi, Y.; Sato, T.; Tono, K.; Katayama, T.; Kameshima, T.; Ogawa, K.; Togashi, T.; Owada, S.; Amemiya, Y.; Tanaka, T.; Hara, T.; Yabashi, M. Observation of femtosecond X-ray interactions with matter using an X-ray–X-ray pump–probe scheme. *Proceedings of the National Academy of Sciences* **2016**, *113*, 1492–1497.

[388] Onsager, L. Theories of Concentrated Electrolytes. *Chemical Reviews* **1933**, *13*, 73–89.

[389] Onsager, L. Electric Moments of Molecules in Liquids. *Journal of the American Chemical Society* **1936**, *58*, 1486–1493.

[390] Knight, C.; Voth, G. A. The Curious Case of the Hydrated Proton. *Accounts of Chemical Research* **2012**, *45*, 101–109.

[391] Marx, D.; Chandra, A.; Tuckerman, M. E. Aqueous Basic Solutions: Hydroxide Solvation, Structural Diffusion, and Comparison to the Hydrated Proton. *Chemical Reviews* **2010**, *110*, 2174–2216.

[392] Kloss, T.; Heil, J.; Kast, S. M. Quantum Chemistry in Solution by Combining 3D Integral Equation Theory with a Cluster Embedding Approach. *The Journal of Physical Chemistry B* **2008**, *112*, 4337–4343.

[393] Hoffgaard, F.; Heil, J.; Kast, S. M. Three-Dimensional RISM Integral Equation Theory for Polarizable Solute Models. *Journal of Chemical Theory and Computation* **2013**, *9*, 4718–4726.

[394] Neugebauer, J.; Louwerse, M. J.; Baerends, E. J.; Wesolowski, T. A. The merits of the frozen-density embedding scheme to model solvatochromic shifts. *The Journal of Chemical Physics* **2005**, *122*, 094115.

[395] Neugebauer, J.; Jacob, C. R.; Wesolowski, T. A.; Baerends, E. J. An Explicit Quantum Chemical Method for Modeling Large Solvation Shells Applied to Aminocoumarin C151. *The Journal of Physical Chemistry A* **2005**, *109*, 7805–7814.

[396] Schwabe, T.; Olsen, J. M. H.; Sneskov, K.; Kongsted, J.; Christiansen, O. Solvation Effects on Electronic Transitions: Exploring the Performance of Advanced Solvent Potentials in Polarizable Embedding Calculations. *Journal of Chemical Theory and Computation* **2011**, *7*, 2209–2217.

[397] Herbert, J. M. Dielectric continuum methods for quantum chemistry. *WIREs Computational Molecular Science* **2021**, *11*, e1519.

[398] Tomasi, J.; Mennucci, B.; Cammi, R. Quantum Mechanical Continuum Solvation Models. *Chemical Reviews* **2005**, *105*, 2999–3094.

[399] Mennucci, B. Continuum Solvation Models: What Else Can We Learn from Them? *The Journal of Physical Chemistry Letters* **2010**, *1*, 1666–1674.

[400] Caricato, M. Coupled cluster theory with the polarizable continuum model of solvation. *International Journal of Quantum Chemistry* **2019**, *119*, e25710.

[401] Miertuš, S.; Scrocco, E.; Tomasi, J. Electrostatic interaction of a solute with a continuum. A direct utilizaion of AB initio molecular potentials for the prevision of solvent effects. *Chemical Physics* **1981**, *55*, 117–129.

[402] Barone, V.; Cossi, M. Quantum Calculation of Molecular Energies and Energy Gradients in Solution by a Conductor Solvent Model. *The Journal of Physical Chemistry A* **1998**, *102*, 1995–2001.

[403] Cossi, M.; Rega, N.; Scalmani, G.; Barone, V. Energies, structures, and electronic properties of molecules in solution with the C-PCM solvation model. *Journal of Computational Chemistry* **2003**, *24*, 669–681.

[404] Cramer, C. J.; Truhlar, D. G. A Universal Approach to Solvation Modeling. *Accounts of Chemical Research* **2008**, *41*, 760–768.

[405] Marenich, A. V.; Cramer, C. J.; Truhlar, D. G. Generalized Born Solvation Model SM12. *Journal of Chemical Theory and Computation* **2013**, *9*, 609–620.

[406] Marenich, A. V.; Cramer, C. J.; Truhlar, D. G. Universal Solvation Model Based on Solute Electron Density and on a Continuum Model of the Solvent Defined by the Bulk Dielectric Constant and Atomic Surface Tensions. *The Journal of Physical Chemistry B* **2009**, *113*, 6378–6396.

[407] Born, M. Volumen und Hydratationswärme der Ionen. *Zeitschrift für Physik* **1920**, *1*, 45–48.

[408] Kirkwood, J. G. The Dielectric Polarization of Polar Liquids. *The Journal of Chemical Physics* **1939**, *7*, 911–919.

[409] Pliego Jr, J. R.; Riveros, J. M. Hybrid discrete-continuum solvation methods. *WIREs Computational Molecular Science* **2020**, *10*, e1440.

[410] Cramer, C. J.; Truhlar, D. G. Implicit Solvation Models: Equilibria, Structure, Spectra, and Dynamics. *Chemical Reviews* **1999**, *99*, 2161–2200.

[411] Tapia, O.; Goscinski, O. Self-consistent reaction field theory of solvent effects. *Molecular Physics* **1975**, *29*, 1653–1661.

[412] Cossi, M.; Barone, V.; Cammi, R.; Tomasi, J. Ab initio study of solvated molecules: a new implementation of the polarizable continuum model. *Chemical Physics Letters* **1996**, *255*, 327–335.

[413] Klamt, A.; Moya, C.; Palomar, J. A Comprehensive Comparison of the IEFPCM and SS(V)PE Continuum Solvation Methods with the COSMO Approach. *Journal of Chemical Theory and Computation* **2015**, *11*, 4220–4225.

[414] Klamt, A.; Jonas, V. Treatment of the outlying charge in continuum solvation models. *The Journal of Chemical Physics* **1996**, *105*, 9972–9981.

[415] Mennucci, B.; Cancès, E.; Tomasi, J. Evaluation of Solvent Effects in Isotropic and Anisotropic Dielectrics and in Ionic Solutions with a Unified Integral Equation Method: Theoretical Bases, Computational Implementation, and Numerical Applications. *The Journal of Physical Chemistry B* **1997**, *101*, 10506–10517.

[416] Balasubramani, S. G. et al. TURBOMOLE: Modular program suite for ab initio quantum-chemical and condensed-matter simulations. *The Journal of Chemical Physics* **2020**, *152*, 184107.

[417] TURBOMOLE V7.7 2022, a development of University of Karlsruhe and Forschungszentrum Karlsruhe GmbH, 1989-2007, TURBOMOLE GmbH, since 2007; available from `https://www.turbomole.org`.

[418] BIOVIA COSMO*therm*, Release 2021; Dassault Systèmes. `http://www.3ds.com`.

[419] Klamt, A.; Mennucci, B.; Tomasi, J.; Barone, V.; Curutchet, C.; Orozco, M.; Luque, F. J. On the Performance of Continuum Solvation Methods. A Comment on "Universal Approaches to Solvation Modeling". *Accounts of Chemical Research* **2009**, *42*, 489–492.

[420] Klamt, A.; Diedenhofen, M. Calculation of Solvation Free Energies with DCOSMO-RS. *The Journal of Physical Chemistry A* **2015**, *119*, 5439–5445.

[421] Klamt, A.; Eckert, F. COSMO-RS: a novel and efficient method for the a priori prediction of thermophysical data of liquids. *Fluid Phase Equilibria* **2000**, *172*, 43–72.

[422] Klamt, A.; Eckert, F.; Hornig, M. COSMO-RS: A novel view to physiological solvation and partition questions. *Journal of Computer-Aided Molecular Design* **2001**, *15*, 355–365.

[423] Marsh, K. N.; Deev, A.; Wu, A. C.-T.; Tran, E.; Klamt, A. Room temperature ionic liquids as replacements for conventional solvents – A review. *Korean Journal of Chemical Engineering* **2002**, *19*, 357–362.

[424] Klamt, A.; Eckert, F.; Hornig, M.; Beck, M. E.; Bürger, T. Prediction of aqueous solubility of drugs and pesticides with COSMO-RS. *Journal of Computational Chemistry* **2002**, *23*, 275–281.

[425] Klamt, A. Prediction of the mutual solubilities of hydrocarbons and water with COSMO-RS. *Fluid Phase Equilibria* **2003**, *206*, 223–235.

[426] Diedenhofen, M.; Eckert, F.; Klamt, A. Prediction of Infinite Dilution Activity Coefficients of Organic Compounds in Ionic Liquids Using COSMO-RS. *Journal of Chemical & Engineering Data* **2003**, *48*, 475–479.

[427] Diedenhofen, M.; Klamt, A. COSMO-RS as a tool for property prediction of IL mixtures–A review. *Fluid Phase Equilibria* **2010**, *294*, 31–38.

[428] Klamt, A.; Eckert, F.; Arlt, W. COSMO-RS: An Alternative to Simulation for Calculating Thermodynamic Properties of Liquid Mixtures. *Annual Review of Chemical and Biomolecular Engineering* **2010**, *1*, 101–122.

[429] Klamt, A. COSMO-RS for aqueous solvation and interfaces. *Fluid Phase Equilibria* **2016**, *407*, 152–158.

[430] Ehlert, S.; Stahn, M.; Spicher, S.; Grimme, S. Robust and Efficient Implicit Solvation Model for Fast Semiempirical Methods. *Journal of Chemical Theory and Computation* **2021**, *17*, 4250–4261.

[431] Grimme, S.; Bohle, F.; Hansen, A.; Pracht, P.; Spicher, S.; Stahn, M. Efficient Quantum Chemical Calculation of Structure Ensembles and Free Energies for Nonrigid Molecules. *The Journal of Physical Chemistry A* **2021**, *125*, 4039–4054.

[432] Bannwarth, C.; Caldeweyher, E.; Ehlert, S.; Hansen, A.; Pracht, P.; Seibert, J.; Spicher, S.; Grimme, S. Extended tight-binding quantum chemistry methods. *WIREs Computational Molecular Science* **2021**, *11*, e1493.

[433] Spicher, S.; Grimme, S. Robust Atomistic Modeling of Materials, Organometallic, and Biochemical Systems. *Angewandte Chemie International Edition* **2020**, *59*, 15665–15673.

[434] Pracht, P.; Grimme, S. Efficient Quantum-Chemical Calculations of Acid Dissociation Constants from Free-Energy Relationships. *The Journal of Physical Chemistry A* **2021**, *125*, 5681–5692.

[435] Pye, C. C.; Ziegler, T. An implementation of the conductor-like screening model of solvation within the Amsterdam density functional package. *Theoretical Chemistry Accounts* **1999**, *101*, 396–408.

[436] Pye, C. C.; Ziegler, T.; van Lenthe, E.; Louwen, J. N. An implementation of the conductor-like screening model of solvation within the Amsterdam density functional package – Part II. COSMO for real solvents. *Canadian Journal of Chemistry* **2009**, *87*, 790–797.

[437] Lin, S.-T.; Sandler, S. I. A Priori Phase Equilibrium Prediction from a Segment Contribution Solvation Model. *Industrial & Engineering Chemistry Research* **2002**, *41*, 899–913.

[438] Bell, I. H.; Mickoleit, E.; Hsieh, C.-M.; Lin, S.-T.; Vrabec, J.; Breitkopf, C.; Jäger, A. A Benchmark Open-Source Implementation of COSMO-SAC. *Journal of Chemical Theory and Computation* **2020**, *16*, 2635–2646.

[439] Grensemann, H.; Gmehling, J. Performance of a Conductor-Like Screening Model for Real Solvents Model in Comparison to Classical Group Contribution Methods. *Industrial & Engineering Chemistry Research* **2005**, *44*, 1610–1624.

[440] Banerjee, T.; Singh, M. K.; Khanna, A. Prediction of Binary VLE for Imidazolium Based Ionic Liquid Systems Using COSMO-RS. *Industrial & Engineering Chemistry Research* **2006**, *45*, 3207–3219.

[441] Gerlach, T.; Müller, S.; de Castilla, A. G.; Smirnova, I. An open source COSMO-RS implementation and parameterization supporting the efficient implementation of multiple segment descriptors. *Fluid Phase Equilibria* **2022**, *560*, 113472.

[442] Hellweg, A.; Eckert, F. Brick by brick computation of the gibbs free energy of reaction in solution using quantum chemistry and COSMO-RS. *AIChE Journal* **2017**, *63*, 3944–3954.

[443] Reinisch, J.; Diedenhofen, M.; Wilcken, R.; Udvarhelyi, A.; Glöß, A. Benchmarking Different QM Levels for Usage with COSMO-RS. *Journal of Chemical Information and Modeling* **2019**, *59*, 4806–4813.

[444] Klamt, A.; Diedenhofen, M. A refined cavity construction algorithm for the conductor-like screening model. *Journal of Computational Chemistry* **2018**, *39*, 1648–1655.

[445] Sinnecker, S.; Rajendran, A.; Klamt, A.; Diedenhofen, M.; Neese, F. Calculation of Solvent Shifts on Electronic g-Tensors with the Conductor-Like Screening Model (COSMO) and Its Self-Consistent Generalization to Real Solvents (Direct COSMO-RS). *The Journal of Physical Chemistry A* **2006**, *110*, 2235–2245.

[446] Bartlett, R. J. Many-Body Perturbation Theory and Coupled Cluster Theory for Electron Correlation in Molecules. *Annual Review of Physical Chemistry* **1981**, *32*, 359–401.

[447] Møller, C.; Plesset, M. S. Note on an Approximation Treatment for Many-Electron Systems. *Physical Review* **1934**, *46*, 618–622.

[448] Shavitt, I.; Bartlett, R. J. *Many-Body Methods in Chemistry and Physics: MBPT and Coupled-Cluster Theory*; Cambridge Molecular Science; Cambridge University Press: Cambridge, 2009.

[449] Jurečka, P.; Šponer, J.; Černý, J.; Hobza, P. Benchmark database of accurate (MP2 and CCSD(T) complete basis set limit) interaction energies of small model complexes, DNA base pairs, and amino acid pairs. *Physical Chemistry Chemical Physics* **2006**, *8*, 1985–1993.

[450] Kabeláč, M.; Valdes, H.; C. Sherer, E.; J. Cramer, C.; Hobza, P. Benchmark RI-MP2 database of nucleic acid base trimers: performance of different density functional models for prediction of structures and binding energies. *Physical Chemistry Chemical Physics* **2007**, *9*, 5000–5008.

[451] Olsen, J.; Jørgensen, P.; Helgaker, T.; Christiansen, O. Divergence in Møller–Plesset theory: A simple explanation based on a two-state model. *The Journal of Chemical Physics* **2000**, *112*, 9736–9748.

[452] Christiansen, O. Coupled Cluster Theory with Emphasis on Selected New Developments. *Theoretical Chemistry Accounts* **2006**, *116*, 106–123.

[453] Bartlett, R. J.; Musiał, M. Coupled-cluster theory in quantum chemistry. *Reviews of Modern Physics* **2007**, *79*, 291–352.

[454] Bartlett, R. J. Coupled-cluster theory and its equation-of-motion extensions. *WIREs Computational Molecular Science* **2012**, *2*, 126–138.

[455] Eriksen, J. J.; Kristensen, K.; Kjærgaard, T.; Jørgensen, P.; Gauss, J. A Lagrangian framework for deriving triples and quadruples corrections to the CCSD energy. *The Journal of Chemical Physics* **2014**, *140*, 064108.

[456] Christiansen, O.; Koch, H.; Jørgensen, P. The second-order approximate coupled cluster singles and doubles model CC2. *Chemical Physics Letters* **1995**, *243*, 409–418.

[457] Koch, H.; Christiansen, O.; Jørgensen, P.; Sanchez de Merás, A. M.; Helgaker, T. The CC3 model: An iterative coupled cluster approach including connected triples. *The Journal of Chemical Physics* **1997**, *106*, 1808–1818.

[458] Sneskov, K.; Christiansen, O. Excited state coupled cluster methods. *WIREs Computational Molecular Science* **2012**, *2*, 566–584.

[459] Mennucci, B.; Cammi, R.; Tomasi, J. Excited states and solvatochromic shifts within a nonequilibrium solvation approach: A new formulation of the integral equation formalism method at the self-consistent field, configuration interaction, and multiconfiguration self-consistent field level. *The Journal of Chemical Physics* **1998**, *109*, 2798–2807.

[460] Mikkelsen, K. V.; Jørgensen, P.; Jensen, H. J. A. A multiconfiguration self-consistent reaction field response method. *The Journal of Chemical Physics* **1994**, *100*, 6597–6607.

[461] Christiansen, O.; Jørgensen, P.; Hättig, C. Response functions from Fourier component variational perturbation theory applied to a time-averaged quasienergy. *International Journal of Quantum Chemistry* **1998**, *68*, 1–52.

[462] Dreuw, A.; Wormit, M. The algebraic diagrammatic construction scheme for the polarization propagator for the calculation of excited states. *WIREs Computational Molecular Science* **2015**, *5*, 82–95.

[463] Hättig, C. In *Advances in Quantum Chemistry*; Jensen, H. J. a., Ed.; Response Theory and Molecular Properties (A Tribute to Jan Linderberg and Poul Jørgensen); Academic Press, 2005; Vol. 50; pp 37–60.

[464] C. Winter, N. O.; K. Graf, N.; Leutwyler, S.; Hättig, C. Benchmarks for 0–0 transitions of aromatic organic molecules: DFT/B3LYP, ADC(2), CC2, SOS-CC2 and SCS-CC2 compared to high-resolution gas-phase data. *Physical Chemistry Chemical Physics* **2013**, *15*, 6623–6630.

[465] Jacquemin, D.; Duchemin, I.; Blase, X. 0–0 Energies Using Hybrid Schemes: Benchmarks of TD-DFT, CIS(D), ADC(2), CC2, and BSE/GW formalisms for 80 Real-Life Compounds. *Journal of Chemical Theory and Computation* **2015**, *11*, 5340–5359.

[466] Schreiber, M.; Silva-Junior, M. R.; Sauer, S. P. A.; Thiel, W. Benchmarks for electronically excited states: CASPT2, CC2, CCSD, and CC3. *The Journal of Chemical Physics* **2008**, *128*, 134110.

[467] Silva-Junior, M. R.; Sauer, S. P.; Schreiber, M.; Thiel, W. Basis set effects on coupled cluster benchmarks of electronically excited states: CC3, CCSDR(3) and CC2. *Molecular Physics* **2010**, *108*, 453–465.

[468] Sauer, S. P. A.; Schreiber, M.; Silva-Junior, M. R.; Thiel, W. Benchmarks for Electronically Excited States: A Comparison of Noniterative and Iterative Triples Corrections in Linear Response Coupled Cluster Methods: CCSDR(3) versus CC3. *Journal of Chemical Theory and Computation* **2009**, *5*, 555–564.

[469] Jacquemin, D. What is the Key for Accurate Absorption and Emission Calculations, Energy or Geometry? *Journal of Chemical Theory and Computation* **2018**, *14*, 1534–1543.

[470] Christiansen, O.; Mikkelsen, K. V. A coupled-cluster solvent reaction field method. *The Journal of Chemical Physics* **1999**, *110*, 1365–1375.

[471] Christiansen, O.; Mikkelsen, K. V. Coupled cluster response theory for solvated molecules in equilibrium and nonequilibrium solvation. *The Journal of Chemical Physics* **1999**, *110*, 8348–8360.

[472] Karbalaei Khani, S.; Marefat Khah, A.; Hättig, C. Comparison of Reaction Field Schemes for Coupling Continuum Solvation Models with Wave Function Methods for Excitation Energies. *Journal of Chemical Theory and Computation* **2020**, *16*, 4554–4564.

[473] Aguilar, M. A.; del Valle, F. J. O.; Tomasi, J. Electron correlation and solvation effects. II. The description of the vibrational properties of a water molecule in a dielectric given by the application of the polarizable continuum model with inclusion of correlation effects. *Chemical Physics* **1991**, *150*, 151–161.

[474] del Valle, F. J. O.; Tomasi, J. Electron correlation and solvation effects. I. Basic formulation and preliminary attempt to include the electron correlation in the quantum mechanical polarizable continuum model so as to study solvation phenomena. *Chemical Physics* **1991**, *150*, 139–150.

[475] Cammi, R. Quantum cluster theory for the polarizable continuum model. I. The CCSD level with analytical first and second derivatives. *The Journal of Chemical Physics* **2009**, *131*, 164104.

[476] Lunkenheimer, B.; Köhn, A. Solvent Effects on Electronically Excited States Using the Conductor-Like Screening Model and the Second-Order Correlated Method ADC(2). *Journal of Chemical Theory and Computation* **2013**, *9*, 977–994.

[477] Schwabe, T.; Sneskov, K.; Haugaard Olsen, J. M.; Kongsted, J.; Christiansen, O.; Hättig, C. PERI–CC2: A Polarizable Embedded RI-CC2 Method. *Journal of Chemical Theory and Computation* **2012**, *8*, 3274–3283.

[478] Khani, S. K.; Khah, A. M.; Hättig, C. COSMO-RI-ADC(2) excitation energies and excited state gradients. *Physical Chemistry Chemical Physics* **2018**, *20*, 16354–16363.

[479] Caricato, M.; Mennucci, B.; Tomasi, J.; Ingrosso, F.; Cammi, R.; Corni, S.; Scalmani, G. Formation and relaxation of excited states in solution: A new time dependent polarizable continuum model based on time dependent density functional theory. *The Journal of Chemical Physics* **2006**, *124*, 124520.

[480] Marefat Khah, A.; Karbalaei Khani, S.; Hättig, C. Analytic Excited State Gradients for the QM/MM Polarizable Embedded Second-Order Algebraic Diagrammatic Construction for the Polarization Propagator PE-ADC(2). *Journal of Chemical Theory and Computation* **2018**, *14*, 4640–4650.

[481] Sülzner, N. Time-Resolved Fluorescence Studies on Emission and Proton-Transfer Dynamics of a Super-Photoacid in Acetone-Water Mixtures. M.Sc. thesis, Ruhr-Universität Bochum, Bochum, Germany, 2018.

[482] TURBOMOLE V7-6-1323-gf7bfc1e, a development of University of Karlsruhe and Forschungszentrum Karlsruhe GmbH, 1989-2007, TURBOMOLE GmbH, since 2007; available from `https://www.turbomole.org`.

[483] Dunning, T. H. Gaussian basis sets for use in correlated molecular calculations. I. The atoms boron through neon and hydrogen. *The Journal of Chemical Physics* **1989**, *90*, 1007–1023.

[484] Woon, D. E.; Dunning, T. H. Gaussian basis sets for use in correlated molecular calculations. III. The atoms aluminum through argon. *The Journal of Chemical Physics* **1993**, *98*, 1358–1371.

[485] Weigend, F.; Häser, M. RI-MP2: first derivatives and global consistency. *Theoretical Chemistry Accounts* **1997**, *97*, 331–340.

[486] Hättig, C.; Hellweg, A.; Köhn, A. Distributed memory parallel implementation of energies and gradients for second-order Møller-Plesset perturbation theory with the resolution-of-the-identity approximation. *Phys. Chem. Chem. Phys.* **2006**, *8*, 1159–1169.

[487] Hättig, C. Geometry optimizations with the coupled-cluster model CC2 using the resolution-of-the-identity approximation. *The Journal of Chemical Physics* **2003**, *118*, 7751–7761.

[488] Cammi, R.; Mennucci, B.; Tomasi, J. Second-Order Møller-Plesset Analytical Derivatives for the Polarizable Continuum Model Using the Relaxed Density Approach. *J. Phys. Chem. A* **1999**, *103*, 9100–9108.

[489] Köhn, A.; Hättig, C. Analytic gradients for excited states in the coupled-cluster model CC2 employing the resolution-of-the-identity approximation. *The Journal of Chemical Physics* **2003**, *119*, 5021–5036.

[490] Sülzner, N.; Hättig, C. Raw Data to "Theoretical Spectroscopy of HTPS-Based Super-Photoacids in DMSO". *Zenodo* **2022**,

[491] Kendall, R. A.; Dunning, T. H.; Harrison, R. J. Electron affinities of the first-row atoms revisited. Systematic basis sets and wave functions. *The Journal of Chemical Physics* **1992**, *96*, 6796–6806.

[492] Hättig, C.; Weigend, F. CC2 excitation energy calculations on large molecules using the resolution of the identity approximation. *The Journal of Chemical Physics* **2000**, *113*, 5154–5161.

[493] Sülzner, N.; Haberhauer, J.; Hättig, C.; Hellweg, A. Prediction of acid p$K_a$ values in the solvent acetone based on COSMO-RS. *Journal of Computational Chemistry* **2022**, *43*, 1011–1022.

[494] Sülzner, N.; Geissler, B.; Grandjean, A.; Jung, G.; Nuernberger, P. Excited-State Proton Transfer Dynamics of a Super-Photoacid in Acetone-Water Mixtures. *ChemPhotoChem* **2022**, *6*, e202200041.

[495] Kamlet, M. J.; Abboud, J. L. M.; Abraham, M. H.; Taft, R. W. Linear solvation energy relationships. 23. A comprehensive collection of the solvatochromic parameters, $\pi^*$, $\alpha$, and $\beta$, and some methods for simplifying the generalized solvatochromic equation. *The Journal of Organic Chemistry* **1983**, *48*, 2877–2887.

[496] McGarry, P. F.; Jockusch, S.; Fujiwara, Y.; Kaprinidis, N. A.; Turro, N. J. DMSO Solvent Induced Photochemistry in Highly Photostable Compounds. The Role of Intermolecular Hydrogen Bonding. *The Journal of Physical Chemistry A* **1997**, *101*, 764–767.

[497] Yuan, Z.; Tang, Q.; Sreenath, K.; Simmons, J. T.; Younes, A. H.; Jiang, D.-e.; Zhu, L. Absorption and Emission Sensitivity of 2-(2'-Hydroxyphenyl)benzoxazole to Solvents and Impurities. *Photochemistry and Photobiology* **2015**, *91*, 586–598.

[498] Wortmann, S.; Schloeglmann, S.; Nuernberger, P. Sensitivity of Isomerization Kinetics of 1,3,5-Triphenylformazan on Cosolvents Added to Toluene. *The Journal of Organic Chemistry* **2022**, *87*, 1745–1755.

[499] Akerlof, G. Dielectric constants of some organic solvent–water mixtures at various temperatures. *Journal of the American Chemical Society* **1932**, *54*, 4125–4139.

[500] Grandjean, A.; Pérez Lustres, J. L.; Muth, S.; Maus, D.; Jung, G. Steady-State Spectroscopy to Single Out the Contact Ion Pair in Excited-State Proton Transfer. *The Journal of Physical Chemistry Letters* **2021**, *12*, 1683–1689.

[501] Grandjean, A.; Pérez Lustres, J. L.; Jung, G. Solvent-Controlled Intermolecular Proton-Transfer Follows an Irreversible Eigen-Weller Model from fs to ns. *ChemPhotoChem* **2021**, *5*, 1094–1105.

[502] Brenlla, A.; Veiga Gutiérrez, M.; Ríos Rodríguez, M. C.; Rodríguez-Prieto, F.; Mosquera, M.; Pérez Lustres, J. L. Moderately Strong Photoacid Dissociates in Alcohols with High Transient Concentration of the Proton-Transfer Contact Pair. *The Journal of Physical Chemistry Letters* **2014**, *5*, 989–994.

[503] Izutsu, K. *Acid-base Dissociation Constants in Dipolar Aprotic Solvents, IUPAC Chemical Data Series No. 35, Blackwells Scientific*; Oxford, 1990.

[504] Ludwig, M.; Pytela, O.; Večeřa, M. Solvent effects on dissociation of substituted benzenesulphonamides in acetone, 1,2-dichloroethane, tetramethylene sulphone, pyridine and some aqueous organic solvent mixtures. *Collection of Czechoslovak Chemical Communications* **1986**, *51*, 1948–1957.

[505] Ludwig, M.; Baron, V.; Kalfus, K.; Pytela, O.; Večeřa, M. Dissociation constants of substituted benzoic acids in water and in organic solvents. *Collection of Czechoslovak Chemical Communications* **1986**, *51*, 2135–2142.

[506] Pytela, O.; Kulhánek, J.; Ludwig, M.; Říha, V. Chemometrical Analysis of Substituent Effects. III. Additivity of Substituent Effects in Dissociation of 3,4-Disubstituted Benzoic Acids in Organic Solvents. *Collection of Czechoslovak Chemical Communications* **1994**, *59*, 627–638.

[507] Pytela, O.; Kulhánek, J.; Ludwig, M. Chemometrical Analysis of Substituent Effects. IV. Additivity of Substituent Effects in Dissociation of 3,5-Disubstituted Benzoic Acids in Organic Solvents. *Collection of Czechoslovak Chemical Communications* **1994**, *59*, 1637–1644.

[508] Pytela, O.; Liška, J. Chemometrical Analysis of Substituent Effects. V. *ortho* Effect. *Collection of Czechoslovak Chemical Communications* **1994**, *59*, 2005–2021.

[509] Kulhánek, J.; Pytela, O. Chemometric Analysis of Substituent Effects. XI. Solvent Effects on Dissociation of 2,6-Disubstituted Benzoic Acids. *Collection of Czechoslovak Chemical Communications* **1997**, *62*, 913–924.

[510] Yang, Q.; Li, Y.; Yang, J.-D.; Liu, Y.; Zhang, L.; Luo, S.; Cheng, J.-P. Holistic Prediction of the p$K_a$ in Diverse Solvents Based on a Machine-Learning Approach. *Angewandte Chemie* **2020**, *132*, 19444–19453.

[511] Wu, J.; Kang, Y.; Pan, P.; Hou, T. Machine learning methods for p$K_a$ prediction of small molecules: Advances and challenges. *Drug Discovery Today* **2022**, *27*, 103372.

[512] Megerle, U.; Pugliesi, I.; Schriever, C.; Sailer, C. F.; Riedle, E. Sub-50 fs broadband absorption spectroscopy with tunable excitation: putting the analysis of ultrafast molecular dynamics on solid ground. *Applied Physics B* **2009**, *96*, 215–231.

# A. Experimental Details

## A.1. Time-Resolved Fluorescence Spectroscopy

### A.1.1. Experimental Setup

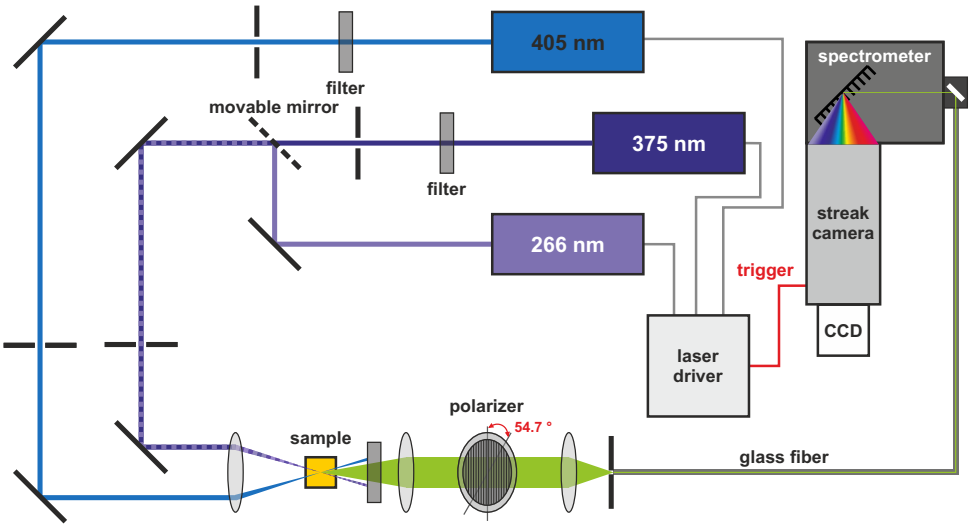



Figure A.1.: **Experimental setup for TRF spectroscopy.** Optical paths of the lasers are shown in blue (405 nm), violet (375 nm), and light violet (266 nm). Fluorescence radiation is indicated in green. A movable mirror allows to switch between 375 nm and 266 nm excitation. A detailed explanation is given in Section B.1. Reprinted with permission from Ref. 481.

### A.1.2. Post-Processing of Acquired Data

Prior to an analysis, the streak images should be corrected for calibration, proper intensity normalization, and chirp in order to obtain a good comparability. This task, called *post processing*, is schematically illustrated in Fig. A.2.

Directly after importing the time-resolved fluorescence data as images, intensity and wavelength calibrations are performed. The actual shape of the images depends on the current parameter settings of the streaking setup and thus intensity calibration is needed whenever one of these changes. Time-resolved spectra of a white-light lamp were therefore measured 20 times, averaged, background subtracted, and normalized (to one). Using the intensity value of each pixel as a scaling factor, all sample streak images were calibrated afterward. Moreover, the spectrum of a mercury-vapor (Hg-Ar) lamp was measured in the non-streaking mode for wavelength calibration. The positions of the observed emission lines were subjected to a linear fit and used to shift the fluorescence wavelengths.

Despite calibration and intensity normalization, the images still revealed a significant chirp, i.e. a temporal delay concerning shorter (“blue”) and longer (“red”) wavelengths, due to the severe group-

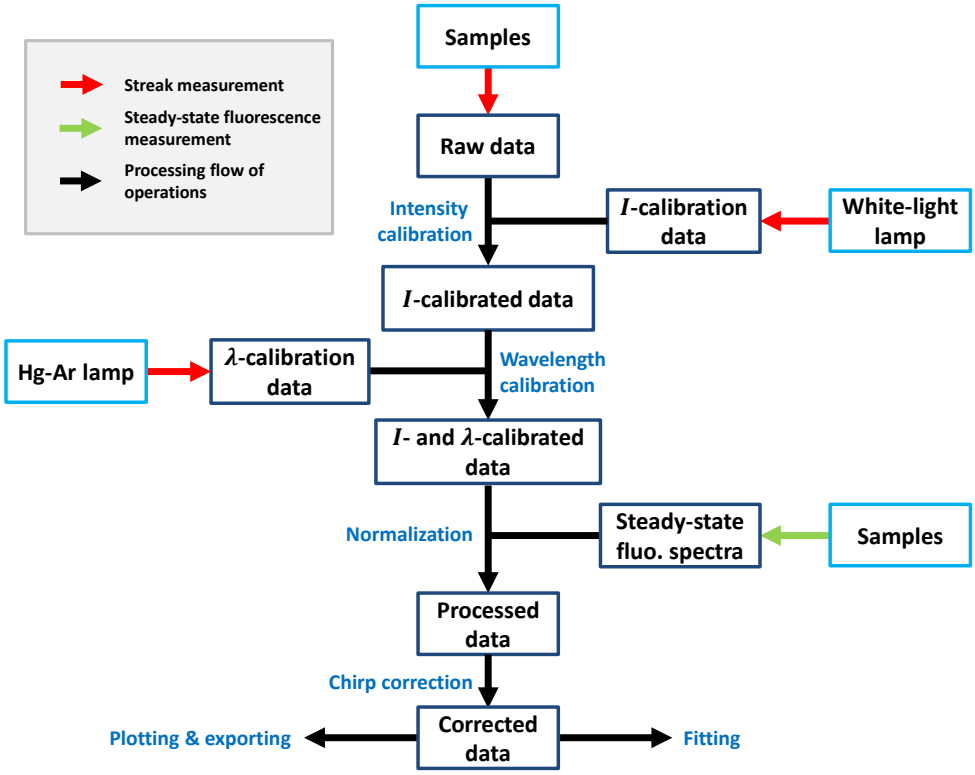



Figure A.2.: Illustration of the post-processing after data acquisition as performed by the developed MATLAB (MathWorks, Inc.) routine `ReadData`.

velocity dispersion (GVD) after passing through the 3 m long optical fiber. This dispersion was treated by fitting the positions $(t, \lambda)$ of the intensity maxima to a function of time using a third-order polynomial [512] of the form

$$t = f(\lambda) = a \cdot \left(\frac{\lambda - \lambda_c}{100}\right)^3 + b \cdot \left(\frac{\lambda - \lambda_c}{100}\right)^2 + c \cdot \left(\frac{\lambda - \lambda_c}{100}\right) + d, \tag{A.1}$$

where $a, b, c, d$ are the coefficients and $\lambda_c$ is the central wavelength of the spectra, respectively. Chirp correction, based on this polynomial fit, was subsequently achieved by transforming the streak images in such a way that the temporal delay of shorter wavelengths is compensated. A matrix that describes this geometric transformation was constructed from a defined set of moving points, lying on the fitted polynomial, and fixed points, lying on a constant function that approximates the early spectral regime. Each pixel array (wavelength) of the streak image was individually re-scaled according to its matrix entries, a method called *warping*. Finally, the chirp-corrected images could be plotted, exported as an ASCII file and/or subjected to fitting.

## A.2. Transient UV/Vis Absorption Spectroscopy

### A.2.1. Experimental Setup

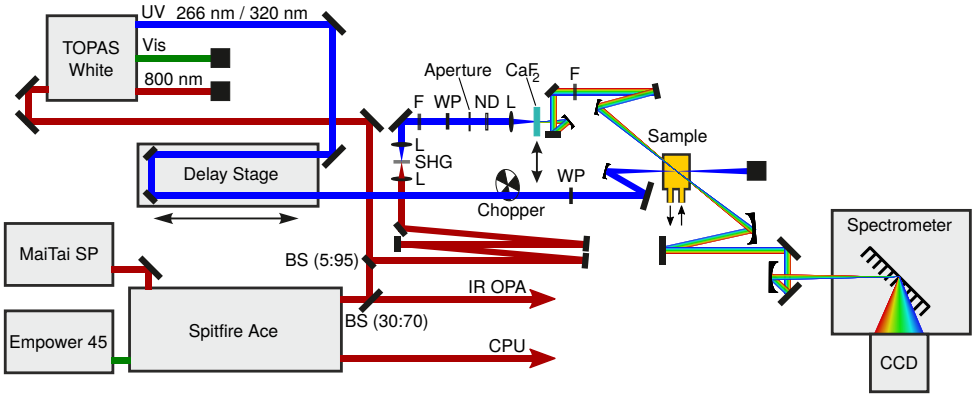



Figure A.3.: **Experimental setup for TA spectroscopy.** BS(R:T): beam splitter (reflection:transmission), WP: half-wave plate, SHG: $\beta$-barium-borate crystal for the second-harmonic generation, F: filter, ND: neutral-density filter, L: lens, $CaF_2$ : calcium fluoride plate for the generation of the white-light continuum, CCD: charge-coupled device, IR OPA: optical parametric amplifier working in the IR region, CPU: chirped-pulse up-conversion. Note that not all optical elements are drawn for clarity. Reprinted with permission from Ref. 377.

# B. Supporting Information of the Articles

## B.1. ESPT in Acetone–Water Mixtures

The following Supporting Information belongs to the publication *ChemPhotoChem* **2022**, *6*, e202200041; **Copyright © 2022 The Authors. ChemPhotoChem published by Wiley-VCH GmbH.** Available online at `https://doi.org/10.1002/cptc.202200041` and reprinted in Chapter 3.

ChemPhotoChem

Supporting Information

# Excited-State Proton Transfer Dynamics of a Super-Photoacid in Acetone-Water Mixtures

Niklas Sülzner, Bastian Geissler, Alexander Grandjean, Gregor Jung, and Patrick Nuernberger*

## Sample Preparation

The photoacid tris(1,1,1,3,3,3-hexafluoropropan-2-yl)-8-hydroxypyrene-1,3,6-trisulfonate was used as received from the Jung group. For sample preparation, acetone (99.5 %, spectrophotometric grade; abcr), purified water (Milli-Q, Millipore Corp.), and trifluoroacetic acid (99 %, extra pure; Acros Organics) were used. All samples were prepared from a 26 µM parent solution, i.e., dissolving 2.3 mg photoacid in 100 mL acetone.

For the water sample series in neutral solution, 600 µL of a ~ 26 µM parent solution of the photoacid in acetone were filled into the static sample cell. Afterward, the following amounts of water were gradually added to the same sample: 4 × 1.5 µL, 8 × 3.0 µL and 6.0 µL. This corresponds to increasing concentrations of water covering 0 M, 0.14 M, 0.28 M, 0.41 M, 0.55 M, 0.82 M, 1.09 M, 1.35 M, 1.62 M, 1.89 M, 2.14 M, 2.39 M, 2.64 M, and 3.14 M.

For the water sample series in acidic solution, 600 µL of a ~ 26 µM parent solution of the photoacid in acetone and 3 µL of a 1:10 solution of TFA in acetone were filled into the static sample, corresponding to a final TFA concentration of ~ 6.5 mM. Afterward, the following amounts of water were gradually added to the same sample: 4 × 1.5 µL and 2 × 3.0 µL. This corresponds to the following concentrations of added water: 0 M, 0.14 M, 0.28 M, 0.41 M, 0.55 M, 0.82 M and 1.09 M.

For the TFA sample series, one individual sample was prepared for each initial amount of water, i.e. for 0 M, 0.14 M, 0.28 M, 0.41 M, and 0.55 M. First, 600 µL of a ~ 26 µM parent solution of the photoacid in acetone were filled into the static sample cell. The respective volume of 0 µL, 1.5 µL, 3.0 µL, 4.5 µL or 5.0 µL of $H_2O$ was then added to the parent solution. These volumes correspond to initial concentrations of 0 M, 0.14 M, 0.28 M, 0.41 M, and 0.55 M of $H_2O$. Afterward, the following amounts of pure TFA were gradually added to the same sample: 2 × 1.5 µL, 3 × 3.0 µL, and 2 × 6.0 µL. These correspond to increasing concentrations of added TFA covering 0 M, 0.03 M, 0.06 M, 0.13 M, 0.19 M, 0.25 M, 0.38 M, 0.50 M, 0.73 M, and 0.96 M. For the series with the largest concentration of water (0.55 M), two additional volumes of TFA were added: 2 × 12.0 µL, yielding final concentrations of 1.38 M and 1.78 M.

## Basic Spectroscopic Characterization

Prior to the time-resolved measurements, steady-state linear absorption and fluorescence emission spectra were measured using the commercially available JASCO V-770 spectrophotometer and JASCO FP-8300 spectrofluorometer. A 10 mm × 10 mm quartz cuvette (Hellma Analytics 115-F-10-40) was used as static sample cell for both investigations. Absorption was measured along the 2 mm optical path of the cell and referenced to acetone (spectroscopic grade). To prevent self-absorption (reabsorption) of fluorescence, the optical density at excitation wavelength (400 nm) was monitored to fall below 100 mOD for all samples. Fluorescence emission spectra were recorded *via* excitation at 400 nm along the 10 mm path and perpendicular detection along the 2 mm path. Subsequently, the emission spectra were subjected to a white-light spectral correction.

## Time-resolved fluorescence spectroscopy

Time-resolved fluorescence measurements were performed by use of a custom-made spectrometer. The excitation light (405 nm) was provided by a pulsed laser diode (PicoQuant LDH-P-C-405B) driven by an oscillator module (PicoQuant PDL800-B) and operating at 20 MHz. Using a collinear excitation-detection geometry, this light was first focused into the static sample cell (Hellma Analytics 115-F-10-40: 10 mm× 10 mm quartz cuvette, 2 mm path length) and removed by a low-pass reflective filter afterward. The emitted fluorescence radiation was collected (at 180°) using a system of two lenses imaging the excitation focus onto the entrance of a glass fiber. In addition, a polarizer was set at magic angle (54.7°) in between the lenses to exclude fluorescence anisotropy contributions. After passing through a glass fiber (3 m, fused silica), spectral separation of the emitted light was accomplished by use of a spectroscope (Princeton Instruments SP2150i) with a 150 mm grating. The streak camera (Hamamatsu C10627-11) subsequently performed the temporal analysis creating a two-dimensional image on its phosphor screen that was recorded by employing a 2D-CCD camera (Hamamatsu C9300-508) with an acquisition rate of 20 MHz.

## Global analysis scheme

For global analysis of the time-resolved emission data, the measured fluorescence intensity was modeled by the decay function

$$I(t;\lambda) = \int_{-\infty}^{\infty} L(t)D(t-t';\lambda)dt' \tag{S1}$$

representing a convolution of the normalized (usually Gaussian) instrument response function (IRF) $L(t)$ and the molecular response $D(t)$. The molecular response $D(t)$ was expanded in terms of exponential decays starting at $t = 0$

$$D(t) = \sum_{i=1}^{3} \Theta(t)\, A_i(\lambda) e^{-t/\tau_i} \tag{S2}$$

where $\Theta(t)$ is the Heaviside step function, $A_i(\lambda)$ are the amplitudes and $\tau_i$ the lifetimes (i.e., the inverse of the rates $k_i$). The FWHM of the (Gaussian) IRF was ~ 300 ps.

## Water Titration: Large Amounts of Water

Upon addition of water to the photoacid in acetoneous environment, the peak intensities show a two-step progression (as indicated by the arrows in Figure S1). The ROH peak intensity initially increases under $H_2O$ addition and finally starts to decrease at about 2 M $H_2O$ and, vice versa, the $RO^-$ peak intensity initially decreases and then starts to slightly increase again. The reversal in the progression seems to indicate a combination of two effects. Since water-induced deprotonation would shift the equilibrium, i.e., increase the concentration of $RO^-$, we can conclude from the actually observed initial $RO^-$ peak intensity decrease that ground-state deprotonation is at most marginal for small [$H_2O$] values. However, a comparison to a reference series, where water had been replaced by equal volumes of acetone, demonstrated that simple dilution was not the cause for the initial intensity decrease either. Besides, the actual initial ROH peak intensity increase also contradicts dilution effects. Furthermore, an isosbestic point near 570 nm, i.e., in the $RO^-$ regime, can be observed. A second isosbestic point expected in the range around 480 nm that would be characteristic for ROH/$RO^-$ interconversion (confer Fig. S2) is absent, which is an indication that a process other than deprotonation takes place during the addition of water. Hence, the early intensity progression of $RO^-$ can be rather explained by assuming the formation of a photoacid-water complex in the ground state with slightly different spectroscopic properties. Water-induced deprotonation is found to affect the ground-state equilibrium only at water concentrations larger than 2 M.

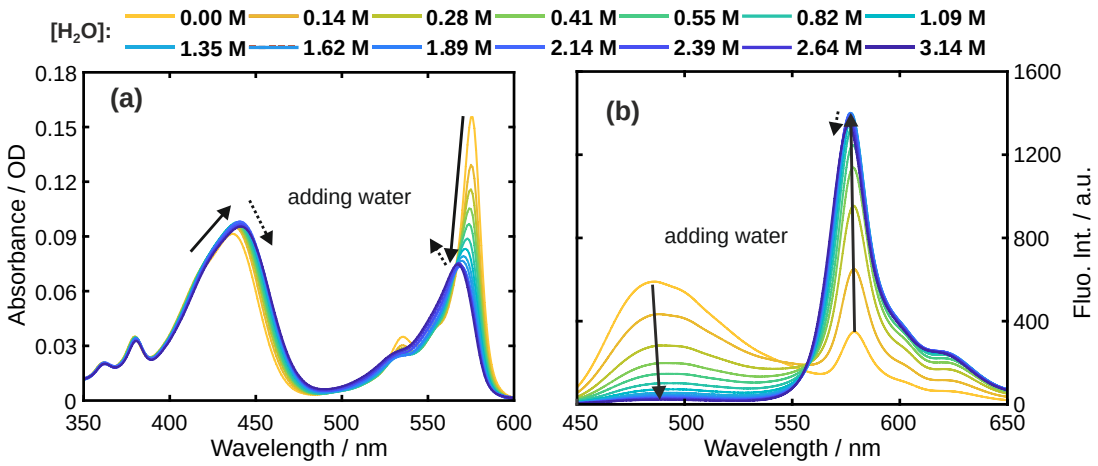



**Figure S1:** Steady-state characterization of samples with increasing concentration of water in neutral acetone solution via UV/Vis absorption (a) and fluorescence emission (b) spectroscopy after 400 nm excitation. All samples refer to 20 µM photoacid [with absorption spectra (a) being compensated accordingly to exclude dilution effects]. Concentrations of water are color-coded according to the legend; first-row values correspond to the data also shown in Figure 1a and 1c of the main manuscript, while second-row values (dashed lines) are shown here in addition to visualize the effect of larger amounts of water. Arrows indicate the peak progressions upon the addition of water.

## Acid Titration Monitored by UV/Vis Absorption Spectroscopy

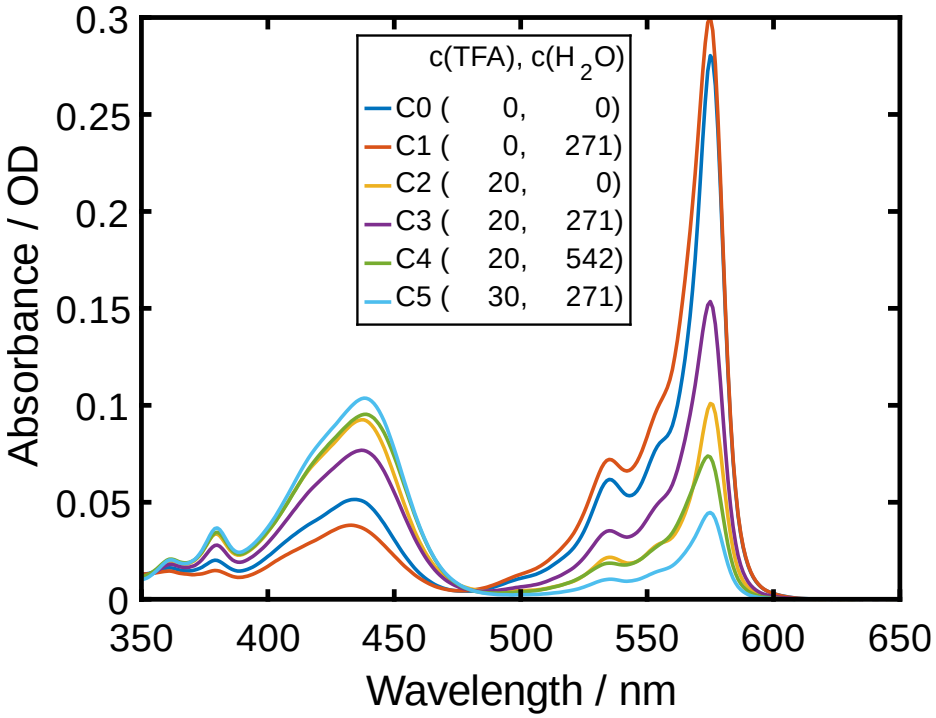



**Figure S2:** Steady-state absorption spectra referring to solutions of the photoacid in acetone with varying concentrations of water (in mM) and TFA (in µM) according to the values and the color coding in the legend. Neglecting the effect of water admixtures on the absorption spectra and focusing only on samples with identical amounts of water (e.g., comparing C1, C3, and C5 or C0 and C2), a clear isosbestic point for the acid-base titration near 480 nm can be observed. This point is distinctly different from the other two isosbestic points observed in Fig. 1(a-b) of the main text, which were assigned to complex formation.

## Benesi-Hildebrand Analysis

The Benesi-Hildebrand approach is frequently applied in host-guest chemistry to determine the association constant $K$ of a host-guest complex *via* absorption spectroscopy. For this, we consider the following association equilibrium between one host molecule (H) and $n$ guest molecules (G)

$$\mathrm{H} + n\,\mathrm{G} \rightleftharpoons \mathrm{H}\cdot(\mathrm{G})_n. \tag{S3}$$

From now on, we will refer to the complex $\mathrm{H}\cdot(\mathrm{G})_n$ as HG. The corresponding equilibrium constant $K$ is given by the association isotherm

$$K = \frac{[\mathrm{HG}]}{[\mathrm{H}][\mathrm{G}]^n}. \tag{S4}$$

First, we assume that either the host or the guest is in great excess relative to the other. For $[\mathrm{G}] \gg [\mathrm{H}]$, we can then approximate the equilibrium concentration of the guest as

$$[\mathrm{G}] = [\mathrm{G}]_0 - [\mathrm{HG}] \approx [\mathrm{G}]_0 \tag{S5}$$

while the equilibrium concentration of the host is

$$[\mathrm{H}] = [\mathrm{H}]_0 - [\mathrm{HG}]. \tag{S6}$$

Inserting (S5) and (S6) into Eq. (S4) yields

$$K = \frac{[\mathrm{HG}]}{([\mathrm{H}]_0 - [\mathrm{HG}]) \cdot [\mathrm{G}]_0^n} \tag{S7}$$

that can be rearranged to the equilibrium concentration of the complex

$$[\mathrm{HG}] = \frac{K[\mathrm{H}]_0[\mathrm{G}]_0^n}{1 + K[\mathrm{G}]_0^n}. \tag{S8}$$

Next, the validity of Beer-Lambert's law is assumed to relate $K$ to the absorption spectra. The total absorbance ($A$) of the solution (at a given wavelength) is thereby assumed to be the sum of absorbances of all components:

$$A = A_{\mathrm{H}} + A_{\mathrm{G}} + A_{\mathrm{HG}}. \tag{S9}$$

The second approximation is that the guest does not significantly contribute to the total absorbance, i.e., $A_G \approx 0$. Furthermore, by introducing $A_{\mathrm{H}} = \epsilon_{\mathrm{H}}[\mathrm{H}]d = \epsilon_{\mathrm{H}}([\mathrm{H}]_0 - [\mathrm{HG}])d$ and $A_{\mathrm{HG}} = \epsilon_{\mathrm{HG}}[\mathrm{HG}]d$ into (S9), we obtain the following relation for the total absorbance (omitting the mathematical details):

$$A = d[\mathrm{H}]_0 \left(\epsilon_{\mathrm{H}} + \frac{K\Delta\epsilon[\mathrm{G}]_0^n}{1 + K[\mathrm{G}]_0^n}\right) \tag{S10}$$

where $\Delta\epsilon = \epsilon_{\mathrm{HG}} - \epsilon_{\mathrm{H}}$ refers to the difference in the molar attenuation coefficients of HG and H. The difference between the total absorbance $A = A([\mathrm{G}]_0)$ at a given guest concentration $[\mathrm{G}]_0$ and the initial absorbance $A_0 = A([\mathrm{G}]_0 = 0)$, i.e., without the guest, is given by

$$\Delta A = A - A_0 = \frac{K\Delta\epsilon[\mathrm{G}]_0^n}{1 + K[\mathrm{G}]_0^n} \tag{S11}$$

which can be finally rearranged into the linearized form

$$[G]_0^{-n} = Kd\Delta\epsilon[\mathrm{H}]_0(\Delta A)^{-1} - K. \tag{S12}$$

This equation allows to determine $K$ and $\Delta\epsilon$ by finding the best linear fit ($y = ax + b$, with $y = [G]_0^{-n}$ and $x = (\Delta A)^{-1}$) depending on $n$ and computing these desired quantities through the slope $a$ and intercept $b$:

$$K = -b \tag{S13}$$

$$\Delta\epsilon = \frac{a}{Kd[\mathrm{H}]_0} = -\frac{a}{bd[\mathrm{H}]_0}\,. \tag{S14}$$

## Water Series in Neutral Solution: Triexponential Fits

In analogy to the measurements in acidic solution (Fig. 4), the time-resolved fluorescence maps for neutral acetone solutions were also subjected to global analysis with three temporal components, with the results shown in Fig. S3. While these results are generally similar to those in acidic solution, it should be noted that contributions for $RO^{-*}$ formation can be already observed in the fastest component described by $k_1$ and $A_1$ (Fig. S3(a) and S3(d)), especially at large water concentrations. Overall, the observed progressions of the DASs and rate constants constitute a reasonable continuation of those results in neutral solution. However, in direct comparison to Fig. 4, $A_1$ and $A_2$ appear to be more intricate due to a stronger mixing of the individual contributions from CPX*, HBIP*, and $RO^{-*}$ emission.

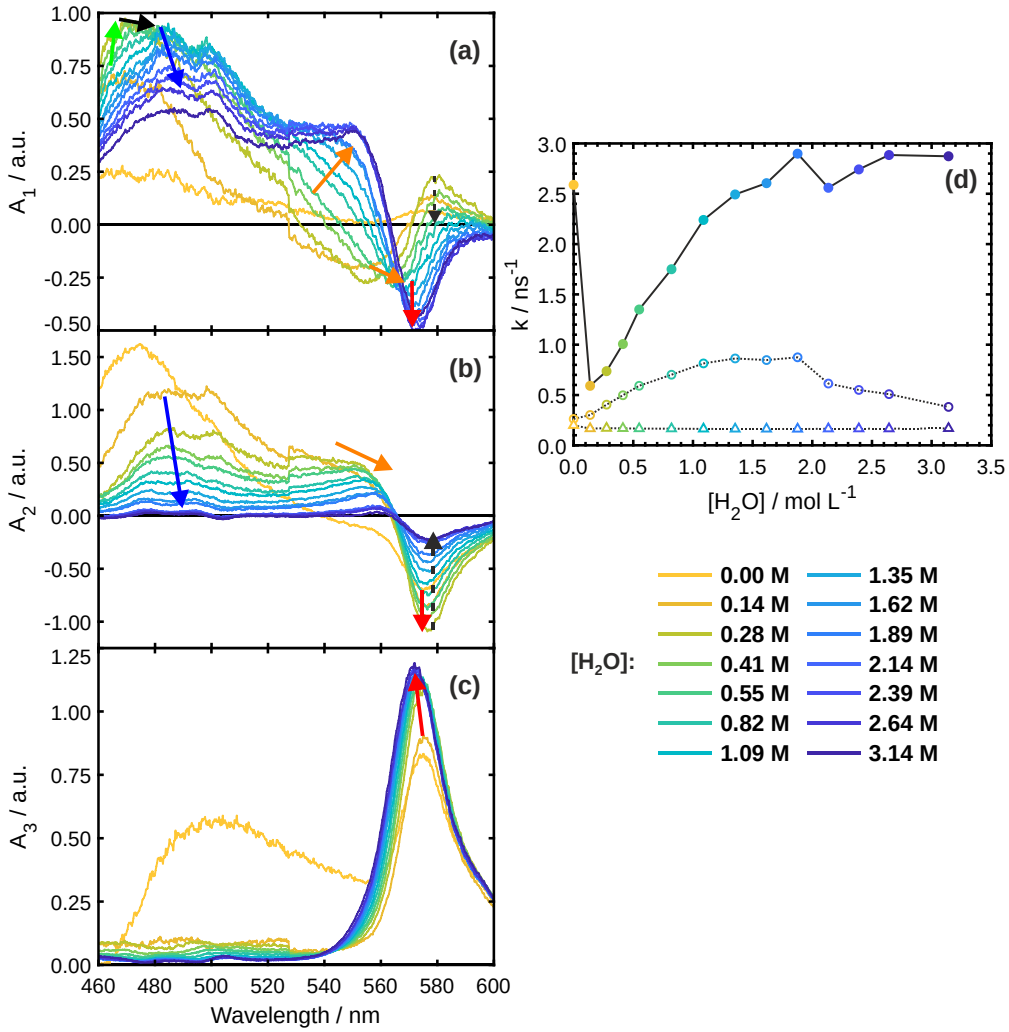
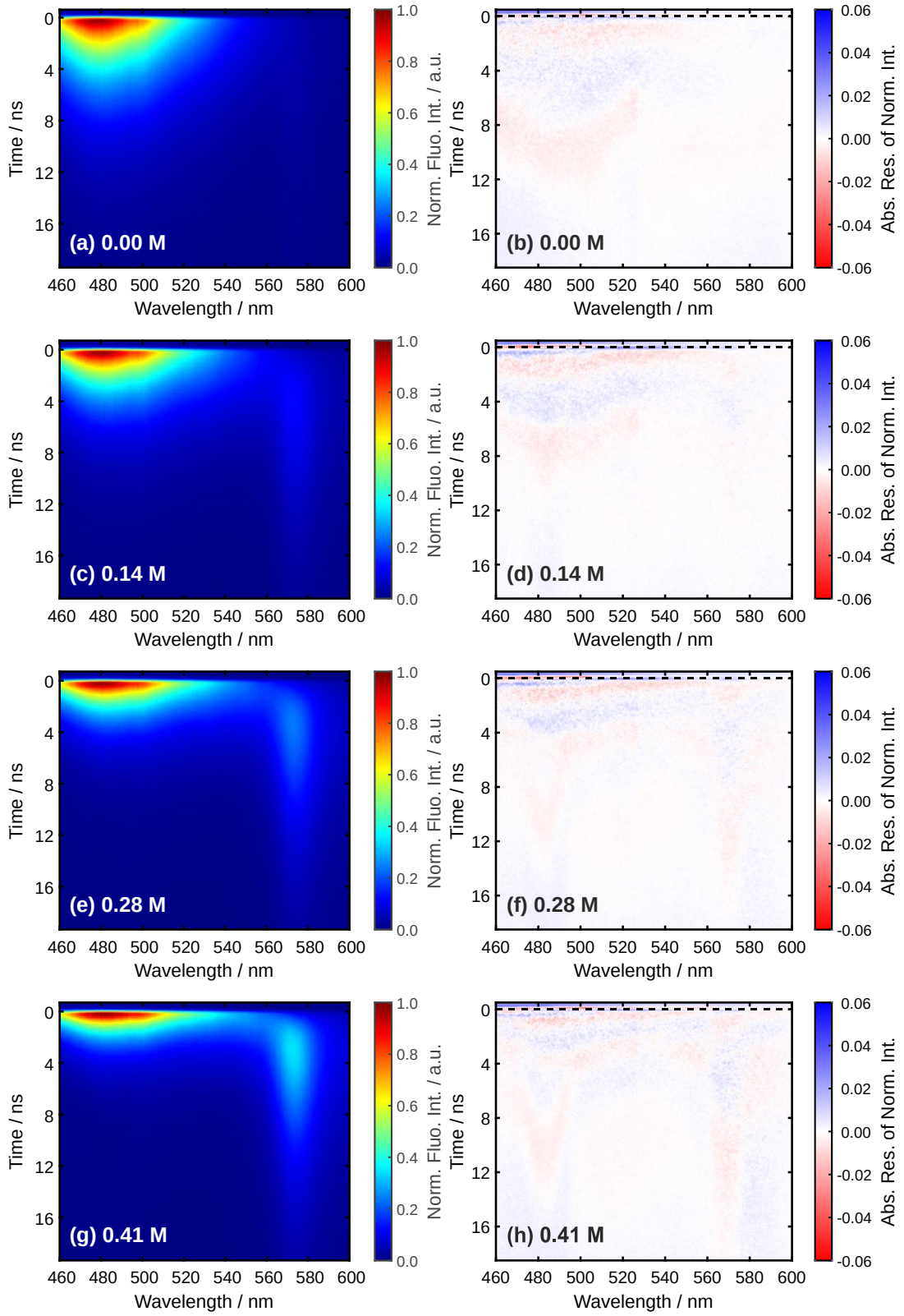



**Figure S3:** Results from the triexponential global fits to the fluorescence intensity decay of samples with increasing $[H_2O]$ in neutral acetone solution (cf. Fig. 1(a, c)) and analogous to Fig. 4. Decay-associated spectra (DAS) relating to amplitudes $A_1$ (a), $A_2$ (b), and $A_3$ (c) are shown, together with a plot of the kinetic constants $k_1$ (dots/solid line), $k_2$ (circles/dashed line), and $k_3$ (triangles/dashed lines) as a function of $[H_2O]$ (c). The values of $[H_2O]$ are color-coded according to the legend. The arrows indicate the progression with increasing $[H_2O]$.

## Water Series in Acidic Solution: Fluorescence and Residual Maps



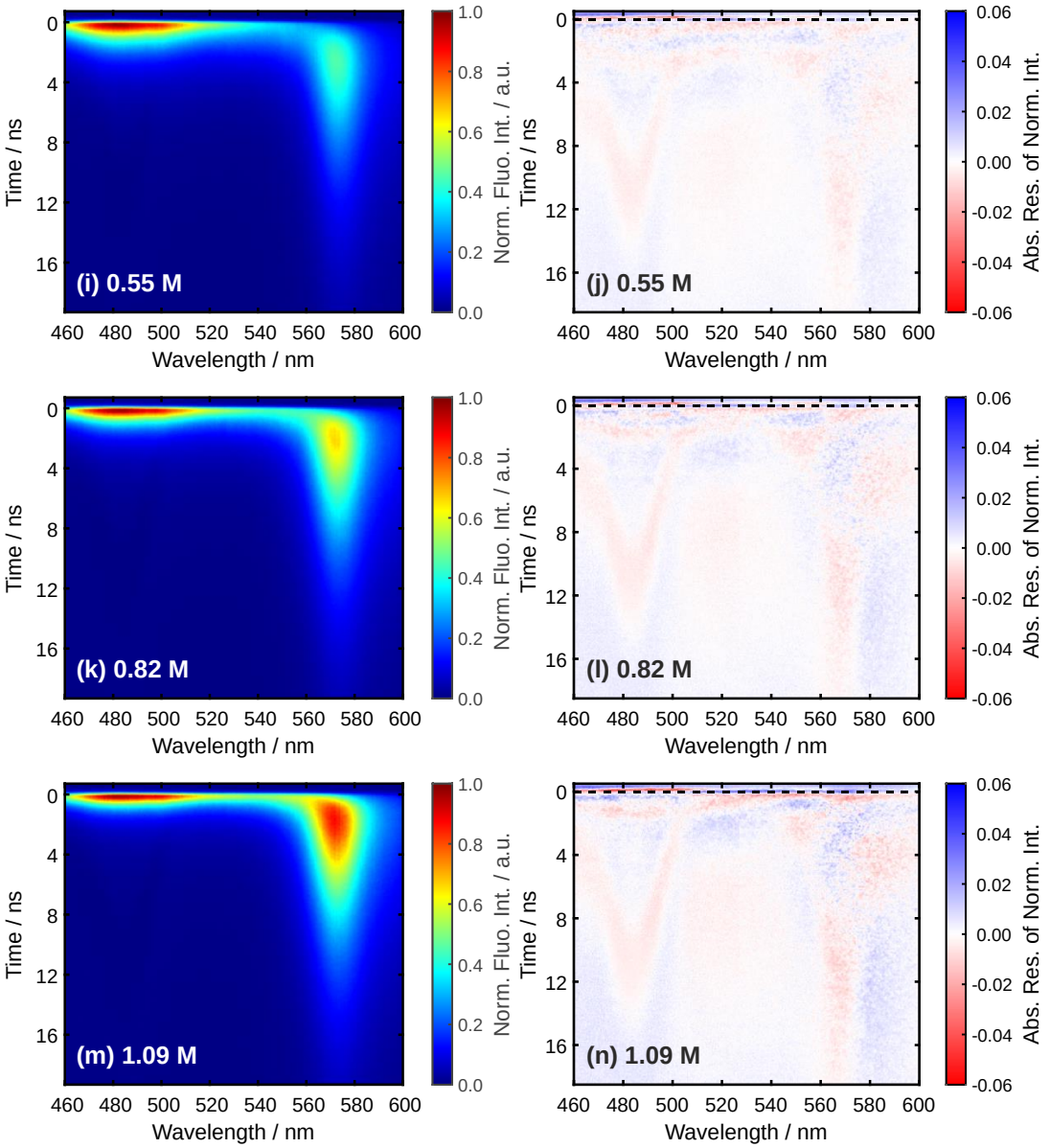



**Figure S4:** Time-resolved fluorescence dynamics at 405 nm of samples with increasing concentration of water (as given in the captions) in acidic solution (6.5 mM TFA), relating to Fig. 1(d) and partially already depicted in Fig. 3(a-d). **Left Column:** Normalized time-resolved fluorescence maps as shown in Fig. 3(a-d). **Right Column:** Maps of the residuals from the triexponential fits to the (normalized) fluorescence intensity as defined by Eq. (S2) (see "Global analysis scheme" section) whose results for the main fit parameters, the decay-associated spectra and kinetic constants, are shown in Fig. 4.

## Reference System: Methylated Analog (ROMe)

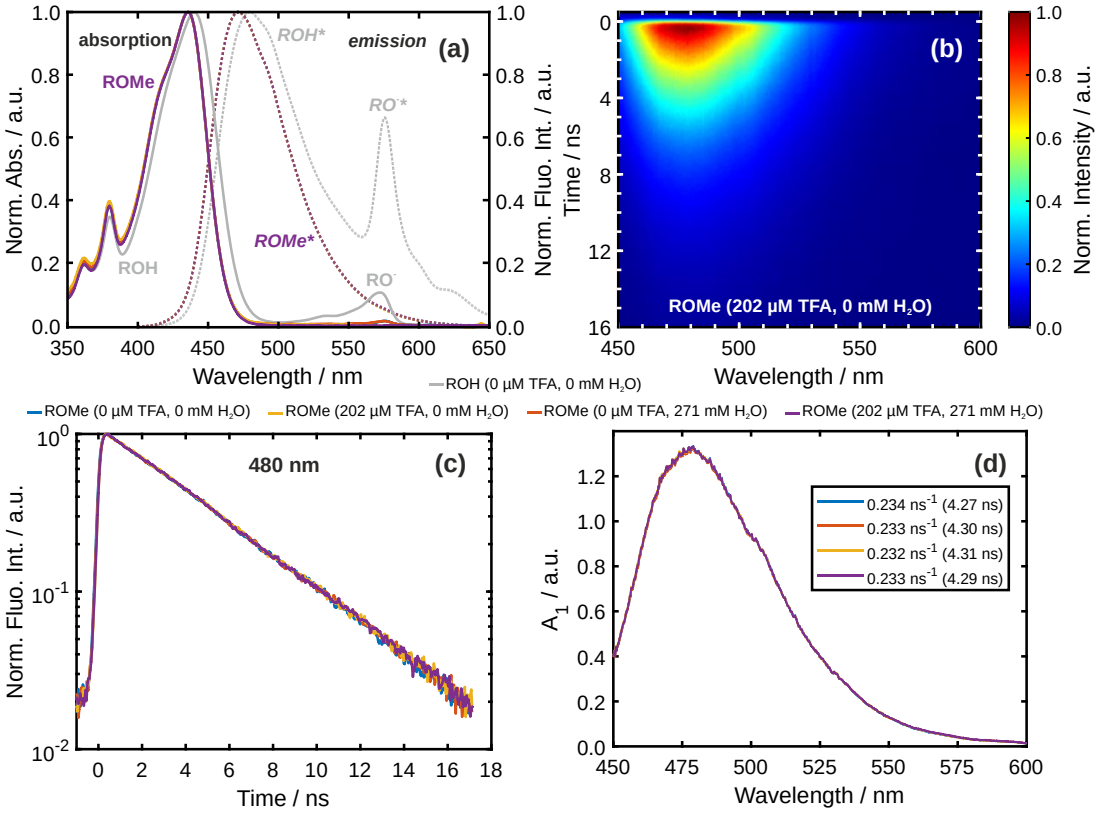



**Figure S5:** Steady-state (a) and time-resolved (b-d) characterization of the methylated analogue ROMe of the photoacid ROH. ROMe was studied in different environments to exclude any effects from acid or water admixtures in acetone. Colors refer to the different combinations of TFA and $H_2O$ concentrations according to the legend. The steady-state measurements (a) comprise both absorption (solid lines) and fluorescence emission (dashed lines) spectra. The spectra for ROH in neutral solution are additionally included as a reference (in gray). The absorption spectra display a major absorption maximum at 440 nm, assigned to ROMe, and also a much weaker peak at 575 nm that disappears after acidification with 202 µM TFA, even in the presence of 271 mM $H_2O$. This signal, matching the $RO^-$ absorption, is possibly due to a minor impurity of the sample with ROH. After excitation at 400 nm, ROMe* reveals a single emission maximum around 480 nm, without any additional features. In particular, with respect to the emission spectrum of a neutral ROH solution, the lack of 575 nm signals excludes any possible contribution from $RO^{-}$*. An exemplary time-resolved map recorded with a streak camera after 405 nm excitation for the ROMe solution with 202 µM TFA is shown in (b) and the corresponding semi-logarithmic plots of the kinetic traces at 480 nm near the ROMe* emission maximum are given in (c). As can be seen in (c), ROMe* decays perfectly monoexponentially. The results from a global analysis are depicted in (d). Here, the time-resolved maps are fitted with Equation (2) of the main text, but with $D(t;\lambda)$ being only a monoexponential function. As is evident from (d), the emission decay is described well with this model, yielding a lifetime of about 4.30 ns (or decay rate of 0.233 $ns^{-1}$). Most remarkably, the emission behavior of ROMe* is virtually independent of TFA and/or $H_2O$ admixtures.

## B.2. Prediction of Ground-State p$K_a$ in Acetone

The following Supporting Information belongs to the publication *J. Comput. Chem.* **2022**, *43* (15), 1011–1022. **Copyright © 2022 The Authors. *Journal of Computational Chemistry* published by Wiley Periodicals LLC.** Available online at `https://doi.org/10.1002/jcc.26864` and reprinted in Chapter 5.

# Supporting Information to 'Prediction of Acid p$K_a$ Values in the Solvent Acetone based on COSMO-RS'

Niklas Sülzner[*], Julia Haberhauer[*], Christof Hättig[*], Arnim Hellweg[†]

March 2, 2022

[*]Lehrstuhl für Theoretische Chemie, Ruhr-Universität Bochum, 44780 Bochum, Germany
[†]Dassault Systèmes Deutschland GmbH, Am Kabellager 11–15, 51063 Köln, Germany

## Phenol Subset: Fit Uncertainty

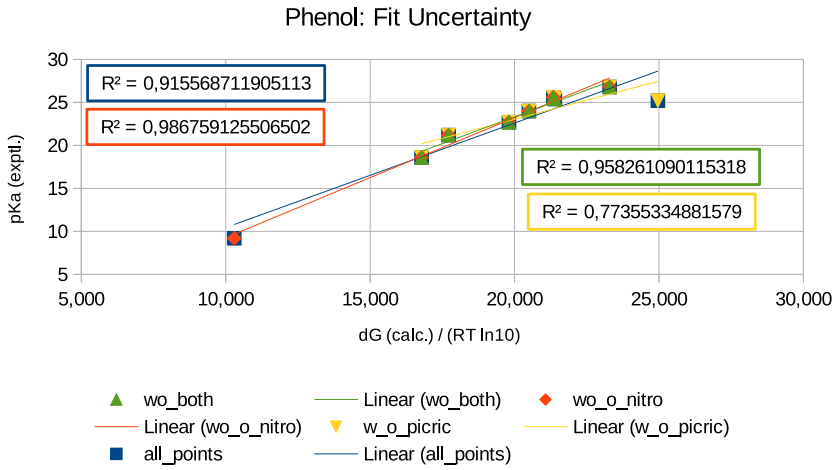



Figure S1: Comparison of different linear regressions for the phenol subset by selectively excluding either one of the data points for o-nitrophenol (red) or 2,4,6-trinitrophenol (picric acid, yellow), none (blue) or both (green): Experimental p$K_\mathrm{a}$ values (p$K_\mathrm{a}^{(\mathrm{exptl.})}$) plotted against reduced calculated Gibbs free energies of dissociation ($\frac{\Delta G}{RT\ln(10)}$) in the solvent acetone at the computational level BP-TZVP. Linear regressions lines are included in the respective color. The LFER fit parameters and correlation coefficients are given in Tab. S1.

| Data point range | $c_1$ | $c_0$ | $R^2$ |
|---|---|---|---|
| all points included | 1.216 | -1.708 | 0.916 |
| excluding o-nitrophenol | 1.398 | -4.714 | 0.987 |
| excluding picric acid | 0.887 | 5.312 | 0.774 |
| excluding both | 1.245 | -1.577 | 0.958 |

Table S1: Comparison of the results for the LFER parameters, i.e., the slopes $c_1$ and the intercepts $c_0$ (cf. Eq. (1) of the main text) together the squared correlation coefficients $R^2$ as a measure of the fit quality for fits that selectively exclude some of the data points as described in Fig. S1.

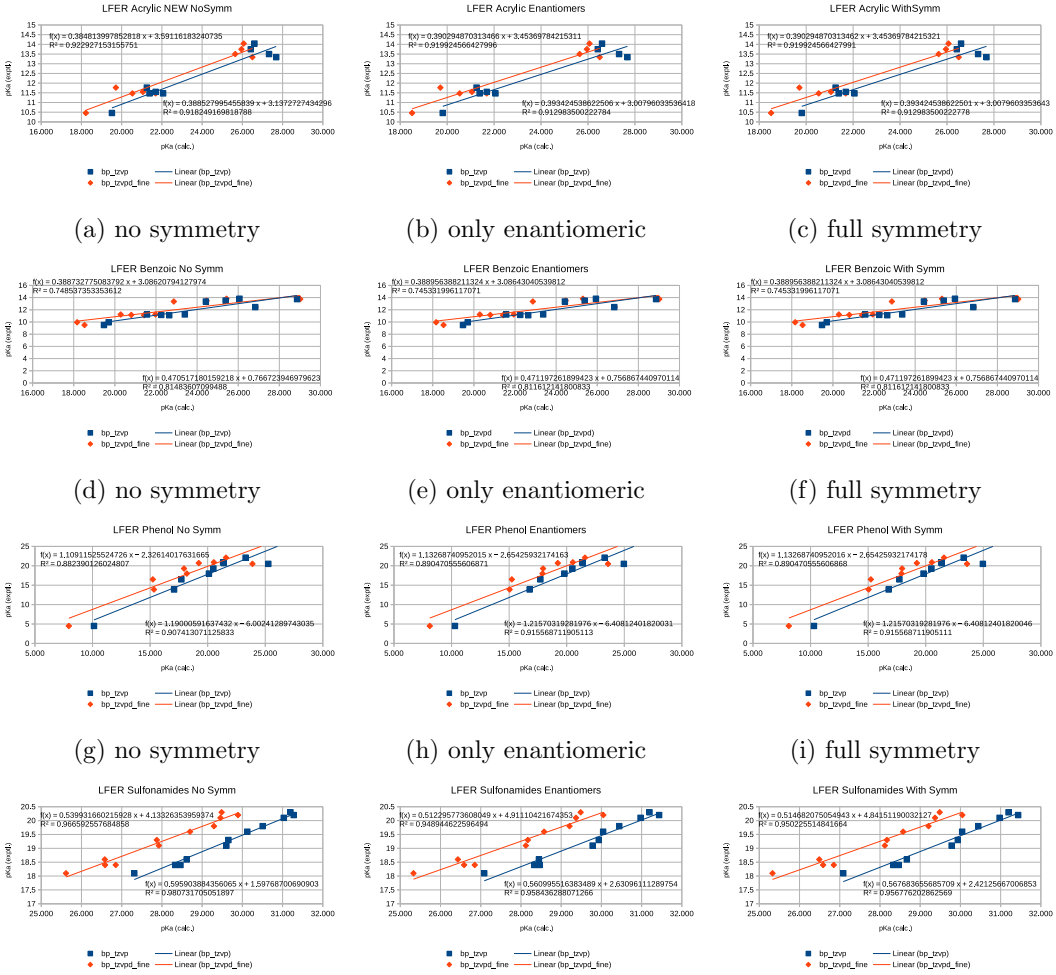
## Effect of Symmetry Factors

For all compound classes (referring to rows in Fig. S2), the LFER parameters fits were also re-done by varying the symmetry factors. We distinguish three levels:

- **no symmetry:** A *naive* case in which the conformer set, as an output of COSMOconf, was simply used as it is, without checking and compensating for chiral structures (to prevent a bias from chirality). I.e., all symmetry factors where set to one.
- **enantiomeric symmetry:** Symmetry factors of chiral conformers, whose other enantiomer was not included in the set, were set to two for avoiding a chiral bias.
- **full symmetry:** In addition to the chirality check, symmetry factors of conformers that exhibit molecular symmetry were set accordingly with respect to the symmetry operations.

The results relating to these three different levels of accounting for symmetry are shown in Fig. S2, which each column referring to one of the three levels. As can be seen from this figure, the results appear almost independent from the symmetry level for the acrylic and benzoic acids (with both $c_1$ and $r^2$ changing in the third decimal), with a more pronounced dependence for the sulfonamides ($c_1$ and $r^2$ changing in the second decimal). However, the quality of the LFER fits in terms of the linear correlation (slightly) reduces for all these three classes (especially the sulfonamides) when moving from *no symmetry* to *full symmetry*. It should be noted that both protonated (acid) and deprotonated (base) forms are typically planar (i.e., achiral) for the carboxylic acids, while both forms are chiral for the sulfonamides. Hence, chirality (i.e., including both enantiomers of all conformers) does not play a significant role for the former, and seems to cancel out for the latter.

The phenols behave differently though: this class also exhibits a moderate dependence, but the fit quality actually increases toward *full symmetry*. Here, the dominant (i.e., energetically lower) acid conformers are usually achiral (planar), while the low-energy base conformers tend to be chiral. In particular, 2-nitro-, 2,4-dinitro-, 2,5-dinitro, and 2,4,6-trinitrophenol have exclusively non-planar chiral conformers. It should be also noted that 2-nitrophenol displays the largest maximum absolute error in p$K_a$ in this subset.




(a) no symmetry (b) only enantiomeric (c) full symmetry

(d) no symmetry (e) only enantiomeric (f) full symmetry

(g) no symmetry (h) only enantiomeric (i) full symmetry

(j) no symmetry (k) only enantiomeric (l) full symmetry

Figure S2: Comparison of results from COSMO-RS calculations including symmetry to different extents (based on adjusting the symmetry factors): no symmetry (first column), only enantiomeric symmetry (middle column), and full symmetry (last column). The rows refer to the four different compounds classes in the order acrylic acids, benzoic acids, phenols, and benzenesulfonamides (from top to bottom). Experimental $\mathrm{p}K_\mathrm{a}$ values ($\mathrm{p}K_\mathrm{a}^{(\mathrm{exptl.})}$) plotted against reduced calculated Gibbs free energies of dissociation ($\frac{\Delta G}{RT\ln(10)}$) in the solvent acetone at the two computational levels BP-TZVP (blue) and BP-TZVPD-FINE (orange), together the linear regression lines in the respective color. The line equations and squared correlation coefficients are included as well.

## B.3. Theoretical Spectroscopy in DMSO

The following Supporting Information belongs to the publication *J. Phys. Chem. A* **2022**, *126* (35), 5911–5923. **Copyright © 2022 American Chemical Society**. Available online at `https://doi.org/10.1021/acs.jpca.2c04436` and reprinted in Chapter 6.

# Supporting Information

# to

# "Theoretical Study on the Photoacidity of Hydroxypyrene Derivatives in DMSO using ADC(2) and CC2"

Niklas Sülzner* and Christof Hättig

*Lehrstuhl für Theoretische Chemie, Ruhr-Universität Bochum, 44780 Bochum, Germany*

E-mail: niklas.suelzner@rub.de

Phone: +49 (0)234 32-24250

# Conformational Analysis

**Table S1: Comparison of the global minima (lowest) and highest local maxima (highest) conformers of the protonated (Acid) and deprotonated (Base) species of all photoacids A–F.** The conformer sets refer to the BP-TZVPD-FINE level of COSMO*conf*, i.e., DFT geometries using the BP86 functional and the def-TZVP basis set in combination with COSMO for implicit solvation.

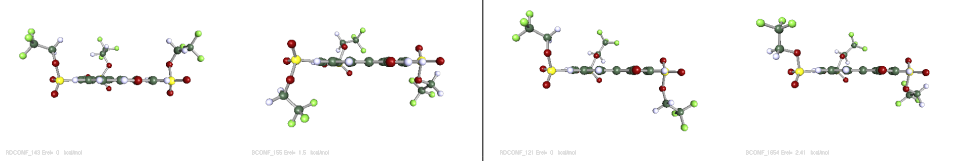
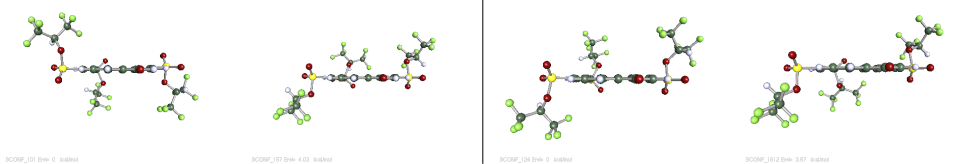
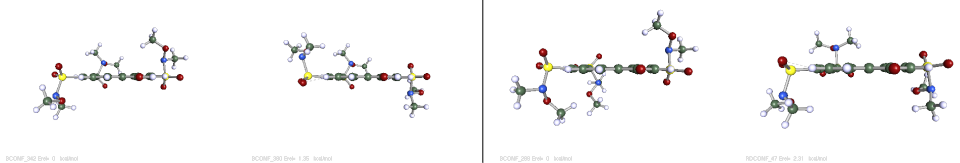
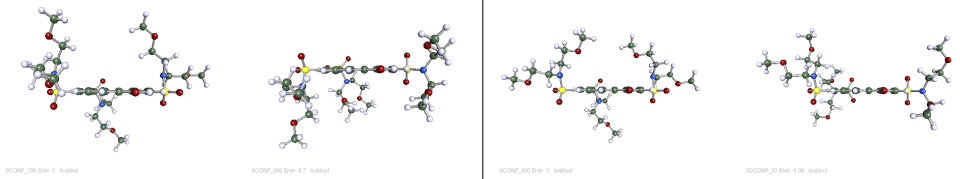
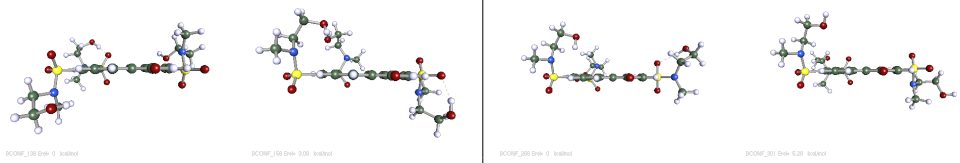
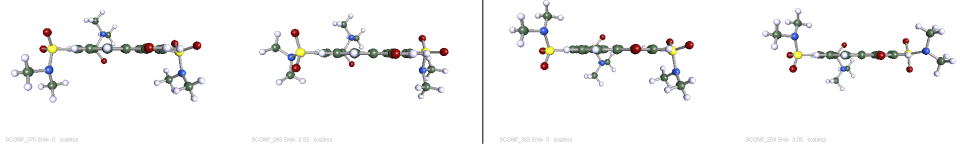
| | Acid | | Base | |
|---|---|---|---|---|
| **Photoacid** | **Lowest** | **Highest** | **Lowest** | **Highest** |
| **A** |  | | | |
| **B** |  | | | |
| **C** |  | | | |
| **D** |  | | | |
| **E** |  | | | |
| **F** |  | | | |

**Table S2: Comparison of the number of conformers $N_{\mathbf{conf}}$ in the determined conformer sets and the energies $E_{\mathbf{rel,\ max}}$ of the highest-energy conformers relative to the global minima for the protonated (Acid) and deprotonated (Base) species of all photoacids A–F.** The results refer to the BP-TZVPD-FINE level of COSMO*conf*, i.e., refined BP86 DFT energies in the def2-TZVPD basis set with a refined COSMO cavity calculated at the COSMO-DFT geometries using the BP86 functional and the def-TZVP basis set (shown in Tab. S1). Energies are given in kJ mol$^{-1}$.

| | **Acid** | | **Base** | |
|---|---|---|---|---|
| **Photoacid** | $N_{\mathrm{conf}}$ | $E_{\mathrm{rel,\ max}}$ | $N_{\mathrm{conf}}$ | $E_{\mathrm{rel,\ max}}$ |
| A | 22 | 6.3 | 16 | 10.0 |
| B | 14 | 16.7 | 11 | 16.3 |
| C | 7 | 9.6 | 9 5.9 | 9.6 |
| D | 19 | 28.0 | 17 | 17.2 |
| E | 30 | 13.0 | 27 | 22.2 |
| F | 17 | 10.5 | 13 | 8.8 |

# Method Evaluation (Bench-marking)

## Computational Details

Start structures were taken from a previous conformer search with COSMO*conf* (version 2021)[1] at the BP-TZVP level (*vide infra*) in the gas phase. The ground-state geometries for energetically most stable conformers of the protonated and deprotonated species of photoacid **F** were then re-optimized using RI-DFT[2–4] with the functionals BP86,[5,6] PBE,[7] PBE0,[8] and B3-LYP[9,10] as well as with RI-MP2,[11,12] either in the def2-TZVP[13] or def2-TZVPD[14] basis set (and with the corresponding auxiliary basis sets[15–18]), for the protonated or deprotonated species, respectively. In addition, the geometries were further optimized in the smaller def2-SVP[13] and larger def2-QZVP[14] basis sets for B3-LYP, and in Dunning's correlation-consistent basis sets[19,20] cc-pVDZ, cc-pVTZ, and cc-pVQZ (and additionally aug-cc-pVDZ and aug-cc-pVTZ for the deprotonated species)[20,21] for MP2, utilizing the corresponding auxiliary basis sets.[22] To probe geometrical changes, vertical electronic excitation energies using ADC(2)[23] in the aug-cc-pVDZ basis set[19–21] were calculated at all of these geometries.

At the minimum structures at the MP2/def2-TZVP (protonated) or MP2/def2-TZVPD (deprotonated) level, the ADC(2) vertical excitation energies were additionally calculated in the cc-pVXZ and aug-cc-pVXZ with X = D,T,Q basis sets.

## Convergence of ground-state geometries

Different combinations of electronic structure methods, i.e., several DFT functionals and MP2, and basis sets were used for geometry optimizations of the electronic ground state, consequently probed by the electronic excitation energy for the first vertical transition calculated with ADC(2) in the aug-cc-pVDZ basis set (see Tab. S3).

Considering the acid first, the excitation energies at the def2-TZVP geometries based on GGA functionals are shifted by ca. 80 meV to the blue compared to those for the hybrid functionals, and the MP2 result lies in between the two. For B3-LYP and referencing to the

**Table S3: Method and basis-set dependence of the ground-state geometry probed by the first vertical excitation.** Comparison of ADC(2)/aug-cc-pVDZ excitation energies in eV for the protonated (acid) and deprotonated (base) species of photoacid F at the respective geometries.

| Method and basis set | Vertical Excitation Energies | |
|---|---|---|
| | Acid | Base |
| BP/def2-TZVP(D)[a] | 3.158 | 2.201 |
| PBE/def2-TZVP(D)[a] | 3.155 | 2.202 |
| PBE0/def2-TZVP(D)[a] | 3.240 | 2.265 |
| B3-LYP/def2-SVP | 3.176 | 2.218 |
| B3-LYP/def2-TZVP | 3.233 | 2.248 |
| B3-LYP/def2-TZVPD | — | 2.250 |
| B3-LYP/def2-QZVP | 3.239 | 2.253 |
| MP2/def2-TZVP(D)[a] | 3.196 | 2.208 |
| MP2/cc-pVDZ | 3.135 | 2.163 |
| MP2/cc-pVTZ | 3.190 | 2.219 |
| MP2/cc-pVQZ | 3.195 | 2.224 |
| MP2/aug-cc-pVDZ | — | 2.140 |

[a] (D): larger def2-TZVPD basis set only used for base form

def2-TZVP result, the excitation energy noticeably shifts to the red (57 meV) in the smaller def2-SVP basis set, but only slightly to the blue (6 meV) in the larger def2-QZVP basis set. Similarly, it can be seen for the MP2 geometries that the largest change is found when moving from cc-pVDZ to cc-pVTZ (55 meV), and only marginal when further proceeding toward cc-pVQZ (5 meV). Hence, the geometries appear to be converged in the larger TZ and QZ basis sets, but the MP2 geometries generally give red-shifted excitation energies compared to the DFT geometries with hybrid functionals.

Similar observations are made for the base, for which def2-TZVP was replaced by the def2-TZVPD basis set due to the anionic character. Here, the GGA functional geometries also yield red-shifted excitation energies compared to the hybrid functionals with similarly large shifts. In addition, no pronounced differences between the def2-TZVP, def2-TZVPD, and def2-QZVP results with B3-LYP are found. While the MP2 results in the cc-pVXZ basis sets fall again in between GGA and hybrid functional DFT, the excitation energy in the larger aug-cc-pVDZ basis set, additionally including diffuse functions, is even more

largely red-shifted than the GGA/def2-TZVPD results, indicating that aug-cc-pVDZ is not suitable for geometries.

## Convergence of electronic excitation energies

The effect of different basis sets on the electronic excitation energies themselves was another part of our initial test calculations. Table S4 compares the ADC(2) excitation energies for the first five vertical transitions in the cc-pVXZ and aug-cc-pVDZ (X=D,T,Z) basis sets for the acid and base. Due to the dominating role in the discussion of photoacids, we will stick to the results for the first excitation in the following.

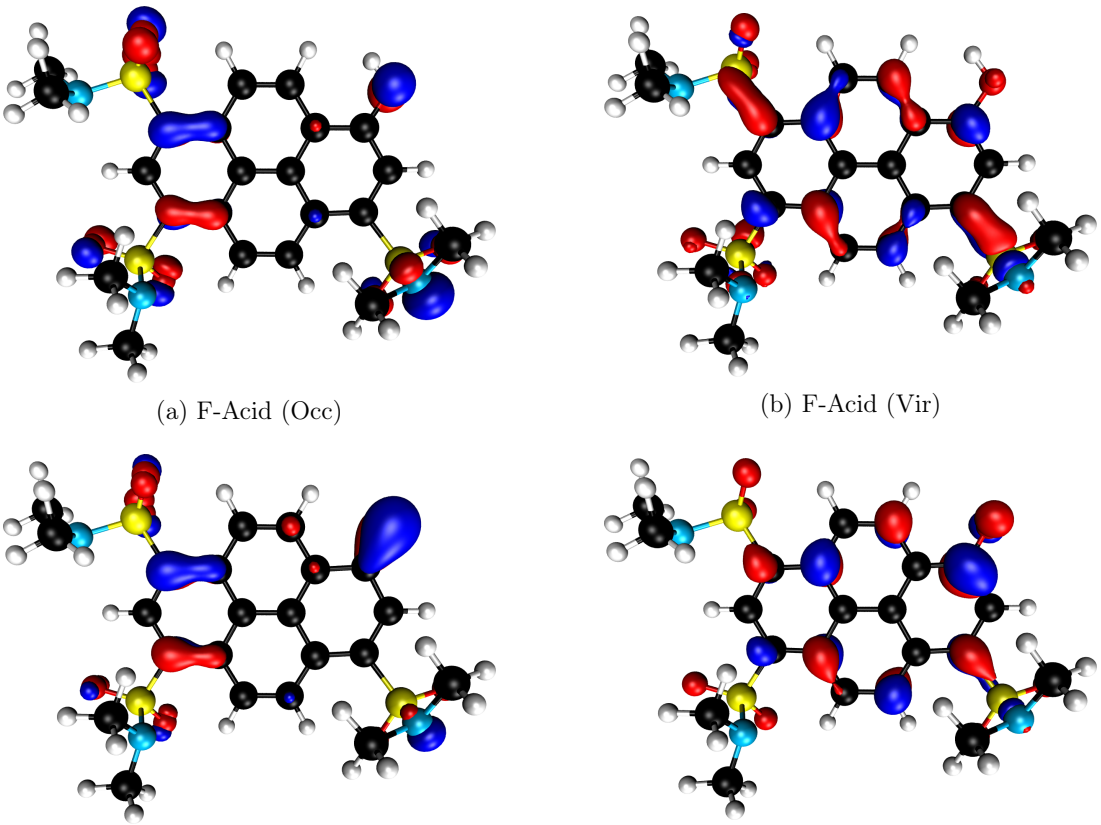
**Table S4: Basis-set convergence of the electronic excitation energies.** Comparison of ADC(2) electronic excitation energies in eV for the first five vertical transitions computed at the COSMO-MP2/cc-pVDZ ground-state geometries of the acid and base form of photoacid F.

| Transition | cc-pVDZ | cc-pVTZ | cc-pVQZ | aug-cc-pVDZ | aug-cc-pVTZ | aug-cc-pVQZ |
|---|---|---|---|---|---|---|
| | **Acid** | | | | | |
| 1 | 3.200 | 3.115 | 3.094 | 3.128 | 3.095 | 3.089 |
| 2 | 3.486 | 3.407 | 3.388 | 3.412 | 3.386 | 3.381 |
| 3 | 4.248 | 4.122 | 4.092 | 4.149 | 4.096 | 4.085 |
| 4 | 4.368 | 4.249 | 4.219 | 4.261 | 4.218 | 4.209 |
| 5 | 4.466 | 4.342 | 4.314 | 4.348 | 4.312 | 4.305 |
| | **Base** | | | | | |
| 1 | 2.291 | 2.209 | 2.187 | 2.208 | 2.180 | 2.176 |
| 2 | 2.694 | 2.660 | 2.666 | 2.637 | 2.637 | 2.658 |
| 3 | 2.888 | 2.811 | 2.799 | 2.804 | 2.791 | 2.793 |
| 4 | 3.580 | 3.474 | 3.451 | 3.424 | 3.434 | 3.435 |
| 5 | 3.770 | 3.712 | 3.715 | 3.472 | 3.593 | 3.635 |

For both the acid and base, a systematic convergence of the excitation energy can be observed for the series of correlation consistent basis sets as well as the related series of augment basis sets. As anticipated, the results for aug-cc-pVXZ are always slightly red-shifted and hence closer to the basis-set limit comapred to cc-pVXZ at the same cardinal number (X). The convergence consists in an almost monotonous decrease of the excitation energy from 3.200 eV at cc-pVDZ to 3.089 eV at aug-cc-pVQZ for the acid and from 2.291 eV to 2.176 eV for the base, respectively. Hence, the acid and base exhibit roughly the same decrease in energy by approx. 110 meV. It should be noted that the largest change (70-80 meV) takes place when moving from cc-pVDZ to its augment counterpart aug-cc-pVDZ,

i.e., when providing additional diffuse functions. This effect is slightly larger for the base (∼80 meV) compared to the acid (∼70 meV) as can be rationalized based on the higher demand for charge delocalization in the base due to its anionic nature. Furthermore, the addition of diffuse functions seems to have almost the same effect on the first transition as increasing the cardinal number, i.e., adding basis functions for each valence electron. For the higher excitations, similar observations can be made, but the addition of diffusive functions becomes more important than increasing the cardinal number due to the increasingly diffusive character of the excited states.

## Difference between ADC(2) and CC2 Excitation Energies



(a) F-Acid (Occ)

(b) F-Acid (Vir)

(c) F-Base (Occ)

(d) F-Base (Vir)

Figure S1: Overview of the occupied (occ) and virtual (vir) NTOs for the first NTO pair of the ground-state COSMO-CC2 $T_1$ amplitudes of the acid and base forms of photoacid **F**; Based on COSMO-CC2/aug-cc-pVDZ single-point calculations for the ground state at the COSMO-MP2/cc-pVDZ geometries. The weights of these NTO pairs are 11.3 % (acid) and 14.2 % (base), respectively.

# UV/VIS Absorption and Fluorescence Emission Spectra of all Photoacids

## NTO Analysis – Acid and Base of Photoacid F

**Table S5: Comparison of the first five electronic transitions of F-Acid in terms of vertical excitation energy (VEE; in eV), oscillator strength, contribution (in %) of the first NTO pair, and plots of the occupied and virtual NTOs.** Excitations calculated with COSMO-ADC(2)/aug-cc-pVDZ at the COSMO-MP2/cc-pVDZ ground-state equilibrium geometry.

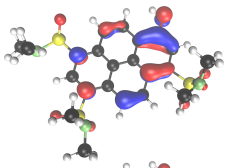
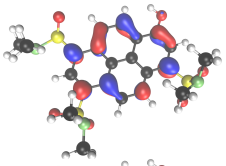
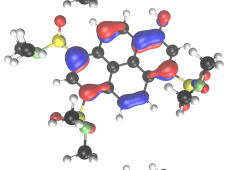
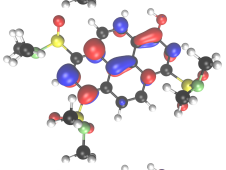
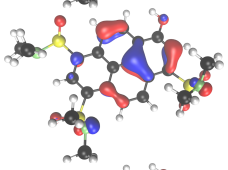
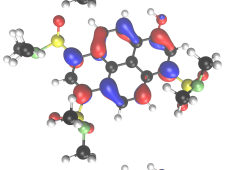
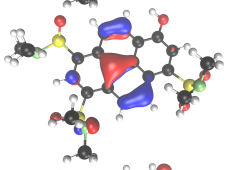
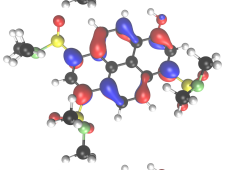
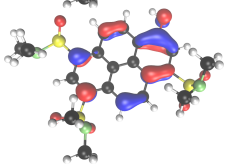
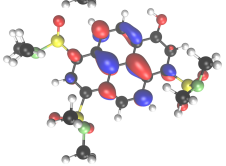
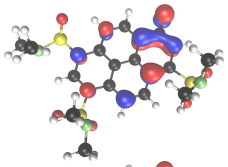
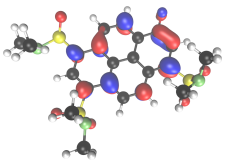
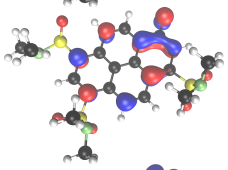
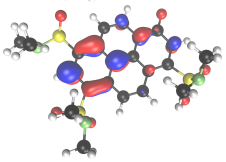
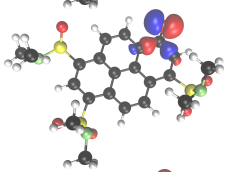
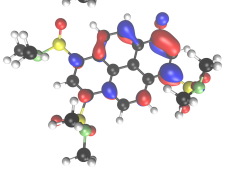
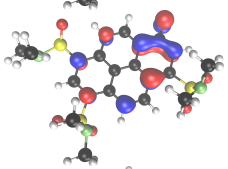
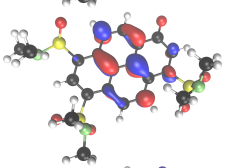
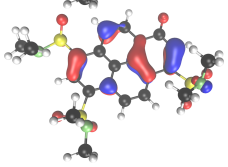
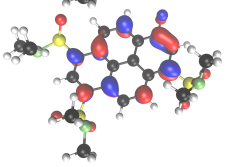
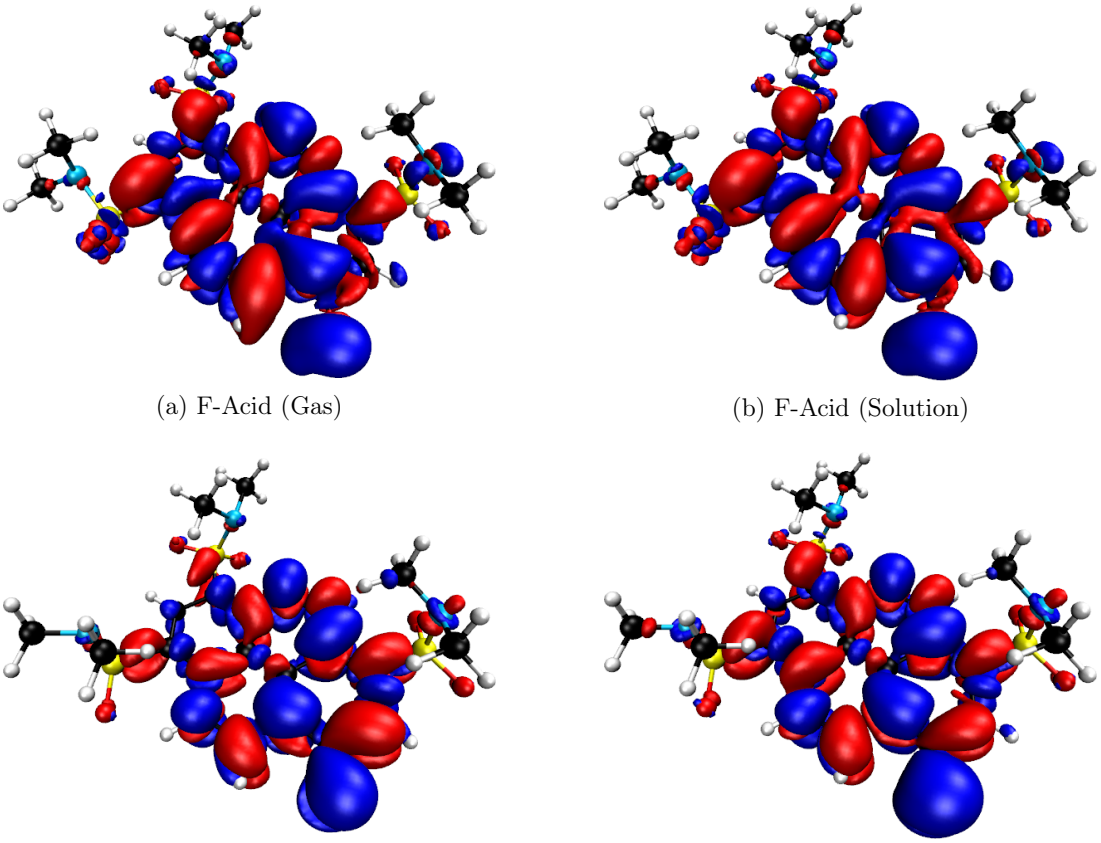
| # | VEE [eV] | Oscil. Str. | contri. | occ. NTO | vir. NTO |
|---|---|---|---|---|---|
| 1 | 2.96 | 0.66552924 | 97.40 |  |  |
| 2 | 3.42 | 0.03302052 | 66.75 |  |  |
| 3 | 4.00 | 0.32931335 | 71.55 |  |  |
| 4 | 4.18 | 0.25536917 | 81.09 |  |  |
| 5 | 4.28 | 0.00975374 | 74.47 |  |  |

**Table S6: Comparison of the first five electronic transitions of F-Base in terms of vertical excitation energy (VEE; in eV), oscillator strength, contribution (in %) of the first NTO pair, and plots of the occupied and virtual NTOs.** Excitations calculated with COSMO-ADC(2)/aug-cc-pVDZ at the COSMO-MP2/cc-pVDZ ground-state equilibrium geometry.

| # | VEE [eV] | Oscil. Str. | contri. | occ. NTO | vir. NTO |
|---|---|---|---|---|---|
| 1 | 2.17 | 0.55065512 | 98.01 |  |  |
| 2 | 2.97 | 0.07865403 | 96.03 |  |  |
| 3 | 3.10 | 0.00032939 | 99.79 |  |  |
| 4 | 3.54 | 0.02819263 | 97.37 |  |  |
| 5 | 3.88 | 0.14997231 | 84.51 |  |  |

## Intramolecular Charge Transfer – Difference Electron Density



(a) F-Acid (Gas)

(b) F-Acid (Solution)

(c) F-Base (Gas)

(d) F-Base (Solution)

Figure S2: Difference electron density between the excited state ($S_1$) and the ground state ($S_0$) plotted at isosurface values of $-5 \times 10^{-4}$ (blue) and $+5 \times 10^{-4}$ (red) of photoacid **F**. Acid (Base) on the top (bottom) and gas-phase (solution-phase) on the left (right). Densities calculated at MP2 for $S_0$ and ADC(2) for $S_1$ in the aug-cc-pVDZ basis set using the MP2/cc-pVDZ gas-phase geometry. Solution-phase refers to COSMO calculations at the same gas-phase geometry.

## NTO Analysis – Comparison of all Photoacids

**Table S7: Comparison of the first NTO occupied-virtual pair for the first vertical electronic transition corresponding to ground-state absorption of the protonated (Acid) and deprotonated (Base) species of all photoacids A–F.** Excitations calculated with COSMO-ADC(2)/aug-cc-pVDZ at the COSMO-MP2/cc-pVDZ ground-state ($S_0$) equilibrium geometries.

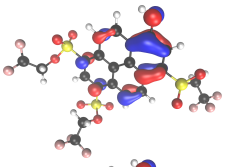
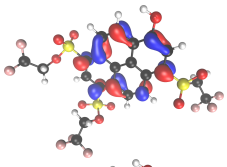
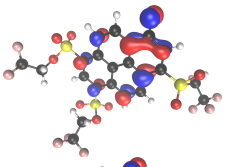
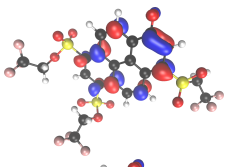
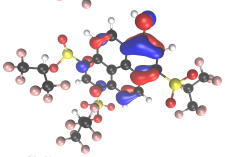
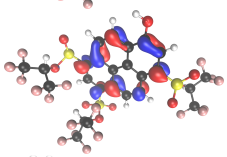
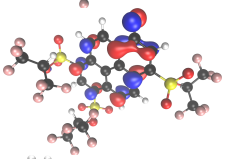
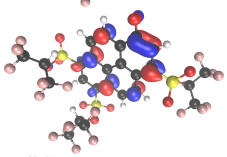
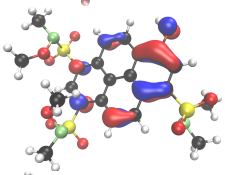
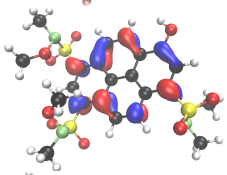
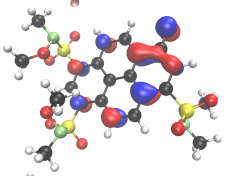
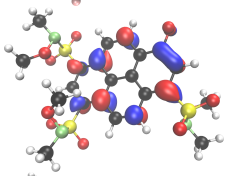
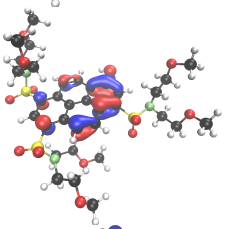
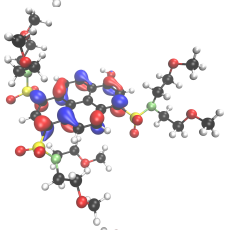
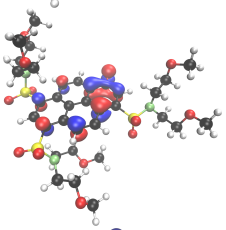
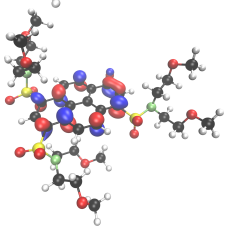
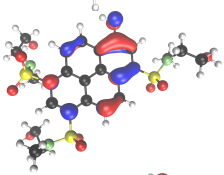
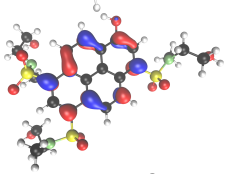
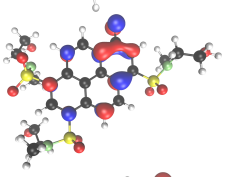
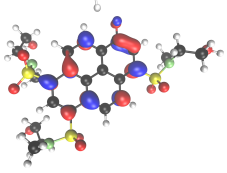
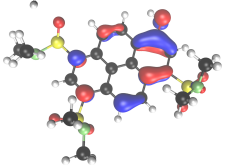
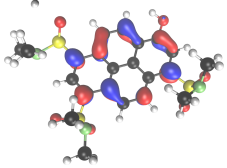
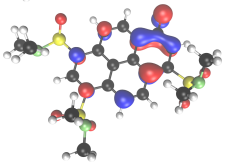
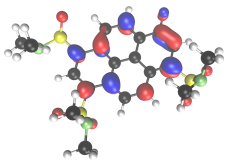
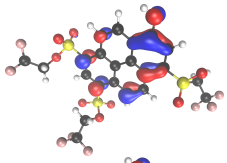
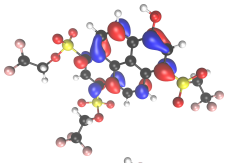
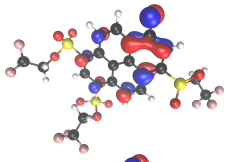
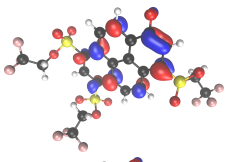
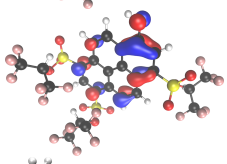
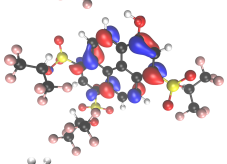
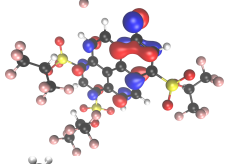
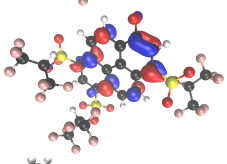
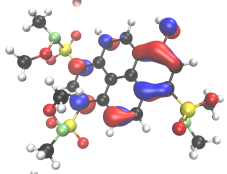
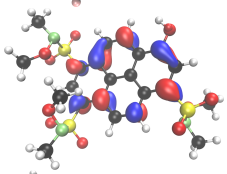
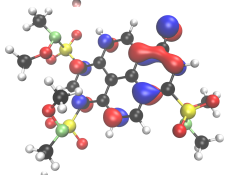
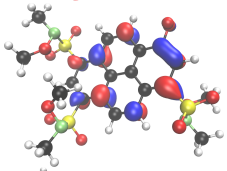
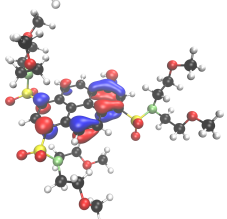
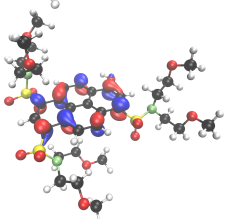
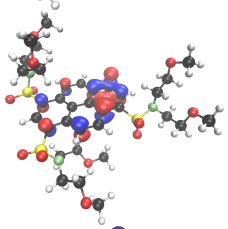
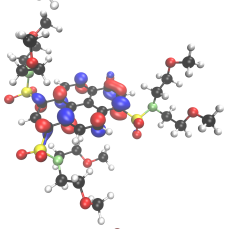
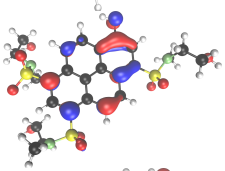
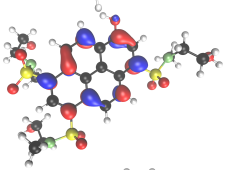
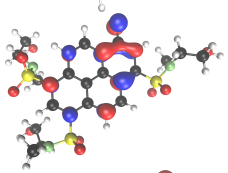
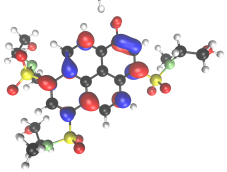
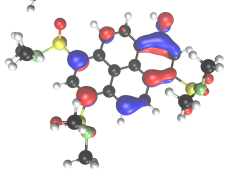
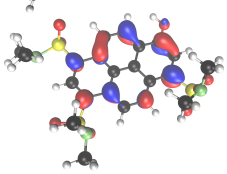
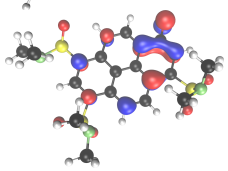
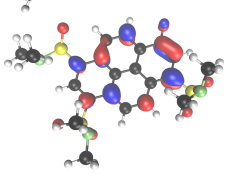
| Photoacid | Acid | | Base | |
|---|---|---|---|---|
| | Occ | Vir | Occ | Vir |
| **A** |  |  |  |  |
| **B** |  |  |  |  |
| **C** |  |  |  |  |
| **D** |  |  |  |  |
| **E** |  |  |  |  |
| **F** |  |  |  |  |

**Table S8: Comparison of the first NTO occupied-virtual pair for the first vertical electronic transition corresponding to excited-state emission of the protonated (Acid) and deprotonated (Base) species of all photoacids A–F.** Excitations calculated with COSMO-ADC(2)/aug-cc-pVDZ at the COSMO-ADC(2)/cc-pVDZ excited-state ($S_1$) equilibrium geometry.

| Photoacid | Acid | | Base | |
|---|---|---|---|---|
| | Occ | Vir | Occ | Vir |
| **A** |  |  |  |  |
| **B** |  |  |  |  |
| **C** |  |  |  |  |
| **D** |  |  |  |  |
| **E** |  |  |  |  |
| **F** |  |  |  |  |

## UV/VIS Absorption and Fluorescence Emission Energies

**Table S9: Comparison of vertical electronic (de-)excitation energies in eV for the first transition calculated at the COSMO-MP2/cc-pVDZ ground-state geometry (for $S_0$ absorption) and at the COSMO-ADC(2)/cc-pVDZ excited-state geomtery (for $S_1$ emission) of the acid and base form of the six photoacids A–F in DMSO.**

| | | Photoacids | | | | | |
|---|---|---|---|---|---|---|---|
| | **Level** | **A** | **B** | **C** | **D** | **E** | **F** |
| | | **Acid** | | | | | |
| **$S_0$** | COSMO-ADC(2) | 2.885 | 2.818 | 2.901 | 2.870 | 2.963 | 2.957 |
| | COSMO-CC2 | 2.938 | 2.882 | 2.946 | 2.921 | 3.006 | 2.999 |
| | Experiment[a] | 2.818 | 2.761 | 2.831 | 2.877 | 2.883 | 2.877 |
| **$S_1$** | COSMO-ADC(2) | 2.477 | 2.410 | 2.494 | 2.470 | 2.555 | 2.547 |
| | COSMO-CC2 | 2.605 | 2.539 | 2.610 | 2.589 | 2.671 | 2.655 |
| | Experiment[a] | — | — | 2.450 | 2.588 | 2.599 | 2.599 |
| | | **Base** | | | | | |
| **$S_0$** | COSMO-ADC(2) | 2.106 | 2.024 | 2.101 | 2.106 | 2.189 | 2.174 |
| | COSMO-CC2 | 2.229 | 2.155 | 2.220 | 2.229 | 2.300 | 2.283 |
| | Experiment[a] | 2.183 | 2.153 | 2.183 | 2.234 | 2.238 | 2.238 |
| **$S_1$** | COSMO-ADC(2) | 1.943 | 1.850 | 1.936 | 1.942 | 2.025 | 2.001 |
| | COSMO-CC2 | 2.078 | 1.995 | 2.068 | 2.079 | 2.155 | 2.129 |
| | Experiment[a] | 2.160 | 2.134 | 2.153 | 2.187 | 2.191 | 2.194 |

[a] Experimental values are taken from Ref. 24 and converted into eV.

## Stokes Shifts

**Table S10: Comparison of calculated and experimental Stokes shifts of the acid and base forms of the photoacids A–F in the solvent DMSO. Stokes shifts based on the calculated absorption and emission energies of the first vertical transition at the COSMO-ADC(2) and COSMO-CC2 levels (cf. Tab. S9) as well as for the experimental values taken from Ref. 24.**

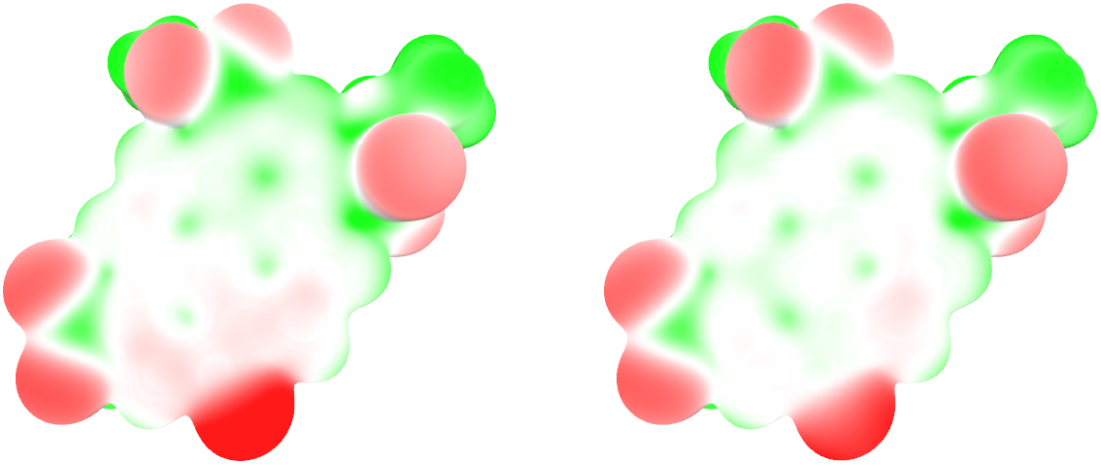
| | | Photoacids | | | | | |
|---|---|---|---|---|---|---|---|
| | **Levels** | **A** | **B** | **C** | **D** | **E** | **F** |
| **Acid** | COSMO-ADC(2) | 0.408 | 0.408 | 0.407 | 0.401 | 0.409 | 0.410 |
| | COSMO-CC2 | 0.333 | 0.343 | 0.337 | 0.332 | 0.335 | 0.344 |
| | Experiment | — | — | 0.380 | 0.288 | 0.284 | 0.277 |
| **Base** | COSMO-ADC(2) | 0.162 | 0.173 | 0.165 | 0.165 | 0.164 | 0.172 |
| | COSMO-CC2 | 0.151 | 0.160 | 0.151 | 0.151 | 0.145 | 0.153 |
| | Experiment | 0.023 | 0.019 | 0.030 | 0.047 | 0.047 | 0.044 |

## Ground-state and Excited-state Acidity in Water

**Table S11: Comparison of ground-state and excited-state acidities of all photoacids A–F in the solvent water.** Predicted p$K_a$ values using COSMO-RS at the BP-TZVP and BP-TZVPD-FINE levels and experimental values taken from Ref. 24. Calculated experimental $\Delta$p$K_a$ values based on the Förster cycle using either the absorption, emission, or averaged excitation energies; in comparison to the reported value. Comparison of reported experimental p$K_a^*$ in water as determined using the Förster-cycle or fluorescence titration and of our calculated p$K_a^*$ estimate using the BP-TZVP p$K_a$ in water and the averaged COSMO-CC2 $\Delta$p$K_a$ value determined in DMSO.

| | | **Photoacids** | | | | | |
|---|---|---|---|---|---|---|---|
| | | **A** | **B** | **C** | **D** | **E** | **F** |
| p$K_a$ | calc. (BP-TZVP) | 4.6 | 4.6 | 4.9 | 5.3 | 4.9 | 5.4 |
| | calc. (BP-TZVPD-FINE) | 4.0 | 4.9 | 4.1 | 5.0 | 4.9 | 4.9 |
| | experimental | 4.7 | 4.4 | 5.6 | 5.7 | 5.6 | 5.6 |
| $\Delta$p$K_a$ | absorption (exptl.) | -8.6 | -10.8 | -7.7 | -7.1 | -7.2 | -7.2 |
| | emission (exptl.) | -6.1 | -5.6 | -5.8 | -5.8 | -5.8 | -6.0 |
| | mean (exptl.) | -7.3 | -8.2 | -6.7 | -6.4 | -6.5 | -6.6 |
| | experimental (reported) | -7.4 | -8.3 | -6.8 | -6.5 | -6.5 | -6.6 |
| p$K_a^*$ | exptl. (Förster cycle) | -2.7 | -3.9 | -1.2 | -0.8 | -0.9 | -1.0 |
| | exptl. (Fluorescence Titration) | -2.9 | -2.5 | -1.0 | -1.0 | -0.6 | -0.3 |

## Electrostatic Potential – Base of Photoacid F



(a) (b)

Figure S3: Electrostatic potential plotted in the range from −0.20 (red) to 0.00 (green) [a. u.] at the electron density isosurface (contour value: 0.01 a. u.) of the electronic ground state $S_0$ (a) and excited state $S_1$ (b) of the deprotonated species of photoacid **F** in solution. Densities calculated at COSMO-MP2 for $S_0$ and COSMO-ADC(2) for $S_1$ in the aug-cc-pVDZ basis set using the COSMO-MP2/cc-pVDZ solution-phase geometry. The molecule is oriented such that the $O^-$ (formerly OH) group is located at the bottom.

## References

(1) BIOVIA COSMO*conf*, Release 2021; Dassault Systèmes. `http://www.3ds.com`.

(2) Treutler, O.; Ahlrichs, R. Efficient Molecular Numerical Integration Schemes. J. Chem. Phys. **1995**, 102, 346–354.

(3) Eichkorn, K.; Treutler, O.; Öhm, H.; Häser, M.; Ahlrichs, R. Auxiliary Basis Sets to Approximate Coulomb Potentials. Chem. Phys. Lett. **1995**, 240, 283–290.

(4) Eichkorn, K.; Weigend, F.; Treutler, O.; Ahlrichs, R. Auxiliary Basis Sets for Main Row Atoms and Transition Metals and their Use to Approximate Coulomb Potentials. Theor. Chem. Acc. **1997**, 97, 119–124.

(5) Becke, A. D. Density-Functional Exchange-Energy Approximation with Correct Asymptotic Behavior. Phys. Rev. A **1988**, 38, 3098–3100.

(6) Perdew, J. P. Density-Functional Approximation for the Correlation Energy of the Inhomogeneous Electron Gas. Phys. Rev. B **1986**, 33, 8822–8824.

(7) Perdew, J. P.; Burke, K.; Ernzerhof, M. Generalized Gradient Approximation Made Simple. Phys. Rev. Lett. **1996**, 77, 3865–3868.

(8) Perdew, J. P.; Ernzerhof, M.; Burke, K. Rationale for Mixing Exact Exchange with Density Functional Approximations. J. Chem. Phys. **1996**, 105, 9982–9985.

(9) Lee, C.; Yang, W.; Parr, R. G. Development of the Colle-Salvetti Correlation-Energy Formula into a Functional of the Electron Density. Phys. Rev. B **1988**, 37, 785–789.

(10) Becke, A. D. Density-Functional Thermochemistry. III. The Role of Exact Exchange. J. Chem. Phys. **1993**, 98, 5648–5652.

(11) Weigend, F.; Häser, M. RI-MP2: First Derivatives and Global Consistency. Theor. Chem. Acc. **1997**, 97, 331–340.

(12) Hättig, C.; Hellweg, A.; Köhn, A. Distributed Memory Parallel Implementation of Energies and Gradients for Second-Order Møller-Plesset Perturbation Theory with the Resolution-of-the-Identity Approximation. Phys. Chem. Chem. Phys. **2006**, 8, 1159–1169.

(13) Weigend, F.; Ahlrichs, R. Balanced Basis Sets of Split Valence, Triple Zeta Valence and Quadruple Zeta Valence Quality for H to Rn: Design and Assessment of Accuracy. Phys. Chem. Chem. Phys. **2005**, 7, 3297–3305.

(14) Rappoport, D.; Furche, F. Property-Optimized Gaussian Basis Sets for Molecular Response Calculations. J. Chem. Phys. **2010**, 133, 134105.

(15) Weigend, F. Accurate Coulomb-Fitting Basis Sets for H to Rn. Phys. Chem. Chem. Phys. **2006**, 8, 1057–1065.

(16) Weigend, F.; Häser, M.; Patzelt, H.; Ahlrichs, R. RI-MP2: Optimized Auxiliary Basis Sets and Demonstration of Efficiency. Chem. Phys. Lett. **1998**, 294, 143–152.

(17) Hellweg, A.; Hättig, C.; Höfener, S.; Klopper, W. Optimized Accurate Auxiliary Basis Sets for RI-MP2 and RI-CC2 Calculations for the Atoms Rb to Rn. Theor. Chem. Acc. **2007**, 117, 587–597.

(18) Hellweg, A.; Rappoport, D. Development of New Auxiliary Basis Functions of the Karlsruhe Segmented Contracted Basis Sets including Diffuse Basis Functions (def2-SVPD, def2-TZVPPD, and def2-QVPPD) for RI-MP2 and RI-CC Calculations. Phys. Chem. Chem. Phys. **2015**, 17, 1010–1017.

(19) Dunning, T. H. Gaussian Basis Sets for Tse in Correlated Molecular Calculations. I. The Atoms Boron through Neon and Hydrogen. J. Chem. Phys. **1989**, 90, 1007–1023.

(20) Woon, D. E.; Dunning, T. H. Gaussian Basis Sets for Use in Correlated Molecular

Calculations. III. The Atoms Aluminum through Argon. J. Chem. Phys. **1993**, 98, 1358–1371.

(21) Kendall, R. A.; Dunning, T. H.; Harrison, R. J. Electron Affinities of the First-Row Atoms Revisited. Systematic Basis Sets and Wave Functions. J. Chem. Phys. **1992**, 96, 6796–6806.

(22) Weigend, F.; Köhn, A.; Hättig, C. Efficient Use of the Correlation Consistent Basis Sets in Resolution of the Identity MP2 Calculations. J. Chem. Phys. **2002**, 116, 3175–3183.

(23) Hättig, C. In Response Theory and Molecular Properties (A Tribute to Jan Linderberg and Poul Jørgensen); Jensen, H., Ed.; Advances in Quantum Chemistry; Academic Press, 2005; Vol. 50; pp 37–60.

(24) Finkler, B.; Spies, C.; Vester, M.; Walte, F.; Omlor, K.; Riemann, I.; Zimmer, M.; Stracke, F.; Gerhards, M.; Jung, G. Highly Photostable "Super"-Photoacids for Ultrasensitive Fluorescence Spectroscopy. Photochem. Photobiol. Sci. **2014**, 13, 548–562.

# C. Additional Materials for Chapter 7

## C.1. Numerical Complements to Plotted Data

Table C.1.: **Numerical values for Fig. 7.1.** Comparison of vertical electronic excitation energies in eV for the first transition with different combinations of equilibrium structures for $S_0$ or $S_1$ (rows) and methods for the calculation of the electronic excitation energy (columns) of the protonated and deprotonated species of photoacid **F**. For comparison, the experimental results from Ref. 494 are from top to bottom: 2.844 eV, 2.551 eV, 2.156 eV, 2.141 eV.

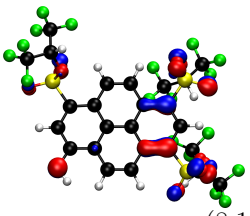
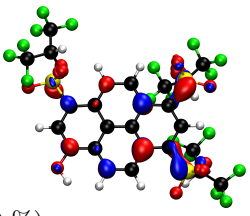
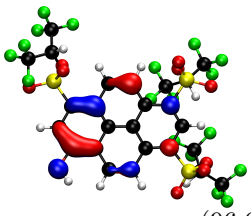
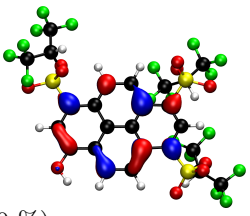
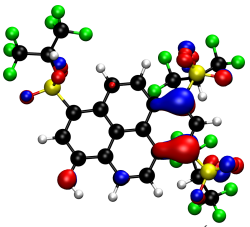
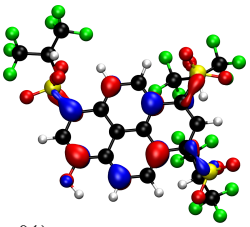
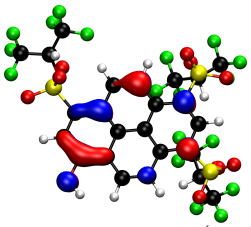
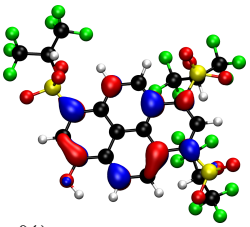
| | | **Excitation Energies** | | | |
|---|---|---|---|---|---|
| | **Geometries** | **ADC(2)** | **COSMO-ADC(2)** | **CC2** | **COSMO-CC2** |
| | | **Acid** | | | |
| **$S_0$** | **MP2** | 3.028 | 2.888 | 3.103 | 2.954 |
| | **COSMO-MP2** | 2.992 | 2.848 | 3.070 | 2.916 |
| | **CC2** | 2.968 | 2.821 | 3.050 | 2.896 |
| | **COSMO-CC2** | 2.932 | 2.779 | 3.018 | 2.858 |
| **$S_1$** | **ADC(2)** | 2.670 | 2.514 | 2.784 | 2.629 |
| | **COSMO-ADC(2)** | 2.621 | 2.442 | 2.749 | 2.573 |
| | **CC2** | 2.636 | 2.480 | 2.752 | 2.597 |
| | | **Base** | | | |
| **$S_0$** | **MP2** | 2.133 | 2.055 | 2.309 | 2.190 |
| | **COSMO-MP2** | 2.121 | 2.051 | 2.305 | 2.191 |
| | **CC2** | 2.097 | 2.023 | 2.282 | 2.163 |
| | **COSMO-CC2** | 2.083 | 2.017 | 2.277 | 2.162 |
| **$S_1$** | **ADC(2)** | 0.573 | 1.410 | 1.061 | 1.462 |
| | **COSMO-ADC(2)** | 1.883 | 1.867 | 2.132 | 2.027 |
| | **CC2** | 1.909 | 1.864 | 2.129 | 2.022 |

Table C.2.: **Numerical values for Fig. 7.2.** Comparison of vertical electronic excitation energies in eV for the first transition calculated of the acid and base form of the photoacids A–F in acetone. Absorption energies were calculated at the COSMO-MP2/cc-pVDZ $S_0$ geometry, while emission energies were calculated at the COSMO-ADC(2)/cc-pVDZ $S_1$ geometry; both either with COSMO-ADC(2) or COSMO-CC2 in the aug-cc-pVDZ basis set. In addition, COSMO-CC2/aug-cc-pVDZ absorption energies were also calculated at the re-optimized COSMO-CC2 $S_0$ geometry. Experimental values are taken from Ref. 309.

| | | **Photoacids** | | | | | |
|---|---|---|---|---|---|---|---|
| | **Level** | **A** | **B** | **C** | **D** | **E** | **F** |
| | | **Acid** | | | | | |
| **$S_0$** | COSMO-ADC(2)//COSMO-MP2 | 2.912 | 2.848 | 2.927 | 2.898 | 2.987 | 2.983 |
| | COSMO-CC2//COSMO-MP2 | 2.970 | 2.916 | 2.977 | 2.951 | 3.033 | 3.029 |
| | COSMO-CC2//COSMO-CC2 | 2.920 | 2.858 | 2.935 | 2.905 | 2.989 | 2.989 |
| | Experiment | 2.883 | 2.831 | 2.904 | 2.938 | 2.945 | 2.945 |
| **$S_1$** | COSMO-ADC(2)//COSMO-ADC(2) | 2.483 | 2.428 | 2.535 | 2.500 | 2.598 | 2.588 |
| | COSMO-CC2//COSMO-ADC(2) | 2.603 | 2.561 | 2.652 | 2.621 | 2.714 | 2.698 |
| | Experiment | 2.605 | 2.551 | 2.684 | 2.713 | 2.719 | 2.719 |
| | | **Base** | | | | | |
| **$S_0$** | COSMO-ADC(2)//COSMO-MP2 | 2.130 | 2.048 | 2.121 | 2.126 | 2.206 | 2.190 |
| | COSMO-CC2//COSMO-MP2 | 2.263 | 2.189 | 2.249 | 2.258 | 2.326 | 2.310 |
| | COSMO-CC2//COSMO-CC2 | 2.235 | 2.153 | 2.224 | 2.231 | 2.298 | 2.281 |
| | Experiment | 2.187 | 2.156 | 2.183 | 2.242 | 2.450 | 2.234 |
| **$S_1$** | COSMO-ADC(2)//COSMO-ADC(2) | 1.928 | 1.851 | 1.958 | 1.962 | 2.048 | 2.017 |
| | COSMO-CC2//COSMO-ADC(2) | 2.080 | 2.011 | 2.100 | 2.108 | 2.186 | 2.152 |
| | Experiment | 2.168 | 2.141 | 2.160 | 2.191 | 2.309 | 2.194 |

## C.2. NTO Analysis

Table C.3.: **Comparison of NTOs for $T_1$ amplitudes and first electronic excitations.** Overview of the occupied (Occ) and virtual (Vir) NTOs for the first NTO pair of the ground-state $T_1$ amplitudes and first electronic excitation with COSMO-CC2/aug-cc-pVDZ at the COSMO-MP2/cc-pVDZ ($S_0$) and COSMO-ADC(2)/cc-pVDZ ($S_1$) equilibrium geometries of the acid species of photoacid **B**. The weights of the corresponding NTO pairs and the CC2 $D_1$ diagnostic are included as well.

| | **$T_1$ Amplitudes** | | **First Electronic Excitation** | |
|---|---|---|---|---|
| | **Occ** | **Vir** | **Occ** | **Vir** |
| **$S_0$(eq.)** |  |  |  |  |
| | (8.162 %) | | (96.640 %) | |
| | ($D_1 = 0.1075$) | | | |
| **$S_1$(eq.)** |  |  |  |  |
| | (11.178 %) | | (97.116 %) | |
| | ($D_1 = 0.1298$) | | | |

## C.3. Additional Results

Table C.4.: **Supplement to Tab. 7.4.** $\Delta pK_a$ based on the Förster cycle (cf. Eq. (7.1)) using either absorption, emission, or averaged excitation energies calculated with COSMO-ADC(2) and COSMO-CC2 at the COSMO-MP2 ($S_0$) or COSMO-ADC(2) ($S_1$) geometries (cf. Tab. C.2) and the experimental results (taken from Ref. 309). For absorption, COSMO-CC2 absorption energies at the COSMO-CC2 $S_0$ geometry are additionally included.

| | | **Photoacids** | | | | | |
|---|---|---|---|---|---|---|---|
| | **Level** | **A** | **B** | **C** | **D** | **E** | **F** |
| **Absorption** | COSMO-ADC(2)//COSMO-MP2 | −13.2 | −13.5 | −13.6 | −13.1 | −13.2 | −13.4 |
| | COSMO-CC2/COSMO-MP2 | −12.0 | −12.3 | −12.3 | −11.7 | −11.9 | −12.2 |
| | COSMO-CC2//COSMO-CC2 | −11.6 | −11.9 | −12.0 | −11.4 | −11.7 | −12.0 |
| | Experimental | −11.8 | −11.4 | −12.2 | −11.8 | −8.4 | −12.0 |
| **Emission** | COSMO-ADC(2)//COSMO-ADC(2) | −9.4 | −9.7 | −9.8 | −9.1 | −9.3 | −9.7 |
| | COSMO-CC2//COSMO-ADC(2) | −8.8 | −9.3 | −9.3 | −8.7 | −8.9 | −9.2 |
| | Experimental | −7.4 | −6.9 | −8.9 | −8.8 | −6.9 | −8.9 |
| **Averaged** | COSMO-ADC(2) | −11.3 | −11.6 | −11.7 | −11.1 | −11.2 | −11.5 |
| | COSMO-CC2 | −10.4 | −10.8 | −10.8 | −10.2 | −10.4 | −10.7 |
| | Experimental | −9.6 | −9.2 | −10.5 | −10.3 | −7.6 | −10.4 |